Optimum design for sustainable 'green' bonded concrete overlays failure due to sheer and delamination

Olubanwo, Adegoke Omotayo

Award date:
2013

Awarding institution:
Coventry University

“Optimum design for Sustainable ‘Green’ Bonded Concrete Overlays: Failure due to shear and delamination”

ADEGOKE OMOTAYO OLUBANWO

A Thesis submitted in partial fulfilment of the University’s requirements for the Degree of Doctor of Philosophy

2013

Coventry University

Department of Civil Engineering, Architecture and Building in collaboration with Aggregate Industries, UK.

Abstract

Adequate interfacial bond performance of Bonded Concrete Overlay (BCO) systems requires novel integration of material mixture design, compatibility model development, and interfacial bond design. This entails the use of the right materials, on the right substrate, in the right way, in order to secure the best possible composite behaviour. The overall composite performance of BCOs depends largely on achieving the right proportion of blend for the overlay material. The use of mixture experiments provides a flexible, easy, and quick way of optimizing multi-component materials of this nature. This study describes the use of optimization techniques within the concept of material mixture experiments for proportioning and designing the material constituents of a Bonded Roller Compacted Fibre Reinforced Polymer Modified Concrete (BRCFRPMC). By constraining the range of variability of the constituents, a feasible design space was created with 13 experimental points treated based on the required structural and elastic properties of the overlay. The optimum consistency-time for full consolidation and composite behaviour with the substrate ordinary Portland cement concrete (OPCC) was established between 34.05 and 34.87 seconds, while the resulting apparent maximum density achieves between 97.11% - 98.03% of the theoretical air-free density. In addition, compressive strength response at early and matured ages of 3 and 28 days were satisfied at 100% desirability. The elastic modulus response at age 3 showed 0% desirability, but attains about 99.96% of the target response by 28 days. The verification experiments conducted on each response property shows that positive correlations exist between the measured responses and the predicted values from the optimization analysis. Also, the bond capability of the optimum designed overlay material was evaluated using both tensile and shear bond strengths parameters. The overall assessment results showed that the overlay material exhibits good bonding with the substrate OPCC and would be able to withstand substantial stresses where sufficient surface texture is provided for aggregates interlocking. Other material properties included in the evaluation process of the overlay material included its tensile strength, coefficient of thermal expansion, and drying shrinkage. Stresses in the overlay, substrate, and at the interface were assessed analytically under various differential movement related conditions. Though the interface and the overlay material exhibited sufficient strength against thermal and shrinkage cracking, the theoretical shrinkage cracking in the overlay was predicted at 6.92MPa when fully restrained axially. Further, for effective fracture process description of the interface, experimentally determined parameters in shear and tension were coupled in

Mixed-Mode Finite Element Analysis using differential edge deformation model between the overlay and the underlay. The results indicated that delamination in partial fracture process varied from that of complete fracture process, influenced distinctly and largely by the magnitude of the applied load. Other influencing factors in the analyses included the elastic mismatched properties, initial edge defect size, and the plane of loading. Lastly, analytical solution to the FEA problem was implemented using the proposed *Modified* Eigenvalue Buckling Analysis (MEBA). The result indicated that the proposed analytical method simulates and compares well with the FEA result. The proposed method also provided a good technique for predicting the Mixed-Mode Buckling failure Mode-Shape of the overlay.

Acknowledgements

The author wishes to thank several people who contributed immensely in making this doctoral thesis a reality. Foremost, I would like to express my profound gratitude to my Director of Studies Dr. John Karadelis for his thoughtful support while supervising this research. He stimulated the concept of this work, and his wealth of experience in the field of computational mechanics contributed largely to the success of this work.

In addition, similar in-depth appreciation is expressed to two other supervisors – Professor Peter Claisse and Dr. Salah Zoorob – who worked alongside in stirring this work to consummation.

Also, my unreserved gratitude goes to my wife Adeyinka Olubanwo and my kids Toluwa, Temiloluwa and Imioluwa for their endless support and great patience all through the period of this research. Also, it would not have been possible to attain this height of academic height without the early support of my older brother Adebayo Ogunbanwo and my late parents Mr. and Mrs. Adebola Ogunbanwo.

Above all, to my Saviour and Creator I ascribe all wisdom, glory and power.

List of Abbreviations and definitions

AASHTO = American Association of State Highway and Transportation Officials

AASHO = American Association of State Highway Officials

AMD = Apparent Maximum Density

ANOVA = Analysis of variance

BCOs = Bonded concrete overlays

BRCFRPMC = Bonded Roller Compacted Fibre Reinforced Polymer Modified Concrete

ECC = Engineered Cementitious Composites

FCM = Fictitious crack model

FEA = Finite Element Analysis

HPFRCC = High Performance Fibre-Reinforced Cementitious Composites

LEFM = Linear elastic fracture mechanics

MEBA = *Modified* Eigenvalue Buckling Analysis

MVB = Modified-Vebe-test

OPCC = ordinary Portland cement concrete

PMM = Polymer Modified Mortar

PMC = Polymer Modified Concrete

RCC = Roller Compacted Concrete

SBR = Styrene-Butadiene Rubber

TAFD= Theoretical air free density

TRL = Transport Research Laboratory

UTW = Ultrathin white-topping

Table of Contents

List of Tables

List of Figures

1.0 Introduction

1.1 Background

The structural failure and repair of pavement structures have continued to gain worthwhile attentions among researchers and engineers, considering today's limited available funding for highway maintenance, the ageing highway pavement structures, and the increased heavy traffic loading. Clearly, as sustainability and environmental goals sharpen, it is expedient to redirect global efforts in order to ensure that the collapse of existing damaged pavement is prevented, thereby ensuring better returns on investment.

In this regard, the use of "green" structural solution in form of bonded overlay material is becoming more emphasized than ever. Laudable stride in this line of thought is the use of High Performance Fibre-Reinforced Cementitious Composites (HPFRCC) in the overlays construction. Some common nomenclatures within this class of HPFRCC include ECC (Engineered Cementitious Composites), PMM (Polymer Modified Mortar), and PMC (Polymer Modified Concrete).

Research wise, successful attempts have been made on high quality Polymer Modified Mortar (PMM), using inexpensive laboratory mixing and rolling techniques (Hughes and Lubis, 1996). Similarly, the use of ECC as a ductile material has been advanced as a better way of effectively eliminating reflective cracking in bonded overlay systems compared to ordinary Portland cement concrete (OPCC) material (Lepech et al, 2008). However, while these materials are believed to enhance both sustainability and structural properties, their long-term performance investigations are still underway in different quarters, including here at Coventry University, of which this research stems from.

Common argument to these innovations is that with new overlay materials, practitioners are unavoidably faced with a lot of technical parameters and concerns (Jepsen, 1999) such as strength, thermal properties, permeability, versatility, flexure, shear, durability properties, their availability and the market to serve, and possible failure modes, which perhaps are still undefined yet. Intuitively, a superior material that is too expensive or one that requires high technology to apply may never be used by the people. This then brings to mind typical questions one might ask: How are new bonded overlay materials designed and evaluated for optimum performance? Are there reliable means of establishing the performance level of these novel materials? And above all, what constitutes failure in overlay or pavement structures?

In view of the above, would this research by any means provide satisfactory answers to these age-long yearnings? These and perhaps many more are predominant questions that are still open to discussion, and possibly at this moment, can only be answered with big uncertainties. Undoubtedly, research opportunities in this line will not only advance previous knowledge in the field of pavement engineering, but will also help reduce appreciably capital expenditure incurred on road maintenance and rehabilitation annually by various highway agencies.

It is worth noting that highways constitute the largest component of the global transport sector, and are considered fundamentally vital for both economic and social development (Kerali, 2000). In generic terms, the cost of keeping highways fit for purpose has also remained enormous globally. In the UK where there are about 285,000km of roads of which 1,500 lane-km are of concrete pavements (Hall et al, 2007), the annual survey carried out recently by ALARM (Annual Local Authority Road Maintenance) put the total allocated budget to road maintenance in England and Wales alone in the region of £2.7 billion for 2008/2009 financial year, of which 41% accounts for structural maintenance and about £35.2 million paid as compensation claims to road users.

Indisputably, the trend is the same around the world in the past decades. In the OECD (Organization for Economic Co-operation and Development) report (1987), pavement maintenance expenditure compared with other road maintenance expenditure accounts for the largest single item ranging from approximately 33% in France to 73% in the United States. Table 1.1 depicts expenditures per member country.

Table 1.1: Comparison of Pavement Expenditure with Total Road Expenditure (OECD, 1987).

Technically, pavement structures - rigid, semi-rigid, or flexible - are designed in principle to correspond to a projected service life during which they may not suffer substantial functional or structural failure. However, fractures do occur due mainly to the cyclic effects of traffic loading and the environment. Under fatigue, all pavements, no matter how well-designed or constructed will fracture and deteriorate in serviceability at some point (pavementinteractive.org). Common fractures include fatigue, shrinkage, flexural, shear, and interfacial delamination.

Unfortunately, there is yet no known design method that has completely debugged pavement of all associated inherent problems. For instance, in concrete pavements and overlays, early-age cracks are somewhat inevitable. The microstructure studies of concrete have shown concrete to be porous and inherently containing a number of micro-cracks even before load is applied. Besides, the dynamic and pragmatic nature of the causes of distress in pavement structures which perhaps are difficult to capture adequately during the design stage further complicates the issue. Therefore, to prevent any functional or structural breakdown in pavement structures, sustainable maintenance strategies (SMS) that incorporate improvement, preventive and curative actions must be planned and implemented by the highway authorities.

Rehabilitating structural pavements with overlay systems – “Black Topping” where asphaltic or bituminous mixes are used, and “White Topping” (Mowris, 1996; BCA, 1993) where concrete is used as an un-bonded overlay - is common in modern civil engineering practice, particularly in the UK. Both techniques make partial use of the original pavement when compared with complete removal and replacement of the existing pavement (Karadelis and Koutselas, 2003).

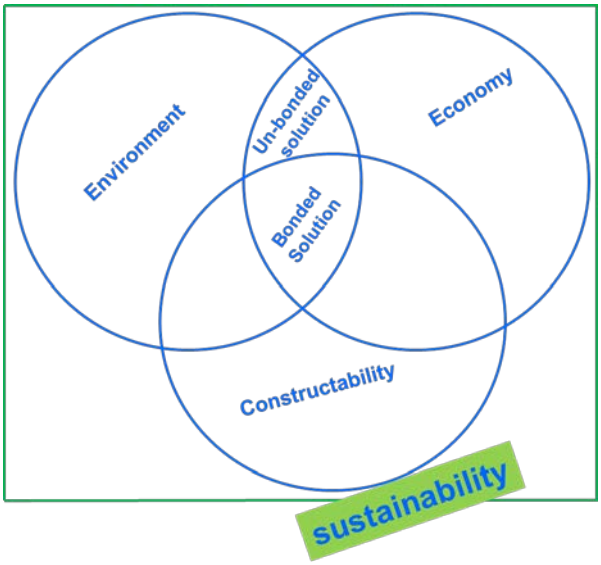

Figure 1.1: Sustainability aspect of pavement repair systems

From sustainability point of view, complete removal of a worn pavement structure is generally uneconomical and unfriendly to the environment. Optimum sustainable solution as illustrated in Figure 1 is expected to promote expedited construction process, less impact on the environment, and reduced cost and time of construction. Relatively, using a bonded overlay system affords greater savings than un-bonded solutions. In bonded solutions, the underlying objective is to ensure both layers act a unit. Performance wise, all bonded concrete overlays (BCOs) depend on the flexural stiffness of the underlying substrate, the interfacial bond strength, and effective horizontal shear transfer (Harrington et.al, 2007).

With adequate bonding, the two layers perform as a monolithic composite section; thus, the neutral axis shifts downward from the middle of the concrete overlay while the horizontal shear transfers stresses into the underlying layers, thereby reducing the tensile stresses in the bonded overlay (Karadelis and Koutselas, 2003; and Harrington et.al, 2007). The mechanics and the mathematical determination of the position of the neutral axis in a two-layered slab with full friction, 50% friction, and full slip is well undertaken elsewhere (Van Cauwelaert, 2004).

Apparently, where adequate bond strength cannot be achieved, the resultant effects are shear failure and delamination at the interface between the overlay and the substrate pavement, which constitute major causes of premature failure in BCO systems. Until now, this has remained a huge set back to the great potential savings afforded by BCOs. But these problems can be overcome by ensuring that optimum material mixture selection,

interfacial preparation, and good consolidation of the overlay during compaction are adequately secured during the design and construction procedures. This research presents methods of implementing each of the identified elements necessary for optimum bond performance. The research uses statistical optimization techniques within the concept of material mixture design, and extensive interfacial bond investigations using experimental and numerical / analytical methods.

1.2 Aim and Objectives

This research aims to optimize a high performing Bonded Roller Compacted Fibre Reinforced Polymer Modified Concrete (BRCFRPMC) for both structural performance and bond compatibility with the substrate ordinary Portland cement concrete (OPCC). As such, potential mechanisms of interfacial delamination at area of high stress concentration and at discontinuities are primary concern of interests.

This research work together with other two studies, where both reflective and flexural failure modes are concurrently undertaken, will make a significant contribution to the economic competiveness of the UK by "*conserving*" existing road infrastructure, use their remaining salvage value, and provide sustainable, low life-cycle cost solutions to a vast economic and social problem.

Thus, the following objectives were set:

I. To design and establish quantitatively and qualitatively the constituents of the Roller compacted overlay material for structural and bond performances, using experimental and statistical optimization techniques within the concept of material mixture experiment.
II. To study the fracture problems of the interface under tensile, shear, and mixed-mode conditions at areas of high stress concentration and at discontinuities, under the effects of differential length change between the overlay and the substrate.
III. To study the effects of substrate surface preparation and the overlay curing age on the bond performance of the interface.
IV. To propose optimum design benchmarks for the overlay material and the interface.

1.3 Layout of Thesis

Hereafter, the layout of this thesis follows: Chapter 2 reviews the existing methods for the design of concrete pavement and examines the modes of failure associated with concrete pavements and overlays. Chapter 4 highlights the theoretical basis for both optimum material mixture design and delamination process described in this work. In chapter 4, research methodology is presented. In chapters 5 and 6, experimental methods, procedures, and techniques for testing and characterising the overlay material and the interface are presented. In chapter 7, numerical interfacial fracture analyses are implemented using non-linear fracture mechanics approach. Similarly, the corresponding analytical solution to buckling-driven delamination model is also presented using the Modified Eigenvalue Buckling Analysis. Chapter 8 draws conclusions and proposes recommendations for future works.

2.0 Literature Review

2.1 Background

In practice, the successful implementation of reliability designs for concrete pavements and bonded concrete overlays (BCOs) is generically dependent on proven scientific and engineering techniques; though sound engineering judgement and experience also play an indispensable role. It is incumbent on the design engineer, as a professional, to duly acquaint himself with existing rational approaches and at the same time propel innovative concepts as a means of ensuring optimum design in terms of cost, sustainability, and novel material selection and utilization.

To a great extent, pavement or overlay structural designer is expected to demonstrate reasonable expertise and versatility in the choice of materials, given that material technology is central to engineering artefact. Evidently, within the field of structural engineering, lack of material ingenuity among designers contributes adversely to the so-called engineering deficits that are, considering the fact that most designs undertaken by engineers who have thorough theoretical and adequate hands-on experience in construction materials, coupled with sound structural design skills, tend to turn out better.

In this context, it behoves designers in the field of BCOs to ensure that they make the most of the numerous benefits inherent in the vast novel and superior construction materials available in the market and by extension appropriate their fiscal values correctly in the

schemes of BCOs design. But the obvious challenge the now BCOs' designers would have to contend with lies in the fact that many of the so-called new materials do not yet have a secured place in the codes of practice. Besides, the issue of compatibility row between the new materials and the conventional construction concrete is also yet to be redressed, which at the present appears to have posed further uncertainty on their broad acceptability.

But beyond the horizon of today's knowledge, it is feasible that ambitious expectations in the area of optimum design of novel materials can invariably be met or surpassed, via concerted cutting-edge research efforts between the material engineers and their structural counterparts.

A quick observation from the advances made so far in the design of conventional concrete (i.e. material and structural design), one can only but appreciate that there exists a sure groundwork of hope and possibility for the newly developed materials. Moreover, the inclusion of optimization techniques in material design and structural sizing (Barthelemy and Haftka, 2009) of Portland cement concrete seems to be providing the headway.

In this thesis, this section sets to pull together state-of-the-art literature pertinent to the analysis and design approaches in the field of concrete pavement and bonded concrete overlays (BCOs) with special heed on their material constituents and characterization, conventional and current design trend, mechanisms of failure, and dominant modes of failures. Concisely, failure due to interfacial shear and delamination between existing worn pavement and bonded concrete overlays is central to this review.

2.2 Basics of Concrete Pavement system Analysis and Design

Hitherto, in the field of structural engineering, there exist three basic approaches to structural analysis and design of structures: the mechanics or strength of material approach, the elastic theory approach, and the finite element techniques. In addition, the application of the principles of fracture mechanics, notably linear elastic fracture mechanics (LEFM) and fictitious crack model (FCM), to the field of pavement engineering is fast evolving, since they are capable of handling elevated stress profile developing at discontinuities and crack regions which perhaps are beyond the scope of the so-called analytical approaches (Dias da Silva, 2006).

The traditional strength of material approach employs phenomenological and praxis oriented methods to proffer physical solutions to structural problems which are relatively of

simple geometry, but whose material behaviour is relatively complex compared to those that may be resolved via the theory of elasticity approach. On the other hand, the theory of elasticity approach, affords the opportunities of mathematical derivations and formulations that are able to handle problems with complex geometry. Usually, the easy-to-do thing is to explore the principle of synergy; under certain circumstance the two methods can be integrated to produce a complementary closed-form solution (Dias da Silva, 2006).

Unlike these two approaches mentioned above, the finite element techniques, in principle, discretize the continuum, and work well as a numerical tool for solving difficult-to-solve by hand differential equations resulting from the previously identified analytical methods (Liu, 2003).

Irrespective of the method chosen, it is apparent that while undertaking structural analysis and design for concrete pavement or BCO systems, three sources of input data are fundamental: (1) data relating to the supporting subgrade, (2) data about the constructed layers, and (3) data describing the geometry of the applied loads. A comprehensive review of these input data is found in Ioannides (2006).

In addition, the unavoidable effects of the ambient environmental conditions under which pavement structures are serviceable have also found a profound recognition in the lately developed mechanistic-empirical design method (Thompson, 1996). Thus, effectively, four input data sources are required for an optimum analytical exercise. These input data sources are discussed in brief, and subsequently related to the design approach of concrete pavement systems as follows:

2.3 The Subgrade data

It is clear that virtually every civil engineering structure has its base on the soil. Engineering soil may be described as weak or strong, depending on the subgrade conditions. Advances in literature suggest and relate the choice of concrete pavement over flexible type of pavement to intrinsic subsoil conditions, such as low subgrade strength, susceptibility to frost action, and swelling due to moisture effects; other imperative rationale include the anticipated conditions of exceptional heavy point loads, and flow flashpoint petrochemical spillage (Griffiths and Thom, 2007).

Performance wise, concrete pavements and BCOs rely on their rigidity, sustained bending action, and their ability to distribute loads over a much large area of the underneath soil

structure (Hughes, 2006). In this context, the stresses on underlying soil are widely dispersed and relatively low, hence the effects of bearing capacity of the subsoil are less critical in the design of concrete pavement (Delatte, 2008) compared to that of flexible pavement.

Nonetheless, as conditions demand onsite, the use of borrowed material as sub-base, or preferably subsoil stabilization - either with lime or cement, is incorporated to improve low-strength soil, and by extension preclude the possibility of subgrade regression during the pavement life (Garg, 2005). A pertinent review of subgrade improvement, and subsoil stabilization; techniques involved and order of preferences for specific pavement solution are undertaken by Yoder (1964) and Delatte (2008).

For design purposes, it is common to characterize the support quality of subgrade by its modulus of reaction k (MPa/m), which represents the spring constant of Winkler (1867) medium (dense liquid foundation). In Winkler's model, the reactive pressure of the subgrade is assumed proportional to the deflection of a thin elastic loaded plate as illustrated in Figure 2.1, from where equation 2.1 is deduced.

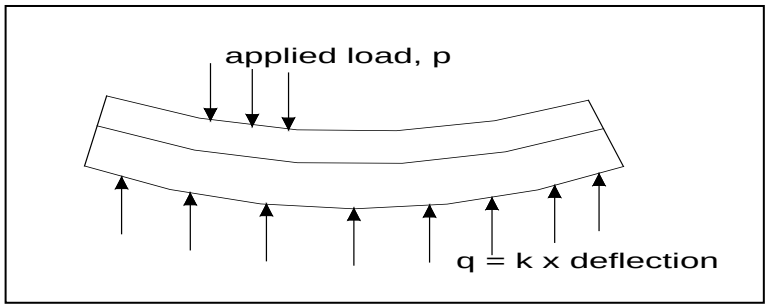

Figure 2.1: Deflection of beam on elastic foundation

$$q = kw \qquad (2.1)$$

where,

$q = reactive\ pressure\ (N/mm2)$

$k = modulus\ of\ subgrade\ reaction\ (N/mm3)$

$w = deflection\ of\ slab\ (mm)$

As seen, the implication of equation 2.1 where k is assumed constant means subgrade is expected to behave in a linear elastic manner. In practical terms, most soils neither have a definite elastic limit, nor exhibit perfect stress-strain relationship, therefore the validity of the

equation is rather subjective, and its application is usually confined to a narrow range (Yoder, 1964).

Besides, the model only assumes vertical reaction without accounting for the possibility of the horizontal shear interactions between the subgrade spring elements and the overlaying element, which later investigators spotted as a further weak-point of Winkler's subgrade idealization. A comprehensive review of the modified models of Winkler foundation by Pasternak (1954) and other investigators is found in Ioannides (2006) and Van Cauwelaert (2004).

Nevertheless, elastic solutions involving slabs on Winkler foundation are fundamental and extremely useful in rigid pavement engineering. Some of the pioneering works along this line of thought were undertaken by Westergaard (1926, 1939, 1947) who provided rational treatment to the problem of rigid pavement design (Ioannides, 2006; Gupta and Gupta, 2003; Das, 1999).

In determining the value of k, direct in-situ method by means of a plate bearing test or indirect methods by correlation with other tests, including California Bearing Ratio (CBR), Resistance value (R - value) or Resilient modulus, may be employed. The direct method as noted by practitioners is known to be more accurate, but for reasons of cost, indirect methods are commonplace (Houben, 2006). The numerical value of k is known to be influenced greatly by factors that affect soil strength, like soil texture, density and moisture content; while its typical value ranges in the proximity of $13.5MPa/m$ to over $270MPa/m$ for weak and strong supports respectively (Pavement Interactive, 2010).

In practice, it is usually conservative to use a low $k-value$ for the thickness design since concrete pavements are not very sensitive to it; cost-effective joint spacing, however, requires higher $k-value$ (Delatte, 2008). In that sense, the designer is expected to apply engineering ingenuity in his choice of $k-value$.

2.4 The Constructed Concrete Layer

The constructed layer of a rigid pavement is made up of concrete, either as a jointed plain, jointed reinforced or continuously reinforced slab. A comprehensive design of concrete pavement therefore comprises both the material mix design and the structural design.

2.4.1 Concrete Mix design

In the mix design, attempts must be made to achieve the optimum mixture of the material constituents for a given application. In the conventional concrete, the three basic constituents that are involved in the mixture are aggregates (coarse and fine), Portland cement, and water. Occasionally, admixtures are added for specific purposes. For instance, some chemical admixtures are used to modify the setting and hardening process of the hydration of cement paste. Air-entraining admixtures serve the durability performance of concrete exposed to cold weather better. Mineral admixtures like pozzolans are useful in minimizing thermal cracking in mass concrete (Mehta and Monteiro, 2006), while the inclusion of fibres in form of steels or synthetics enhances both flexural toughness and fatigue performance of concrete; albeit, their applications are rather more frequent with BCOs and UTW (Ultrathin white-topping) compared with pavement structures (Delatte, 2008).

In general, conventional concrete mix ratio design is undertaken in a two-step procedure: (1) Mix proportioning, and (2) Mix Testing. In the mix proportioning, the desired properties of the concrete are used as inputs to determine the required materials and proportions; the resulting trial mixes, under mix testing, are then subjected to several laboratory tests for evaluation and characterization (Pavement Interactive, 2010).

With the advent of computer programmes, it is now easy to undertake quick mix optimization study and design. Statistical optimization techniques have found successful applications in petrochemical, pharmaceutical and food industries, and have also provided satisfactory statistical basis in concrete mix technology for optimizing given performance criteria like slump, strength, cost, etc (Ruiz et al., 2005). Commendably, the concerted efforts by the Federal Highway Administration (FHWA) and the National Institute of Standard and Technology (NIST) have yielded positive results in this area of research by providing concrete mix designers with a ready-to-use web-based application known as COST - Concrete Optimization Software Tool - (Simon, 2003).

Simulating field performance of concrete material with mix design is welcome to a great extent, but not without drawbacks, considering the size and the laboratory conditions under which mix samples are treated. However, the far-reaching results of such simulations are reliable in promoting in-situ concrete quality control, and by extension securing reliable

evaluation of concrete properties. A comprehensive review of selection of concrete materials for pavement construction is undertaken in Delatte (2008).

2.4.2 Material Properties and Characterization

In practice, it is common to base the selection of an engineering material for a particular application on its ability to resist the applied load. The same principle applies to material selection and design for concrete pavement and bonded concrete overlays. The material characterizations of such structures are usually guided by the properties, behaviour and responses they exhibit under loading conditions. For instance, all known engineering materials exhibit linear elasticity within a tolerable range during which they are able to dispel any imposed deformation on removal of load. Hence, strain is said to be proportional to the forces producing it. In engineering terms, the measure of the intensity of these forces at any cross section of a given member is referred to as stress. Effectively, strain is a linear function of engineering or nominal stress in a structural member and the two variables are related in a constitutive equation called Hooke's law, i.e.

$$\sigma = E\varepsilon \qquad (2.2)$$

where,

$\sigma = stress\ in\ (MPa)$

$\varepsilon = strain\ (dimensionless)$

$E = modulus\ of\ elasticity\ (MPa)$

Mathematically, the stress given in equation 2.2 is expressed as force per unit sectional area of a structural member, while its maximum value prior to material fracture is defined as strength.

In the design of concrete structures, this strength is fundamental as many other properties are known to be dependent on it. In order to achieve maximum strength therefore in heterogeneous material like concrete where voids are intrinsic, efforts must be made to keep porosity to minimum via specified water-cement ratio, optimum compaction during placing, and curing during hydration process; considering the fact that inverse relationship exists between voids and strength in solid (Mehta and Monteiro, 2006).

Similarly, the modulus of elasticity (E) in equation 2.2 corresponds to the stiffness or rigidity of a material, and it is the ratio of applied stress to reversible strain. For many homogeneous engineering materials, the value of E tends to be the same in tension and compression (Megson, 1996), since it measures the interatomic bonding forces and is usually unaffected by micro-structural changes (Mehta and Monteiro, 2006). But in heterogeneous materials like concrete where micro-cracks are intrinsic, the value of E differs in tension and compression. Consequently, the fracture effects of concrete micro-cracks are known to be more dominant in tension than in compression (Ouyang et al., 1995), and that possibly explains the wide margin between the compressive strength of concrete and its tensile or flexural strength (modulus of rupture – MOR).

Typical tensile and flexural strengths of concrete are of the order of 10 and 15 per cent respectively, of the compressive strength (Mehta and Monteiro, 2006). Different mathematical relationships presented in numerous technical reports and codes of practice linking flexural and tensile strengths to compressive strength of concrete are examined in Griffiths and Thom (2007).

Apparently, considering the wide difference between the compressive strength, and the tensile or flexural strength of concrete, the latter is considered most critical characteristic strength in concrete pavement or bonded concrete overlay system design and therefore governs the fatigue life of the structure. Typically, for durable construction of concrete pavement, moderate compressive strength in the range of 35 – 40MPa is sufficient in most cases. It is worth noting that, that with increased compressive strength, modulus of elasticity of concrete also increases, which in some respect increases the tendencies for higher curling and warping stresses in pavement (Ruiz et al. 2005). In order to prevent such tendencies, it is commonplace to match the modulus of elasticity of concrete with any of the strengths, i.e., tensile, flexural or compressive.

However, due to ease of determination, concretes used for construction purposes are usually classified based on compressive cube or cylinder strength, either as low-strength ($< 20MPa$), moderate-strength ($20 - 40MPa$) or High-strength ($> 40\,MPa$) from where both tensile and flexural strengths can be estimated accordingly. In the construction of concrete pavement or BCOs, material specifications are usually made in favour of moderate to high-strength concrete, mainly for purposes of adequate strength, and durability under stringent environmental factors.

2.5 Structural analysis of Concrete Pavement

Unlike in reinforced concrete (RC) structural design where standardized methods of analysis and design are available and well coded, there seems to be no unified design methods for concrete pavement or BCOs yet. The complexity of the system, ranging from material selection and design, unpredictable environmental factors, to varying advances in automobile and aircraft technologies, renders some of the conventional design methods inadequate.

Traditionally, full scale field observations over a considerable period are employed to develop models for predicting long-term behaviour and performance of pavement structures. The TRL (Transport Research Laboratory, UK) and AASHO Road Test are a major source of information for this type of design method. They formed the basis for the design methods and specifications recommended by Highway Agency in the DMRB (Design Manual for Roads and Bridges) and AASHTO (American Association of State Highway and Transportation Officials) respectively. While these empirical models have served considerably well over the years, it has now become evident that their applications are only considered valid within the boundaries of the collected data (Ruiz et al., 2005). Hence, the resulting regression models cannot be applied to all situations. For instance, the inability of the model to take reconnaissance of the consequences of new loading conditions (e.g. higher tyre pressure, increased loading and different axle configuration), new materials, and different environmental conditions, places a major limitation on the design model. Graphical illustration depicting such drawbacks and reasonable modification that could be applied is presented in Figure 2.2.

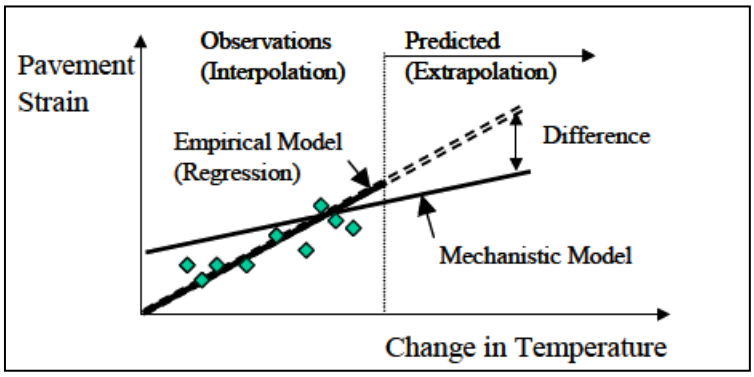

Figure 2.2: Drawback in the use of empirical (regression) model for prediction (Adapted from Ruiz et al., 2005)

From Figure 2.2, it makes common sense, rather than altering or discarding the long subsisting empirical data, it suffices to employ structural calculations to provide supplement and extension for the applications of the regression model. With analytical methods (e.g. linear elastic analysis) it is possible to tinker with the mechanics of the materials and the physics of the entire pavement system. Analytical methods allow stress, strain or resulting deflection to be computed in order to relate the effects of internal or external forces on the pavement system (Ruiz et al., 2005).

In practice, the mechanistic procedure involved in these methods is undertaken in a four-key-step to translate the analytical calculations of pavement response (stresses in slab) into field performance (distress history) as shown in Figure 2.3. A comprehensive review of the procedure is found in Ruiz et al. (2005).

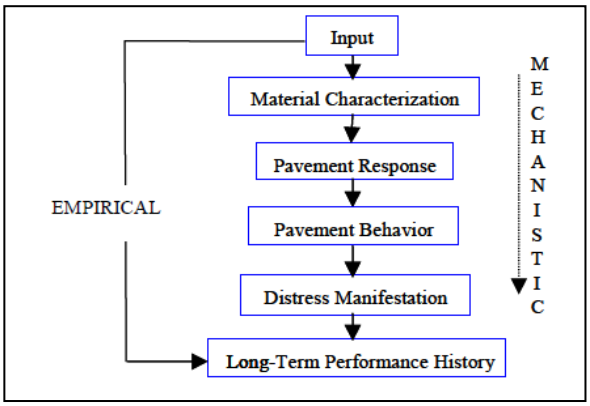

Figure 2.3: Schematic of empirical and mechanistic solutions for prediction of pavement distress (Adapted from Ruiz et al., 2005).

Typically, the traditional approach involved in these analytical methods is weakened by the fact that elevated stress level at discontinuities or due to the existence of micro - or macro-cracks in concrete pavement system are not commonly captured. Thus, incorporating the principles of fracture mechanics, as earlier noted, in concrete pavement and BCOs may provide potential solution to the current limitations. Fracture-mechanics-based design concepts are widely used today in engineering, but have received little applications in pavement engineering. Few but commendable attempts in this direction are currently confronted with the challenge of specimen-size effect, which is prevalent during laboratory and in-situ testings.

As it stands today, theoretically, there are no established mechanisms of relating stresses to definite performance such as cracking in concrete pavement; rather output from analytical

calculations is currently calibrated by researchers with empirical algorithm which converts it into a measurable performance (Ioannides, 2006), hence the term Mechanistic – Empirical (M-E) design method.

2.5.1 Stresses and Deformations in Concrete Pavement systems

Stresses and deformations in concrete pavement systems are induced from a variety of sources earlier identified, and they can be broadly grouped as due to:

I. traffic loadings;
II. cyclic temperature variations in concrete;
III. moisture variation in concrete;
IV. shrinkage during the hardening process of concrete;
V. volumetric changes in the subgrade;
VI. discontinuity of subgrade support from beneath the concrete pavement.

In general, stresses in concrete pavements are induced as a result of accompanying construction restraints while the structure undergoes deformations under the applied or environmental loading. These restraints may be due to the slab self-weight, interfacial friction between the slab and the subgrade, and restraints at the joints. In principle, restraints along the transverse and longitudinal joints are usually kept to the allowable value in order to accommodate stress redistribution and at the same time prevent excessive differential displacement of adjacent slabs. Local deformation in pavement structures may be either elastic or inelastic depending on the strain threshold of the material. Where local inelastic deformations exist, they are usually accompanied by residual stresses during elastic recovery of the surrounding regions (Houben, 2006).

Normally, many of the stresses highlighted above are reduced to the bearable minimum in field by constructional methodology. For instance, the effects of stresses due to concrete pavement shrinkage and regular temperature change are practically contained by dividing the pavement layer into panel of slabs or by introducing longitudinal reinforcement. On the other hand, stresses due to moisture variation in concrete are only considered critical in extreme climate conditions where drying out phenomenon is dominant (Houben, 2006).

Moreover, where continuity of the subgrade under the pavement is ensured during the pavement life, stresses and the resulting deformations in concrete pavements are basically resisted by the combined stiffness effect of the concrete slab and the underlying medium.

But in cases of subgrade discontinuities, differential settlements become prevalent, thus, inducing additional flexural stresses in the slab under applied loads. It is well established that the magnitude of such stresses are dependent on the geometric pattern and the rate of settlements. In practice therefore, the use of sand subsoil is common to abate the likelihood of differential settlements (Houben, 2006).

In any case, more stresses are usually borne by the concrete slab, considering its higher modulus of elasticity over that of the supporting subgrade. Hence, the effects of the subgrade bearing capacity remain nominal in terms of stresses within the system once settlements are kept to minimum or uniform, but are considered enormous in respect of vertical deflection of the concrete layer.

2.5.2 Stresses and deformations under structural loads

In order to be able to estimate the stresses and deformations in concrete pavement system under wheel loads, Westergaard's (1926) characteristic equation which defines the relative stiffness of the subgrade and the slab for an infinite or semi-finite slab, modelled as resting on a dense liquid foundation provides necessary insight.

The equation is given by:

$$l = \left[\frac{E.h^3}{12(1-\mu^2)k}\right]^{1/4} \qquad (2.3)$$

Based on the derivation of the relative stiffness (*l*) in equation 2.3, Westergaard (1926) advanced his thoughts to analyse three typical loading conditions: (1) interior, (2) edge, and (3) corner for the design of concrete pavement. The graphical position for each case is illustrated in Figure 2.4.

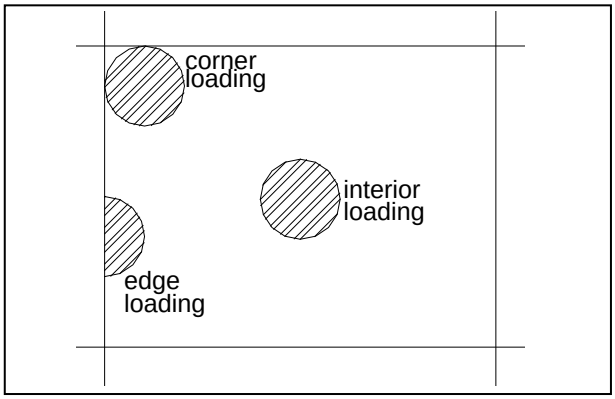

Figure 2.4 Positions of load in Westergaard's theory

The final modified versions of Westergaard's (1926) original equations for calculating the maximum tensile stresses at the bottom of a slab due to internal and edge loading conditions, and at the top due to corner loading condition had been undertaken by Westergaard (1939, 1947) and later investigators like Loseberg (1960), Kelly (1939), Pickett (1951) and Ioannides et al. (1985), just to mention a few. Some of these equations are found in Griffiths and Thom (2007), and are presented below.

- The stress and deflection equations together with the deflected shape for internally loaded slab by Westergaard (1926; 1939) are given by:

$$\sigma_{interior} = \left[3P\,(1+\mu)\frac{1}{2\pi h^2}\right] X \left[log\left(\frac{2l}{a}\right) + 0.25 - 0.577215\right] + BSI2OT \qquad (2.4a)$$

Where *BSI20T* is supplementary stress given by: $\left[3P(1+\mu)\frac{1}{64h^2}\right]\left(\frac{a}{l}\right)^2$ (2.4b)

$$\delta_{interior} = \left[\frac{P}{8kl^2}\left(1+\frac{1}{2\pi}\right)\right] X \left[log\left(\frac{a}{2l}\right) + 0.577215 - 1.25\right]\left(\frac{a}{l}\right)^2 \qquad (2.4c)$$

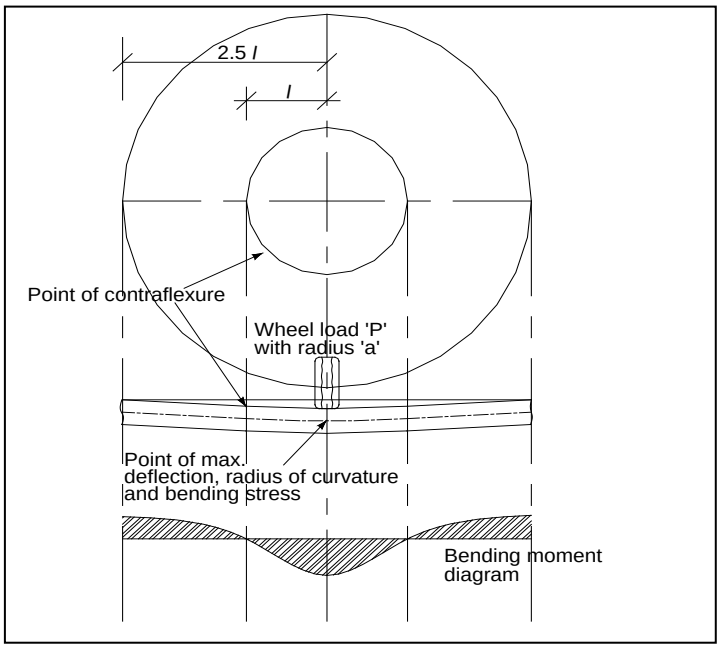

Figure 2.5 The deflected shape of an internally loaded slab (Adapted from Griffiths and Thom, 2007)

- The simplified edge stress and deflection equations undertaken by Loseberg (1960) based on Westergaard's original equation are recommended in Ioannides et al. (1985), based on their ILLI-SLAB finite element analysis. These equations are given by:

$$\sigma_{edge} = \left(\frac{-6P}{h^2}\right)(1 + 0.5\mu)\, X \left[0.489\, log_{10}\left(\frac{a}{l}\right) - 0.012 - 0.0063\left(\frac{a}{l}\right)\right] \quad (2.5a)$$

$$\delta_{edge} = \left(\frac{1}{6^{0.5}}\right)(1 + 0.4\mu)\left(\frac{P}{kl^2}\right)\left[1 - 0.760(1 + 0.5\mu)\left(\frac{a}{l}\right)\right] \quad (2.5b)$$

- The relevant stress and deflection equations by Westergaard for corner loading condition are expressed as:

$$\sigma_{corner} = \frac{3P}{h^2}\left[1 - \left(\frac{a_1}{l}\right)^{0.6}\right] \quad (2.6a)$$

$$\delta_{corner} = \frac{P}{kl^2}\left(1.1 - 0.88\left(\frac{a_1}{l}\right)\right) \quad (2.6b)$$

Where,

$l = radius\ of\ relative\ stiffness\ (m)$

$E = slab\ Young's\ modulus\ (Pa)$

$h = thickness\ of\ the\ slab\ (m)$

μ $= poisson's\ ratio\ of\ the\ concrete\ slab$

$k = modulus\ of\ subgrade\ reaction\ (Pa/m)$

$\sigma\ interior$ = $maximum\ tensile\ stress\ at\ the\ bottom\ of\ the\ pavement\ due\ to\ loading\ at\ the\ interior\ (Pa)$.

$\sigma\ edge$ = $maximum\ tensile\ stress\ at\ the\ bottom\ of\ the\ pavement\ due\ to$

$loading\ at\ the\ edge\ (Pa)$.

$\sigma\ corner$=$maximum\ tensile\ stress\ at\ the\ top\ of\ the\ pavement\ due\ to\ loading$

$at\ the\ corner\ (Pa)$.

$P = Wheel\ load\ (N)$

$a = radius\ of\ contact\ area\ for\ the\ point\ load\ (m)$

$\delta_{interior} = interior\ deflection\ (m)$

$\delta_{edge} = edge\ deflection\ (m)$

$\delta_{corner} = corner\ deflection\ (m)$

It is however worth noting that the application of equations 2.4 to 2.6 should be undertaken bearing in mind certain restrictive assumptions on which the equations are based, which

also necessitates the need for field calibration adjustments as no theory on its own may be sufficient. Westergaard's models, for instance, assumes the following:

- A single-wheel load, which precludes the possibility of multiple loading system as occurring in real field conditions;
- Infinite or semi-finite slab such that load transfer effects are neglected for all loading conditions considered.
- Slab resting on dense liquid foundation characterized with k (modulus of subgrade reaction), the possible effects of modelling subgrade as elastic solid foundation were therefore not considered.

In reality, the new pavements do not fulfil many of the restrictions assumed; Pickett and Ray (1951) however succeeded in removing the bound of single-wheel condition through their bending stress distribution chart. Hogg (1938) and Holl (1938) provided alternative means of subgrade characterization, using Young's modulus of subgrade (E_s) having replaced Westergaard's model with plate on elastic foundation. Consequently, the corresponding radius of relative stiffness of the slab-subgrade system advanced independently by Hogg (1938) and Holl (1938) is presented by Losberg (1960), and is given by:

$$l = \left[\frac{Eh^3(1-\mu_s^2)}{6(1-\mu^2)E_s}\right]^{1/3} \qquad (2.7)$$

Where,

$E_s = Young's\ modulus\ of\ the\ subgrade, considered\ as\ infinitely\ thick\ (MPa)$

$\mu_S = Poisson's\ ratio\ of\ the\ subgrade$

Further, it is observed that Westergaard's solutions are also restricted to plain concrete pavement; alternative equations based on rational limit state bearing capacity approach for determining stresses and deflections in reinforced concrete pavement was introduced by Meyerhof (1962), but the techniques involved are generally treated as unnecessarily complex for a practical design method (Griffiths and Thom, 2007).

2.5.3 Stresses due to temperature variations

In dealing with the stresses associated with temperature variations in concrete pavement, three kinds of stresses are identified, and are illustrated in Figure 2.6. The stresses are as follows:

- Those due to uniform temperature change (ΔT) through the thickness of the concrete slab (see Figure 2.6 (1));
- Those due to linear temperature gradient (Δt) through the thickness of the concrete slab (see Figure 2.6 (2)); and
- Those due to irregular or non-linear temperature changes through the thickness of the concrete slab (see Figure 2.6 (3)).

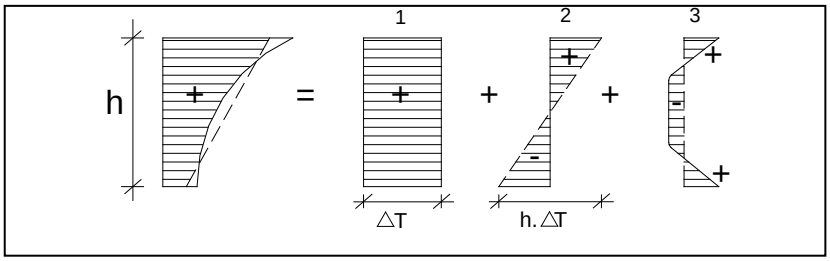

Figure 2.6: Temperature variations in Concrete pavement (Adapted from Houben, L.J.M., 2006)

As shown in Figure 2.6 (1), a uniform increase or decrease in temperature (ΔT) will result in compressive stress (contraction) and tensile stress (expansion) respectively at the top layer of the concrete due to the frictional restriction of the subgrade. The resulting effects may however be neglected in design for small concrete slab width under 5 meters; on the contrary, the effects of temperature gradient illustrated in Figure 2.6 (2) are usually considered substantial, and their magnitude may be of the same order as those caused by traffic loading; hence they form the critical stresses in the design of concrete pavement, especially those tending toward the edges (Houben, 2006).

Mathematically, temperature gradient (Δt) is given by:

$$\Delta t = \frac{T_t - T_b}{h} \qquad (2.8)$$

Where,

T_t= temperature at the top surface of concrete slab (^{0}C)

T_b = temperature at the bottom of concrete slab (^{0}C)

h= thickness of the concrete slab (mm)

Considering equation 2.8, temperature distribution assumes a linear relationship, which several field studies suggest as too simplistic. Primarily, temperature distribution through the depth of concrete pavement is a nonlinear function (Armaghani et al., 1987). Hence in the literature, different mathematical functions are proposed, including quadratic and third degree polynomial, for simulating nonlinearity of temperature distribution through the depth of concrete pavement. In Houben (2006), however, nonlinear or irregular temperature distribution is thought to be more prevalent with very thick concrete slabs, therefore, its effects on normal concrete pavement thickness is minimal, and may not contribute immensely in the design.

In effect, the whole concept of linear gradient may be taken therefore as fundamental, and generally required for simplicity functions in solving temperature related stresses and deformations problems in design. In practice, due to the complexity of nonlinear temperature analysis, it is common to find practitioners convert regression data from nonlinear temperature distribution measurements into a linear regression coefficient. Such regression coefficient is usually required to generate an equivalent linear gradient with similar curling or warping effects as that caused by linear temperature solutions derived by Westergaard, (1927) and Bradbury, (1938) (Mohamed and Hansen, 1997; Jeong and Zollinger, 2005). Subsequently, the equivalent linear temperature can be used to calculate stresses in the concrete pavement due to the nonlinear temperature profiles (Asbahan, 2009).

In Jansen and Snyder (2000), for instance, the equivalent linear gradient corresponding to temperature moment in their non-linear temperature distribution analysis is given by:

$$ELG = -\frac{12(TM)}{h^3} \qquad (2.9)$$

where,

$ELG = Equivalent\ Linear\ Gradient$

$h = slab\ thickness$

$TM = Temperature\ moment, given\ by\ equation.\ 2.10.$

$$TM - 0.25\sum_{i=1}^{n}[(t_i + t_{i+1})(d_i^2 + d_{i+1}^2) - 2(d_1^2 - d_n^2)T_{wave}] \qquad (2.10)$$

where,

t_i = $temperature\ at\ location\ i$

d_i = $depth\ at\ location\ i$

T_{wave} = $weighted\ average\ temperature\ given\ by\ eq.2.11$

$$T_{wave} = \sum_{i=1}^{n} \left[\frac{(0.5)(t_1 - t_{i+1})(d_i + d_{i+1})}{d_1 - d_n} \right] \quad (2.11)$$

Linear temperature gradient may be taken as positive or negative, depending on the time of the day. Generally, the resulting deformations under the effects of temperature assume the classic theory of plate where the cross section of the plate is taken as remaining plane after bending. The corresponding deformation shapes due to positive and negative temperature gradients are shown in Figure 2.7.

Figure 2.7: Deformation shapes due to (a) positive and (b) negative temperature gradients (www.pavement interactive, 2009).

In principle, especially in unreinforced concrete pavement, the effects of warping due to positive temperature gradient during the day give rise to uni-axial stress condition near and parallel to the edges, such that stresses may be assumed as acting on a beam at the edges rather than on the entire slab surface (Houben, 2006). Moreover, the effects of positive temperature gradient are more critical in the day time when they occur in combination with stresses due to traffic loading in critical position shown in Figure 2.8(a); the resulting flexural

tensile stresses therefore occur at the bottom of the concrete pavement where cracks may initiate.

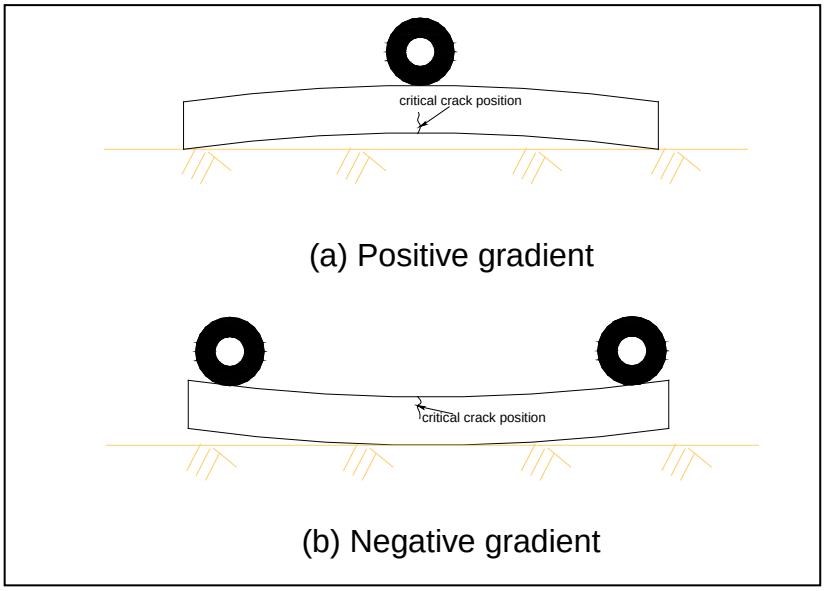

Figure 2.8: Critical loading conditions due to combined effects of environmental and vehicular loads

Conversely, as shown in Figure 2.8(b), in the cooler night, when the temperature at the slab top is minimum, the top part of the pavement contracts more than the bottom, causing the slab to warp upward at the corners and edges, which sometimes might separate partially or completely from the subgrade. Stresses are induced at the top surface subsequently due to the pullback weight from the pavement slab as it tends to restrict the warping. In addition, Figure 2.8(b) illustrates the positions of critical loading condition under this negative temperature gradient, but in effect, critical crack initiates from the top part of the midspan, unlike in the case of positive gradient loading condition (Asbahan, 2009).

Ideally in design (Houben, 2006), the effects of negative temperature gradient are treated as trivial and may not form part of the design considerations for the following reasons:

- The magnitude of negative temperature gradient is small and negligible compared with that of positive temperature gradient;
- Minimal combined stress effects are generated under limited or reduced amount of heavy traffic during the night.
- The resulting combined stress effects are also considered not critical since they result in flexural compressive stresses compared with flexural tensile stresses produced by the positive temperature gradient.

In general, rational approaches to solving curling problem in concrete pavement were first advanced by Westergaard (1927) and later simplified and extended by Bradbury (1938). In solving for warping stresses (Yoder, 1964), Westergaard assumed three cases conditioned on the longitudinal and transverse dimensions of the plate. The cases being:

I. The slab is infinite in both directions (say, *x* and *y*);
II. The slab is infinite in the plus y and plus or minus *x* direction;
III. The slab is infinite in both plus or minus *x* direction but with a finite width, say '*b'*.

In case (i), *z* becomes zero, so *Mz = 0*; while moments in the *x* and *y* directions are given by:

$$M_x = M_y = -\frac{Eh^2\alpha\Delta t}{12(1-\mu)} \qquad (2.12)$$

Dividing both sides by section modulus, stress is determined as given in equation 2.13.

$$\sigma_0 = -\frac{E\alpha\Delta t}{2(1-\mu)} \qquad (2.13)$$

Stresses for cases (ii) and (iii) are however expressed in terms of equation 2.13

In case (ii), the corresponding stress in the y-direction is given by:

$$\sigma_y = \sigma_0\left[1-\sqrt{2}\,sin\left(\frac{y}{l\sqrt{2}}+\frac{\pi}{4}\right)e^{\frac{-y}{l\sqrt{2}}}\right] \qquad (2.14)$$

While the stress in x-direction results in equation 2.15 due to poisson's effect.

$$\sigma_x = \sigma_0\left[1-\mu\sqrt{2}\,sin\left(\frac{y}{l\sqrt{2}}+\frac{\pi}{4}\right)e^{\frac{-y}{l\sqrt{2}}}\right] \qquad (2.15)$$

For case (iii), stresses in y and x directions are given by:

$$\sigma_y = \sigma_0\left[1-\frac{2\,cos\,\lambda\,cosh\,\lambda}{sin\,2\lambda\,sinh\,2\lambda}\left((tan\,\lambda+tanh\,\lambda)cos\frac{y}{l\sqrt{2}}cosh\frac{y}{l\sqrt{2}}+(tan\lambda-tanh\lambda)\,sin\frac{y}{l\sqrt{2}}sinh\frac{y}{l\sqrt{2}}\right)\right] \qquad (2.16)$$

Where $\lambda = \frac{b}{l}\sqrt{8}$

$$\sigma_x = \sigma_0 + \mu\left(\sigma_y - \sigma_0\right) \qquad (2.17)$$

Following Westergaard's (1927) initial publication, Bradbury (1938) developed his chart with coefficients for solving problems due to concrete warping through his empirical equations which are given by:

$$\sigma_{edge\ warping} = 0.5\ E\alpha\Delta TC \qquad (2.18)$$

where,

$E = \ modulus\ of\ Elasticity\ of\ PCC$

$\alpha = \ thermal\ coefficient\ of\ PCC$

$\Delta T = \ temperature\ differential\ between\ the\ top\ and\ bottom\ of\ the\ slab$

C = coefficient which is a function of slab length and the radius of relative stiffness (see figure 2.9).

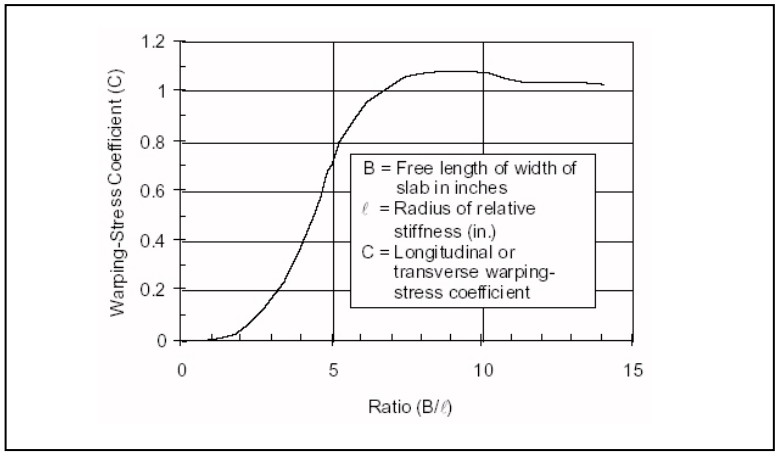

Figure 2.9: Curve showing variation in the differential temperature stress coefficient C for different values of the ratio B/l (redrawn from Bradbury, 1938).

The corresponding interior warping stress is given in equation 2.19.

$$\sigma_{interior\ warping} = 0.5\ E\alpha\Delta T\left(\frac{C_1+\mu C_2}{1-\mu^2}\right) \qquad 2.19$$

Where,

C_1= $coefficient\ in\ the\ direction\ of\ calculated\ stress$

C_2= $coefficient\ in\ the\ direction\ perpendicular\ to\ C1$

$\mu = Poisson's\ ratio\ for\ PCC$

$E, \alpha, and\ \Delta T$ are as defined in equation 2.18

The corner warping stress is expressed by equation 2.20

$$\sigma_{corner\ warping} = \frac{E\alpha\Delta T}{3(1-\mu)}\left[\sqrt{\frac{a}{l}}\right] \qquad 2.20$$

Where,

$a = radius\ of\ wheel\ load\ distribution\ for\ corner\ loading$

$l = radius\ of\ relative\ stiffness$

$E, \alpha, \mu\ and\ \Delta T$ are as defined previously

While the preceding equations are those common among practitioners, the application of Eisenmann's (1979) theory has also proven to be a meaningful and useful design tool in practice. The possibility of achieving a reduced warping stress is undertaken by keeping the slab dimensions in both longitudinal and transverse directions smaller than the critical slab length (l_{crit}) criterion proposed in Eisenmann's concept (Houben, 2006). Such critical slab length is defined as the length where a concrete slab heated equally over its entire top surface, only touches the substructure at the four corners and in the centre of the slab. So, the equations governing different slab dimension are represented by:

Long slab: (L/W > 1.2): $I_{crit} = 200h\sqrt{E\alpha\Delta t}$ 2.21(a)

Square slab: ($0.8 \leq {}^{L}/_{W} \leq 1.2$): $I_{crit} = 228h\sqrt{E\alpha\Delta t}$ 2.21(b)

Where,

I_{crit}= $critical\ slab\ length\ (mm)$

$h = slab\ thickness\ (mm)$

$E = Young's\ modulus\ of\ Elasticity\ (MPa)$

$\alpha = Coefficient\ of\ linear\ thermal\ expansion$ ($^0C^{-1}$)

$\Delta t = Positive\ temperature\ gradient$ (^{0}C/mm)

$L = slab\ length\ (mm)$

$W = slab\ width\ (mm)$

Based on the critical length definition, the effective slab length (L') of the concrete slab is therefore taken as being less than the actual slab length (L) on the assumption that the edges of the concrete slab is only supported over a certain distance (C) (Houben, 2006) as illustrated in Figure 2.10.

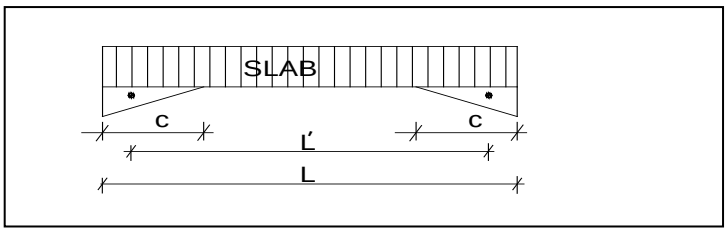

Figure 2.10: Slab supported at distance C from the edges (Adapted from Houben, L.J.M., 2006)

Furthermore from Figure 2.10, Eisenmann (1979) defines a mathematical relationship between L, L' and C as:

$$L' = L - \frac{2}{3}C \qquad (2.22a)$$

Where support length C is approximated to be:

$$C = 4.5\sqrt{\frac{h}{k\Delta t}} \qquad if\ C \ll L \qquad (2.22b)$$

Where,

$h = concrete\ slab\ thickness\ (mm)$

$k = modulus\ of\ substructure\ reaction\ (MPa/m)$

$\Delta t = positive\ temperature\ gradient$ (^{0}C/mm)

In a bid to determine stresses due to concrete slab warping, Eisenmann (1979) also identified three distinct cases based on the ratio between the effective slab span (L') and the critical slab length l_{crit} defined previously in equation 2.21. The cases are as follows:

I. A condition when the effective span (L') is far greater than the critical length (l_{crit}), hence the midspan of the slab rests on the substructure as shown in figure 2.11(1a & 1b).

The longitudinal warping stress at the bottom of the midspan of the slab corresponds to that given in equation 2.23.

$$\sigma_t = \frac{h\alpha E\Delta t}{2(1-\mu)} \qquad (2.23a)$$

II. A condition of increased (disturbed) warping stresses just adjacent to the midspan position that rests on the substructure as shown in Figure 2.11 (2a & 2b); the stresses being about 20% greater than the warping stress defined in equation 2.23(a), i.e.,

$$\sigma_t' = 1.2\sigma_t \qquad (2.23b)$$

It is also noted that the disturbed warping stress can occur in the centre of the slab when $L' = I_{crit}$ (Houben, 2006).

III. A condition when the slab effective span (L') is far smaller than the critical span length (I_{crit}) as illustrated in figure 2.11(3a & 3b), hence a reduced warping stress (σ'') develops and is given by:

$$\sigma_t'' = \left(\frac{L'}{0.9I_{crit}}\right)^2 \sigma_t \qquad if\ L' < 0.9I_{crit} \qquad 2.23(c)$$

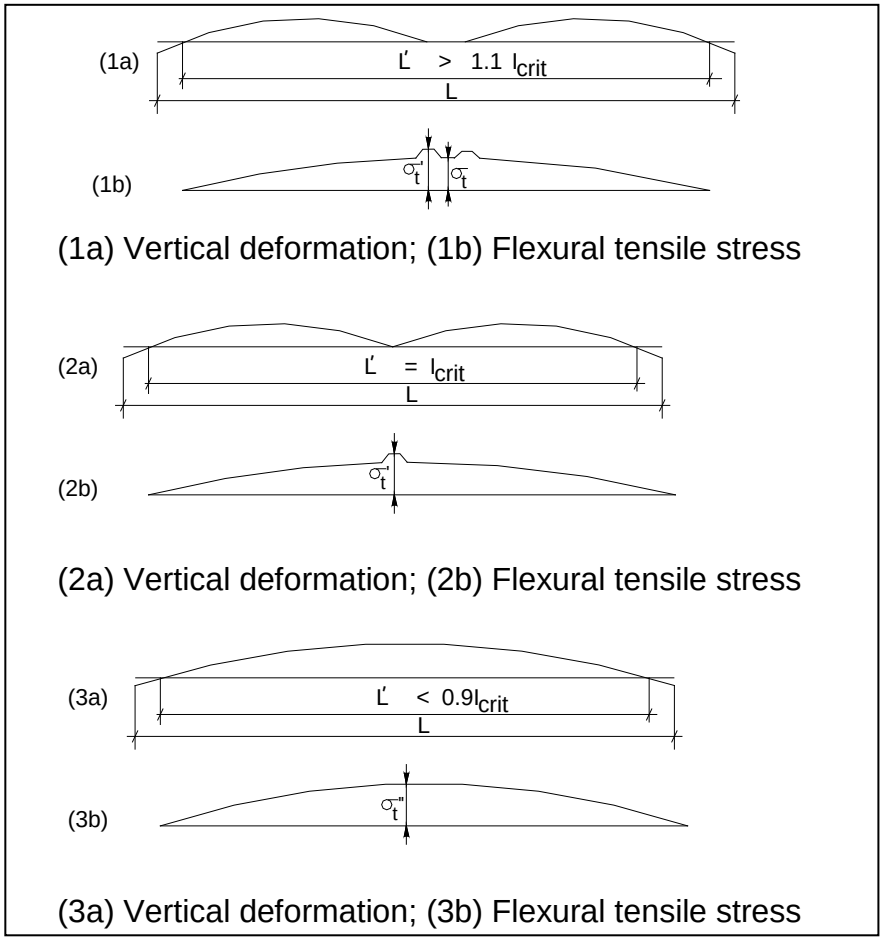

Figure 2.11: Vertical deformations and warping stresses due to positive temperature gradients along longitudinal section of the slab (Adapted from Houben, L.J.M., 2006).

Similarly, warping stresses in the transverse direction can be calculated by replacing the actual span length (L) and the effective length with the overall slab width (W) and effective slab width (W') respectively. However, it is noted vividly in the literature that the validity of stress equation calculated by Eisenmann (1979) is for small temperature gradient; obviously at positive temperature gradient beyond a certain limit, the concrete slab will only be supported at support length (C) along the edges and corners. The resulting curvature may be represented by Figure 2.12 representing a simplified beam section under bending at the edge. The corresponding flexural stress thus develops at the bottom side of the slab mid-span due to the resistance from the slab self-weight.

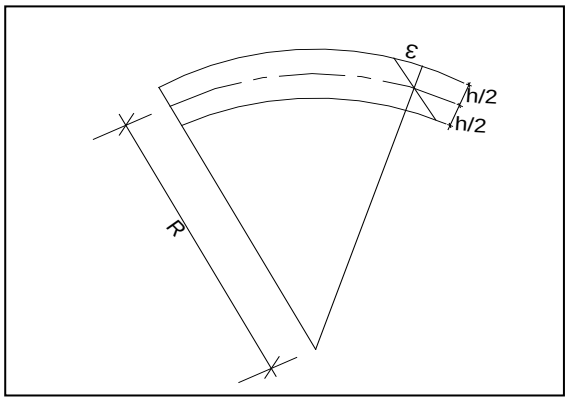

Figure 2.12: Curvature at the slab edge

From figure 2.12, equation 2.24 forms:

$$\frac{1}{R} = \frac{\varepsilon}{{}^{1}/_{2}h} = \frac{M}{EI} \qquad (2.24)$$

Where,

$$\varepsilon = \alpha.\Delta t\, {}^{1}/_{2}\, h \qquad (2.25a)$$

Or

$$\varepsilon = \frac{0.5\, Mh}{EI} \qquad (2.25b)$$

Or

$$\varepsilon = \frac{6M}{Eh^2} \qquad (2.25c)$$

Where,

$M = \ moment\ (Nmm)$

$E = \ Young's\ modulus\ of\ elasticity\ (MPa)$

$h = \ slab\ thickness\ (mm)$

$\varepsilon = \ flexural\ strain\ (dimensionless)$

$I = \ second\ moment\ of\ area\ (mm4)$

$R = \ radius\ of\ curvature$

From Figure 2.10, the resulting maximum moment at the midspan when the slab edge loses contact with the substructure and is only supported over support length C, is given by:

$$M = 0.125FL'^{2} \qquad (2.26)$$

Now, substituting for M in equation 2.25(c) and put ε in equation 2.25(c) into equation 2.2, the flexural stress at the bottom of the midspan can be calculated as given in equation 2.27.

$$Longitudinal\ edge: \sigma_t = \frac{0.75FL'^2}{h^2} \qquad (2.27a)$$

$$Transverse\ edge: \sigma_t = \frac{0.75FW'^2}{h^2} \qquad (2.27b)$$

Where,

$F = \ slab\ self - weight\ (N/mm)$

$L' = \ effective\ slab\ length\ (mm)$

$W' = \ effective\ slab\ width\ (mm)$

$h = \ slab\ thickness\ (mm)$

2.6 Concrete Pavement Design Methods

As earlier discussed, it is evident that the structural design and approaches to concrete pavements have grown beyond a single convention. While some methods utilize regression models, others are based on mechanistic procedures. Although numerous research works are undertaken on this subject, it is clear crystal that direct mathematical solutions for basic design requirement, like thickness, still remains a complex engineering problem (Delatte, 2008).

For instance, in the United States, the American Association of State Highway Officials (AASHO) fundamental empirical road work (1958 – 1960) remains the pilot guides for AASHTO design publications (1972, 1986, 1993 and 1998 supplement), and for many states. A few states however use a design catalog, the Portland Cement Association (PCA) procedure, or their own empirical or mechanistic-empirical procedure.

Nonetheless, the AASHTO design guides remain the widely used procedure; its design criterion is serviceability. The development of AASHTO design equation is found in Huang (2004), while the principal design equation given by equation 2.28 can be reliably applied to URC, JRC and CPC (Griffiths and Thom, 2007).

- The basic AASHTO design equation for rigid pavement in US unit is:

$$Log_{10}W_{18} = \ Z_R S_O + 7.35Q - 0.06 + V + H_a \left[Log_{10}\left(\frac{A}{B(N-F)}\right)\right] \qquad 2.28$$

Where,

$$Q = Log_{10}(D-1) \quad 2.29(a)$$

$$V = Log_{10}\left[\left(\frac{\Delta PSI/(4.5-1)}{1+(1.624\ X\ 10^7/(D+1)^{8.46})}\right)+1\right] \quad 2.29(b)$$

$$H_a = 4.22 - 0.32P_t \quad 2.29(c)$$

$$N = D^{0.75} \quad 2.29(d)$$

$$A = S'_C\ C_d\ (D^{0.75} - 1.132) \quad 2.29(e)$$

$$B = 215.63J \quad 2.29(f)$$

$$F = 18.42/((E_C/k)^{0.25}) \quad 2.29(g)$$

$$\Delta PSI = P_O - P_t - weather\ factor \quad 2.29(h)$$

W_{18}= $traffic\ loading\ in\ standard\ 18\ kip\ (80KN)\ axle$

D= $slab\ thickness\ in\ inches$

E_C= $Young's\ Modulus\ of\ concrete\ in\ psi$

k= $Modulus\ of\ subgrade\ reaction\ in\ psi/in$

S'_C= $the\ mean\ 28-day\ modulus\ of\ rupture\ (taken\ as\ 863\ psi)$

S_O= $the\ overall\ standard\ deviation$

Z_R= $the\ standard\ normal\ deviate\ for\ the\ desired\ reliability$

J= $load\ transfer\ coefficient$

C_d= $drainage\ coefficient$

ΔPSI= $design\ change\ in\ serviceability\ index\ during\ pavement\ life$

P_O= $initial\ serviceability\ index\ (taken\ as\ 4.5\ in\ the\ AASHO\ road\ test)$

P_t= $terminal\ (final)\ serviceability\ index$

Detailed procedures for applying the design equation are discussed in Houben (2006), Delatte (2008) and Griffiths and Thom (2007).

Similarly in the UK, the common design procedure is based purely on the empirical work of Transport Research Laboratory (TRL Report RR 87 – 1987), and encompasses whole life cycle of the pavement structure, i.e., design, construction, assessment and maintenance. By specification, continuous concrete constructions (CRCB and CRCP) are distinguished

from jointed constructions (URC and JRC). However, the standard design life for all types of concrete pavement in the UK is 40 years. The concrete specification for rigid continuous constructions relates directly to 28 days flexural strength of the concrete (4.5 – 6.0 MPa) while those of jointed constructions (URC and JRC) are specified based on the mean compressive strength of the concrete (C40 air-entrained).

In general, thickness design of jointed concrete pavements in the UK is usually guided by the empirical equations given in 2.30 and 2.31, while that of continuous pavement uses charts based on the estimated millions of standard (80KN) axles, composite foundation stiffness classes, and the flexural strength of concrete. A classic example showing the applications of the charts is given in Figure 2.13 educed from DMRB - volume 7.

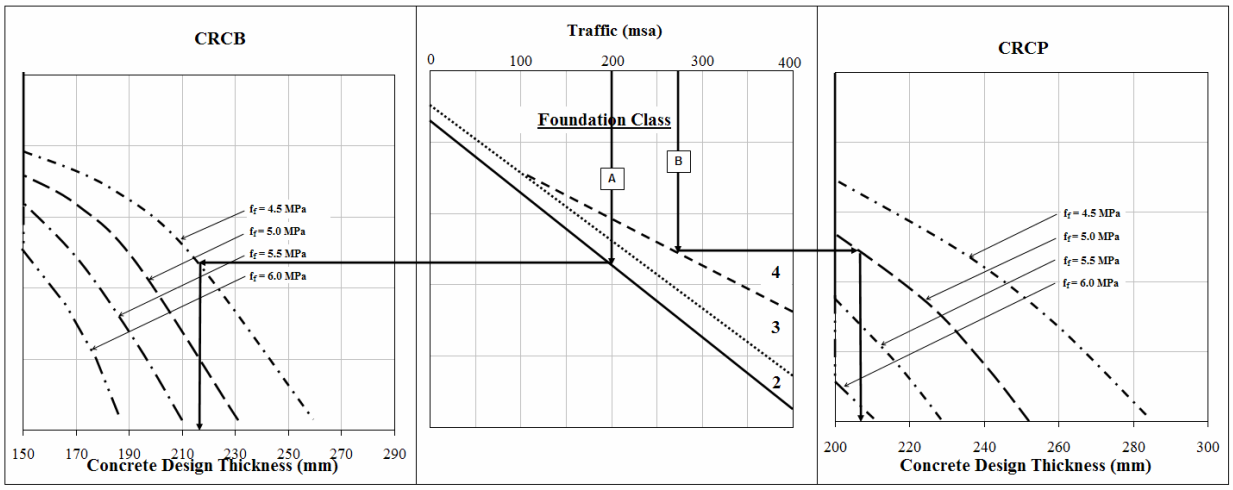

Figure 2.13: Charts relating parameters for continuous concrete pavement thickness design (Adapted from HD 26/06 – Page 2/12)

In Figure 2.13, two design options are indicated – (A) Continuously Reinforced Concrete Base (CRCB) with 100mm asphaltic overlay, and (B) Continuously Reinforced Concrete Pavement (CRCP) with 30mm asphaltic overlay. For a given projected design traffic value and a specified Foundation class, design thickness may be determined as a function of the flexural strength of the concrete. Clearly, with an increased flexural strength of concrete, while keeping all other parameters constant; the thickness reduces accordingly, but minimum allowable thickness are restricted to 150mm and 200mm for CRCB and CRCP respectively. Requirements for longitudinal reinforcements, transverse steel (if required), and ground anchor beams are detailed and given in HD 26/06 and other specialized texts.

For jointed concrete pavement however, thickness design is guided by the following regression equations:

- For unreinforced jointed concrete pavements (URC):

$$Ln\,(H_1) = \{Ln(T) - 3.466\,Ln(R_C) - 0.484Ln(E) + 40.483\}/5.094 \qquad (2.30)$$

- For reinforced jointed concrete pavements (JRC):

$$Ln\,(H_1) = \{Ln(T) - R - 3.171\,Ln(R_C) - 0.326Ln(E) + 45.150\}/4.786 \qquad (2.31)$$

Where,

$R = 8.812\ for\ 500\ mm2/m\ reinforcement$

$R = 9.071\ for\ 600\ mm2/m\ reinforcement$

$R = 9.289\ for\ 700\ mm2/m\ reinforcement$

$R = 9.479\ for\ 800\ mm2/m\ reinforcement$

$H1 = the\ thickness\ (mm)\ of\ the\ concrete\ slab\ without\ a\ tied\ shoulder\ or\ 1m\ edge\ strip$

$usually\ minimum\ 150mm,$

$H2 = the\ thickness\ (mm) of\ the\ concrete\ slab\ with\ a\ tied\ shoulder\ or\ 1m\ edge\ strip,$

$given\ by:\ H2 = 0.934\,H1 - 12.5,$

$Ln\ is\ the\ natural\ logarithm$

$T\ is\ the\ design\ traffic\ (msa) = maximum\ 400msa$

$Rc\ is\ the\ mean\ compressive\ cube\ strength\ (N/mm2\ or\ MPa)\ at\ 28\ days$

$E\ is\ the\ Foundation\ Class\ Stiffness\ (MPa)$

$E = 200MPa\ for\ Foundation\ Class\ 3\ or$

$E = 400\ MPa\ for\ Foundation\ Class\ 4$

While it is accepted that concrete pavements do not fail suddenly, but gradually deteriorate in serviceability, the omission of failure criteria in the AASHTO and UK pavement design procedures as a function of material mechanics or structural behaviour is not justifiable. It is now well understood through the principles of mechanics of materials that under fatigue loadings, which are known to be common with pavement structures, design life of a structure may be short-changed (that is may not survive its service life); hence methods of defining pavement structural failure during or after its design life are a necessary requirement in ensuring reliability design. Incorporating this thought will require some analytical procedures which can then be used to calibrate field observations.

Such design procedures have found useful applications in the United States and many parts of the world. For instance, the Portland Cement Association (PCA – 1966, 1984) design method, unlike AASHTO (1993 and 1998) and TRL Report (1987) is mainly based on results from finite element analysis/tests of stresses induced in concrete pavements due to edge, corner and joint loading, but utilizes AASHO Road Test concepts in its model. Pavements are thus evaluated based on two failure design criteria – concrete fatigue, and pavement erosion (Houben, 2006; Delatte, 2008).

In undertaking the pavement thickness design using this procedure, the traffic-induced flexural stress is determined for a trial pavement thickness, then the flexural stress is divided by the modulus of rupture to obtain the stress ratio SR (see equation 2.32), and fatigue models such as equations 2.33 and 2.36 are used to find the allowable number of repetitions. The trial pavement thickness is then adjusted until the design will be able to carry the projected number of load repetitions.

- Stress Ratio is given by: $SR = \frac{\sigma}{MOR}$ (2.32)

Where,

$\sigma = Load - induced\ tensile\ stress\ in\ the\ concrete$

$MOR = Modulus\ of\ rupture\ or\ flexural\ strength\ of\ the\ concrete$

For a given SR, a certain number of cyclic loads are predicted prior to pavement failure in flexural fatigue. Evidently, from equation 2.32, for stress ratio at or close to 1, the pavement is expected to fail after a few cycles. Other fatigue equations given in PCA (1984) include:

- For SR $\geq 0.55, \log N_f = 11.737 - 12.077(SR)$ (2.33)
- For $0.45 < SR < 0.55, N_f = \left(\frac{4.2577}{SR - 0.4325}\right)^{3.268}$ (2.34)
- For SR$\leq$ 0.45, the number of repetitions is unlimited.

Invariably, reducing SR satisfies conditions for a longer pavement life; which may be achieved by lowering the flexural stresses in the pavement or increasing the concrete MOR. The former may be achieved by simply making the slab thicker; although this seems easier and readily achievable, it is relatively more expensive.

Furthermore, the combined fatigue effects due to different loading magnitude and configurations may be determined by using Miner's fatigue hypothesis which is given by:

$$CDF = \sum_i \frac{n_i}{N_{fi}} \quad (2.35)$$

An enhanced fatigue model utilized by American Concrete Pavement Association (ACPA) however incorporates a reliability parameter which allows not more than 10% pavement failure prior to the end of its design life (Titus – Glover et al., 2005) and is expressed as:

$$\log N_f = \left[\frac{-SR^{-10.24}\log(1-P)}{0.0112}\right]^{0.217} \quad (2.36)$$

Where,

i= $the\ number\ of\ load\ group\ or\ configuration$,

n_i= $the\ actual\ or\ projected\ number\ of\ repetitions\ of\ load\ group\ i$,

N_{fi}= $the\ allowable\ number\ of\ repetition\ for\ load\ group\ i$

P= $Probability\ of\ failure, hence, (1 - P) = Probability\ of\ pavement\ survival$,

$and\ is\ used\ as\ the\ design\ safety\ factor\ (Griffiths\ and\ Thom, 2007)$.

It is noted that the ratio $\left(\frac{n_i}{N_{fi}}\right)$ in equation 2.35 represents the fraction of the pavement fatigue life consumed by load group i, while CDM (Cumulative Damage Function) may be expressed as a ratio and must be ≤ 1.0 or as a percent by multiplying by 100 (Delatte, 2008). A comprehensive review of the proposed NCHRP/AASHTO M-EPDG design guide may be found in Delatte (2008) and other dedicated Technical reports.

2.7 Concrete Pavement Distress and Rehabilitation

From fatigue perspective, as demonstrate above, it is expected that every concrete pavement will fracture or deteriorate in serviceability at some point. However, it must be clarified that not all fractures in concrete pavement especially at the early age indicate a major structural failure. For instance, cracks due to concrete shrinkage and heat during drying process and hydration process are usually treated as intrinsic, and frequently are easy to repair.

On the contrary, certain conspicuous cracks resulting from intense induced stresses from wheel and stern environmental loadings are usually considered exigent in nature and often require rehabilitation intervention of the required authorities.

While grouping the general distresses that may develop in concrete pavements, Majidzadeh (1988) identifies two broad categories:

- Those requiring predictive models, e.g. fatigue cracking, shrinkage cracking, pumping, faulting, punchouts;
- Those that may be controlled via design specifications and material selection, construction practices, drainage etc; such as D-cracking, spalling, frozen joints, and blowups.

Despite considerable efforts on the subject of concrete pavement distress, the state-of-the-art design methods are still currently veiled with some unknowns; consequently, the cost of maintaining and rehabilitating pavement structures for airports and highways remains colossal. Modern engineering solutions in the area of structural rehabilitation of pavements should seek mainly to minimize life-cycle cost and simultaneously maximize structural performance of the repaired structure.

2.8 Basics of Delamination in a BCO system

Basically, the concept of BCOs design and construction is concerned with reducing stresses in the new overlay concrete while the existing pavement layer continues to carry significant portion of the load (Harrington, 2008). In design, assumption is made of full friction between the bonded layers, thus forming a monolithic composite section. Here, the concept assumes an adequate interfacial bond strength that is capable of transferring horizontal shear effectively across the interface; however, under certain conditions delamination does occur which invariably forces the system to perform below expectations.

In engineering and generally in all disciples, a common approach to solving technical problems of this nature is to probe into the mechanisms that govern their initiation and propagation. Several investigators including Nawy and Ukadike (1983), Delatte et al. (1998), Saucier and Pigeon (1991), Granju (1996, 2001), and Walraven (2007), just to mention a few, have shown keen interest on the subject of interfacial bonding and effective shear transfer between substrate concrete and new concrete, with promising results. Some of the results are timeless, while others afford more room for improvement.

Generally, at the interface, under service and thermal loadings, three types of stresses may develop: compressive normal stress, tensile stress and shear stress. The first type of stress due to wheel load is treated as trivial with respect to delamination failure and may be

neglected in its design since its contributions tend to be beneficial to the monolithic status of the composite, except where vertical cracking already develops within the system (Granju, 2001).

However, the other two stresses resulting from differential length change (Delatte, et al. 1998) of the concrete layer elements under shrinkage and temperature differentials are critical and cannot be ignored. While some (Saucier and Pigeon, 1991; Asad et al., 1997) argued that the effects of horizontal shear stresses are dominant on delamination failure between new-to-old concrete, investigators like Granju (2001) hold a contrary view, demonstrating that tensile stresses are dominant and should therefore govern the design considerations.

Whatever the case, from fracture mechanics perspective, the two stress conditions are rarely distinguishable in field, hence the term Mixed-Mode fracture mechanism. This has been demonstrated in the results presented in Granju (2001) where delamination was caused by the combined effects of shear and tensile stresses. But then, it has been shown that since cement-to-cement bond at the interface is more likely weak in tension than in shear, the interface therefore is more prone to fail in tension. Research has shown that the tensile interfacial bond strength lies around ~2MPa, which is just about half of the shear bond strength (Granju, 2001; Saucier and Pigeon, 1991; Grandhaie, 1993; Chausson, 1997).

Thus, solving this problem of delamination requires a more rational approach, as in the techniques involved in fracture mechanics. The basics of fracture mechanics have remained a useful tool for numerous cutting edge research works in the field of delamination. In fracture mechanics, three distinct modes of failure are identified: opening mode (Mode I), sliding mode (Mode II) and tearing mode (Mode III). The corresponding diagrammatical illustration for each mode is shown in Figure 2.14.

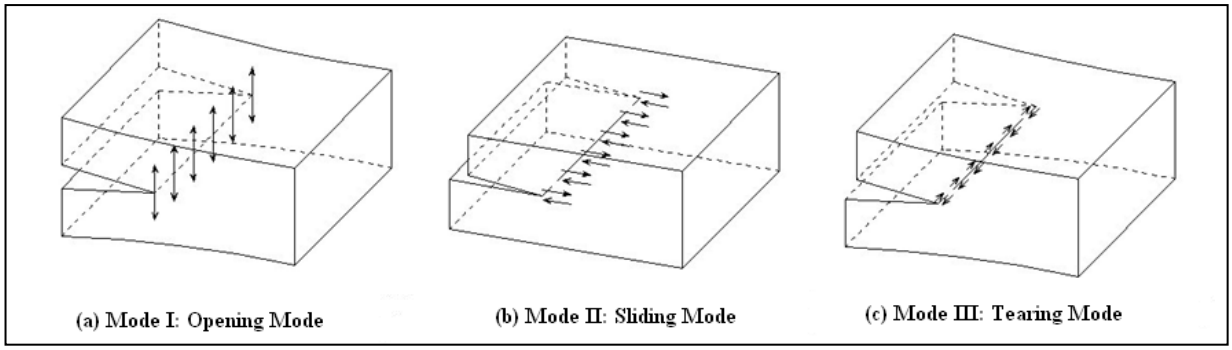

Figure 2.14: Fundamental fracture modes (Adapted from Lahitou *et al.* Center for Transportation Research The University of Texas at Austin, 2008).

The Mode I shown in Figure 2.14(a) relates to the opening of crack and is due to the normal tensile stress acting perpendicularly to the crack plane; Mode II (Figure 2.14b) however, corresponds to sliding at the crack plane due to the effect of horizontal shear stress. The Mode III (Figure 2.14c) is usually triggered by horizontal shear stress acting parallel to the crack front; such a phenomenon is uncommon with BCO interface.

Delamination is generally expected to occur when bond strength at the interface is exceeded by the normal tensile or horizontal shear stress or both stresses combined. Note that in a composite system like BCOs, fracture initiates and propagates through the weakest-link-in-the-chain (i.e. the most vulnerable region of the composite section) under intense stresses. Within the macro-anatomy of the BCO system, three equally important zones are named: the overlay, the interface, and the concrete substrate; of which the interface appears most vulnerable. Thus, in order to resist the tendency of delamination, the BCO interface must be optimized for bonding (Morgan, 1996).

Currently in practice less emphasis is said about optimizing the interface for bonding, rather much of the optimization works for BCOs design revolves around thickness requirement. In fact, the issue of interfacial bond compatibility and durability is treated more as a construction theme rather than an integral part of the overall design process. Until now, this inept approach to BCOs schemes has placed a major bound on the general perception and performance of BCOs. In this respect, the works in this thesis is particularly planned and designed to provide methods of designing the interface for optimum bond performance through experimental and numerical methods.

2.9 Durability Performance of BCO systems

Generally, in composite sections where stresses must be transmitted across a supposed weak plane, the shear transfer capacity of the interfacial bond is very crucial and must be design to withstand all shearing loads (Nawy and Ukadike, 1983). The shear transfer capacity of a BCO is dependent on the interlocking action of the aggregates, the cement-to-cement adhesion at the interface, and the dowel action of the rebar where shear reinforcement is present (Nawy and Ukadike, 1983; Delatte et al., 1998).

The interlocking action of the aggregates is provided by the substrate surface preparation (roughness), while the interfacial adhesion is due to the chemical bond of the paste. The inclusion of shear connectors, no doubt, enhances shear transfer capacity of the system, but their application may be neglected if sufficient bond strength can be secured through surface preparation and adhesive force of the cement paste.

Enhancement of the adhesive bond with bonding agents like epoxy or grout was once common, but they sometimes turn out as bond breakers if allowed to cure prior to placing the overlay concrete (Whitney et al., 1992). In most cases, the strength at the interface zone depends largely on the water-cement ratio, enhanced surface preparation, ambient temperature and RH at the time of BCOs application, and curing weather conditions and method used.

The relative importance of each of the parameters mentioned above has been a subject of debate. In Suprenant's (1988), three of the factors are identified and represented in a bond strength chain model. Figure 2.15 depicts this model.

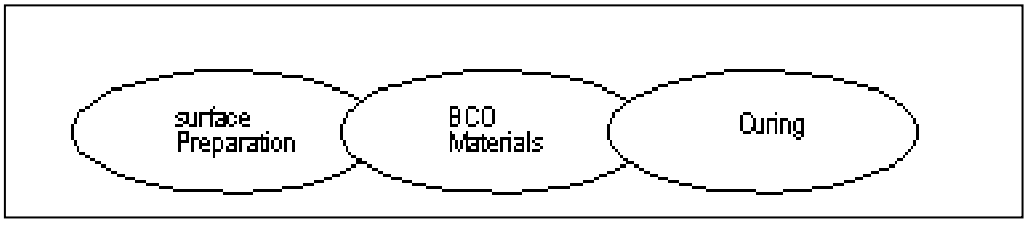

Figure 2.15: Chain Model of Bond Strength (Drawn from Delatte et al, 1998)

As illustrated above, the factors include: surface preparation, selection and use of materials (i.e. material compatibility), and curing. The three factors when treated as interdependent serve as a tool for ensuring optimum BCO durability performance.

From Figure 2.15, the relevance of chain relationship is highly recommended in Delatte et al. (1998). However, the true threshold below or above which interfacial bonding conditions are satisfied under each of the parameter considered in the model has remained a difficult task. The task is generally complicated by the fact that the two 'apparent parameters' (i.e. surface roughness and concrete-to-concrete chemical adhesion) on which bonding performance is depended are difficult to quantify in field. It is well-known that the adhesion at the interface changes over the period of curing (Dellate et al., 1998), while means of quantifying and expressing the effects of interlocking (roughness) over a large area as wide as pavement surface still remain a task to resolve. Hence, the simplistic nature of the model projects it more as a laboratory tool.

Considering the above in view of available literature and relevant codes of practice, till date, there are no unified baselines for defining the satisfactory levels of these parameters. For instance, while it is generally accepted that a minimum level of roughness texture is required to foster adequate interfacial bond, the ideal degree of roughness has however remained a growing variance of suggestion (Gohnert, 2002).

Further, from material point of view, it is noted in Suprenant (1988) and Delatte et al. (1998) that incompatibility in physical properties between bonded materials can result in delamination. As illustrated in Delatte et al., (1998), it is specified that BCO materials should be selected and proportioned for rapid strength, minimum thermal expansion and contraction, and minimum shrinkage. This view agrees with other investigators like Emberson and Mays (1990), Morgan (1996), and Emmons and Vaysburd (1996).

However, Morgan (1996) unlike others stresses the importance of compatibility in light of overlay material properties, sensitivity, and durability to the entire BCO system. This systemic view provides designers with a reasonable level of material selection and matching, especially when viewed in line with Emberson and Mays' (1990) material categorization table given in Table 2.1 and Mays and Wilkinson's (1987) mechanical properties table illustrated in Table 2.2.

Table 2.1: Categories of system for concrete patch repair (Emberson, N.K. and Mays, G.C., 1990).

As illustrated in table 2.1, and as mentioned earlier, the material investigations in this research work is categorised as Polymer Modified Cementitious material, following class D.

Figure 2.2: Typical mechanical properties of repair materials (Mays, G. and Wilkinson, W., 1987).

As shown clearly in tables 2.1 and 2.2, it is apparent that an ideal material that will satisfy all the compatibility requirements may not exist though; a relative perfect match could be achieved if one is guided by the structural compatibility table of Emberson and Mays (1990) – Table 2.3.

Table 2.3: General requirements of patch repair materials for structural compatibility (Emberson, N.K. and Mays, G.C., 1990).

In practice, the underpinning principle governing material characterization on a long-term performance is to ensure reasonably approximate match between the moduli of elasticity and also satisfy movement-related properties, such as expansion and contraction, of the overlay material and the existing pavement (Harrington et al., 2007). In that respect, aggregates with high thermal coefficient or absorption should generally be avoided (Delatte, et al., 1998).

In sum, this chapter reviewed and discussed three input data sources for the design of pavement and BCO structural systems. The first input data focused on the idealized sub-grade model based on Winkler's foundation and other elastic foundation models mostly within the works of Westergaard and other investigators like Hogg, Holl, and Pasternak. The second data source related to the material mixture design methods of the constructed layers and their properties evaluation using the traditional or the statistical optimization method. Compatibility aspect between the overlay and the substrate was highlighted as well. The third source of design data considered information obtained from the historical observation of old pavement structures and their regression model formulation; modifications of regression models with modern mechanistic approach were likewise reviewed. In addition, potential application of fracture mechanics-based concepts to capture the elevated stress levels in pavement and BCO structures which are beyond the scope of the mechanistic approach was simultaneously advanced.

Note that the input data sources and the related methods presented in this section provide necessary groundwork for the subsequent work presented in this thesis. Both material mixture design and optimization analysis and computational mechanistic approach were employed for providing a common solution relating interfacial bonding and delamination mechanisms.

3.0 Research Theoretical Basis

This section presents the theoretical basis for the implementation of material mixture design of the overlay and the computational interfacial fracture mechanics described in this thesis.

3.1 Material Mixture Model and Optimization

The BRCFRPMC used in this study contains six components: Portland cement (CEM I), water, polymer (SBR), fine aggregate (FA), coarse aggregate (CA), and steel-fibre (SF). Its overall composite response, like any concrete mixture, depends essentially on the proportions of its constituents. In practice, several experimental design proportioning methods exist, including Factorial, Response surface, Taguchi, and Mixture design (Simon, 2003). The choice of a particular design method depends on the approach and objectives of the experimenter. In this study, Mixture Design method was chosen because its design response depends exclusively on the relative proportions of the input components, and typically its experimental region of interest is more defined naturally (Simon, 2003; Simon et al., 1987). In essence, the design space in Mixture Experiment represents the possible combinations of the relative proportion of each component in the total volume, and usually adds up to 1.

3.1.1 Mixture Model

Consider a mixture made of N components such that the i^{th} component occupies x_i of the total space. If the setting for each component space (x_i) is constrained by:

$$x_i \geq 0, \qquad \forall i: \ i \in N$$

and

$$\sum_i^N x_i = x_1 + x_2 + x_3 + \cdots + x_N = 1 \tag{3.1}$$

then, for a standard mixture experiment, the design region can be represented with a simplex of N vertices with regular sides of $(N-1)$ dimension. Thus, for a blend containing

three components as the one illustrated in Figure 3.1, the design space is an equilateral figure constrained by the conditions stated in equation (3.1) and its vertices correspond to (1,0,0), (0,1,0), and (0,0,1).

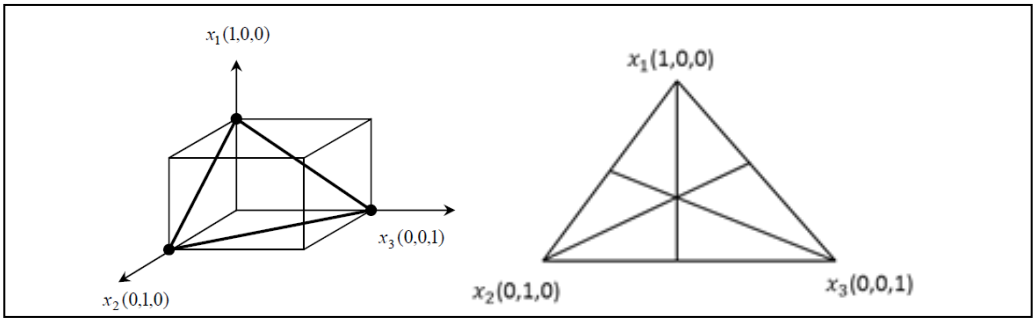

Figure 3.1: Mixture Design Space for Three components

As seen in Figure 3.1, each vertex represents a pure component where other components are absent; while the centroid depicts a mixture where the three components are present in equal proportion of $(1/3,\ 1/3, 1/3)$; hence, the term simplex-centroid. Numerically, the axis of each component stretches from its vertex ($x_i = 1$) to the midpoint of the opposite side where $x_i = 0$. For modelling purposes, all desired properties can be measured experimentally for each possible mix in the design space and subsequently modelled as a function of the input variables. In many instances, mathematical formulations based on polynomial functions are used, though other forms can be employed (Czarnecki et al., 1999; Simon et al., 1987).

Typically, for a three-component mixture experiment, the usual first order polynomial is given by:

$$E(y) = \beta^* + \sum_i^N \beta_i x_i \qquad (3.2)$$

Where, β^* is the constant and β_i is the coefficient associated with the model.

Based on the constraint given in equation (3.1), where $\sum_i^N x_i = 1$; the solution to β_i cannot be uniquely determined. Hence, using the approach suggested by Scheffe (1958); if β^* is multiplied by $\sum_i^N x_i = 1$, then equation (3.2) becomes:

$$E(y) = \sum_i^N (\beta^* + \beta_i) x_i \qquad (3.3)$$

Typically equation (3.3) is re-parameterized in the form:

$$E(y) = \sum_{i=1}^N \beta_i x_i \qquad (3.4)$$

So that its quadratic polynomial can be written as:

$$E(y) = \sum_{i=1}^{N} \beta_i x_i + \sum \sum_{i<j}^{N} \beta_{ij} x_i x_j \qquad (3.5)$$

Where, β_{ij} represents the nonlinear or quadratic blending term. When β_{ij} is positive, the term is synergistic, while negative value suggests an antagonistic blend response.

In addition, where full cubic and special cubic functions are considered, equations (3.6) and (3.7) result respectively:

$$E(y) = \sum_{i=1}^{N} \beta_i x_i + \sum \sum_{i<j}^{N} \beta_{ij} x_i x_j + \sum \sum_{i<j}^{N} \delta_{ij} x_i x_j (x_i - x_j) + \sum \sum_{i<j<k} \sum \beta_{ij} x_i x_j x_k \qquad (3.6)$$

$$E(y) = \sum_{i=1}^{N} \beta_i x_i + \sum \sum_{i<j}^{N} \beta_{ij} x_i x_j + \sum \sum_{i<j<k} \sum \beta_{ij} x_i x_j x_k \qquad (3.7)$$

Accordingly, the appropriate model for an experiment usually follows the method of analysis of variance (ANOVA).

3.1.2 Mixture Optimization Techniques

Following the three-component design space shown in Figure 3.1, it is evident that no viable concrete mixture can be obtained over the entire simplex-space without constraining the mixture design to a sub-region of the equilateral triangle. The constraint is usually obtained by applying a lower bound, or an upper bound, or both restrictions on the mixture components in addition to the initial condition that the total of all component proportions must add up to 1. In this respect it can be shown that:

$$\left.\begin{array}{rl} 0 \le L_i \le x_i & for\ lower\ limit \\ 0 \le x_i \le U_i & for\ upper\ limit \\ 0 \le L_i \le x_i \le U_i \le 1 & for\ combined\ limits \end{array}\right\} \qquad (3.8)$$

$where, i = 1,2, \dots, N;\ \ L_i = Lower\ limit;\ U = U\ pper\ limit;$

$and\ x_i = component\ proportion$

By definition, when a mixture is constrained by the restrictions given in inequalities (3.8), it is referred to as Constrained Mixture Design. In the present study, therefore, a classical constrained fitting model based on Extreme-Vertices Design (EVD) approach of (McLean, and Anderson, 1966) was adopted. In the model, both lower and upper bounds were set a priori, and a list of all combinations based on $[N(2)^{N-1} + 1]$ possible blends was made. In addition to the choice of model, an overall desirability function (D) was incorporated and

used as a metric for multi-criteria optimization. For each criterion, two values, 0 and 1, were defined, such that the desirability scale satisfies the condition $0 \leq d(y_i) \leq 1$. In this case, '0' indicates that one or more criteria lie outside their acceptable values, while '1' corresponds to the ideal response. The conditions for acceptance or rejection generally depend on the set goal, i.e. the direction of optimization – maximum, minimum or target; in reference to equation (3.9), (3.10), or (3.11):

Here, a maximized response indicates that a larger value is better, and its desirability is calculated by:

$$d(y_i) = \begin{cases} 0 & y_i < L \\ \left(\frac{y-L}{T-L}\right)^{r_i} & L \leq y_i \leq T \\ 1 & y_i > T \end{cases} \qquad (3.9)$$

while, a minimized response shows that a smaller value is better, with its desirability given by:

$$d(y_i) = \begin{cases} 1 & y_i < T \\ \left(\frac{U-y_i}{U-T}\right)^{r_i} & T \leq y_i \leq U \\ 0 & y_i > U \end{cases} \qquad (3.10)$$

Finally, the "target" indicates the best response, and its desirability corresponds to:

$$d(y_i) = \begin{cases} 0 & y_i < L \\ 0 & y_i > U \\ \left(\frac{U-y_i}{U-T}\right)^{r_i} & T \leq y_i \leq U \\ \left(\frac{y_i-L}{T-L}\right)^{r_i} & L \leq y_i \leq T \end{cases} \qquad (3.11)$$

Where y_i is predicted value of ith response; T is target value; U is highest acceptable value; L is lowest acceptable value; and r_i is weight of ith desirability function. Based on the conditions given in equations 3.9, 3.10 and 3.11, a multi-response numerical optimization was performed, during which the optimum mix maximizes the weighted geometric mean of individual desirability function ($d(y_i)$) over the feasible composite space. In the process, a model where the responses are given equal weight was adopted; hence, the composite desirability takes the form:

$$D = [d(y_1) \times d(y_2) \times \ldots \times d(y_n)]^{1/n} \qquad (3.12)$$

Where, n is total number of all individual responses.

3.2 Interface Fracture Description

From analytical viewpoint, two basic approaches are common for simulating and describing failure analysis of the interface: (1) stress-based failure criterion approach, and (2) Energy-based fracture criterion approach. By definition, the two approaches defer in concepts and computational techniques. For instance, in the limit analysis or the so-called stress-based approach, the interface is assumed as perfectly bonded, while the classical energy-based method - linear elastic fracture mechanics (LEFM) - treats the interface as having some well-known intrinsic defects.

Contrariwise, in quasi-brittle materials like concrete, the two extreme collapse models cited above are rear and mostly impractical; therefore, a more robust nonlinear collapse model is required. In this thesis, an Interface Cohesive Zone Model (ICZM) within the domain of non-linear fracture mechanics was employed. In the analysis, both delamination initiation and propagation processes are represented within a unified model. Thus, the progressive failure analysis of the interface can be described.

The following sections presents each of the failure criteria identified above:

3.2.1 Traditional Stress-based Criterion

In order to ensure that delamination process of the interface is adequately represented, the mechanical characterization of the interface requires two basic descriptive states: (1) a state representing perfectly bonded condition, and (2) a state defining delamination onset and propagation.

In the former, adhesion between the bonded layers is assumed sufficiently strong thereby imposing both stress and displacement continuity across the interface. Using Figure 3.2, the kinetics and the kinematics for continuity requirements follow equation 3.13 (Shah and Stang, 1996):

$$\left.\begin{aligned} \tau_{top} &= \tau_{btm} \\ \sigma_{top} &= \sigma_{btm} \\ u_{top} &= u_{btm} \\ v_{top} &= v_{btm} \end{aligned}\right\} \quad on\ I_b \qquad (3.13)$$

Where, I_b is all points on the bonded interface, τ and σ are respective shear and normal stresses of a point on the interface, while v and u are their corresponding tangential and

normal displacements. Note, the subscripts 'top' and 'btm' represent the top and bottom layer respectively.

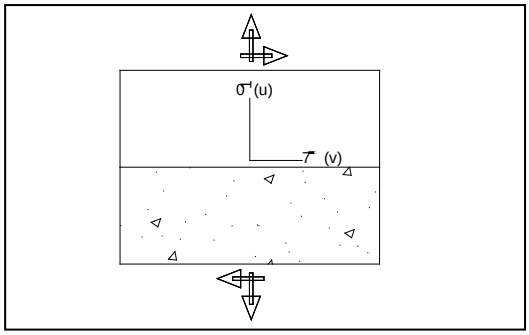

Figure 3.2: Stress states and notations on perfectly bonded interface

A quick examination of the model represented by equation 3.13 shows that it lacks practicality in many instances, since it is basically premised on the assumption of a perfectly elastically bonded interface with no possibility of yielding or de-bonding. In reality, the interface is expected to yield at considerable lower stresses compared to the two adjacent bulk materials, as stresses localize or concentrate in the region of the interface largely due to bond imperfection and elastic properties mismatch between the bulk materials. In the literature, it has been shown that such localized or concentrated stresses can be in the order of about 3 times the average stresses developing in the adjacent materials (Kirsch, 1898; Dantu, 1958). Thus, characterizing the interface by a finite strength is commonplace in practice. Typically, for composite interface model of this nature, a general stress-based failure criterion could take the form:

$$F\left(\tau, \sigma, P_i\right) = 0 \qquad i = 1 \ldots, n \tag{3.14}$$

Where, P_i is one of n strength parameters, while other parameters are as given before.

Invariably from equation 3.14, the interfacial de-bonding process within the domain of limit analysis thus permits the bonded interface to separate once it is loaded beyond its critical bond strength. The governing constitutive relations in this case are generally based on the kinematics of the interface, as the interface changes from its continuity condition to a prescribed surface traction boundary condition. In this case, the failure criterion takes the form (Shah and Stang, 1996):

$$\left.\begin{array}{l} \tau_{top} = \tau_{btm} = f \\ v_{top} = v_{btm} = g \\ u_{top} - u_{btm} \geq 0 \end{array}\right\} \; on\; I_d \tag{3.15}$$

Where, I_d is all points on the de-bonded interface, while 'f' and 'g' are prescribed surface tractions in the general case.

Again, while the conditions given in equation (3.15) show a high explicit level about the nature of the de-bonding, possibility of surface overlapping during de-bonding process is precluded a *priori*; and often this can be difficult to substantiate in practice, especially in cementitious materials where complicated interfacial contact problems dominate during de-bonding initiation stage (Shah and Stang, 1996). Further, during subsequent steps, and at critical cracking stage of the interface, it is expected that the interface attains a stress-free state (Atkinson *et al*., 1982; Stang and Shah, 1986; and Morrison *et al*., 1988); hence, the frictional stress given in equation (3.15) vanishes accordingly, so that it reads:

$$\left.\begin{matrix} \tau_{top} = \tau_{btm} = 0 \\ v_{top} = v_{btm} = 0 \end{matrix}\right\} \; on \; I_d \qquad (3.16)$$

Following the above, if the interface is simultaneously influenced by stress and displacement continuities perpendicular to the interface, then, the boundary conditions given in equation (3.16) can be extended to include:

$$\left.\begin{matrix} \sigma_{top} = \sigma_{btm} = 0 \\ u_{top} = u_{btm} = 0 \end{matrix}\right\} \; on \; I_d \qquad (3.17)$$

So far, from engineering perspective, the use of limit analysis as demonstrated for both perfectly bonded and de-bonded interface surface characterizations seems reasonable and acceptable, but its inability to explain or capture the infinite stress condition at the crack-tip between the perfectly bonded region and the de-bonded zone of the interface is still seen as a major drawback. It should be noted that the analytical proof of such stress singularities are based on complete linear elastic solution of the de-bonded interface problem.

In the literature, it has been shown that the presence of these singularities is the reason why finite element analysis involving interface problem is mesh-dependent, especially with respect to its interface stress response (Mormonier *et al*., 1988). In contrast, the justification of infinite stress state is also hard, if not impossible, since no material can be loaded beyond its yield strength.

Therefore, it can be concluded that many of the parameters employed in determining stress-based de-bonding criterion cannot be regarded as absolute material parameters, knowing that their values vary widely according to the type and complexity of the analysis used.

Besides, it is likely - due to the incompleteness of the analysis - that the value of the strength parameters corresponding to a given interface will depend on the geometry and the loading conditions of the composite system. Size effects have been observed in similar tests, which, for instance, pure shear analysis fails to predict (Shah and Stang, 1996; Bazant and Zi, 2003). With the advent of modern computational tools, however, many of the problems associated with incomplete analysis or rigorous analytical solutions for de-bonded interface can be overcome.

3.2.2 Energy-based criterion

In terms of energy-based criterion, methods based on classical linear elastic Interface fracture mechanics (LEIFM) have been found effective in describing and modelling crack propagation, especially where material nonlinearities cannot be neglected (Turon, *et. al*, 2004). As illustrated in Figure 3.3, for a bonded bi-material interface with adjacent domains characterized linearly by E_i, μ_i and v_i for Young's Modulus, shear modulus, and Poisson's ratio of each domain respectively; it has been shown that there exists an intrinsic singularity with oscillatory field ahead of the crack tip (Williams, 1959), caused largely by the asymmetry in the elastic properties across the interface. The oscillatory, afterward, controls the measure of the competing or complex stress state near the crack-tip, which in terms of stress intensity factors takes the form:

$$\sigma_{yy} + i\tau_{xy} = \frac{(K_1 + iK_2)r^{i\varepsilon}}{\sqrt{(2\pi r)}} \qquad (3.18)$$

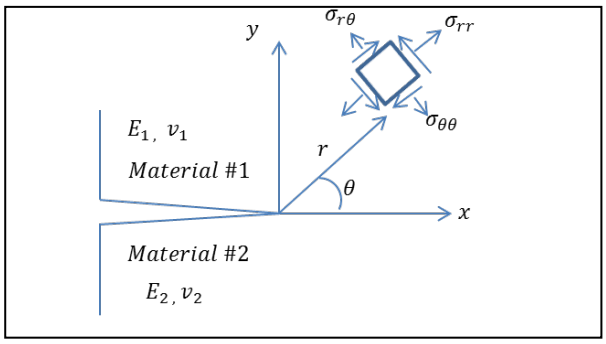

Figure 3.3: Linear crack along a Bi-material Interface

Where $r^{i\varepsilon} = \exp(i\varepsilon\, log\, r) = \cos(\varepsilon \log r) + i\, sin\, (\varepsilon \log r)$, $i = \sqrt{-1}$, r is the distance ahead of the crack-tip, ε is the oscillatory index defined by equation (3.21), K_1 and K_2 are components of the complex stress intensity factor derived by Rice and Sih (1965) by solving

the following logarithmic expressions arising from a full boundary-value problem of a given test specimen (Carlsson and Prasad, 1993; Chandra, 2002):

$$K_1 = \frac{\sigma[\cos(\varepsilon \log 2a)+2\varepsilon \sin(\varepsilon \log 2a)]+\{\tau[\sin(\varepsilon \log 2a)-2\varepsilon \cos(\varepsilon \log 2a)]\}}{\cosh \pi\varepsilon} \sqrt{a} \qquad (3.19)$$

$$K_2 = \frac{\tau[\cos(\varepsilon \log 2a)+2\varepsilon \sin(\varepsilon \log 2a)]-\{\sigma[\sin(\varepsilon \log 2a)-2\varepsilon \cos(\varepsilon \log 2a)]\}}{\cosh \pi\varepsilon} \sqrt{a} \qquad (3.20)$$

From where, ε can be estimated:

$$\varepsilon = \frac{1}{2\pi} \text{In } \left[\frac{1-\beta}{1+\beta}\right] \qquad (3.21)$$

In equation (3.21), (β) relates to one of Dundur's elastic mismatched parameters (Dundur, 1969) and is a measure of the relative compressibilities of the two bonded materials, commonly estimated by equation (3.22), say, for plane strain problems (Mei *et. al*, 2007); while its counterpart (α) given in equation (3.23) measures the corresponding relative stiffness (Mei *et. al*, 2007; Schmauder, 1990; Bower, 2010).

$$\beta = \frac{1}{2} \left[\frac{\mu_1 (1-2v_2)-\mu_2(1-2v_1)}{\mu_1(1- v_2)+\mu_2(1 + v_1)}\right] \qquad (3.22a)$$

Which on simplifying yields:

$$\beta = \frac{E_1' (1-v_1)(1-2v_2)-E_2'(1- v_2)(1-2v_1)}{2(1-v_1)(1- v_2)(E_1' + E_2')} \qquad (3.22b)$$

Where, $E_i' = E_i/(1 - v_i^2)$ *plain strain Young's Modulus for material* i

$$\alpha = \frac{E_1' - E_2'}{E_1' + E_2'} \qquad (3.23)$$

Subsequently, under Mode-Mixity, the energy release rate, (G), for crack extension per unit length along the interface for a plain strain analysis is generally given by (Carlsson and Prasad, 1993):

$$G = \frac{|K|^2}{E^* cosh^2 \pi\varepsilon} \qquad (3.24)$$

Where,

$$|K| = \sqrt{K_1^2 + K_2^2} \qquad (3.25)$$

$$cosh^2 \pi\varepsilon = 1/(1 - \beta^2) \qquad (3.26)$$

$$\frac{1}{E^*} = \frac{1}{2}\left(\frac{1}{E_1'} + \frac{1}{E_2'}\right) \tag{3.27}$$

Thus, by Mode-Mixity, the value of (G) as a function of the loading phase angle $(\acute{\Psi})$, follows the real and imaginary stress intensity factors of the remote field lying ahead of the crack tip. This can be written as:

$$\acute{\Psi} = tan^{-1}\left[\frac{Im(K_1+iK_2)L^{i\varepsilon}}{Re(K_1+iK_2)L^{i\varepsilon}}\right] \tag{3.28a}$$

Where, L is the arbitrary reference length selected to characterize the remote field. For most bi-material systems, it is clear that the value and the effect of nonzero (β) is small, and usually insignificant (Bower, 2010; Buyukozturk and Hearing 1998); thus, by setting $\varepsilon = 0$, for most material combinations, equation 3.28a then simplifies to:

$$\acute{\Psi} = tan^{-1}\left(\frac{K_2}{K_1}\right) \tag{3.28b}$$

The corresponding displacement components behind the crack tip are given in Bower (2010) by:

$$d_y + id_x = \frac{4|K|e^{i\acute{\Psi}}}{E^*(1+2i\varepsilon)\cosh(\pi\varepsilon)}\sqrt{\frac{r}{2\pi}}\left(\frac{r}{L}\right)^{i\varepsilon} \tag{3.29}$$

From the above equations, it is clear that the asymptotic solution for the interface crack differs significantly from the corresponding solution for a homogenous solid, because the oscillatory character due to both stresses and displacements increases frequency as the crack tip is approached; hence, making it difficult to discretize the remote loading. Besides, the crack planes are predicted a *priori* as overlapping near the crack-tip, which perhaps is still unclear in many practical instances (Bower, 2010).

In sum, the above LEIFM model is attractive when considering crack propagation process for brittle materials; and a critical condition is usually assumed to have been reached when the energy release rate G equals the fracture toughness of the interface $G(\acute{\Psi})$. That is:

$$G = G(\acute{\Psi}) \tag{3.30}$$

Experimentally, it has been shown (Suo and Hutchinson, 1989; Charalambides *et. al.*, 1990) that this interface resistance to delamination increases rapidly with phase angle.

In essence, while both approaches described above provide some level of analytical comfort; in reality, evidence of initial perfect interfacial bonding or the presence of initial interfacial crack, together with its location and size may be difficult to spot or substantiate in cementitious overlay composite system. It is therefore imperative to think of an enhanced method, where both interfacial crack initiation and propagation processes are described within a unified model. Evidently, employing nonlinear interface cohesive models affords a common opportunity for implementing such task. The models are well-known as particularly suitable for representing adhesion and de-cohesion processes between dissimilar materials (Mei *et al*, 2010).

3.2.3 Interface Cohesive Zone Model (ICZM)

In the Interface Cohesive Zone Model (ICZM), the primary consequence of nonlinear fracture models is based on the assumption of a finite fracture (cohesive) zone existing in the vicinity and ahead of the crack-tip, based on Dugdale's strip yield (1960) and Barenblatt's cohesive force (1962) models shown in Figure 2.3. Apparently, the models as depicted imply that the so-called stress singularity (infinite stress state) concept associated with crack-tips in the elasticity theory (see Figure 2.3b) is somewhat unrealistic (Cornec, *et al*., 2003).

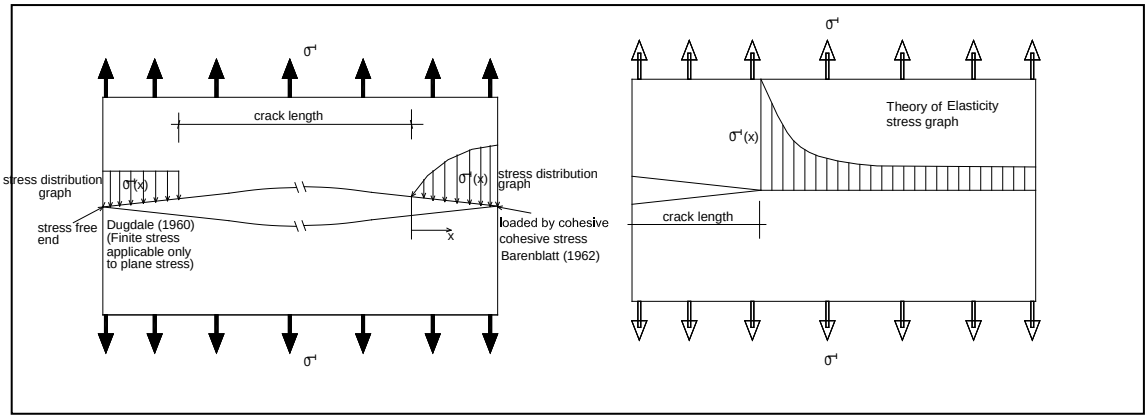

Figure 3.4: Comparison between (a) Dugdale and Barenblatt Models and (b) Stress singularity in Elasticity theory

Thus, for description purpose (Shah and Stang, 1996), the cohesive interface models represent a condition of a perfectly bonded interface changing to a de-bonded regime when the cohesive strength of the bonded interface varnishes with displacement discontinuity. Hence, for nucleation and propagation descriptions, ICZM appears most attractive; in particular in materials like concrete, where the non-linearity in the vicinity of crack-tip cannot be neglected, due to the presence of a large damage zone lying ahead of the crack-tip.

In this respect, for a complete interface nonlinear fracture model description, the following are essential:

- The behaviour of the bulk materials, and
- The behaviour of the fracture zone, where conditions for crack formation and evolution are pre-defined along a known crack path.

For instance, in this thesis, the cementitious bi-material was classified as quasi-brittle. Besides, because the bi-material exhibits no bulk dissipation, an isotropic linear elastic behaviour, characterized by elastic modulus (E) and Poisson's ratio (v), was assumed. With respect to the fracture zone behaviour, a softening damage characteristic along the interface was assumed based on the kinetics and kinematics relations defined in Figure 3.5.

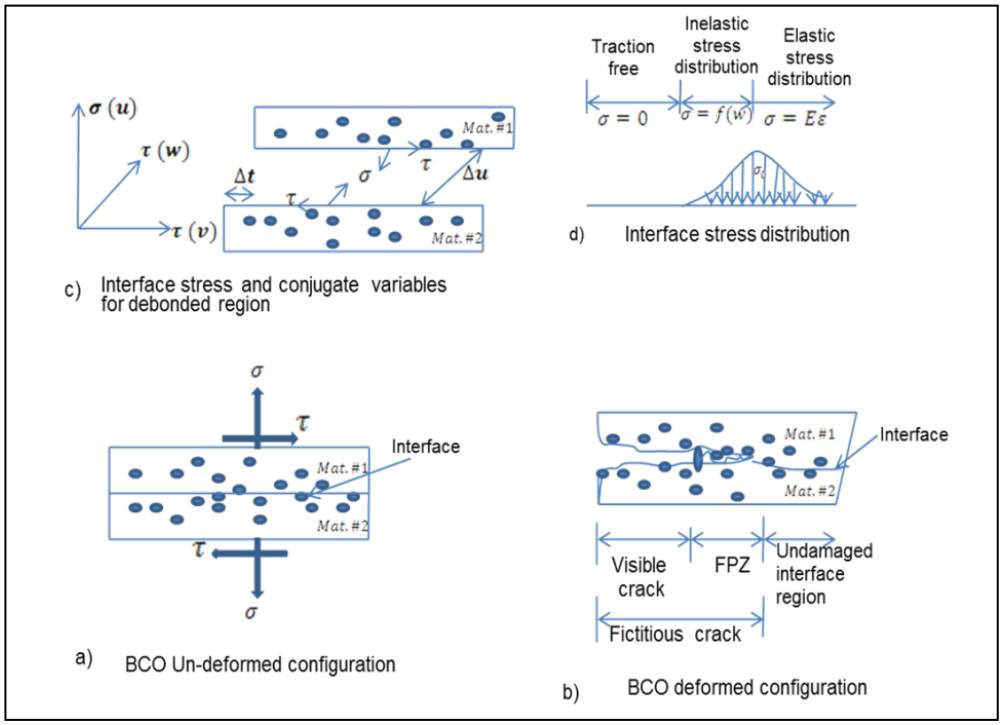

Figure 3.5: Interface configurations with Fracture Process Zone (FPZ) and Interface Stress Distribution

Broadly, Figure 3.5 shows a BCO in its un-deformed and deformed configurations with a visible or true crack. The resulting FPZ, interface stress / conjugate variables, stress distribution curve between the FPZ and the elastic bi-material interface, and the constitutive relation defining each zone in the cohesive model after deformation are equally depicted. The overall cohesive model defined here follows the assumptions given below:

- The FPZ along the interface localizes into a single line ahead of the crack tip, with no possibility of kinking.
- The FPZ or the fictitious crack length is assumed mostly dominated by inelastic deformation.
- The materials lying adjacent the fictitious crack behave linearly elastic.
- The constitutive law governing the inelastic deformation at the FPZ assumes stress-displacement relationship.

Consequently, the associated kinematics refers to the relative motion of the two deformed layers at the interface and may be described as follows:

- In Figure 3.5(c), u represents a unit vector in normal direction to the interface.
- At the interface, two mutual tangential unit vectors, $\boldsymbol{v}$ and $\boldsymbol{w}$, are introduced.
- But for cementitious interface of this nature, it is usual to assume an isotropic condition; thus, the tangential deformation along $\boldsymbol{v}$ and $\boldsymbol{w}$ directions is treated as equal, hence, the constitutive relation can be defined in terms of scalar Cartesian components $\Delta\boldsymbol{u}$ and $\Delta\boldsymbol{t}$ only (Bower, 2010), which represent the relative displacements of two initially coincident points at the interface, in normal and tangential directions respectively. (Note: $\Delta\boldsymbol{t} = \sqrt{\boldsymbol{v}^{2+}\boldsymbol{w}^{2}}$).

The kinetics of the interface on the other hand, relate to the forces acting between the two contacting layers. In this case, the two equal and opposite tractions are assumed acting on two initially coinciding points before and during interface deformation. Thus, under isotropic condition, the corresponding interface tractions are given by the scalar components $\boldsymbol{T_n}$ and $\boldsymbol{T_t}$ in the normal and tangential plane respectively.

Ultimately, the kinetics and kinematics descriptions given above result in an irreversible (cumulative) force-displacement relation which helps simulate the fracture process that creates two delaminated surface at the interface. From here, the subsequent section discusses the theory employed to represent full interfacial fracture process within the framework of cohesive zone model. In addition, methods for characterizing the interface are also underlined.

3.2.4 Modelling Interface Cohesive Zone Model with ANSYS FEA

The use of finite cohesive zone for cementitious materials is well-established following Hillerborg *et al*. (1976) linear softening model. Subsequently, the use of cohesive zone

model (CZM) for cementitious materials has grown into popularity due mainly to its computational convenience, and as it stands today, CZM is probably the best fracture model for simulating fracture processes in cementitious materials and structures (Bazant, *et al*., 2002).

Interestingly, for concrete, both linear softening model, introduced by Hillerborg *et al.* (1976), and bilinear softening model, developed by Petersson (1981), can be implemented. With ANSYS FEA, the surface traction was obtained as an extrapolation of standard Gauss nodal stresses between adjacent continuum interface elements.

In this thesis, the delamination model assumes a zero-thickness contact interface, and uses associative cohesive elements with constitutive properties along a pre-defined interface between two adjacent continuum elements. The resulting interface damage initiation and evolution was governed by the nonlinear traction-separation (bi-linear) law described in Alfano and Crisfield (2001) and illustrated in Figure 3.6.

In the bi-linear model shown in Figure 3.6, it is assumed that the interface behaves elastically under loading with initial stiffness (k_0) until the applied stress reaches the cohesive strength (σ_0) of the interface, at which point the damage initiation occurs. Note here that the initial elastic stiffness (k_0) has a character of a penalty factor only rather than a physical stiffness, and is often discretionary kept high to ensure minimum elastic deformations of the interface (i.e. of negligible degree), so as to minimise interpenetration or sliding prior to cracking.

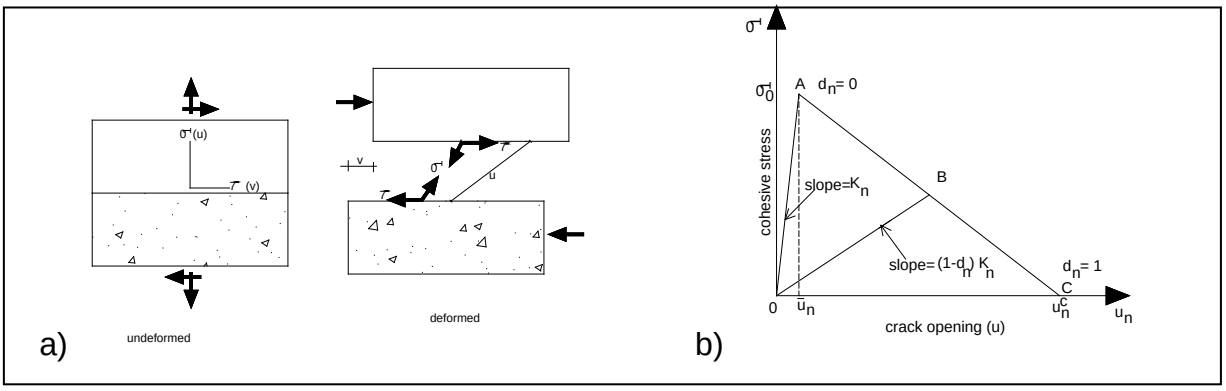

Figure 3.6: a) Definition of stress and conjugate variables, and b) Bilinear softening relation

As illustrated in Figure 3.6, the delamination process is defined by two slopes OA and AC. The initial slope OA represents the linear elastic regime of the curve, while the second slope defines the softening part of the curve in a linear function. De-bonding is assumed to

initiates at peak contact stress (σ_0) at point A, and grows linearly as a function of de-bonding parameter (d). The value of (d) evolves progressively from 0 to 1 as shown in equation 3.31 till all the interface stresses reduce to zero at critical crack point C (u_n^c).

$$d = \begin{cases} 0 & for \;\; u_n = \bar{u}_n \\ 0 < d \leq 1 & for \;\; u_n > \bar{u}_n \end{cases} \qquad (3.31)$$

Where,

$u_n = separation\ for\ the\ interface\ elements\ over\ the\ entire\ loading\ history.$

$\overline{u}_n = \dfrac{\sigma_0}{k_0} = critical\ separation\ for\ damage\ initiation$

$\sigma_0 = cohesive\ strength$

$k_0 = initial\ elastic\ contact\ stiffness$

Thus, for each pure mode of failure during loading, the fracture cohesive stress (T) can be related to the opening or sliding displacement linearly by:

$$T = \begin{cases} \sigma = k_n u_n\,(1 - d_n) & for \;\; Mode\ I \\ \tau = k_t u_t\,(1 - d_t) & for \;\; Mode\ II \end{cases} \qquad (3.32)$$

Where, σ and τ are the cohesive stresses in the normal and tangential directions respectively, while k_n and k_t denote the corresponding contact stiffnesses. u_n and u_t represent the accompany displacements after deformation while d_n and d_t are the resulting de-bonding parameters in Mode I and Mode II respectively.

However, for bonded dissimilar materials, Mixed-Mode delamination is a common phenomenon due to the competing interfacial stress effect during loading and failure process, which implies that criteria for damage initiation and final failure must account for the concomitant effects of Mode I and Mode II. In that case, both normal and tangential traction-separation curves can be expanded in the ($u_n\ and\ u_t$) - plane, as illustrated in Figure 3.7, such that the normal and shear stresses depend not only on their corresponding displacement, but on both the shear and normal opening; which follows the expression in equation 3.33.

$$\left.\begin{matrix} \sigma\,(u_n,\, u_t) \\ \tau\,(u_n,\, u_t) \end{matrix}\right\} \qquad (3.33)$$

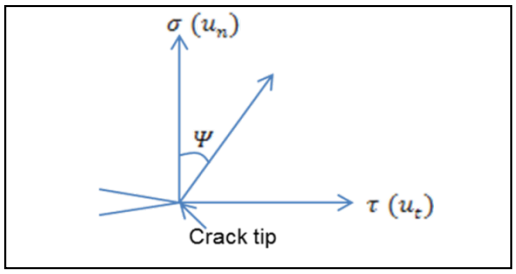

Figure 3.7: Mixed-Mode oscillatory field at crack-tip

Consequently, the effective traction vector and the corresponding effective displacement can respectively be given by:

$$\lambda_m = \sqrt{\langle\sigma\rangle^2 + \tau^2} \tag{3.34}$$

$$\bar{u}_m = \sqrt{\langle u_n\rangle^2 + {u_t}^2} \tag{3.35}$$

Thus, for local Mixed-Mode fracture, the critical magnitude of the traction vector now depends on the ratio between the shear and normal tractions, which by definition is the phase angle given in equation 3.36.

$$\Psi = tan^{-1}\left(\frac{\tau}{\langle\sigma\rangle}\right) \tag{3.36}$$

Combining equations 3.34 and 3.36, it can be shown that:

$$\lambda_m = \sqrt{\langle\sigma\rangle^2 + \tau^2} \ = \frac{\langle\sigma\rangle}{Cos\,\Psi} = \frac{\tau}{Sin\,\Psi} \tag{3.37}$$

So that by considering identical ratios between the two tractions and their corresponding displacements, equation (3.37) can be expanded in the form:

$$\bar{u}_m = \sqrt{\langle u_n\rangle^2 + {u_t}^2} = \frac{\langle u_n\rangle}{Cos\,\Psi} = \frac{u_t}{Sin\,\Psi} \tag{3.38}$$

In effect, as Ψ increases, the normal stress-crack opening curve diminishes from $\Psi = 0^0$, while the shear stress-sliding curve expands towards a maximum for $\Psi = 90^0$.

For clarity purpose, the phase angle (Ψ) defined here can be at variance from the global phase angle ($\acute{\Psi}$) defined earlier in equation (3.28b) for the LEIFM, though they both measure the relative proportion of the effect of Mode II fracture to Mode I fracture on the interface. For many practical systems (Buyukozturk and Hearing, 1998), including

cementitious interface, the effect of non-zero (β) is of secondary consequence; hence, the global phase angle can conveniently be reduced to $\acute{\Psi} = \arctan\left(\frac{K_{II}}{K_I}\right)$ as depicted earlier.

Therefore, since the phase angle given by equation 3.36 is of local Mixed-Mode effect, its numerical value may vary along the interface - from element to element – (Mei *et al*, 2010); though such level of variation with respect to the delamination length, is usually relatively insignificant for short crack limit. Therefore, it sounds reasonable to assume a constant steady-state phase angle during the analysis, while treating the interface toughness as independent of the delamination length, but a dependent function of the phase angle, so that the interface attains its critical fracture condition when the Mixed-Mode energy release rate G_{ic} equals the fracture toughness of the interface $G_{ic}(\Psi)$. Again, as in the LEIFM, it can be stated that:

$$G_{ic} = G_{ic}(\Psi) \qquad (3.39)$$

Note, the value of (Ψ) shown in equation 3.39 is local while that of $(\acute{\Psi})$ is global (see equation 3.30).

In the literature, several de-bonding criteria are available for Mixed-Mode analysis, including the elliptic form (Mei, *et al*., 2010), where the damage initiation criterion is given by:

$$\left(\frac{\langle\sigma\rangle}{\sigma_0}\right)^2 + \left(\frac{\tau}{\tau_0}\right)^2 = 1 \qquad (3.40)$$

Where, τ_0 = shear strength of the interface, $\langle\sigma\rangle = \sigma$ if $\sigma > 0$ (tension) and $\langle\sigma\rangle = 0$ if otherwise. Hence, by including the Macauley bracket it is presumed that interface debonding is impeded under compression.

In addition, de-bonding for Mixed-Mode can also be specified in terms of energy based criterion (Mei, *et al*., 2010):

$$\left(\frac{G_I}{G_{Ic}}\right) + \left(\frac{G_{II}}{G_{IIc}}\right) = 1 \qquad (3.41)$$

With, $$G_I = \int P\, du_n \qquad (3.42)$$

$$G_{II} = \int \sqrt{{\tau_1}^2 + {\tau_2}^2}\; du_n \qquad (3.43)$$

$$G_{Ic} = \tfrac{1}{2}\, \sigma_0 u_n^c \qquad (3.44)$$

$$G_{IIc} = \frac{1}{2}\,\tau_0 u_t^c \qquad (3.45)$$

Where,

$\sigma_0 = maximum\ normal\ contact\ stress$

$\tau_0 = maximum\ equivalent\ tangential\ contact\ stress$

$G_I = Fracture\ energy\ or\ work\ done\ by\ traction\ in\ pure\ mode\ I$

$G_{II} = Fracture\ energy\ or\ work\ done\ by\ traction\ in\ pure\ mode\ II$

$G_{Ic} = Fracture\ toughness\ or\ critical\ fracture\ energy\ in\ pure\ mode\ I$

$G_{IIc} = Fracture\ toughness\ or\ critical\ fracture\ energy\ in\ pure\ mode\ II$

From equations (3.38), (3.40) and (3.41), it can be shown (Mei, *et al*., 2010) that both the strength and toughness depend on the phase angle Ψ. The relationships are given by expressing equation (3.40) in the form:

$$\left(\frac{\lambda_m \cos\Psi}{\sigma_0}\right)^2 + \left(\frac{\lambda_m \sin\Psi}{\tau_0}\right)^2 = 1$$

So, $$\lambda_m^2\left[\left(\frac{\cos^2\Psi}{\sigma_0}\right) + \left(\frac{\sin^2\Psi}{\tau_0}\right)\right] = 1$$

Therefore, $$\lambda_m = \left[\left(\frac{\cos^2\Psi}{\sigma_0}\right) + \left(\frac{\sin^2\Psi}{\tau_0}\right)\right]^{-1/2}$$

From where the critical traction magnitude for damage initiation is given by:

$$\lambda_m = \sigma_0\left(\cos^2\Psi + \frac{\sigma_0^2}{\tau_0^2}\sin^2\Psi\right)^{-1/2} \qquad (3.46)$$

Sequel to definitions obtained from equations (3.37) and (3.38), at the point of final failure it can be shown that:

$$\langle\sigma\rangle = \lambda_m\, cos\Psi \quad and\ \tau = \lambda_m\, sin\Psi \qquad (3.47)$$

and, $$\langle u_n\rangle = u_m^c\, cos\Psi \quad and \quad u_t = u_m^c\, sin\Psi \qquad (3.48)$$

where, $\sigma\ and\ \tau = normal\ traction\ and\ shear\ traction\ respectively.$

$u_n\ and\ u_t$ = $normal\ traction\ and\ shear\ displacement\ respectively.$

So, from equations (3.47) and (3.48), the work done by the tractions can then be expressed as:

$$G_I = \frac{1}{2}\lambda_m u_m^c cos^2\Psi \quad (3.49)$$

$$G_{II} = \frac{1}{2}\lambda_m u_m^c sin^2\Psi \quad (3.50)$$

Again, with reference to equations (3.49) and (3.50), equation (3.41) can be expressed in terms of the phase angle Ψ as:

$$\left(\frac{\frac{1}{2}\lambda_m u_m^c cos^2\Psi}{G_{Ic}}\right) + \left(\frac{\frac{1}{2}\lambda_m u_m^c sin^2\Psi}{G_{IIc}}\right) = 1 \quad (3.51)$$

So that the total Mixed-Mode fracture energy (per unit area) becomes:

$$G_{Total} = G_{Ic} + G_{IIc} = \frac{1}{2}\lambda_m u_m^c = \frac{1}{2}\lambda_m u_m^c G_{Ic}\left(cos^2\Psi + \frac{G_{Ic}}{G_{IIc}} sin^2\Psi\right) \quad (3.52)$$

Which can also be expressed as:

$$G_{Total} = G_{Ic} + G_{IIc} = \frac{1}{2}\lambda_m u_m^c = G_{Ic}\left(cos^2\Psi + \frac{G_{Ic}}{G_{IIc}} sin^2\Psi\right)^{-1} \quad (3.53)$$

From equation 3.53, a graphical representation of the delamination envelop for Mixed-Mode can be drawn as shown in Figure 3.8. In the figure, the Mixed-Mode ratio constitutive relation is defined by the triangle at the middle, and acts to lower the parameters associated with the pure Mode failure criteria.

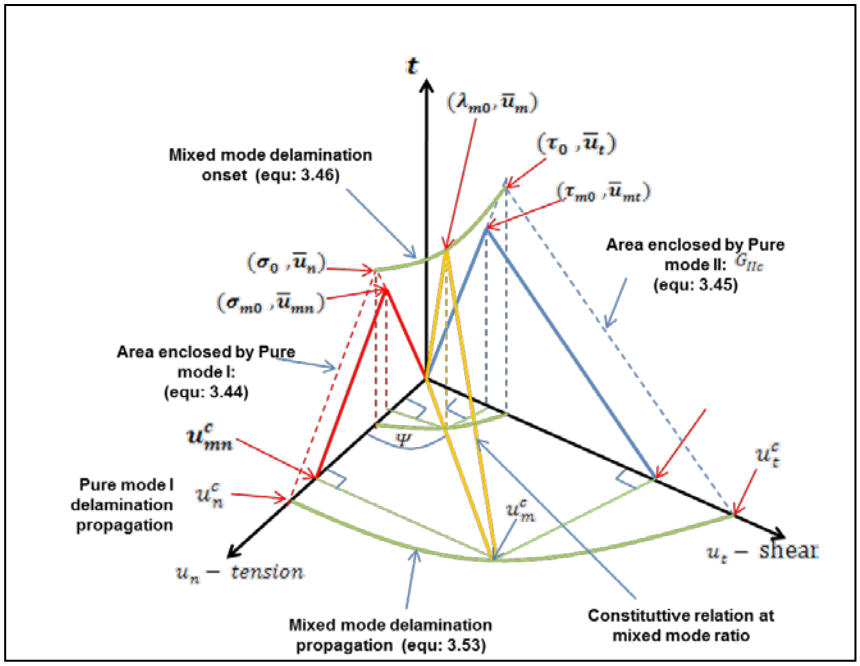

Figure 3.8: Constitutive model for Mixed mode delamination ((Drawn from Gözlüklü, 2009)

From figure 3.8 above, the ICZM implementation under Mixed-Mode loading in this thesis was characterized by the following parameters:

- Stiffness (k_0)
- Strengths ($\sigma_0 \; and \; \tau_0$) and their conjugate variables (displacement)
- G_{Ic} and G_{IIc}

Note, for effective ICZM implementation, two additional special features were provided for both Mixed-Mode and Mode II de-bonding models in FEA ANSYS. These included the possibility of controlling tangential slip under compression normal contact stress by activating the flag (β) when 1 (tangential slip allowed) is used, or 0, implying no tangential slip allowed. The second feature relates to artificial damping coefficient (η). It was desirable to include artificial damping coefficient (η) in order to overcome convergence difficulties during debonding process. Its value may be chosen between 0.01 and 0.1 and has the units of time. It represents a multiplying effect on the smallest time increment to ensure an accurate numerical solution is obtained.

This chapter presented the theoretical concepts and equations governing the material mixture design and optimization techniques used in this thesis; potential mechanisms of delamination process of the overlay under pure mode (Mode I or Mode II) and Mixed-Mode remote loading conditions were clearly shown. Lastly, the fracture parameters defining the bilinear stress-separation softening relation between the two planes of the interface were identified. Note, these parameters are to be experimentally determined together with other thermo-mechanical properties of the overlay. Detailed experimental work and fracture analysis are presented later in chapters 5 and 7 respectively.

4.0 Methodology

This section discusses the methodology adopted in this study for the design of the optimum overlay mixture. The material selection process of the overlay was implemented in terms of qualitative and quantitative assessments experimentally and computationally. Afterward, the bond capability of the optimum mixture was measured, and the structural response of the interface was examined experimentally, numerically and analytically. The numerical and the analytical studies here were employed to extend the pure Mode (Mode I and Mode II) fracture experimental test results into a Mixed-Mode remote response which appears

common with bi-material interface. Finally, possible Mixed-Mode shape was analytically determined for an edge condition buckling-driven delamination.

4.1 Overview of Research Approach

As clearly stated above, adequate description and simulation of interfacial bonding and delamination behaviour require well suited experimental tests with results that can be used as calibration tools for both numerical and analytical studies.

The prime rationale for such interfacial calibration is premised on common notion that many of the experimental results are usually not sufficient to capture and determine all the parameters required for a complete fracture analysis of concrete structures, especially where delamination at the interface is involved.

In this respect, the preference for any particular test method adopted in this thesis was guided by the scale of description involved, coupled with the relative merit associated with the method. In addition, other relevant fundamental factors considered for any choice test method included:

- Availability of testing equipment and measuring devices,
- Accuracy of the method, and
- Versatility of the method.

Specifically, the selected test methods related to critical fracture conditions in composite interface under both elastic property mismatch and differential length change effects between the bonded layers. All fracture tests assumed monotonic remote loadings.

Methodologically, the sequential optimum design process for the proposed BCO system was implemented and discussed as follows:

1. Overlay Material Modelling, Design, and Characterization;
2. Interface Characterisation;
3. Interface Structural (Delamination process) response;
4. Numerical and analytical simulations; and
5. Design output and propositions.

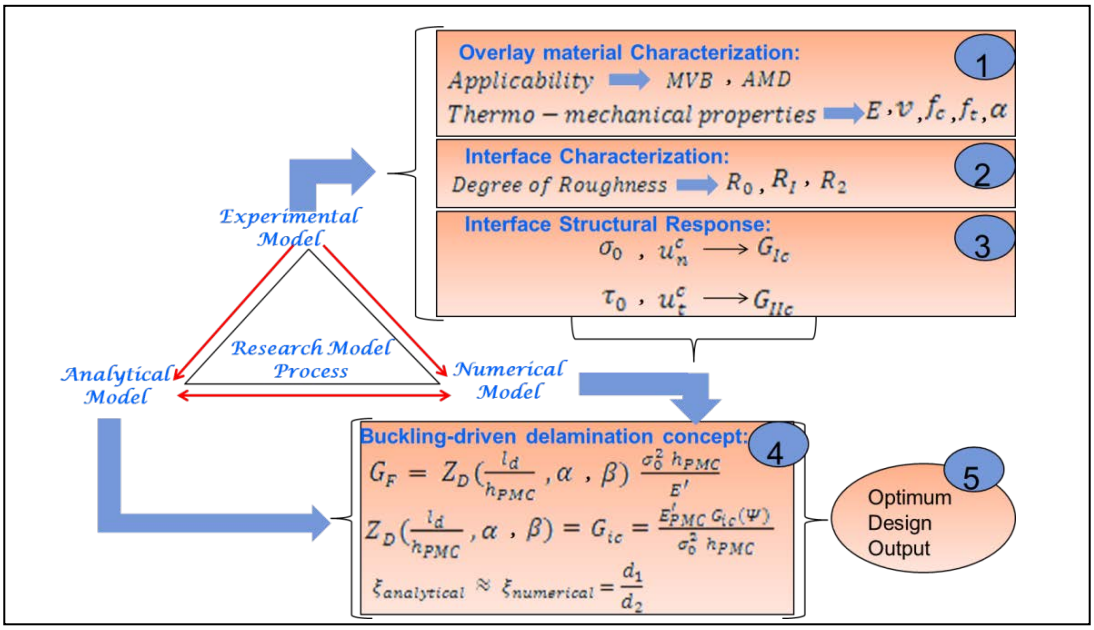

Figure 4.1: BCOs Design Methodology

4.2 Overlay Material Modelling, Design, and Characterisation

This section considers methods of achieving the best possible overlay mixture through experimental and statistical optimization techniques. The process of optimum selection was based on both possible field applicability of the overlay material and its structural performance evaluation within the acceptable desirability range found in various codes of practice and technical publications.

The applicability quality was measured in terms of the material's consistency MVB (Modified-Vebe) performance and its apparent maximum density (AMD) after roller compaction. Conceptually, Roller Compacted Concrete (RCC) differs from conventional concrete principally in its consistency requirement. For effective consolidation and bonding, the concrete mixture must be dry enough to prevent sinking of the vibratory roller equipment, but sufficiently wet to permit adequate distribution of the binder paste in the concrete during mixing.

Following the applicability quality determination, structural performance evaluation of the test material mixtures was implemented. The following were the bulk properties used to characterise and define the relative level of performance of the optimum overlay material:

- Mechanical / Elastic properties: Compressive strength (f_c), Tensile strength (f_t), Elastic modulus (E_c), Poisson's ratio ()v, and Drying shrinkage (ε_c);

- Fresh Mix and Physical properties: Consistency-time (MVB) and Density (AMD);
- Thermal properties: Co-efficient of thermal expansion (α).

Note, the mechanical and elastic properties were used to determine the level of structural and dimensional compatibility between the optimum mixture and the substrate concrete, while the fresh / physical properties help determine the suitability of the same mixture for field application in its wet state and at acceptable level of compaction. Lastly, the thermal properties relates mainly to dimensional variation between the overlay and the substrate under temperature gradient. Note, full test descriptions of each of the above properties and results are given in Chapters 6 and 7 of this thesis.

4.3 Interface Characterization

Following the tasks given in section 4.2 above, substrate surface characterization and interfacial bond evaluations were performed. The surface characterization examines the degree of roughness at three different levels introduced to foster good bonding. Theoretically, surface roughening is known to increase contact area between bonded materials, thus, bond capability of the interface increases as well.

The roughness measurement (R_z) adopts the sand-patch method, while the bond testing uses stress-based and fracture-based experiments. Note, the stress-based experiments measured the delamination initiation stage while the fracture-based experiment determined the propagation process of the interface.

The following were the bond performance properties determined to characterise the interface under a prescribed interface texture:

- Interfacial tensile strength (σ_0) and the corresponding critical crack opening displacement (u_n^c);
- Interfacial shear strength (τ_0) and the corresponding slip displacement (u_t^c);
- Interfacial toughness or resistance to fracture (G_{IC} and G_{IIC}).

Note, full test descriptions of each of the above parameters and results are given in Chapters 7 and 8 of this thesis.

4.4 Interface delamination Numerical and analytical simulations

Because of the difficult and complex nature of determining the Mixed-Mode fracture parameters of the interface experimentally, numerical and analytical simulations were implemented to extend the pure Mode fracture experimental test results given in section 4.3 into a Mixed-Mode delamination concept. The FEA model as illustrated in Figure 4.2, idealizes delamination failure across the BCO slab system into a 2D beam resting on elastic foundation. Note that the generalization of delamination fracture as assumed here is simplistic, it is however reasonable because it addresses areas more prone to elevated stresses and delamination problems.

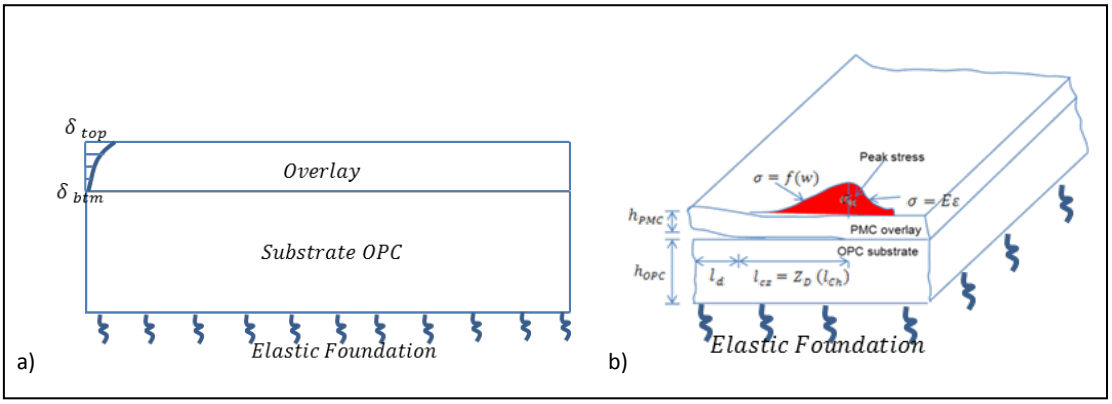

Figure 4.2: Conceptual Overlay Edge Deformation and Delamination FEA Model

The FEA model shown in Figure 4.2, assumed a differential edge deformation between the two bonded materials. The model helps determine the equivalent Mixed-Mode interfacial fracture parameters relative to different elastic mismatched properties between the overlay and the substrate and the possible failure mode shape of the overlay under a buckling-driven delamination state. The analytical solution to the problem was implemented using the proposed *Modified* Eigenvalue Buckling Analysis (MEBA). Afterward, result outputs and propositions for overlay reliability design were presented.

5.0 Material Modelling, Evaluation and Optimization

The overall composite performance of concrete is generally contingent on achieving the right proportion of blend. The use of mixture experiments provides a flexible, easy, and quick way of optimizing multi-component materials of this nature. This chapter describes the use of optimization techniques within the concept of material mixture experiments for

proportioning and designing the constituents of the bonded overlay material (BRCFRPMC) used in this research.

Although, applied optimization techniques are nearly as old as *calculus of variations,* their direct and possibly frequent application to mixture processing in the concrete industry is still relatively new, compared to pharmaceutical, petrochemical, and medical biology where considerable successes have been recorded (Ruiz et al., 2005). In concrete industry, the use of historical data or traditional trail-and-error mixture proportioning methods based on ACI 211.1 is common and has long enjoyed wider acceptance. However its applications can be rigorous and uneconomical, particularly where several material constituents and complex multi-criteria properties are involved. Besides, neither method gives a detailed procedure for optimizing mixtures (Simon 2003), which at this point necessitates the need for a more robust and cost / time-efficient method.

In the present study, a high performing BRCFRPMC overlay is designed using Mixture Optimization Techniques to meet the following multi-criteria performance: (1) No sinking attribute during vibratory compaction, (2) sufficient mechanical and dimensional compatibility properties with the substrate, and (3) early and durable interfacial bond performance.

The overall objective here is to ensure that the designed overlay material is optimized for both structural performance and bond compatibility.

5.1 Material and Test Requirements of BRCFRPMC.

5.1.1 Roller Compacted Concrete Overlay

In ACI 207.5R [5], Roller Compacted Concrete (RCC) is defined as concrete compacted by a vibrating roller. RCC therefore differs from conventional concrete principally in its consistency requirement. For effective consolidation, the concrete mixture must be dry enough to prevent sinking of the vibratory roller equipment, but sufficiently wet to permit adequate distribution of the binder paste in the concrete during mixing. In addition, in situations where RCC is applied as a bonded overlay, it should as a necessity provide good bonding with the substrate.

In order to ensure proper mixture proportioning of RCC, ACI 207.5R identifies five distinct methods, but in practice, two main approaches are common:

I. The first approach is based on the principle of soil compaction, where the optimum water content of the concrete results in a mix with maximum compacted density. Typically, the best compaction is expected to yield the best strength; and that occurs only when the operating vibrating roller is effectively supported.

II. The second approach is based on the use of concrete consistency tests to produce a high-paste RCC mixture. In this method, mixture proportioning is dependent on achieving good consolidation, thereby ensuring that much of the void content is filled with paste, even at considerable low water content.

In the present work, the latter is preferred due to its associated high-paste content required for good bonding with the substrate. Besides, the apparent maximum density (AMD) in concrete consistency approach is normally greater than that of soil compaction approach; typically its value can be as high as 98% of the theoretical air-free density (TAFD) (Mehta and Monteiro 2006).

Hence, for very stiff to extremely dry RCC mixtures like the present; the test samples were prepared with Modified-Vebe (MVB) method in accordance to ASTM C1170 / C1170M-08 requirements. The vibration induced by the apparatus is usually done such that it simulates the field compaction under the action of a 12.5kg or 22.7kg surcharge mass, depending on the observed consistency level as described in ASTM C1170 / C1170M-08. In the field, however, the laboratory determined optimum mix can be adequately consolidated using vibratory rollers.

In the literature, a typical MVB time for RCC pavement and overtopping materials ranges between 30 and 40 seconds (ACI 325.10R-10), though RCC with high consistency times, up to 180 seconds, have been successfully compacted in the laboratory, and probably could be applied in the field with high compaction effort (Casias et al. 1988). As a general guide, it is desirable to ensure that the maximum compaction force exerted does not break or crush the aggregates, so as to prevent any change to the granulometric curve. In this respect, an MVB time range of 25 to 40 seconds was chosen to define the thresholds of acceptance and rejection, with a target of 35 seconds for the optimum mix.

5.1.2 Polymer admixture and Steel-fibre additive.

Polymer-modified concretes essentially contain two binder phases, such that their composite behaviour depends on achieving complete cement hydration and polymer film

formation processes during the curing period (Czarnecki et al., 1999; Ohama, 1995). With proper mixture design, the benefits of Polymer-modified concrete (PMC) over conventional concrete can be enormous, ranging from improved mechanical properties to enhanced bond properties with other materials (Czarnecki and Lukowski, 1998). In addition, the presence of micro-cracks is also limited in PMC due to its lower shrinkage property. When such cracks develop, they are controlled and bridged to a great extent by the polymer films, thus preventing the likelihood of brittle crack propagation.

For polymer modification of concrete, the use of Styrene-Butadiene Latex / Rubber (SBR) is common, while Polyvinyl Acetate Latex and Poly (vinylidene Chloride (VnC) - vinyl Chloride (VC) latexes are not recommended as cement modifiers (Ohama, 1995) due to their respective poor water resistance and chloride ion liberation tendencies. In ASTM C 150, SBR is recommended for concrete or mortar modification with Type I, II or III Portland cement. Most polymer-modified concretes in the literature are however composed of Type I cement and SBR latexes. The use of Type III cement is very limited, except where early rapid strength is required to sustain a service load within 24 hours (ACI 548.3R-03). The investigation in this work was based on the use of SBR polymer emulsion and CEM I Portland cement. The specifications and properties of the materials used are given in Table 5.1, while the combined aggregate grading data is shown in Table 5.2.

Table 5.1: Material specifications and physical properties

Materials	Specification and Physical Properties
Cement (CEM I)	CEM I, 52.5N; specific density 3150 kg/m^3
SBR	White emulsion, solid content 46%, water content 54%; specific density 1040 kg/m^3
Coarse aggregate (CA)	Crushed gritstone; size 4.75 -10mm, water absorption 0.5%, particle density on saturated surface-dried 2770 kg/m^3
Fine aggregates (FA)	Quartz river sand, particle density 2670 kg/m^3
Steel Fibre (SF)	Length 35mm, hooked-end, aspect ratio 60

Table 5.2 Combined aggregate grading

Sieve size	14mm	10 mm	4.75 mm	2.36 mm	1.18 mm	600 µm	300 µm	150 µm	75 µm
Cumulative % passing	100	96	41.2	35.3	33.0	26.8	4.44	1.19	0.14

5.1.3 Mixture Design Method

Hypothetically, BRCFRPMC can be considered as a matrix of two phases: the paste (P) phase and the solid inclusion (SI) phase. The paste phase consists of WATER and Portland cement (CEM 1) modified with SBR, and occupies about 39% by volume of the total mixture; while the remaining 61% is filled with solid inclusion phase comprising coarse aggregate (CA), fine aggregate (FA) and steel fibre (SF).

By this hypothesis, the paste phase was considered central to consistency and optimum bond requirements, in order to ensure ease of applicability during vibrating compaction and satisfactory composite behaviour of the overlay system. Therefore, the mixture experiments in this work investigate variable combinations of the paste constituents that will be required for optimal performance when mixed with a constant proportion of the solid inclusions. Table 3 represents the proportion of the mixture components.

It should be noted that the total volume shown in Table 5.3 indicates a theoretical air-free mixture, while the variable proportions of SBR and WATER depend on the amount of CEMI.

Tables 5.3: Mixture proportion of solid inclusions phase and paste phase

	Solid Inclusion phase			Paste phase		
Material	CA	FA	SF	CEM I	SBR	WATER
Weight (kg)	952.5	635	117	≤ 635	Variable	Variable
Volume (m^3)	0.35	0.24	0.015	-	-	-
Total Vol. (m^3)	0.61			0.39		

In this experiment, the maximum cement content was restricted to ≤635kg, while the trial range of variabilities for Water-Cement (W/C) and Polymer-Cement ratio (P/C) was constrained between 18% - 22% and 10% - 15% respectively.

It has been shown that (P/C) ratios ≥ 20% impair both compressive strength and elastic modulus properties considerably (Van Gemert, 2005), while ratios ≤ 5% are insufficient to create any additional continuous phase within the hardened concrete matrix. In addition, the choice of high cement contents was based on ACI guidelines (ACI 548.1R-92; ACI 548.4-93). Cement contents in the range of 600 – 700 kg/m^3 are typically recommended for bridge deck and pavement overlays modified with SBR, for enhanced bonding and strength development. Although, the use of high cement contents to enhance bonding and strength could also results in high risk of shrinkage and thermal cracking; with adequate polymer content and sufficient inclusion of steel-fibre, usually within 1.5% - 2.0% by volume of the mix (Šušteršič, 2007), the risks can be minimized. Thus, in the present work, a fixed volume of 1.5% steel-fibre was added in the mix at a maximum aspect ratio of 60, thereby limiting the likely effects of curling (Swamy and Mangat, 1975).

From above, since the amount of solid inclusions (SI) shown in Table 5.3 is held fixed for all possible mix combinations of the paste (P), it follows that the proportion of (SI) to (P) can be implemented as a three-component mixture experiment, involving only SBR, CEM 1, and WATER. Thus, in Table 5.4, if the upper and lower bounds are applied on $[SBR/CEM1]$ and $[WATER/CEM1]$ ratios based on the variability limits discussed above, then the actual amount of each component can be estimated. Table 5.5 presents the proportion of each component as a fraction of a constant total paste.

Table 5.4: Actual range of Cement Contents

$Range\ Limit$	$\left(\frac{SBR}{Cem}\right)$ (%)	$\left(\frac{Water}{Cem}\right)$ (%)	SBR (kg)	$Water$(kg)	$Cem.(kg)$	$Total\ amount\ (kg)$
Lower	10	18	63.5	114.3	635	812.8
Upper	15	22	95.25	139.7	577.85	812.8

Table 5.5: Paste Components Proportion

$Range\ Limit$	$SBR\ (x_1)$	$WATER(x_2)$	$CEMENT\ (x_3)$	$TOTAL$
Lower	0.078	0.141	0.781	1.00
Upper	0.117	0.172	0.711	1.00

In Table 5.5, based on the conditions stated in equation (3.1), the sum of each possible paste combination (each row) is constrained to a total of 1. Hence, from the resulting lower and upper bound values given in Table 5.5, an Extreme Vertices Design (EVD) was implemented to formulate some possible mix combinations based on the following constraints:

$$0.078 \leq x_1 \leq 0.117$$

$$0.141 \leq x_2 \leq 0.172$$

$$0.711 \leq x_3 \leq 0.781$$

The implementation of the mixture model was done on the initial assumption that a second-degree (quadratic) design will be sufficient. In the design, 4 vertex design points were created with 4 augmented axial points. In addition, in order to ensure a more robust model, 4 interior and 1 centre points were incorporated. In total, these make up 13 points on which all required properties were associated. The corresponding coordinates and design output space are depicted in Table 5.6 and Figure 5.1 respectively.

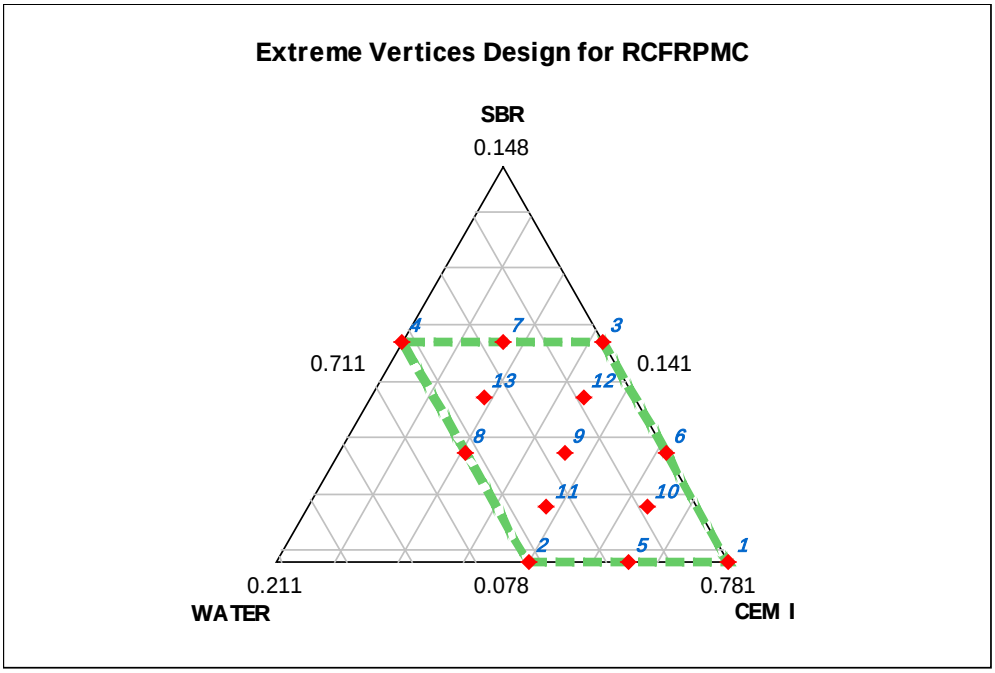

Figure 5.1: Extreme Vertices Design for BRCFRPMC

Table 5.6: BRCFRPMC Paste Component Proportions

$Design\ point$	$Pt\ Type$	$SBR\ (x_1)$	$WATER\ (x_2)$	$CEM\ I\ (x_3)$
1	1	0.078	0.141	0.781
2	1	0.078	0.172	0.750
3	1	0.117	0.141	0.742
4	1	0.117	0.172	0.711
5	2	0.078	0.157	0.766
6	2	0.098	0.141	0.762
7	2	0.117	0.157	0.727
8	2	0.098	0.172	0.731
9	0	0.098	0.157	0.746
10	-1	0.088	0.149	0.764
11	-1	0.088	0.164	0.748
12	-1	0.107	0.149	0.744
13	-1	0.107	0.164	0.729

In Figure 5.1, the thick dashed line defines the design region, while the dots represent the design points. From Table 5.6, the basis for batching by weight in kg of each paste constituent was established. Further, in order to allow for sufficient repeatability of each associated response, a total of five runs for each design point were implemented per specified response. Subsequently, ANOVA was performed with Minitab statistical software. In the analyses, components and models with p-value ≤ 0.05 were selected as viable. Also, for each chosen model, checks on normality, outliers, and consistency of the residuals were carried out accordingly.

5.2 Mixture Proportion Evaluation and Optimization

5.2.1 MVB and Wet Density tests

In order to determine the suitability range of the mixture proportions listed Table 5.7, the test procedures of MVB and wet density used complied with ASTM C1170 / C1170M-08 [7], while the general mixing procedure for each batch followed ASTM C1439-99.

The ASTM C1170 / C1170M-08 method involves proportioning mixture of concrete for optimum consolidation, by using such apparatus as the MVB described in the U.S. Army Corps of Engineer's test procedure CRD-C-53-01 and U.S. Bureau of Reclamation's Technical Memorandum No. 8. By definition, the MVB consistency is the time required for a given mass of stiff-plastic to extremely dry-concrete to be consolidated by vibration in a cylindrical mould under a surcharge mass. Afterward, the wet-density of the compacted mix is determined by measuring the mass of the consolidated specimen and dividing by its volume.

The apparatus as illustrated in Figure 5.2 consists of a vibrating table of fixed frequency ($60\pm1.67Hz$) and a double-amplitude of 0.43 ± 0.08mm which is similar to field compaction when a 27.2 ± 1.1kg surcharge is bolted to the centre of the table. The apparatus also consists of a $0.0091m^3$ metal cylindrical mould securely attached to the table, into which a representative mixture of the concrete specimen can be loosely placed under a surcharge mass of 12.5kg or 22.7kg. Note that the choice of the surcharge mass generally depends on which modified apparatus meets the procedures described in ASTM C1170 / C1170M-08.

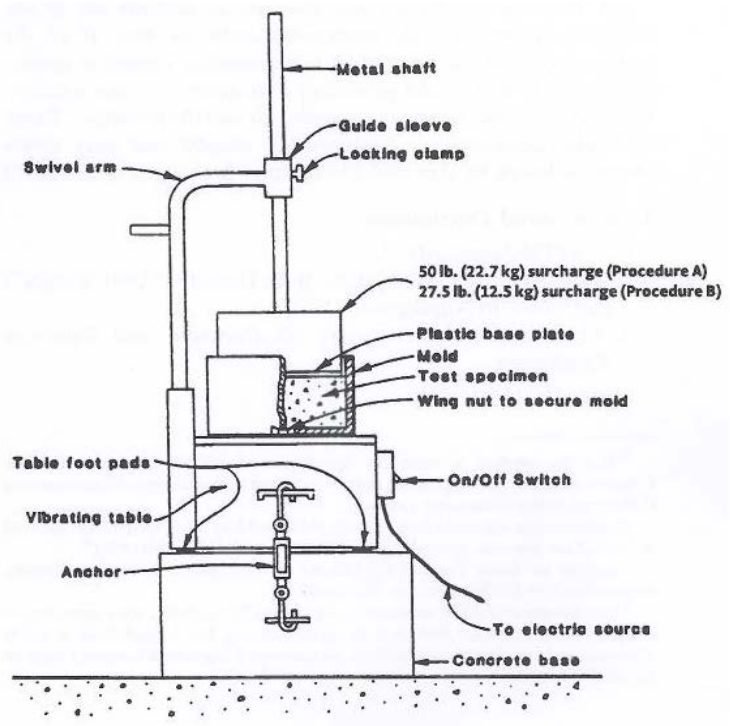

Figure 5.2: Vibrating Table – Modified Vebe consistency test (Adapted from ASTMC 1170-08)

On the basis of visual observations of some trial test specimens, procedure requiring 22.7kg surcharge mass was deemed fit and subsequently maintained all through the experiments. Clearly, the use of a single surcharge mass for all test specimens helps comparison in results. Figure 5.3 shows the visual appearance of some representative mixtures consolidated under the action of the surcharge mass, while Table 5.7 provides the quantity in kg for each mixture combination.

Figure 5.3: Representative mixtures: (a) M1 in the Vebe cylinder (b) 22.7 kg surcharg mass mounted on test specimen (c) Fully consolidate test specimen with a ring of mortar around the disk (d, e, f) Top finished surface of Mix 1, Mix 2 and Mix 3 after consolidation

Table 5.7: BRCFRPMC Components Proportion

$Design\ point$	$Mix\ ID$	$Components\ Quantity\ (kg)$					
		SBR	$WATER$	$CEM\ I$	CA	FA	SF
1	M1	63.40	114.60	634.80	952.50	635.00	117.00
2	M3	63.40	139.80	609.60	952.50	635.00	117.00
3	M7	95.10	114.60	603.10	952.50	635.00	117.00
4	M9	95.10	139.80	577.90	952.50	635.00	117.00
5	M2	63.40	127.20	622.20	952.50	635.00	117.00
6	M4	79.25	114.60	618.95	952.50	635.00	117.00
7	M8	95.10	127.20	590.50	952.50	635.00	117.00
8	M6	79.25	139.80	593.75	952.50	635.00	117.00
9	M5	79.25	127.20	606.35	952.50	635.00	117.00
10	M12	71.32	120.90	620.57	952.50	635.00	117.00
11	M10	71.32	133.50	607.97	952.50	635.00	117.00
12	M11	87.17	120.90	604.72	952.50	635.00	117.00
13	M13	87.17	133.50	592.12	952.50	635.00	117.00

Note: The specified water proportion includes the free water in the aggregates, the water in the latex, and the added water. The Mix ID was discretionarily chosen, and represents the batching order.

The overlaid contour result shown in Figure 5.4 depicts the feasible space, and indicates that not all test samples experienced full consolidation within the desirable consistency-time range of 25 and 40 seconds. The corresponding wet-density response for each test mixture is shown in Table 5.8. Usually, for most RCC mixtures, it is expected that the apparent maximum density (AMD) after rolling vibration shall be $\geq 98\%$ of the theoretical air-free density (TAFD), but where no AMD is specified a priori, compaction shall achieve density $\geq 96\%$ TAFD (National Engineering handbook, 2009).

Hence, in order to simulate these compaction levels, cylindrical specimens were cast from each possible mixture and compacted with a modified electric plate compactor for 20 seconds each layer of four per specimen. Each specimen measured 200mm high by 100mm diameter, and density measured in accordance to ASTM D792. Note, by using similar range of AMD values as those specified here, it was possible to assess the consolidation level of each mixture for equal period of vibration or compaction.

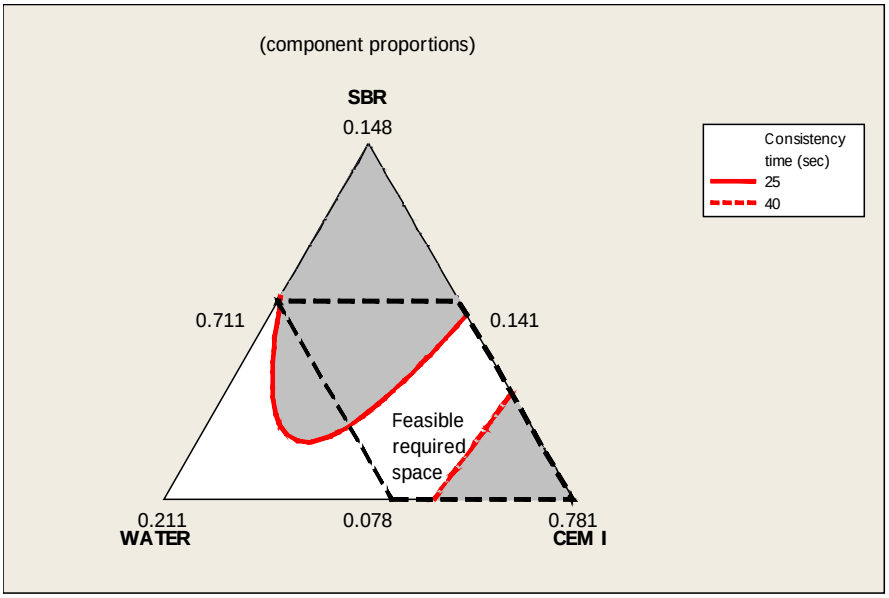

Figure 5.4: Contour Plot of Consistency-time (sec)

Table 5.8: Consistency and Density properties of test specimens

Property	*Test specimen mixture ID*												
Measured	$M1$	$M2$	$M3$	$M4$	$M5$	$M6$	$M7$	$M8$	$M9$	$M10$	$M11$	$M12$	$M13$
Consistency time (sec.)	78	50	32	40	34	29	24.5	22.8	20.7	30.1	23	37	22
Wet density (kg/m3)	2333.77	2421.46	2476.11	2417.73	2417.57	2366.85	2442.06	2423.80	2401.98	2429.32	2446.70	2382.42	2442.21
Compacted density (%TAFD)	95.76	97.19	98.43	96.87	96.99	96.12	97.96	97.39	96.68	97.71	98.26	96.71	98.00
Air-Content (%)	4.24	2.81	1.57	3.13	3.01	3.88	2.04	2.61	3.32	2.29	1.74	3.29	2.00

The TAFD and air-content (%) shown in Table 5.8 were determined using the procedures given in ASTM C138 and ACI 211.3. The result in Table 5.8 demonstrates that for similar condition of compaction, different levels of consolidation were achieved. The optimum mixture based on the two properties defined here, attains about 98.43% TAFD, which in this case has a consistency-time of 32 seconds when vibrated on the MVB table. As seen, the consistency times due to MVB test fall generally between 20 and 80 seconds with a statistical mean of 34.08 seconds. The overall compacted density as seen falls within the limit $97.10 \pm 1.34\ \%TAFD$. Though, this limit falls slightly below the desirable AMD value ($\geq 98\%\ TAFD$) for most of the test mixtures, three mixtures – M3, M11, and M13 – exhibit

considerable high response in the vicinity $\geq 98\%\ TAFD$, while all other mixtures, except M1, show values $\geq 96\%$. At this stage, only M3 seems to satisfy both consistency and density criteria. In details, based on visual observations, a classification for quality evaluation, as illustrated in Table 5.9, was made for specimens falling below 25 seconds, those between 25 and 35 seconds, those between 35 and 40 seconds, and those falling above 40 seconds.

Table 5.9: Mix classification based on consistency time limits and visual observations

Mix ID	Time (sec)	Remark
M1	78	Too dry and loose; exhibit poor consolidation and poor compaction; poor bond capability suspected; require high compaction effort.
M2	50	
M4	40	Dry; set quickly; may require some level of moisture adjustment during rolling and compaction for adequate strength and bond performance.
M12	37	
M5	34	Exhibit good consolidation and compaction; mainly within the prescribed laboratory Vebe-consistency time limit.
M3	32	
M10	30.1	
M6	29	
M7	24.5	Zero-slump concrete; appear wet and sticky, sinking of vibratory roller suspected, mainly below the prescribed practical Vebe-consistency time limit.
M11	23	
M8	22.8	
M13	22	
M9	20.7	

Suspectedly, for those specimens exhibiting lower consistency time below 25 seconds benchmark, the visual effects of high polymer and water contents on consistency became strident even prior to mix specimen testing, hence trying with 12.5kg surcharge mass was not considered appropriate. It is evident that the presence of polymer in concrete increases workability in the same manner as water content. Unlike in conventional RCC where no polymer is included, such effect of polymer on RCC has received little or no attention in the literature. Hence, it is desirable to establish the optimum interaction level between P/C and W/C in a roller compacted concrete containing polymer.

As clearly seen in Tables 5.8 and 5.9, most of the test mixture specimens attained reasonable degree of consolidation at consistency-time below 90 seconds, though mixtures with low consistency-time appeared too wet from practical standpoint. Again, it is clear that the reduced densification level obtained from the wet-density test illustrated in Table 5.8 can easily be compensated for in the field or in the laboratory to the required AMD by applying reasonable increased compaction effort similar to the roller compactor or electric plate compactor. This is usually the case in the field where compaction energy is standardized, and could be achieved with several passes of vibratory rollers; so long the overlay material does not exhibit pumping or causes the roller to sink during static passes.

As illustrated in Figure 5.5, in the field, RCC is commonly compacted with a 10-ton dual-drum vibratory roller just immediately after the concrete is placed, in a two-static pass pattern prior to vibratory and tire rolling operations (ACI 325.10R-10). Usually, right from the time of static rolling passes, one can tell if a mix is of proper consistency for compaction. The distinction made in ACI 325.10R-10 is clear, and follows that: a too dry concrete mixture will appear dusty or grainy and may even shear horizontally, while a too wet concrete will appear pasty, exhibit pumping behaviour under the roller, and often causes the roller to sink. As clearly observed in the laboratory, similar features were prevalent even where an electric hand-held vibrator was used. In addition, the ideal mixture should deflect evenly under the roller passes, and where adjustment is required for workability, only minor adjustments are made in terms of moisture content.

Figure 5.5: Placing and roller compaction of RCC (Adapted from Wayne Adaska, 2012)

Following the response properties given in Table 5.8, analysis of variance was implemented with Minitab16 by fitting and verifying a response model for consistency-time, wet-density, and compacted-density discretely. In all cases, model selection allows prediction based on

a quadratic relation, but through the analysis of variance (ANOVA), a linear model may provide a sufficient fit to the data. The corresponding ANOVA table for each response property is shown in Table 5.10.

Table 5.10: ANOVA table for consistency-time, wet density and compacted density

Analysis of Variance for Consistency time (sec) (Paste component proportions)

Source	DF	Seq SS	Adj SS	Adj MS	F	P
Regression	5	13656.7	13656.74	2731.35	155.44	0.000
Linear	2	10579.9	277.42	138.71	7.89	0.001
Quadratic	3	3076.8	3076.83	1025.61	58.37	0.000

Analysis of Variance for Wet Density (kg/m3) (Paste component proportions)

Source	DF	Seq SS	Adj SS	Adj MS	F	P
Regression	5	57988.2	57988.2	11597.6	26.85	0.000
Linear	2	7789.7	6908.9	3454.4	8.00	0.001
Quadratic	3	50198.5	50198.5	16732.8	38.74	0.000

Analysis of Variance for % Compacted density (Paste component proportions)

Source	DF	Seq SS	Adj SS	Adj MS	F	P
Regression	5	39.0011	39.0011	7.8002	25.76	0.000
Linear	2	3.1490	6.2310	3.1155	10.29	0.000
Quadratic	3	35.8522	35.8522	11.9507	39.46	0.000

In Table 5.10, the rows with “linear” are used to test whether the coefficients of linear terms are equal, while the rows with “quadratic” examine whether any quadratic terms is a non-zero coefficient. As seen in Table 5.10, it is clear that the p-values associated with both linear and quadratic models in each response are less than 0.05. Hence, it was assumed that either a linear or a quadratic model is significant at an α – level of 0.05, thus will suffice to fit the models. In this study, quadratic models were adopted. The resulting model for each response is presented in Table 5.11, while Figure 5.6 depicts the graphical trend of response and interaction between the paste constituents. For the avoidance of repetition, it

should be mentioned that the analyses for other response properties examined in this study followed a similar way.

Table 5.11: Quadratic models for Consistency-time, Wet density, and Compacted density

Property	Model Equation	S.D	R-sq.
Consistency-time(sec)	$8346(x_1) + 9676(x_2) + 1307(x_3) - 168(x_1x_2) - 16291(x_1x_3) - 17876(x_2x_3)$	4.2	92.9
Wet density (kg/m^3)	$44050(x_1) - 4404(x_2) - 1857(x_3) - 94906(x_1x_2) - 26791(x_1x_3) + 83897(x_2x_3)$	20.8	70.0
Compacted density(%TAFD)	$1547(x_1) - 619(x_2) + 5(x_3) - 3701(x_1x_2) - 1112(x_1x_3) - 1517(x_2x_3)$	0.6	70.0

Where: S.D= standard deviation; $x_1 = SBR$; $x_2 = WATER$; and $x_3 = CEM1$

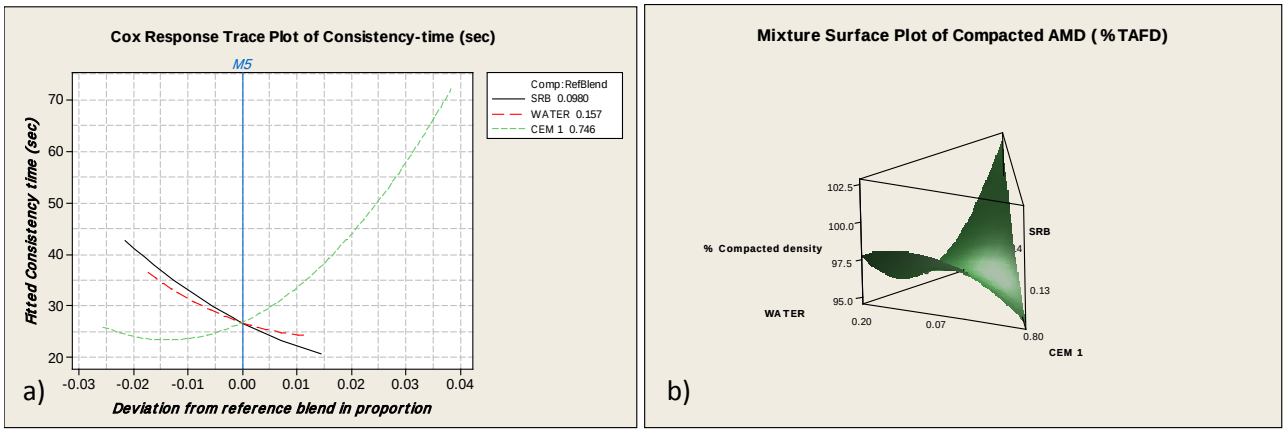

Figure 5.6: Response Trace Plot for Consistency and Mixture Surface Plot for Compacted density

The Response Trace Plot and the Mixture Surface Plot shown in Figure 5.6 above represent the general trend of consistency-time and compacted density measured in this experiment. The variation of the effects of each component relative to other component is distinctly depicted, and is interpreted relative to the reference mixture (M5). The overall consistency response shows that as the proportion of SBR or WATER in the mixture increases, while other components decrease due to the constraint introduced by equation 3.1, consistency-time decreases; but a decrease in SBR or WATER is expected to increase the response accordingly. On the other hand, increase in cement content is likely to increase consistency-time, while decrease in cement decreases mixture consistency response. In Figure 5.6b, mixture response due to compacted density is illustrated. It is evident that densities increase

as SBR increases in proportion. The optimum response occurs around the mid-space of the design region, with %TAFD ranging between 96 and 98%.

5.2.2 Elastic Modulus and Compressive Strength tests

The test specimens used for both compressive and elastic modulus responses were cast into cylinder steel mould and compacted with a modified plate electric vibrator. The compaction effort was maintained for 20 seconds each layer of four per specimen. Each specimen was afterward covered with a light polythene sheet and cured in the mould at 60% RH laboratory condition for 18 hours. After de-moulding, specimens were stored in the curing tank at 100% RH for 24 hours, followed by air curing under laboratory condition. Compressive strength tests were performed at 3, 14, 28, and 90 days, while elastic modulus was determined only for ages 3 and 28 days in accordance to ASTM 469 procedures. Each cylinder measured 200mm high by 100mm diameter. For both experimental tests, five replicates were implemented each for all possible mixtures shown in Table 5.7.

The compressive and elastic modulus responses are shown in Figure 5.7. Here, the material performance of the optimum overlay mixture was assessed in terms of its structural response and elastic compatibility with the substrate material. Table 5.12 represents the mixture constituents of the substrate material used in this work. The substrate material was made of a typical high strength ordinary Portland cement concrete (OPCC). The OPCC was cured for 28 days in water and subsequently in air till when tested at 90 days. It exhibits a characteristic compressive strength of 47MPa, and a mean tensile strength and elastic modulus of 3.97MPa and 22.30GPa respectively.

Table 5.12: OPCC material constituents

Material	*CEM I*	*CA*	*FA*	*WATER*	*TOTAL*
Quantity (kg/m^3)	400	1116	684	200	2400
Specific / particle density (kg/m^3)	3150	2770	2670	1000	-

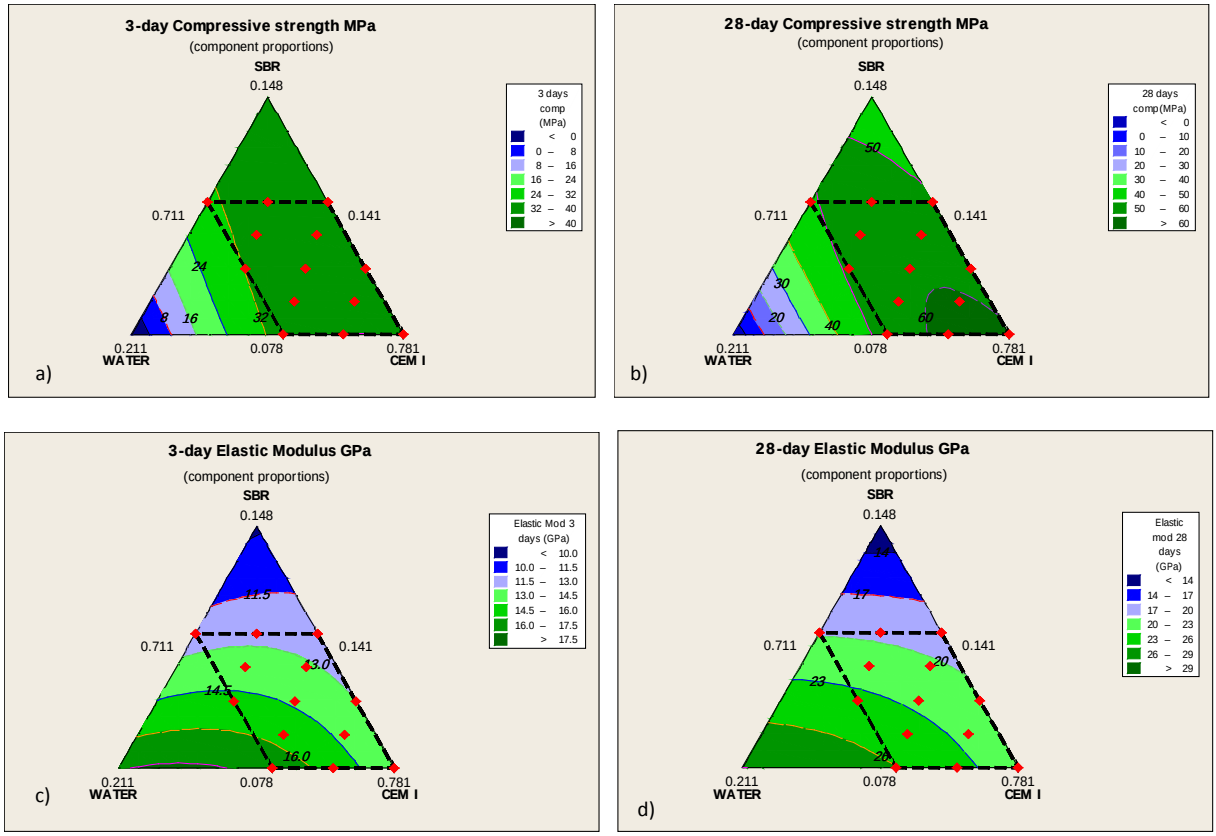

Figure 5.7: Mean Compressive strengths and Elastic Moduli responses at 3 and 28 days

As seen in the contour plots shown Figure 5.7 (a & b), strength decreases clearly with increase in WATER and SBR proportions, but increases as the proportions of CEM I increase; while the contours due to elastic modulus in Figure 5.7 (c & d) show that SBR has a clear reducing effect on the overall elastic response. The observed mean compressive strengths within the design space at 3 and 28 days mostly fall above 32MPa and 50MPa, while the corresponding elastic moduli range between 11.5 – 17.5GPa and 17 – 26GPa respectively. Following similar analysis as in Table 5.10, the resulting regression models for compressive strengths and Elastic Moduli responses for ages 3 and 28 were determined and presented in Table 5.13.

Table 5.13: Quadratic models for Compressive strengths and Elastic Moduli

$Property$	$Model\ Equation$	$S.D$	$R-sq$
Compr. strength (MPa) 3-day	$251(x_1) - 9665(x_2) - 260(x_3) + 12625(x_1x_2) - 740(x_1x_3) + 13538(x_2x_3)$	1.9	70.0
Compr. strength (MPa) 28-day	$-1652(x_1) - 13412(x_2) - 286(x_3) + 23080(x_1x_2) + 656(x_1x_3) + 18262(x_2x_3)$	1.8	83.2
Elastic Moduli (GPa) 3-day	$-305.3(x_1) - 763.9(x_2) - 79.2(x_3) - 745.1(x_1x_2) + 784.7(x_1x_3) + 1516.1(x_2x_3)$	0.07	99.8
Elastic Moduli (GPa) 28-day	$-1358251(x_1) - 478(x_2) - 76(x_3) + 165(x_1x_2) + 2041(x_1x_3) - 1160(x_2x_3)$	0.1	99.8

Where: S.D=standard deviation; $x_1 = SBR$; $x_2 = WATE$; and $x_3 = CEM1$

From the analyses, the optimum overlay mixture was selected based on the desirability requirements specified in some selected codes of practice and published technical papers. In the US, for instance, due to severe exposure condition of concrete pavement and bridges, the minimum compressive characteristic strength for most overlays is usually limited to around 25 - 30MPa (VDOT, 2002). Similarly, EC2 specifies a minimum compressive strength of C30/37*. Consequently, a minimum target characteristic cylinder strength of 30MPa was set for the overlay within the first 72 hours of placing. In the long-term (say 28 days and over), however, the overlay material should have equal or greater strength than the substrate (Emberson and Mays 1990). Also, in terms of elastic property compatibility requirements, the elastic modulus is required to be similar to that of the substrate (Emberson and Mays 1990).

From the target characteristic strength set above, the corresponding target mean strength was estimated based on the computed minimum and maximum standard deviation values associated with the test results. At 5% defect, for age 3, the limits of the target mean strength fall within $32.71 \pm 1.69MPa$; while for age 28, the OPCC characteristic compressive strength was set as the target. Thus, for age 28, the estimated limits of the target mean strength fall within $50.28 \pm 1.92MPa$. Hence, by comparing these limits with the response contours shown in Figure 5.7 (a & b), it shows that all mixtures used in this experiment satisfied the strength requirements for both early age of 3 days and matured age of 28 days.

Similarly, for elastic properties compatibility, the choice of optimum response was constrained within 5% tolerance of that of the substrate OPCC; thus, the optimum limits fall between 21.18GPa and 23.42GPa. From here, by comparing these limits with the response contours shown in Figure 5.7 (c & d), it is evident that at age 3, none of the mixtures employed in the experiment satisfied the elastic compatibility requirement; hence, the resulting desirability based on equation 3.12 automatically yields zero.

Note that the observation here is commonplace with newly cast fresh cementitious materials, and thus demonstrates that the material design of cementitious overlays typically introduces some degree of intrinsic elastic mismatch problem at early age. Intuitively, the rational solution at this stage of the analysis is to allow for some level of "trade-off" between what is intrinsically inherent and what to design against.

Clearly, a direct enhanced mixture solution may not always be economical or practicable due to the autogenous nature of the problem, but its consequential effects on the composite elements can be minimized, especially at the interface, by ensuring that adequate bonding between the overlay and the substrate is achieved. In this respect, the overall composite desirability level was determined using the matured 28-day elastic modulus response.

Similarly, due to time constraint and limited resources, the corresponding elastic modulus values for ages 14, and 90 days were derived as evolution parameters based on the observed compressive strength and the measured 28-day elastic modulus values. From existing codes of practice and relevant standards (ACI 318, CEB-FIP'90, BS8110'85), it is acceptable to derive or relate the elastic modulus of cementitious materials to their compressive strengths and densities.

Note the resulting compressive strength test results at 3, 14, 28 and 90 days are given in Appendix A1, while Table 5.14 shows the measured 28-day elastic modulus results.

Table 5.14 Elastic Modulus and Poisson's ratio for BRCFRPMC and OPCC

Mix ID	*Range of Poisson's ratio*	*Elastic Modulus (GPa) (28-day)*							
		SP1	*SP2*	*SP3*	*SP4*	*SP5*	*Mean (Ec)*	*S.D ($\bar{\sigma}$)*	*Cv (%)*
M1	0.25 -0.29	21.4	21.46	21.38	21.43	21.36	21.41	0.04	0.19
M3	0.22 - 0.30	24.99	28.34	25.55	26.11	25.79	26.16	1.29	4.92
M7	0.23 - 0.27	19.01	19.04	18.04	18.13	18.01	18.45	0.53	2.88
M9	0.23 - 0.29	19.19	21.22	19.21	19.12	19.64	19.68	0.89	4.51
M2	0.23 -0.27	23.76	22.46	23.79	23.11	23.58	23.34	0.56	2.41
M4	0.20 -0.27	19.41	20.11	21.75	20.06	20.25	20.32	0.86	4.26
M8	0.22 -0.28	20.36	19.11	20.05	19.12	19.14	19.56	0.60	3.08
M6	0.20 - 0.25	21.83	24.35	24.21	23.82	23.51	23.54	1.01	4.30
M5	0.22 - 0.29	23.89	23.84	21.83	20.97	23.65	22.84	1.35	5.91
M12	0.22 - 0.26	22.01	22.17	22.24	22.09	22.21	22.14	0.09	0.42
M10	0.23 - 0.31	24.61	24.6	24.56	24.33	24.3	24.48	0.15	0.62
M11	0.21 - 0.27	20.38	20.74	20.48	20.66	20.71	20.59	0.16	0.76
M13	0.24 - 0.30	21.06	21.34	21.16	21.29	21.31	21.23	0.12	0.56
OPC	0.15 – 0.19	22.24	22.41	22.10	22.34	22.39	22.30	0.13	0.57

From Table 5.14, it is evident that the Poisson's ratios for all the mixture specimens range between 0.20 and 0.31 with a statistical mean of 0.25. These values however deviate slightly from that of OPCC, which gives a mean Poisson's value of 0.18, with statistical minimum and maximum values of 0.15 and 0.19 respectively. Technically, the range of deviations here is not too far apart, hence the overall resultant effect of such variations will not be significantly critical if the elastic modulus values are perfectly matched, though the task of matching two dissimilar materials is no trivial.

In order to obtain the elastic modulus values corresponding to 14 and 90 days, the following approximate approach was implemented based on the relationship between relative compressive strength and 28-day elastic modulus:

$$\frac{E_{BRCFRPMC}(t)}{E_{BRCFRPMC28}} = \varphi \frac{\sigma_{BRCFRPMC}(t)}{\sigma_{BRCFRPMC28}} \quad (5.1)$$

From where,

$$E_{RBCFRPMC}(t) = \varphi \left[\frac{\sigma_{BRCFRPMC}(t)}{\sigma_{BRCFRPMC28}} . E_{BRCFRPMC28}\right] \quad (5.2)$$

Where,

$\sigma_{BRCFRPMC28}$ = 28-day Compressive strength for any BRCFRPMC mixture (MPa)

$E_{BRCFRPMC28}$ = 28-day elastic modulus for any BRCFRPMC mixture (GPa)

$\sigma_{BRCFRPMC}\ (t)$ = Compressive strength for any BRCFRPMC mixture at age t (MPa)

$E_{BRCFRPMC}(t)$ = Elastic modulus for any BRCFRPMC mixture at age t (GPa)

φ = variational coefficient accounting for the change in elastic modulus of a mixture specimen as compressive strength changes relatively due to age effect.

Hence, by plotting the expression in the bracket against time, the elastic modulus values for a specified age as φ changes with time can be obtained. The resulting curves are presented in Figure 5.8 for all the mixture test specimens.

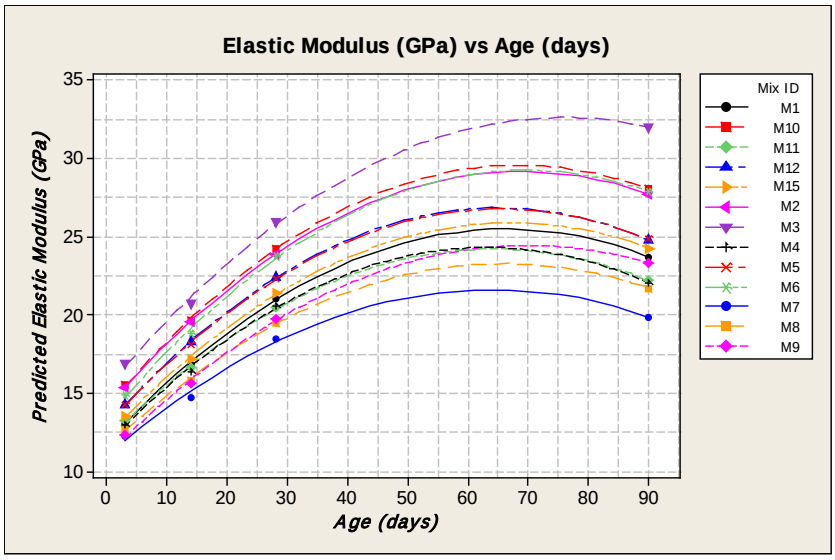

Figure 5.8: Estimated Elastic Modulus vs. Age

So far, basic fresh and hardened material property evaluations have been performed experimentally on all possible mixture combinations given in Table 5.7 in order to determine the optimum mixture. In order to determine the optimum mixture, desirability goals and limits were set and imposed on each measured property respectively, while ensuring that the overall composite desirability response achieves optimum performance. Detailed computational analysis of the process of response optimization is undertaken in section 5.3.

5.3 Composite Desirability analysis and Optimization results

In Table 5.15, the desirability limits for each response (property) measured above are summarized, while Figure 5.9 illustrates the optimal composite desirability result.

Table 5.15: Summary of multi-response desirability limits

Property	*Goal*	*Lower*	*Target*	*Upper*	*Weight*
Consistency-time (sec)	Target	25.00	35.00	40.00	1
Compacted density (%TAFD)	Maximize	96.00	98.00	-	1
Compressive strength (MPa) 3-day	Maximize	31.02	34.40	-	1
Compressive strength (MPa) 28-day	Maximize	48.36	52.20	-	1
Elastic Modulus (GPa) 28-day	Target	21.18	22.30	23.42	1

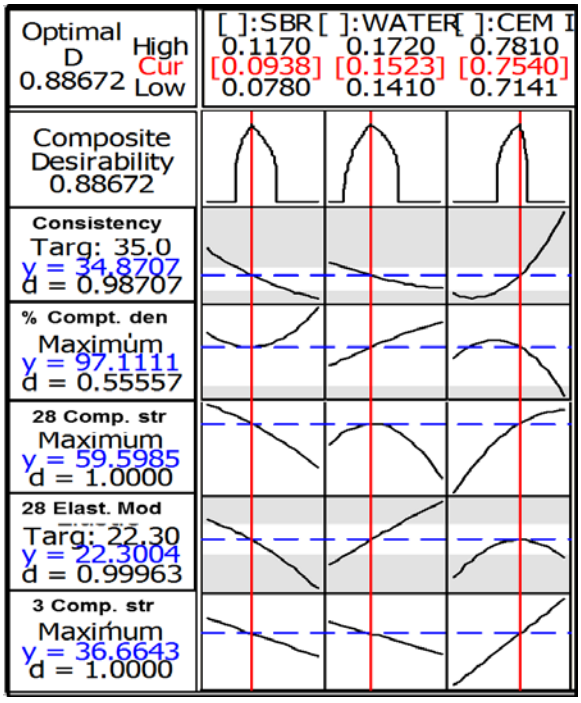

Figure 5.9: Composite optimization Response plot

Figure 5.9 depicts the composite desirability response curves implemented with Minitab statistical software. The input variable settings that optimized all responses are given in Table 5.15. The choices of goal, lower, target, and upper were used to define the desirability function for each individual response as previously expressed in equations 3.9 to 3.11. In addition, equal weight of 1 was assigned for all the responses, therefore permitting composite desirability analysis based on equation 3.12 to be implemented. In the results shown in Figure 5.9, the overall composite desirability yields 0.88672, while the desirability value for individual response is denoted by “d”. As seen, the composite desirability value and individual desirability for each predicted property all show sufficient closeness to 1 as desired.

As observed in Figure 5.9, the curves under each column show the property responses as each paste constituent employed for the computational experiment varies from its upper to its lower bound. Note that the bounds used here were based on the initial prescribed constraints drawn from Table 5.5. The constraints were done such that when one component increases in the mixture, the other two components decrease accordingly, due to the constraint that the overall proportion must add up to 1. From the results, the predicted optimum response “y” associated with each property corresponds strictly to the optimum mixture proportion.

The results indicate that consistency-time decreases when SBR and WATER proportions increase beyond the optimum proportion, but tends to increase with increased CEM I. As seen, the compressive strength response indicates similar trend as that of consistency-time, except for some differences in response curvatures. On the other hand, response due to compacted density shows that density generally decreases with increased CEM I proportion, though increasing the proportions of both SBR and WATER above the optimum may yield a higher response. For elastic modulus, increasing SBR and CEM I proportions above the optimum lowers the response, while increasing WATER may give a higher value.

In the analysis, the optimum mixture achieves about 98.71% of the optimum target response, which gives AMD value of about 97.11% of the TAFD. In addition, compressive strength at early age 3 and matured age 28 days were maximized and achieves 100% of the target response. Lastly, the elastic modulus response at 28 days attains about 99.96% of the target response as well.

As shown in the Figure 5.9, the optimum mixture proportion is indicated by the square brackets at the top of each column. It demonstrates that the optimum predicted responses are recorded when the proportions of SBR, WATER, and CEM I correspond to 0.0938, 0.1523 and 0.7540 respectively in the paste content. Thus, for batching by weight, each optimum component indicated here was multiply by 812.8kg which gives the needed paste weight content in the total mix.

Table 5.16 gives the resulting optimum amount by weight for a complete mixture, while Table 5.17 summarizes its predicted responses based on the results shown in Figure 5.9, and its actual responses when each property was tested experimentally for verification with three replicates each.

Table 5.16: Optimum BRCFRPMC material constituents

$Material$	$CEM\ I$	$WATER$	SBR	CA	FA	SF	$TOTAL$
Quantity (kg/m^3)	612.85	123.79	76.24	952.5	635.0	117.0	2517.38
Specific / particle density (kg/m^3)	3150	1000	1040	2770	2670	7800	-
Volume in mixture (m^3)	0.195	0.124	0.073	0.34	0.24	0.015	0.987

Note: Air Content = 100 (1- V_t) = 100 (1-0.987) = 1.3%

Table 5.17: Response properties of Optimum mixture

Property	*Predicted Response Value*		*Actual (Measured) Response Value*		*Desirable Value / range*	
	Age-3	*Age-28*	*Age-3*	*Age-28*	*Age-3*	*Age-28*
Consistency-time (sec.)	34.87		34.05		35.00	
Compacted Density (%TAFD)	97.11		98.03		96≤ AMD ≥ 98	
Air-Content (%)	2.89		1.97		1.30	
Compressive strength MPa)	36.66	59.6	35.21	54.94	≥32.71±1.69	≥50.28±1.92
Elastic Modulus (GPa)	14.26*	22.3	12.87	19.95	22.30	

*Note: *Predicted Elastic Modulus at age 3 computed from Table 5.13.*

From Table 5.17, it is clear to a great extent that the actual response properties of the optimum mixture correlate reasonably well with the predicted and the desirable values.

Besides, visual observations indicated that the mixture was neither too dry nor too wet as expected; and no lumping, pumping or sinking was generally observed during compaction.

This chapter, in sum, describes the use of optimization techniques within the concept of material mixture experiments for proportioning and designing the paste component of the Bonded Roller Compacted Fibre Reinforced Polymer Modified Concrete (BRCFRPMC) used as the overlay material in this thesis. By constraining the range of variability of the paste constituents, a feasible design space was created with 13 experimental points treated based on the required structural and elastic properties of the overlay. The optimum consistency-time for full consolidation and composite behaviour with the substrate ordinary Portland cement concrete (OPCC) was established between 34.05 and 34.87 seconds, while the resulting apparent maximum density achieves between 97.11% - 98.03% of the theoretical air-free density. In addition, compressive strength response at early and matured ages of 3 and 28 days were satisfied at 100% desirability. The elastic modulus response at age 3 shows 0% desirability, but attains about 99.96% of the target response by 28 days. The verification experiments conducted on each response property shows that positive correlations exist between the measured responses and the predicted values from the optimization analysis.

From here, the on-going analysis was advanced to evaluate the interfacial bond capacity of the optimum mixture with the underlying OPCC substrate by employing the methods of direct shear and indirect tensile tests. The interfacial fracture tests were similarly conducted to assess the progressive fracture response of the interface under monotonic loadings.

6.0 Interfacial Bond Evaluation

In practice, where composite sections are required to transmit stresses across an interfacial plane, the bond capacity of the interface is very crucial and must therefore be designed to withstand all shearing and tensile loads (Nawy and Ukadike, 1983; Granju, 2001). The bond capacity as well-known depends on the interlocking action of the aggregates, the cement-to-cement adhesion at the interface, and the dowel action of the rebar where shear reinforcement is present (Nawy and Ukadike, 1983; Delatte, et al., 1998). In the present study, the use of shear connectors was not considered; the interlocking action of the interface was enhanced through surface roughening of the substrate, while the adhesion at the interface relies on the chemical grip of the optimum paste mixture described in Table 5.16.

In the experiments, seven replicates were implemented each for interfacial tensile and shear strength tests. The interfacial splitting tensile strength test adhered to the provisions given in BS EN 12390-6:2000 and ASTM C496/ C496M, while the direct shear test complied with Iowa Testing Method 406-C. The test specimens were made of bonded overlay material on substrate concrete (OPCC-BRCFRPMC composites). The tensile tests employed 150 x 150 x 75mm identical bonded prismatic square sections, while the shear tests were made of identical bonded 100 x 100mm diameter cylinder sections, and the loadings applied as shown in Figures 6.1. Here, the use of cylinder specimens simulates conventional method where core samples are taken from site for testing in the laboratory

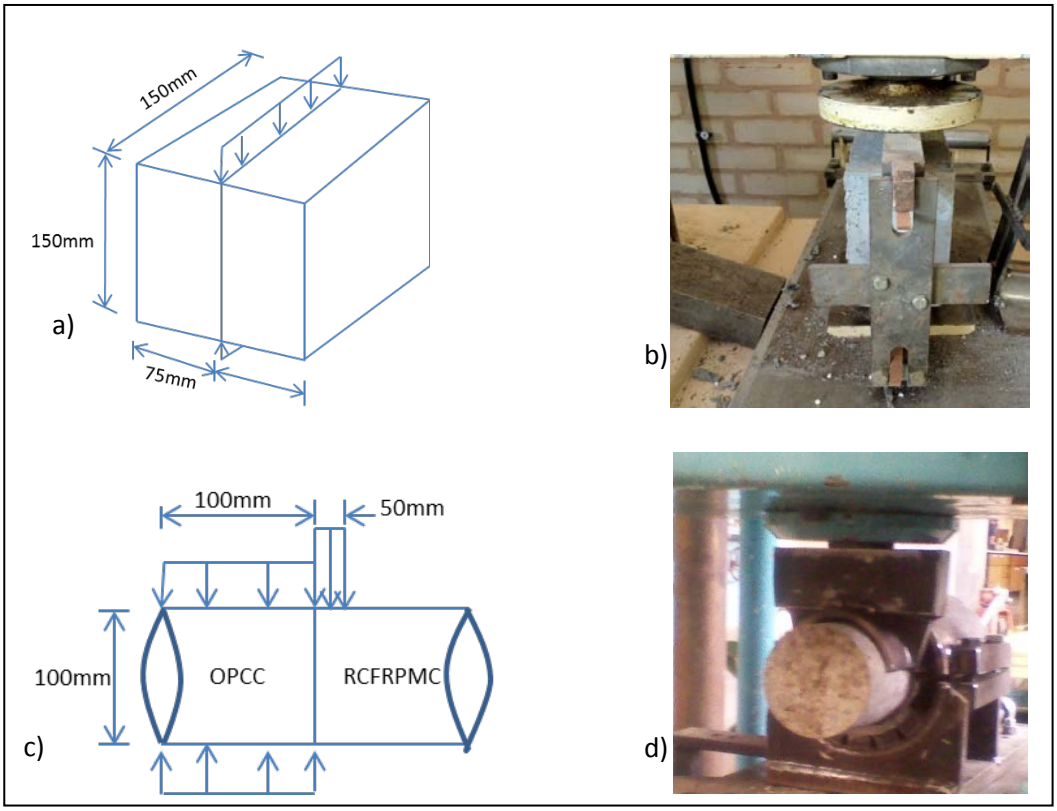

Figure 6.1: (a-b) Tensile splitting test (c-d) Direct cylinder (Guillotine) shear test

The procedures for casting and preparing the substrate OPCC surface were similar in both experiments. In both tests, the hardened OPCC specimens were classified into three distinct surface textures. The classifications followed different degree of roughness intentionally induced on some specimens, while others were left un-roughened as shown in Figure 6.2. In Figure 6.2, the OPCC interface characterization defined as smooth corresponds to the interface cast directly against the mould with no further treatment added. These specimens were assigned 0.00mm (baseline texture). The other two classifications

were roughened intentionally, prepared by rubber brushing at two different controlled levels, just about four and half hours after casting into the moulds.

Note, the reason for preparing the surface just after the initial setting period of the OPCC was to ensure texture repeatability for specimens required for similar degree of roughness during the experiments. It was observed that once the mortar in the concrete matrix becomes hardened, the process of exposing the aggregates or achieving similar degree of texture for effective interlocking action becomes problematic, as it tends to leave some loosed fractured surface behind. Such cracks serve as points of weak bond at the plane of the interface. Hence, for laboratory investigation purposes, the adopted method affords a better surface preparation compared to gunning, drilling or any forceful blasting attempted initially. In the field however, the use of high-pressure water jetting can be employed.

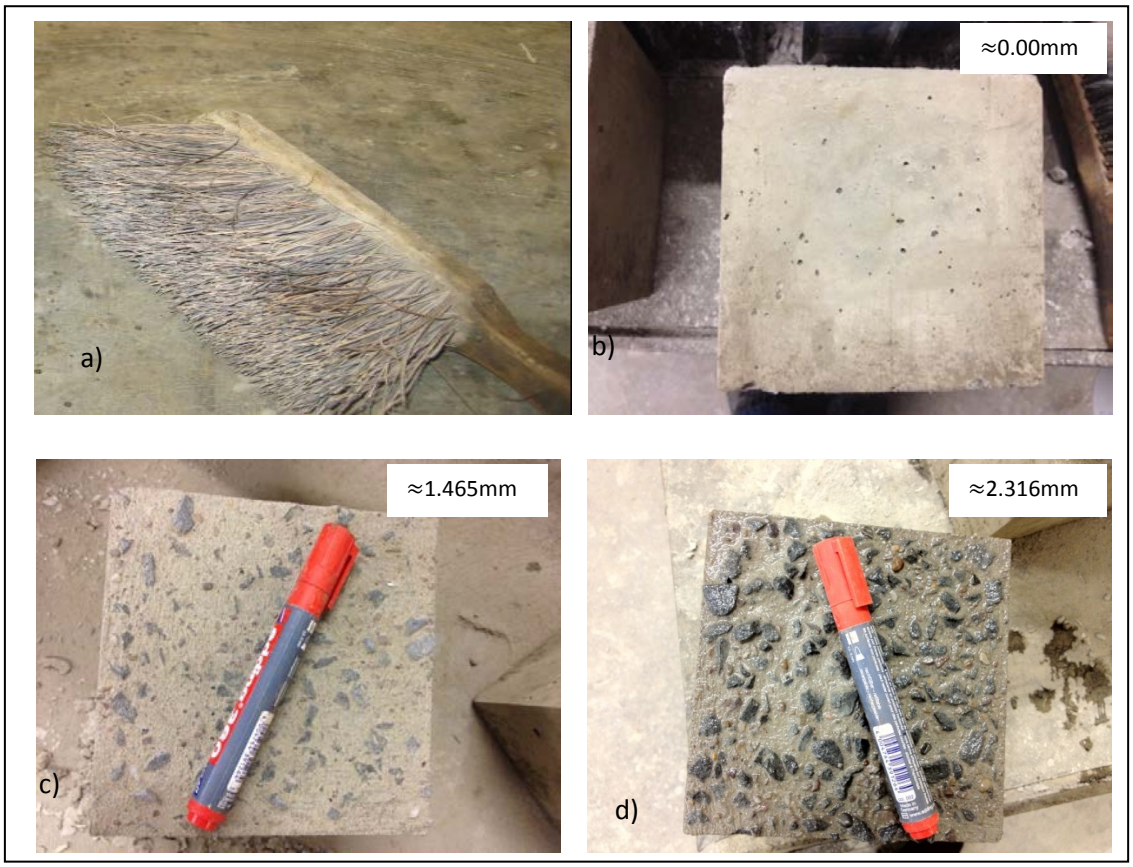

Figure 6.2: a) Roughening brush (b) smooth interface (c) Roughened interface (15-stroke each lateral direction) (d) Roughened interface (30-stroke each lateral direction interface)

The texture figures shown in Figure 6.2 are the mean values obtained by the sand-patch measurement method (BS 598-3 1985; TRRL, 1969) illustrated in Figure 6.3. Before placing the sand; it was ensured that the surface was dry and non-sticky. As a result, all specimens measured were taken out of the curing tank and allowed to dry in the laboratory atmospheric condition for about five days before placing the sand.

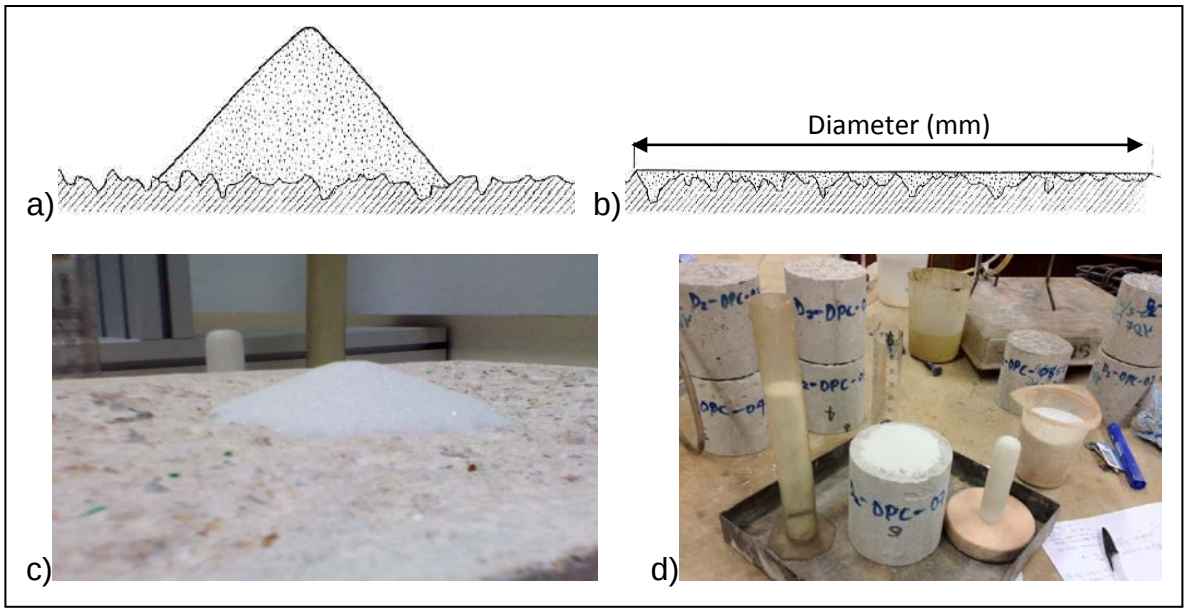

Figure 6.3: Sand Patch texture measurement

In general, curing period of 90 days in water tank was allowed for all substrate specimens, after which they were removed and cured in air for 5 days. The interface was kept clean, free of grease smear, sprayed with tap water for 10 minutes and allowed to dry such that no free water was left on the surface prior to placing and compacting the fresh overlay material with the modified plate vibrator shown in Figure 6.4.

The compaction effort was maintained for 20 seconds each layer of three per specimen. Each specimen was afterward covered with a light polythene sheet and cured in the mould at 60% RH for about 18 hours. After de-moulding, specimens were stored in the curing tank at 100% RH for 24 hours, followed by air curing under laboratory condition. In both experiments, tests were conducted at 3, 14 and 28 days.

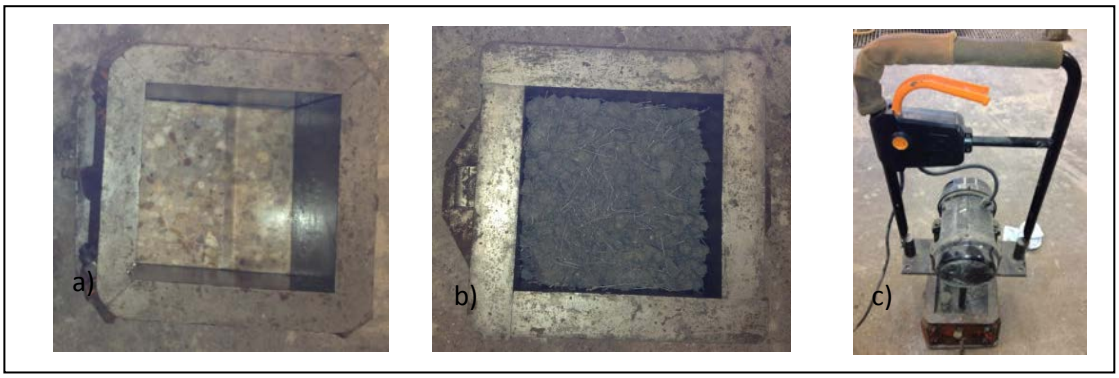

Figure 6.4: Bonding of fresh overlay on old (hardened) concrete: a) Mould containing old OPC, b) Overlay material placed over old OPC prior to compaction, c) Modified electric plate compactor applied at 20sec. per layer

The composite splitting test specimens were loaded as shown in Figure 6.1 continuously in compression between two steel platens to failure along two axial lines which are diametrically opposite. As in the codes (BS EN 12390-6:2000 and ASTM C496/ C496M), standard compression-testing machine was used, with loading rates ranging between 0.01 and 0.04 MPa/s for different age tests. The load was applied through 10mm wide by 4mm thick hardboard strips to prevent local damage. The resulting splitting tensile strength computed from equation 6.1 (Rocco, et al., 2001) are presented in Table 6.1 and Figure 6.6(a).

For the shear tests, the laboratory fabricated set-up loaded in compression is illustrated in Figure 6.1(d). The loading rates in this case also vary for different age test, but generally within 0.01 and 0.02MPa/sec. The shear bond strength was determined based on equation 6.2, by dividing the failure load by the interface cross sectional area. In addition, after testing each shear specimen to failure as shown in Figure 6.5, splitting test was conducted on the remaining half cylinder portion of the overlay and its tensile strength was evaluated using equation 6.3 (Tang, 1994). It should be noted that only four half cylinder specimens were tested in splitting, the remaining three cylinders from the shear test were used for density test based on the method described in ASTM D792, and the percentage of air content was evaluated accordingly using equation 6.4 (ASTM C138, 2001).

The resulting shear strength and the half cylinder splitting tensile strength results are given in Table 6.2 and Figure 6.6(b) and 6.6(d) respectively.

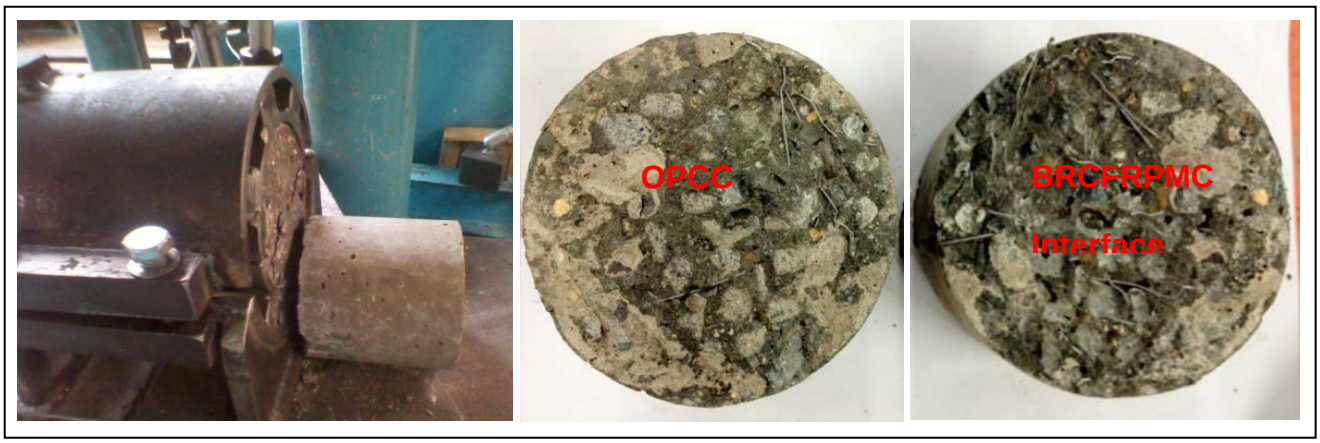

Figure 6.5: OPCC-BRCFRPMC Bi-interface after tested to failure

$$\sigma_{st,mod\ cub.} = \frac{2P}{\pi D}\left[(1-\gamma^2)^{5/3} - 0.0115\right] \quad (6.1)$$

$$\tau_{cyl.} = \frac{P}{A} \quad (6.2)$$

$$\sigma_{st,mod\ cyl.} = \frac{2P}{\pi D}(1-\gamma^2)^{3/2} \quad (6.3)$$

$$Air\ Content\ (\%) = \left(\frac{T-D}{T}\right)100 \quad (6.4)$$

Where, P is failure load, D is prism depth, A is cylinder cross sectional area and γ is relative width of the loading bearing strips, given by (b/D); $b = bearing\ stripswidth$;

$T = theoretical\ air - free\ density\ (2517.30kg/m^3)$;

$D = measured\ density = 2467.71kg/m^3$

Table 6.1: Tensile Bond Strength (MPa)

Smooth Interface (Rz0)													
Component Proportion			**Age (days)**	**Replicate**							***Mean***	***SD***	***COV (%)***
SBR	WATER	CEM 1		***1***	***2***	***3***	***4***	***5***	***6***	***7***			
0.0938	0.1523	0.7540	**3**	1.56	1.64	1.66	1.59	1.58	1.61	1.6	***1.61***	***0.03***	***2.15***
			14	1.74	1.78	1.75	1.79	1.73	1.67	1.73	***1.74***	***0.04***	***2.26***
			28	1.83	1.8	1.85	1.87	1.8	1.79	1.88	***1.83***	***0.04***	***1.98***
Roughened Interface (Rz1)													
0.0938	0.1523	0.7540	3	2	1.96	2.05	1.97	1.98	1.96	1.94	***1.98***	***0.04***	***1.82***
			14	2.09	2.11	2.05	2.09	2.04	2.1	2.03	***2.07***	***0.03***	***1.54***
			28	2.14	2.17	2.15	2.11	2.09	2.13	2.09	***2.13***	***0.03***	***1.43***
Roughened Interface (Rz2)													
0.0938	0.1523	0.7540	3	2.09	2.04	2.13	2.07	2.11	1.99	2.03	***2.07***	***0.05***	***2.37***
			14	2.12	2.09	2.13	2.15	2.14	2.1	2.12	***2.12***	***0.02***	***1.00***
			28	2.25	2.29	2.23	2.18	2.19	2.19	2.2	***2.22***	***0.04***	***1.81***

Table 6.2: Shear Bond Strength (MPa)

Smooth Interface (Rz0)													
Component Proportion			**Age (days)**	**Replicate**							***Mean***	***SD***	***COV (%)***
SBR	WATER	CEM 1		***1***	***2***	***3***	***4***	***5***	***6***	***7***			
0.0938	0.1523	0.7540	**3**	2.28	2.24	2.31	2.22	2.25	2.25	2.24	***2.26***	***0.03***	***1.33***
			14	3.38	3.4	3.33	3.35	3.31	3.29	3.29	***3.34***	***0.04***	***1.29***
			28	3.82	3.77	3.76	3.81	3.77	3.79	3.74	***3.78***	***0.03***	***0.75***
Roughened Interface (Rz1)													
0.0938	0.1523	0.7540	3	3.27	3.31	3.23	3.22	3.21	3.21	3.20	***3.24***	***0.04***	***1.23***
			14	3.79	3.74	3.78	3.84	3.78	3.75	3.76	***3.78***	***0.03***	***0.87***
			28	4.24	4.17	4.26	4.19	4.12	4.14	4.1	***4.17***	***0.06***	***1.44***
Roughened Interface (Rz2)													
0.0938	0.1523	0.7540	3	3.83	3.75	3.86	3.88	3.79	3.74	3.72	***3.80***	***0.06***	***1.64***
			14	4.1	4.13	4.14	4.08	4.08	4.11	4.11	***4.11***	***0.02***	***0.56***
			28	4.92	4.88	4.84	4.85	4.79	4.87	4.87	***4.86***	***0.04***	***0.82***

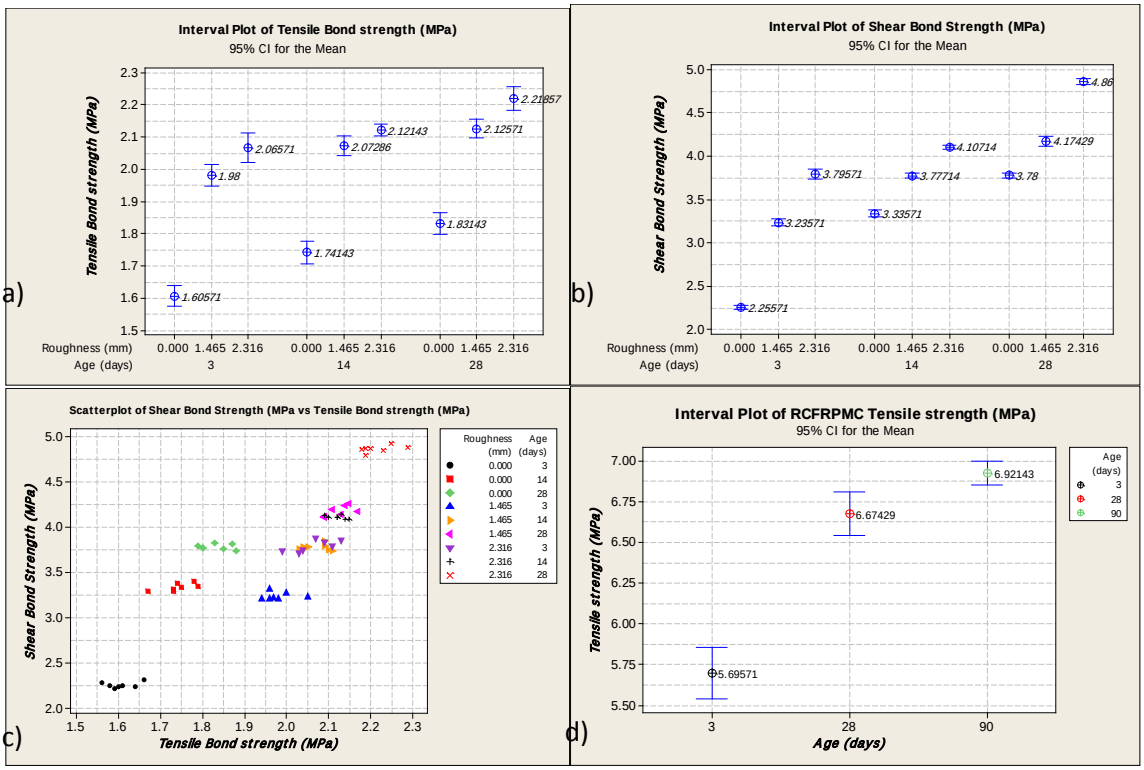

Figure 6.6: (a) Tensile Bond strength (b) Shear bond strength (c) Shear bond vs. Tensile Bond strength (d) Overlay BRCFRPMC Cylinder splitting (tensile) strength

From equation 6.4, the calculated air-content yields about 1.97%. This value was presented in Table 5.17. This value demonstrates that the optimum mixture achieves about 98.03% TAFD. This correlates well with the desirable air content and the predicted compacted density given in Tables 5.16 and 5.17 respectively. In addition, the cylinder splitting tensile result for the optimum mixture illustrated in Figure 6.6(d) exhibits an early high strength tendency. The mixture attains an average tensile strength of 5.69MPa in 3 days and increases averagely by 17.80% in 25 days. In the result, it is indicative that the material should be able to withstand significant tensile stresses before cracking during restrained drying shrinkage, so long the induced strain is gradually applied.

Further, in Figure 6.6(a & b), interfacial tensile and shear strengths as a function of AGE and ROUGHNESS are illustrated. As seen in both cases, strength increases as each predictor increases. For specimens with $0.00mm$ texture, tensile bond increases averagely by 13.66% between age-3 and age-28; while for specimens with $1.465mm$ and $2.316mm$ textures; it increases by 7.58% and 7.25% respectively for the same age difference. The trend of shear bond strength as shown in Figure 6.6(b) is similar to that of tensile, though

the overall contribution of surface texture appears more beneficial in shear than in tensile. This is explicable because the mechanics of interfacial de-bonding and interlocking differ in both cases. Similar observations have been argued elsewhere (Beushausen, 2005; Benoît et al., 2012). Specifically, as shown in Figure 6.6(c), the estimated benefits of surface texture on shear over tensile strength range averagely between 14% and 31% for equal differential texture levels of 1.465mm and 2.316mm respectively.

6.1 Interfacial Bond capacity assessment

For concretes cast at different age, several codes are specific about the requirements for bond capacity. In BS EN 1504-3 for instance, the tensile bond requirement for structural strengthening should be $\geq 2.0MPa$, while for non-structural work, it should exceed or be equal to $0.8MPa$. In other codes like Swedish National Road Administration (SNRA), tensile bond requirements differ in values from those given in BS EN 1504-3. SNRA provisions permit tensile bond capacity to be estimated using the conditions given in inequalities 6.5 (Silfwerbrand, et al., 2012):

$$m \geq f_v + 1.4(s) \;\; ; x \geq 0.8\, f_v \qquad (6.5)$$

Where, $m = mean\ tensile\ bond$; $s = standard\ deviation$;

$f_v = required\ tensile\ bond = 1MPa$;

$x = single\ measuring\ value$.

Thus, by checking the experimental tensile bond results against the conditions given in (6.5) above, the check began with the worst tensile strength value which corresponds to smooth interface composite tested at age 3. Here, $m = 1.61MPa$, and $s = 0.03$, while the lowest observed value $(x) = 1.56MPa$. From here, it can be shown that:

$$1.61 \geq 1 + 1.4(0.03)$$

$$1.61 \geq 1.042 \;\; ; \;\; and\ x \geq 0.8(1) \qquad (ok).$$

By inspection, referring to Figure 6.6(a), it would imply that all test specimens satisfied the bond criterion in this case. Hence, it can be proven at this point that the choice of a code or bond requirements for design purposes depends on the design engineer and the level of

satisfaction one intends to achieve. In all, both strong chemical adhesion and sufficient degree of roughness are required for enhanced tensile bond performance.

Similarly, in terms of interfacial shear capacity, codes provisions (EC2, ACI 318-02, CEP-FIP - 90) differ in opinions and specifications. For instance, in ACI 318-02, where 0.55 MPa is specified as the design interfacial shear resistance, the provision for bond requirement is contingent on clean surface free of laitance and intentional roughening amplitude of approximately 6.4mm. But in CEP-FIP Model Code 90, a more calculative step is involved in determining interfacial shear resistance based on the expression given in equation 6.7:

$$\tau_{Rd\,i} = c(f_{ctd}) - \mu(\sigma_{n\,i}) \qquad (6.7)$$

Where,

$c = multiplying\ factor\ depending\ on\ surface\ category$

$f_{ctd} = tensile\ strength\ of\ the\ weakest\ material\ (OPC\ or\ RCFRPMC) = \frac{f_{ctk,min}}{\gamma_m}$;

$\gamma_m = 1.5$

$\mu = frictional\ parameter$

$\sigma_{n\,i} = confining\ stress$

Using the above expression, for an unconfined overlay with, say 25MPa characteristic strength, bonded on high strength concrete with category II roughness, the design shear resistance yields:

$$\tau_{Rd\,i} = 0.4\,(1.167) - 0.9(0)$$

$$\tau_{Rd\,i} = 0.47\ MPa$$

For similar conditions as the example cited above, the EC2 however yields a different value, following equation 6.8:

$$\tau_{Rd\,i} = c \cdot f_{ctd} + \mu \cdot \sigma_{n\,i} + [\rho \cdot fyd(\mu \cdot sin\,\beta + cos\,\beta)] \leq 0.5\,\nu \cdot fcd \qquad (6.8)$$

Where,

$\rho =$ $reinforcement\ ratio$
$\beta =$ $inclination\ between\ reinforcement\ and\ concrete\ surface$
$fcd = concrete\ design\ compressive\ strength$

$\nu = 0.6\ for fck \leq 60\ MPa = \ 0.9 - fck/200 \geq 0.5\ for fck \geq 60 MPa$

By ignoring the reinforcement terms in the bracket, the resulting design shear gives:

$$\tau_{Rd\,i} = 0.45(1.167) + \ 0.7(0)$$

$$\tau_{Rd\,i} = 0.53\ MPa$$

As demonstrated in the three different codes cited above, it is clear enough that the design shear values will generally be lower compared to most values obtained from the laboratory (Granju, 2001). For comparison purpose, the results obtained in the present study correlate well with those found in the literature (Silfwerbrand et al, 2012); which typically fall well above $3MPa$ for 28-day bond test. However for design purposes, lesser values as those recommended in the appropriate codes would be employed. For instance, if EC2 is considered, the following will be the design shear bond strength limit for smooth and roughened interface:

$$f_{ctd} = \frac{f_{ctk,min}}{1.5} = \ \frac{3.97}{1.5} = 2.65MPa$$

Note, the f_{ctd} used here corresponds to that of OPCC design tensile strength since it is smaller in magnitude compared to that of BRCFRPMC optimum mixture. This is so because yielding at the interface is generally governed by the tensile strength of the weaker material between the substrate and the overlay. Hence,

$$\tau_{Rd\ smooth} = \ 0.35\ (2.65) + \ 0.6(0) = \ 0.93MPa$$

$$\tau_{Rd\ roughened} = 0.45\ (2.65) + \ 0.7(0) = \ 1.19MPa$$

As seen these values are far lesser than the measured values in Figure 6.6(b). The average shear strength for smooth texture specimens is $3.80MPa$, while $1.465mm$ and $2.316mm$ texture specimens yield $4.11MPa$ and $4.86MPa$ respectively. However for design purposes, lesser values as those calculated above or recommended in appropriate codes would be adopted. Usually, these design values are influenced by some long-term material response such as creep and differential length change. Besides, most of the methods for determining design bond strength in many codes do not account for the effect of different chemical bonding per se. Arguably, overlay material with minimal compressive strength can also provide good bonding where a satisfactory interface texture is available and sufficient adhesive like SBR polymer is included as concrete modifier. Whereas, many codes rely

more on the interface texture and material strength parameters, which in this case does not account for extra bond enhancement provided by additives like SBR polymer. No doubt that code provisions are highly conservative and generally incur huge economic implications on bonded concrete overlay construction projects.

In Tables 6.3 and 6.4 the summary of the target, predicted and measured values for the optimum mixture is given for each specified bulk and interface property

Table 6.3 Summary of Bulk Properties of the Optimum Mixture

Property	*Desirable value*	*Predicted value*	*Measured value*
Consistency-Time (sec)	*35*	*34.87*	*34.05*
AMD (%TAFD)	*96*	*97.11*	*98.03*
Compressive strength (MPa) *Age-3* *Age-28*	 *≥32.71±1.69* *≥50.28±1.92*	 *36.66* *59.60*	 *35.21* 54.94
Elastic Modulus (GPa) *Age-3* *Age-28*	 *22.30* *22.30*	 *14.26* *22.30*	 *12.87* *19.95*
Tensile strength (MPa) *Age-3* *Age-28* *Age-90*	 *>4.50* *>4.50* *>4.50*	 - - -	 *5.69* *6.67* *6.92*

Table 6.4: Summary of Interface Bond Properties of Optimum Mixture

Texture Level	*Mean Tensile Bond (MPa)*			*Mean Shear Bond (MPa)*		
	Age (days)					
	3	14	28	3	14	28
R_{z0}	*1.61*	*1.74*	*1.83*	*2.26*	*3.34*	*3.78*
R_{z1}	*1.98*	*2.07*	*2.13*	*3.24*	*3.78*	*4.17*
R_{z2}	*2.07*	*2.12*	*2.22*	*3.80*	*4.11*	*4.86*

From Tables 6.3 and 6.4, it is clear that a significant level of desirability is recorded with optimum mixture response for both bulk and interface bond properties. In terms of bond strength responses, only specimens with texture level R_{z2} seems to satisfy tensile requirement in line with EC2 at any given age. On the other hand, in shear, all specimens show adequate bond strength in the upward of 2.26MPa to 3.80MPa at early-age of 3 and 3.78MPa to 4.86MPa for matured age of 28; though generally less than 5.0MPa.

From here, it is evident that only test specimens with texture level of R_{z2} showed good bond response, hence all subsequent investigations in this research were based on texture R_{z2}.

6.2 Supplementary material properties: Coefficients of thermal expansion and length change measurement

In reality, all materials expand and contract to some degree under variational temperatures. Consequently, since the optimum mixture is also required to satisfy the relative thermal movement / differential length change requirements with the substrate OPCC, coefficients of thermal expansion were experimentally determined for both materials, while shrinkage properties was measured for the BRCFRPMC overlay only.

6.2.1 Coefficients of thermal expansion

The coefficient of thermal expansion is the property of a material which reflects the measure of its expansion or contraction when subjected to temperature variations. As discussed in Chapter 2, the curling phenomenon of concrete pavement is greatly influenced by this parameter, and is generally critical in the overlay systems when the coefficients of thermal expansion are mismatched. Usually, in practice, the coefficients of thermal expansion of bonded materials are kept as close as possible within the concept of dimensional compatibility, unless it is envisaged that the temperature change between the overlay and the substrate will be negligible (Delatte, 2008).

In this respect, in order to account for the coefficients of thermal expansion of the overlay and the substrate, the standard method according to AASHTO TP60-00, also reported in TxDOT (Tex-428-A, 2011), was adopted. The method measures the length change of saturated test specimen under a prescribed temperature range of 10 - 50℃, and is generally based on mounting a cored or cast cylindrical specimen on the set-up shown in Figure 6.7(a).

In this present work, prism specimens measuring 40 x 40 x 230mm were used rather than the standard cylindrical specimens. Prism specimens were used based on the mould available, and it has been shown (Yang et. al, 2003) that specimen shape has no significant effect on such experimental test.

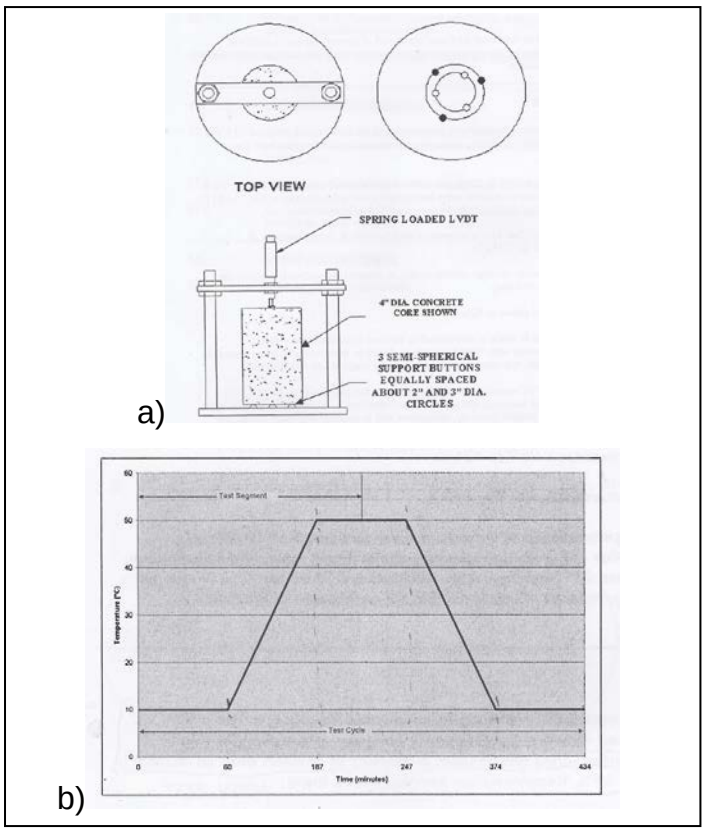

Figure 6.7: a) Set-up for measuring length change b) Typical test cycle graph

The resulting thermal expansion values for three test specimens cast from OPCC and the optimal BRCFRPMC mixture are presented in Table 6.5; while Figure 6.8 shows their representative graphs.

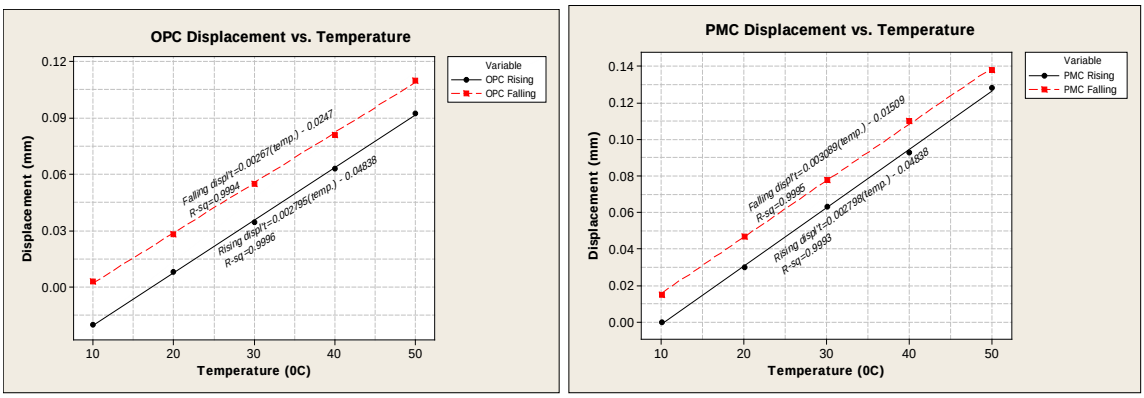

Figure 6.8: Thermal displacement vs. Temperature for OPCC and BRCFRPMC

In order to obtain the coefficient of thermal expansion (CTE) from the graphs shown above, the following procedures were followed:

- The gradient for each regression line shown in the graphs was determined,
- Only regression lines with R-sq. value greater than 0.999 were considered,

- Each gradient was divided by the specimen length (230mm) to obtain the CTE,
- The average CTE for Rising and Falling was determined accordingly.

Table 6.5: Coefficients of thermal expansion for OPCC and BRCFRPMC

Specimen no	CTE (OPCC) (/^{0}C)			CTE (BRCFRPMC) (/^{0}C)		
	Rising	Falling	Average	Rising	Falling	Average
1	12.2 x 10^{-6}	11.7 x 10^{-6}	11.95 x 10^{-6}	13.91 x 10^{-6}	13.48 x 10^{-6}	13.70 x 10^{-6}
2	11.9 x 10^{-6}	11.3 x 10^{-6}	11.6 x 10^{-6}	13.5 x 10^{-6}	13.11 x 10^{-6}	13.31 x 10^{-6}
3	12.0 x 10^{-6}	11.5 x 10^{-6}	11.75 x 10^{-6}	14.11 x 10^{-6}	13.82 x 10^{-6}	13.97 x 10^{-6}
Grand Mean		***11.8 x 10^{-6}***			***13.66 x 10^{-6}***	

As clearly shown in Table 6.5, the CTEs of BRCFRPMC and OPCC match closely, though BRCFRPMC generally shows higher values. The margin of variability here is tolerable since the usual range for cementitious materials lies within 10 and 14 x 10^{-6}.

In practice, for prediction purposes, the CTE values given above can be extended to obtain an approximate estimate of the range of temperature change that will cause the BRCFRPMC overlay to crack. Supposed the BRCFRPMC tensile strength (σ_t) is set as the maximum stress (σ_{max}) that can be resisted before cracking develops; by constitutive relation, it can be shown that the strain (ε_f) at failure, at any given age of the overlay will correspond to:

$$\varepsilon_f = \frac{\sigma_t}{E_{BRCFRPMC}} = \alpha_{BRCFRPMC}\Delta T \qquad (6.9)$$

From where,

Change in temperature, $(\Delta T) = \frac{\varepsilon_f}{\alpha_{BRCFRPMC}}$ (6.10)

Where,

$E_{BRCFRPMC} = Elastic\ modulus\ of\ BRCFRPMC$

$\alpha_{BRCFRPMC} = Coefficient\ of\ thermal\ expansion\ of\ BRCFRPMC$

Thus, from equation 6.10, Table 6.6 can be drawn to illustrate the temperature change in the overlay that will result in cracking.

Table 6.6: Predicted cracking due to temperature change

$Age\ (days)$	$E_{BRCFRPMC}\ (MPa)$	$\sigma_t\ (MPa)$	$\varepsilon_f\ (\%)$	$\alpha_{RCFRPMC}(\ /℃)$	$\Delta T\ (℃)$
3	12870	5.33	0.0442	13.66×10^{-6}	32.36
28	19950	6.67	0.0334	13.66×10^{-6}	24.48
90	21220	6.92	0.0326	13.66×10^{-6}	23.87

Explicably, for an axially restrained overlay, a reduction in temperature will result in increased tensile stress. If, at any time, the increased tensile stress in the BRCFRPMC overlay exceeds its tensile strength value, cracking in the overlay is hypothetically predicted following changes in temperature values as shown in Table 6.6. As seen in Table 6.6, it is envisaged that temperature change in the tune of 23℃ and above can be critical to the BRCFRPMC overlay.

By extension, the stress condition at the interface can be assessed if the estimated temperature change shown here is applied to the expression given in equation 6.11.

$$\sigma = \frac{(\alpha_{BRCFRPMC} - \alpha_{OPCC})(\Delta T)E_{BRCFRPMC}}{1 - v^2{}_{BRCFRPMC}} \qquad (6.11)$$

In his respect, if $\alpha_{BRCFRPMC} = 13.66\ x\ 10^{-6}/℃$; $\alpha_{OPCC}\ x\ 10^{-6}/℃$; $E_{BRCFRPMC} = 12870MPa$; 19950 and 21220; $\Delta T = 32.36℃; 24.48$; and 23.87; $v = 0.25$ based on the experimental data given previously, then the induced stress at the overlay interface under a plane strain condition is given by:

For age 3:

$$\sigma = \frac{(13.66\ X\ 10^{-6} - 11.80\ X\ 10^{-6}\ )(32.36)12870}{1 - 0.25^2} = 0.83MPa$$

For age 28:

$$\sigma = \frac{(13.66\,X\,10^{-6} - 11.80\,X\,10^{-6})(24.48)19950}{1 - 0.25^2} = 0.97MPa$$

For age 90:

$$\sigma = \frac{(13.66\,X\,10^{-6} - 11.80\,X\,10^{-6})(23.87)21220}{1 - 0.25^2} = 1.01MPa$$

From here, by comparing the estimated values shown above with those in Table 6.4, it was concluded that the interface is no likely to de-bond even under the worst thermo-elastic mismatched properties between the designed overlay material and the substrate OPCC used in this experiment. Besides, it is apparent at this juncture that the reduced elastic modulus of the overlay is practically advantageous as illustrated in the computation shown above; the reason being that it reduces tensile and de-bonding stresses in the overlay and at the interface. In fact, in order to initiate cracking in the overlay or induce interfacial separation at the early-age of 3, temperature change well above $32℃$ is needed.

6.2.2 Drying Shrinkage

By definition, drying shrinkage of cementitious materials is the reduction in volume or length as a result of loss of moisture. This length reduction is a time-dependent phenomenon under a constant temperature when no other load is applied on the test specimen. In this work, the specimen size (40 x 40 x 230) used were similar to those used for the coefficient of thermal expansion test; and to ensure constant temperature, the specimens were stored with all sides exposed equitably in the temperature controlled room at 25^0C and 60% humidity.

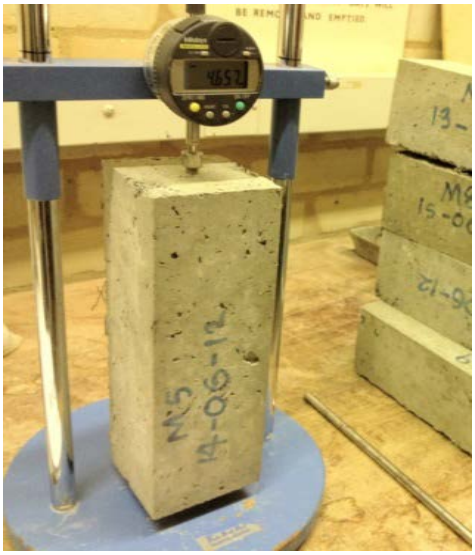

Figure 6.9: Drying shrinkage measurement

Though in most codes and technical documents, a distinction is often made between the drying shrinkage and other kinds of phenomena like autogenous shrinkage and carbonation shrinkage, for simplicity purpose, the ACI 224R-01 on the other hand, suggests no need of distinction from structural standpoint and due to high degree of uncertainty in quantifying such phenomena under several influencing factors such as concrete composition, source of aggregate, ambient relative humidity, specimen geometry, the ratio of the exposed surface to the volume of the structural element and the slow development of shrinkage over time which makes it difficult to obtain accurate prediction from short-term laboratory measurements.

In view of the above, the observations in this research consider only drying shrinkage. The corresponding drying shrinkage response is presented in Figure 6.10 together with the moisture loss graph.

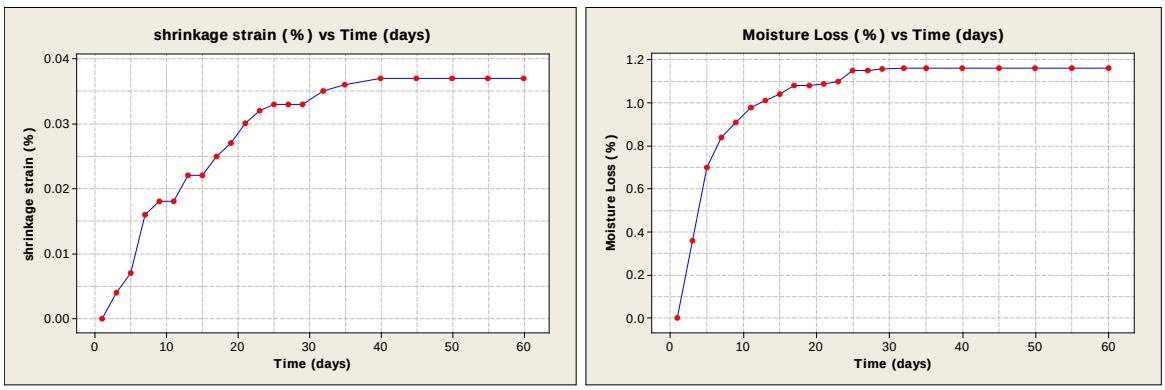

Figure 6.10: Free shrinkage strain and Moisture loss vs. age

Generally, as observed in this work and demonstrated elsewhere (Ohama and Kan, 1982) it has been shown that the addition of polymer to concrete does not usually increase its total shrinkage. Shrinkage measurements observed here at various curing times is the average of three test specimens, and indicates that shrinkage was influenced primarily by the moisture content. By using a quadratic polynomial function, the corresponding fitted regression model between the moisture loss and the resulting drying shrinkage is shown in Figure 6.11 and equation 6.12.

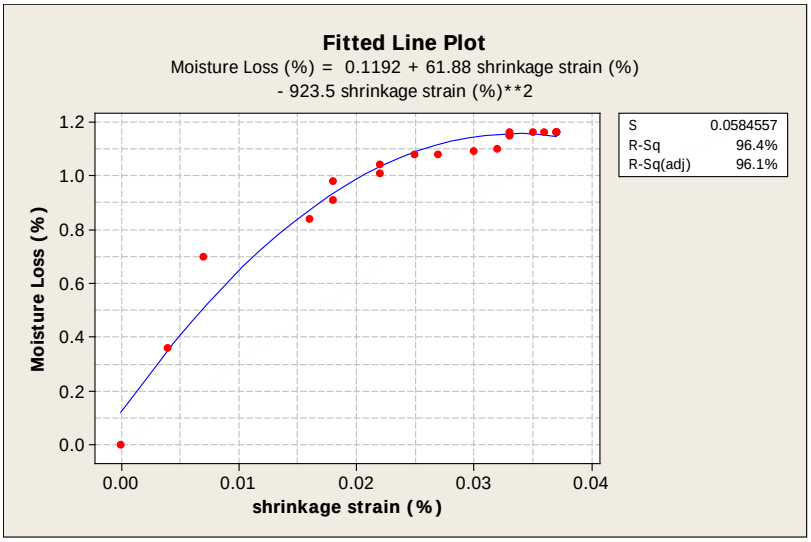

Figure 6.11: Relationship between Moisture loss and Drying shrinkage

$$Moisture\ loss\ (\%) = -923.5\ (shrinkage\ strain\%)^2 + 61.88\ (shrinkage\ strain\%) + 0.1192 \quad (6.12)$$

Further, note that the free strain shown in this case does not cause any stress in the absence of any internal or external restraint to the test specimen. However, in the overlay systems, prior to attaining a reasonable level of moisture equilibrium within the overall section, internal restraint to shrinkage movement is usually imposed (ACI 224R-01) due to moisture gradients, thereby causing self-equilibrating internal stresses, with tension on the exposed overlay surface and compression in the interior depth as illustrated in Figure 6.12. Worse still, the effect of bond restraint at the interface aggravates the stress condition and can cause cracking in the overlay or at the interface if not relieved by creep; depending on the most stressed region, either the bulk overlay material or the interface.

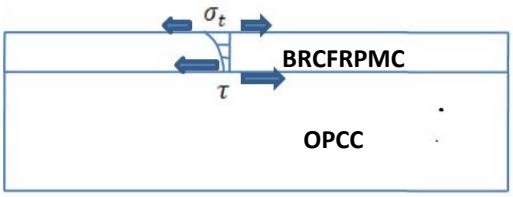

Figure 6.12: Self-equilibrating stress conditions in the BCOs

For instance, from the shrinkage values given in Figure 6.10, the observed free shrinkage ($\varepsilon_{sh.free}$) can be used to estimate the magnitude of tensile stress (σ_t) and the compressive stress (σ_c) developing in the bulk BRCFRPMC and OPCC respectively as shown in Figure 6.13, if the interface is assumed to provide sufficient restraint via its bond and interlocking actions.

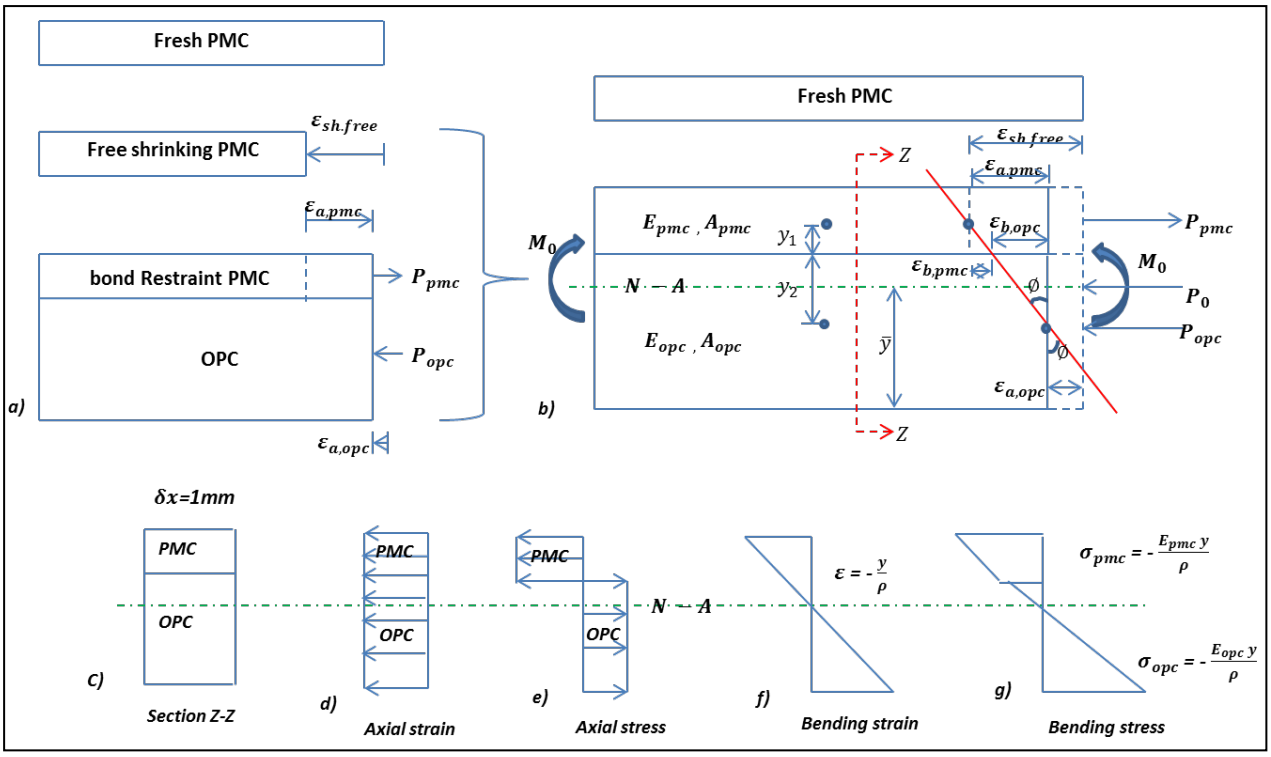

Figure 6.13: Strain and Stresses in Bi-material Composite section under Axial and Bending Loadings

Consider Figure 6.13 (a, d, & e), where the free shrinkage ($\varepsilon_{sh.free}$) of the fresh PMC or BRCFRPMC overlay is restrained by the substrate OPCC; under no slip condition, strain will be continuous across the specimen cross section, but stress will be discontinuous.

Subsequently, under self-equilibrating pure axial deformation; since the two materials deformed monolithically, it can be shown that:

$$\varepsilon_{sh.free} = \varepsilon_{a,pmc} + \varepsilon_{a,opc} = \frac{\sigma_{pmc}}{E_{pmc}} + \frac{\sigma_{opc}}{E_{opc}} \qquad (6.13)$$

So that the equilibrium of forces will be:

$$P_1 = P_2 = \sigma_{a,pmc} A_{pmc} = \sigma_{a,opc} A_{opc} \qquad (6.14)$$

From where,

$$\sigma_{a,pmc} = \frac{\sigma_{a,opc}.A_{opc}}{A_{pmc}} \qquad (TENSION) \qquad (6.15)$$

By substituting for $\sigma_{a,pmc}$ in equation (6.13), it yields:

$$\varepsilon_{sh.free} = \frac{\sigma_{a,opc}.A_{opc}}{E_{pmc}.A_{pmc}} + \frac{\sigma_{a,opc}}{E_{opc}}$$

$$\therefore \varepsilon_{sh.free} = \sigma_{a,opc}\left[\left(\frac{A_{opc}}{E_{pmc}.A_{pmc}}\right) + \frac{1}{E_{opc}}\right] \qquad (6.16)$$

But then, if the ratio of the elastic moduli of the two materials, i.e. $n = \frac{E_{opc}}{E_{pmc}}$, it follows that $E_{pmc} = \frac{E_{opc}}{n}$

Hence, equation (6.16) becomes:

$$\varepsilon_{sh.free} = \sigma_{a,opc}\left[\left(\frac{n\,A_{opc}}{E_{opc}.A_{pmc}}\right) + \frac{1}{E_{opc}}\right]$$

From where,

$$\sigma_{a,opc} = \frac{\varepsilon_{sh.free}\,.\,E_{opc}}{1+n\left(\frac{A_{opc}}{A_{pmc}}\right)} \qquad (COMPRESSION) \qquad (6.17)$$

Thus, equations 6.15 and 6.17 are the respective tensile and compressive stresses developing in the bulk BRCFRPMC and OPC materials, under pure axial deformation or loading due to axial shrinkage effect. In order to determine their numerical values, a measured free shrinkage value in the BRCFRPMC together with the elastic moduli of the two materials is required as illustrated in Table 6.7.

Table 6.7: Overlay Free Shrinkage strain, Elastic Modulus, Tensile strength, Axial Tensile and Compressive stresses in the bulk PMC and OPCC.

Age (days)	Strain, ε_f (%)	Elastic Modulus, $E_{pmc}\ (MPa)$	$\frac{E_{opc}}{E_{pmc}}$ (n)	Tensile strength $\sigma_{pmc.t}\ (MPA)$	Axial Compressive stress $\sigma_{opc}\ (MPa)$	Axial Tensile stress $\sigma_{pmc}\ (MPa)$	Axial Force $P\ (N)$
3	0.004	12,870	1.733	5.69	0.144	0.432	43.2
28	0.033	19,950	1.118	6.67	1.690	5.070	507.0
90	0.037	21,220	1.051	6.92	1.987	5.961	596.1

The estimated stress and force values shown in Table 6.7 above represent conditions of no-slip between the overlay and the substrate layer, as the two layers deform under uni-axial length change effect of drying shrinkage. As seen in the table, while the compressive stresses developing in the bulk OPCC are not critical in magnitude and also from structural integrity viewpoints; the corresponding tensile stresses in the overlay (PMC or RCFRPMC) domain are substantially high, especially for at 28 and 90 days where the stress levels are in the tune of 76.01% and 86.14% of the ultimate failure stress, respectively. In a more severe condition, where the two layers are fully restrained axially, stress values in the BRCFRPMC overlay are expected to be higher in magnitude than those given in Table 6.7; to the tune of 19%, 29% and 31% higher for ages 3, 28 and 90 days respectively.

Thus, if at any age, the net tensile stress in the overlay attains or exceeds its tensile capacity; transverse cracks are expected to occur in the overlay, if not effectively relieved by creep. In Figure 6.14, the predicted point of tensile cracking is illustrated with the red-dashed arrow line, indicating that for fully restrained overlay specimen, shrinkage crack or cracks might be evident after its twenty-eighth day of casting. However, for partly restrained specimen, where restrained is probably induced only by the aggregate interlocking and chemical bonding of the interface, likelihood of crack(s) occurring appears dicey.

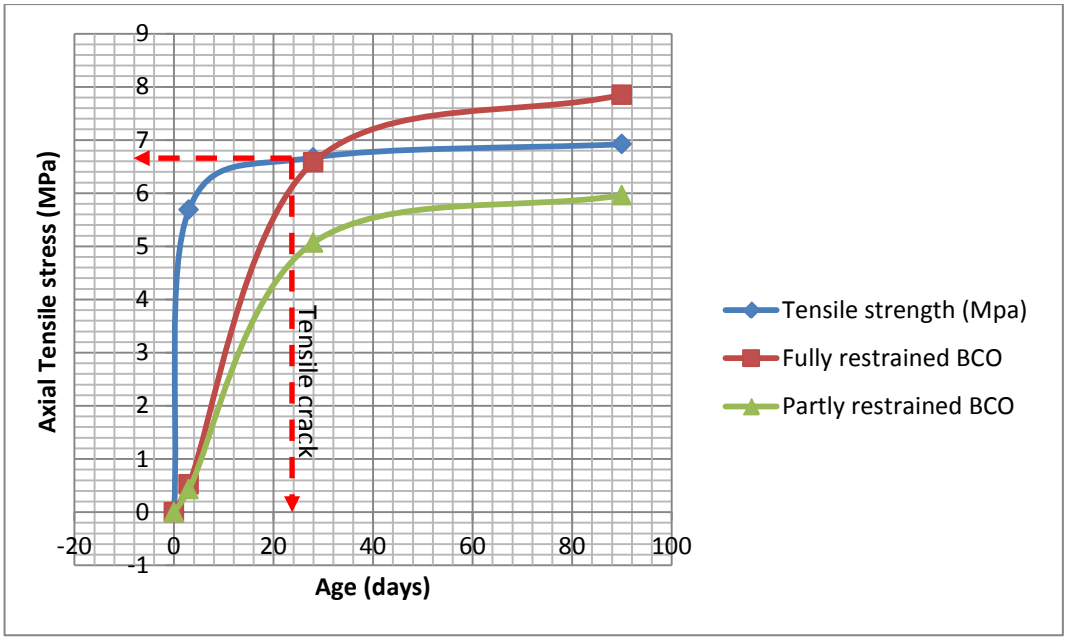

Figure 6.14: Axial Tensile stress vs. Age

Moreover, in the on-going analysis, if the magnitude of the shrinkage deformation shown in Table 6.7 above is considered in terms of bending rather than pure axial effect, stress conditions in the overlay and OPCC will be different. Consider Figure 6.13(b), where the overlay gradient deformation induces a bending moment as shown. As in axially loaded condition, Figure 6.13(b, f, & g) also indicates that strain is still continuous while the stress remains discontinuous. But hen, stain and stress in the current configuration are represented as linear functions of depth (y) through the neutral axis (N-A), on either side of the composite.

In this respect, it can be shown that:

$$\sigma_{a,pmc} = \frac{E_{pmc}\, y}{\rho} \qquad (6.18)$$

$$\sigma_{a,opc} = \frac{E_{opc}\, y}{\rho} \qquad (6.19)$$

From where it can be written that:

$$dF_{pmc} = \sigma_{a,pmc} dA = \frac{E_{pmc}\, y}{\rho}\, dA \qquad (6.20)$$

$$dF_{opc} = \sigma_{a,opc} dA = \frac{E_{opc}\, y}{\rho}\, dA \qquad (6.21)$$

Given that, $n = \frac{E_{opc}}{E_{pmc}}$,

Then, it can be shown that $E_{opc} = nE_{pmc}$ (6.22)

By substituting for E_{opc} in equation (6.21), it becomes:

$$dF_{opc} = \frac{nE_{pmc}\, y}{\rho}\, dA = \frac{E_{pmc}\, y}{\rho}\, (ndA) \qquad (6.23)$$

Which by comparison between equations 6.20 and 6.23, indicates that the same force (dF_{pmc}) would be acting on an element of (ndA) of the OPCC. This then implies that the bending resistance of the composite would remain the same if both portions of the composite were assumed to be made of just one material, so long the width of the other material portion is adjusted by (n) amount. This consequently informs the transformed section analysis illustrated in Figure 6.15 below for different ages of the PMC overlay.

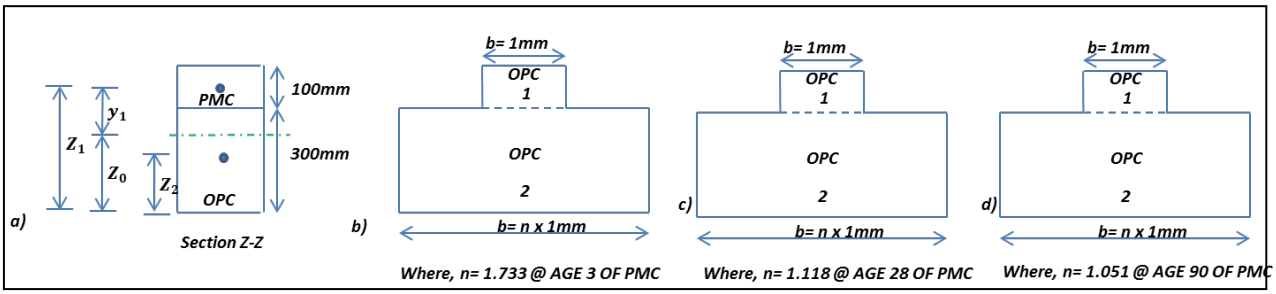

Figure 6.15: Transformed section at ages 3, 28 and 90 days of the overlay

From the transformed sections illustrated above, the following Table 6.8 can be drawn to determine the neutral axis and the corresponding area of inertia for each configuration.

Table 6.8: Properties of the transformed sections

Section Property	*Age 3*	*Age 28*	*Age 90*
Area (A)	100 x 1.00 = 100 300 x 1.733 = 519.9 $\boldsymbol{A_T = 619.9mm^2}$	100 x 1.00 = 100 300 x 1.118 = 335.4 $\boldsymbol{A_T = 435.4mm^2}$	100 x 1.00 = 100 300 x 1.051 = 315.3 $\boldsymbol{A_T = 415.3mm^2}$
First moment of area (Q) (x-x)	$Z_1.A_1 = 350$ x100 = 35000 $Z_2.A_2 = 150$ x 519.9 = 77985 $\boldsymbol{Q_T = 112985mm^3}$	350 x 100 = 35000 150 x 335.4 = 50310 $\boldsymbol{Q_T = 85310mm^3}$	350 x 100=35000 150 x 315.3=47295 $\boldsymbol{Q_T = 82295mm^3}$
Location of N-A from bottom (Z_0)	$Z_0 = \boldsymbol{Q_T \div A_T = 182.26\ mm}$	$Z_0 = \boldsymbol{Q_T \div A_T = 195.93\ mm}$	$Z_0 = \boldsymbol{Q_T \div A_T = 198.16mm}$
Moment of inertia I (x-x)	$b_1{h_1}^3/12 + A_1\,(Z_1 - Z_0)^2 +$ $b_2{h_2}^3/12 + A_2\,(Z_2 - Z_0)^2 =$ $\boldsymbol{I = 7.34\ x\ 10^6\ mm^4}$	$\boldsymbol{I = 5.68\ X\ 10^6 mm^4}$	$\boldsymbol{I = 5.48\ X\ 10^6 mm^4}$

Having determined the properties of the transformed sections, the corresponding bending moment at any given age of the overlay system can be estimated following Figure 6.13. As illustrated in Figure 6.13, the magnitude of the total strain in the composite section is given by:

$$\varepsilon_{sh.free} = \varepsilon_{b,pmc} + \varepsilon_{b,opc} + \varepsilon_{a,opc} \qquad (6.24)$$

From where the bending strain is given by:

$$\varepsilon = y\emptyset = \frac{y}{\rho} \qquad (6.25)$$

Where,

$\varepsilon_{sh.free} = measure\ free\ shrnkage$

$\varepsilon_{b,pmc} = bending\ strain\ in\ PMC\ overlay$

$\varepsilon_{b,opc} = bending\ strain\ in\ OPC$

$\varepsilon_{a,opc} = axial\ strain\ in\ OPC\ if\ not\ fully\ axially\ restrained$

$\emptyset = curvature$

$\rho = radius\ of\ curvature$

$y = distance\ through\ the\ depth\ of\ the\ composite\ section$

Thus, from equations 6.24 and 6.25, it can be written that:

$$\varepsilon_{sh.free} = y_1\emptyset + y_2\emptyset + \varepsilon_{a,opc}$$

So that the curvature $\emptyset$ becomes:

$$\emptyset = \frac{\varepsilon_{sh.free} - \varepsilon_{a,opc}}{y_1 + y_2} \qquad (6.26)$$

If $y_T = y_1 + y_2$ is the lever arm between the points of application of P_{pmc} and P_{opc} as illustrated in Figure 7.13(b); then equation 6.26 can be re-written as:

$$\emptyset = \frac{\varepsilon_{sh.free} - \varepsilon_{a,opc}}{y_T} \qquad (6.27)$$

Therefore by considering force equilibrium, it follows that:

$$P = \sigma A = \varepsilon_{a,pmc}(EA)_{pmc} = \varepsilon_{a,opc}(EA)_{opc}$$

$$\therefore\ \varepsilon_{a,opc} = \frac{\varepsilon_{a,pmc}(EA)_{pmc}}{(EA)_{opc}} \qquad (6.28)$$

Where,

$(EA)_i = axial\ stiffness\ of\ an\ ith\ material\ in\ the\ composite$

$\varepsilon_{a,pmc} = net\ strain\ in\ the\ pmc\ following\ tensile\ stress\ in\ equation\ 6.15 = \frac{\sigma_{a,pmc}}{E_{pmc}}$

Thus, combining equations 6.27 and 6.28, the curvature given in equation 6.27 can now be written as:

$$\emptyset = \frac{\varepsilon_{sh.free} - \left(\frac{\varepsilon_{a,pmc}(EA)_{pmc}}{(EA)_{opc}}\right)}{y_T} \qquad (6.29)$$

The final curvature given in equation 6.29 can subsequently be considered relative to its associated bending moment, following equation 6.30, where:

$$\frac{M}{I} = \frac{E}{\rho} \qquad (6.30)$$

And the resulting bending moment yields,

$$M = \emptyset(IE)_0 \qquad (6.31)$$

Where,

$M = induced\ bending\ moment\ due\ to\ composite\ curvature$
$(IE)_0 = bending\ stiffness\ of\ the\ composite\ section$

The bending stiffness $(IE)_0$ of the composite following Figure 6.15 is generally given by:

$$(IE)_0 = (EI)_{pmc} + (EI)_{OPC} + (Z_1 - Z_0)^2(EA)_{pmc} + (Z_2 - Z_0)^2(EA)_{opc} \quad (6.32)$$

Thus, in Figure 6.15, where the PMC layer is transformed into an equivalent OPC layer, it follows that the new OPC layer must have the same bending stiffness as the actual PMC layer; consequently, it can be written that:

$$(EI)_{pmc} = (EI)_{opc} \quad (6.33)$$

$$\therefore\ I_{pmc} = \left(\frac{E_{OPC}}{E_{pmc}}\right) I_{opc} \quad (6.34)$$

Combining equations 6.22 and 6.34, it follows that:

$$I_{pmc} = n\, I_{opc} \quad (6.35)$$

By using equations 6.29, 6.31, 6.35 and values of I_{opc} given in Table 6.8, the corresponding moments of inertia of the overlay PMC (I_{pmc}), the composite bending stiffness $(EI)_0$, and the bending moment values for each specified age of the composite can be computed as illustrated in Table 6.9.

Table 6.9: Bending parameters of the composite section

Bending parameters	*Age 3*	*Age 28*	*Age 90*
Moment of inertia I_{pmc} (x-x)	$I = 1.733 \text{ x } 7.34 \text{ x } 10^6 = 12.72 \text{ x } 10^6\ mm^4$	$I = 1.118 \text{ x } 5.68 \text{ x } 10^6 = 6.35\ X\ 10^6\ mm^4$	$I = 1.051 \text{ x } 5.48\ X\ 10^6 = 5.76\ X\ 10^6 mm^4$
bending stiffness $(EI)_0$	$(EI)_0 = 3.76 \text{ x } 10^{11}\ Nmm^2$	$(EI)_0 = 3.53 \text{ x } 10^{11}\ Nmm^2$	$(EI)_0 = 3.51 \text{ x } 10^{11}\ Nmm^2$
Curvature ($\emptyset$)	$\emptyset = 1.81 \text{ x } 10^{-7}/mm$	$\emptyset = 1.31\ x\ 10^{-6}/mm$	$\emptyset = 1.43\ x\ 10^{-6}/mm$
Bending Moment (M)	$M_b = \emptyset(IE)_0 = 0.068KNm$	$M_b = \emptyset(IE)_0 = 0.46KNm$	$M_b = \emptyset(IE)_0 = 0.50KNm$

From the estimated bending moment values given in Table 6.9, the corresponding bending stresses at critical locations of the composite can be determined. In this respect, the bending stress at any location in the OPCC layer corresponds to:

$$\sigma_{x,opc} = -\frac{My}{I_{opc}} \qquad (6.36)$$

So, that the bending stress at any location in the BRCFRPMC layer will be given by:

$$\sigma_{x,pmc} = -\frac{My}{nI_{opc}} \qquad (6.37a)$$

Or,

$$\sigma_{x,pmc} = -\frac{My}{I_{pmc}} \qquad (6.37b)$$

Where,

$$y = positive\ distance\ lying\ above\ the\ N-A\ or\ negative\ distance\ lying\ below\ the\ N-A$$

Following these sign conventions, and the values of I_{opc}, I_{pmc}, and M_b given in Tables 6.8 and 6.9, Table 6.10 can be drawn to illustrate the numerical values of the bending stresses at critical locations of the composite.

Table 6.10: Bending stress at critical locations of the BCO composite

Location	*Distance y from N-A (mm)*	*Bending stress Age (MPa)*
PMC top at age		
3	*216.74*	*-1.16*
28	*204.07*	*-14.78*
90	*201.84*	*-17.52*
PMC bottom at age		
3	*116.74*	*-0.63*
28	*104.07*	*-7.54*
90	*101.84*	*-8.84*
OPC top at age		
3	*116.74*	*-1.08*
28	*104.07*	*-8.43*
90	*101.84*	*-9.29*
OPC bottom at age		
3	*-183.26*	*1.70*
28	*-195.93*	*15.87*
90	*-198.16*	*18.08*

Form Table 6.10, it is clear that bending deformation might not be critical to the overlay portion of the composite since it lies in the compression zone. The possibility of tensile cracking developing is therefore not feasible. However, it is expected that the substrate OPCC will take most of the flexural stresses, and can be highly critical in instances where the substrate is not firmly supported by the soil foundation or is not in excellent to fairly good condition before considering bonded overtopping option.

For ease of representation therefore, the respective axial and bending stress distributions together with their combined stress envelop are given Figure 6.16.

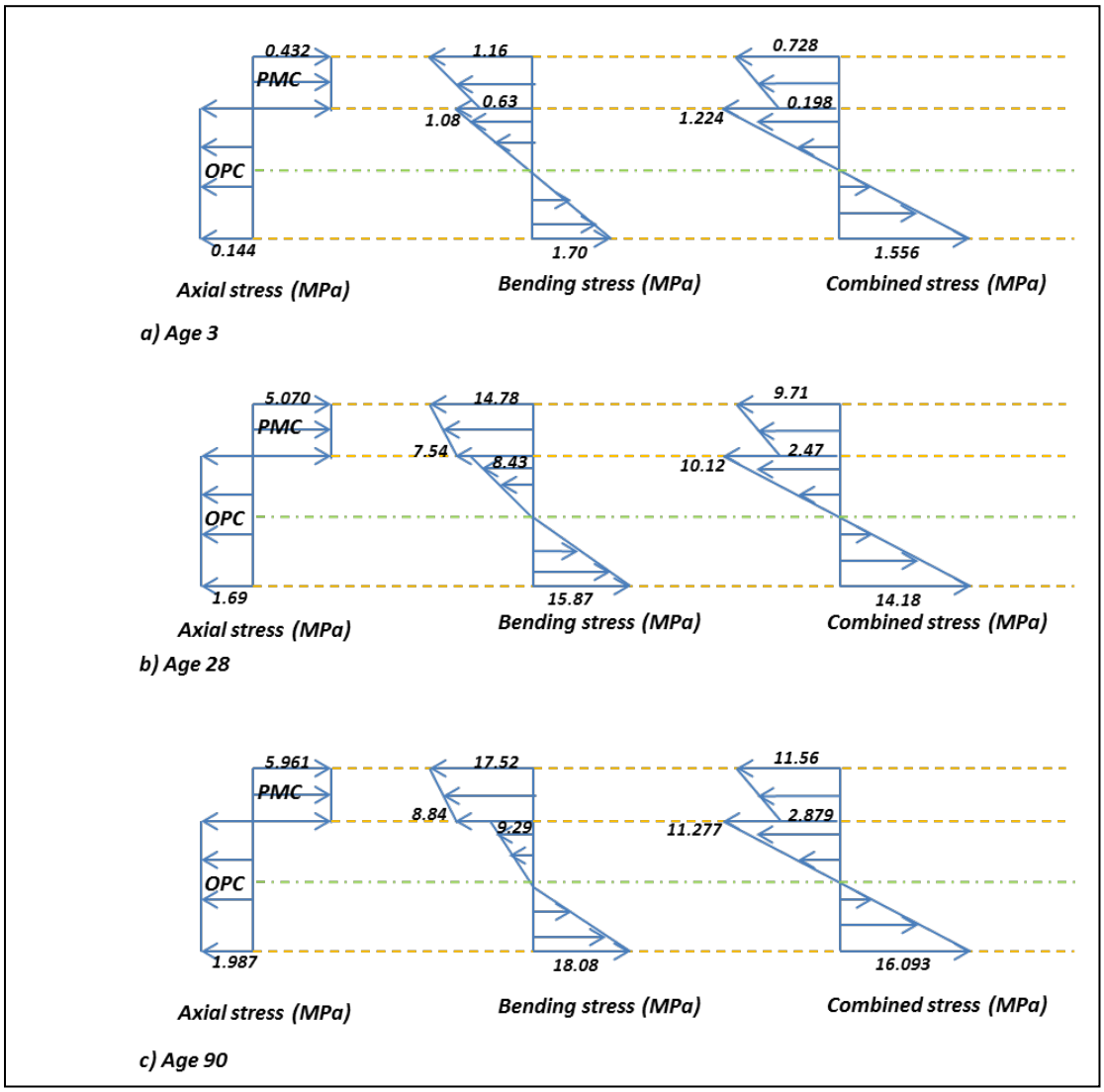

Figure 6.16: Axial, Bending, and combined stress distributions

As clearly seen in Figure 6.16, the stress gradient through the BCO system is illustrated. The combined stress envelopes indicate that compressive bending stress appears dominant in the overlay, while the bulk of the tensile stresses are transferred to the bottom of the underlay. At critical tensile load in the underlay, flexural cracks initiate, and as circumstances under cyclic structural and environmental actions permit, a possible through crack to the region of interface may develop and subsequently initiate delamination or reflect through the overlay; depending on the fracture toughness of the concerned zones.

At this juncture, it can be inferred that flexural strength of the underlay plays a vital role while considering bonded concrete overlay solution. In the above illustration in Figure 6.16, it is expected that the substrate OPCC must be sufficiently strong to resist flexural strength,

up to and above $16MPa$; though a firmly placed soil foundation support is expected to lessen the effect of such flexural tensile response.

This chapter presents the laboratory test methods for evaluating the interfacial bond capability of the optimum designed overlay material. Both tensile and shear bond strengths were established based on relevant codes of practice. Result were presented, analysed and discussed accordingly. In addition, stress transfer capacity of the interface was also assessed based on various code requirements. The overall assessment results showed that the overlay material exhibits good bonding with the substrate OPCC and would be able to withstand substantial stresses where sufficient surface texture is provided for aggregates interlocking.

In addition, supplementary material properties of the optimum designed overlay material were evaluated concurrently. The properties included its tensile strength, coefficient of thermal expansion, and drying shrinkage. Stresses in the overlay, substrate, and at the interface were assessed analytically under various differential movement related conditions. As illustrated, though the interface and the overlay material exhibit sufficient strength against thermal and shrinkage cracking, the theoretical shrinkage cracking in the overlay was predicted at 6.92MPa when fully restrained axially.

7.0 Interfacial Fracture Process Modelling and Analysis

7.1 Determination of Tensile fracture Parameters

In this section, the interface fracture process is implemented via laboratory captured fracture experiments and numerical modelling and analysis. The whole process presented here follows the interface cohesive model described for a bonded contact surface described in chapters 3 of this thesis. The objective of this chapter is to describe the progressive fracture process of the interface under monotonic loadings.

For the Mode I fracture test, wedge splitting test (WST) method was adopted. Generally, the test method is a stable fracture mechanics test capable of measuring tensile fracture parameters, especially the fracture energy, since it traces the complete load-displacement

history of the test specimens beyond their peak loads. The specimens usually are compact in size and do store little elastic energy.

Due to bond requirements characterising this study, common cubical shaped specimens were used while bonding the optimal BRCFRPMC on the substrate OPCC. As illustrated in Figure 7.1. The set-up requires casting or sawing an initial groove and a notch through its top edge. A vertical or compressive load is then applied through which a horizontal tensile force is induced via the wedge / rollers contact mechanism to cause splitting on the test specimen. In this case, the friction between the wedge and the contacting rollers is negligible, thereby simplifying the splitting force estimation.

Figure 7.1: Schematic of a wedge splitting test specimen (Brühwiler and Wittmann, 1990)

In the Figure 7.1 above, because the experiment is usually controlled monotonically by increasing the displacement until the sample fails, the complete applied load vs. crack opening displacement data can be capture via the computer data logging device connected to the load cell and the clip gage placed at the top-mouth of the notch. In the current study, the loading rate of 0.0016mm/s was used and maintained for all test specimens throughout the experiment.

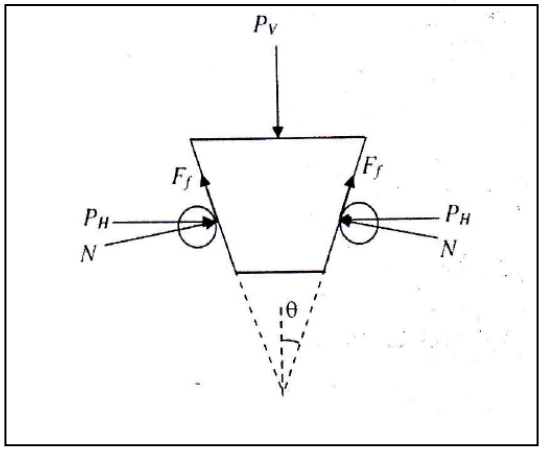

Figure 7.2: Wedge splitting force diagram

From Figure 7.2, under a condition of frictional reaction, the splitting force (P_H) is related to the applied load (P_V) via equation 7.1:

$$P_H = \frac{P_V}{2tan\theta}\left(\frac{1-\mu tan\theta}{1+\mu tan\theta}\right) \qquad (7.1a)$$

Or,

$$P_H = \frac{P_V}{2tan\theta}\left(\frac{1}{1+\mu cot\theta}\right) \qquad (7.1b)$$

Where,

$P_H = horizontal\ splitting\ force\ (KN)$

$P_V = vertical\ compressive\ load\ (KN)$

$\theta = wedge\ angle\ in\ degree$

$\mu = coefficient\ of\ friction$

Often, because the frictional reaction between the wedge and the rollers is small, its effect can be eliminated from equation 7.1, thereby reducing the expressions given in equation 7.1 to that of 7.2:

$$P_H = \frac{P_V}{2tan\theta} \qquad (7.2)$$

In this research, the adopted set-up is illustrated in Figure 7.3, and due to non-availability of a standard set-up as those depicted in Figure 7.1, it became necessary to account for the effect of friction.

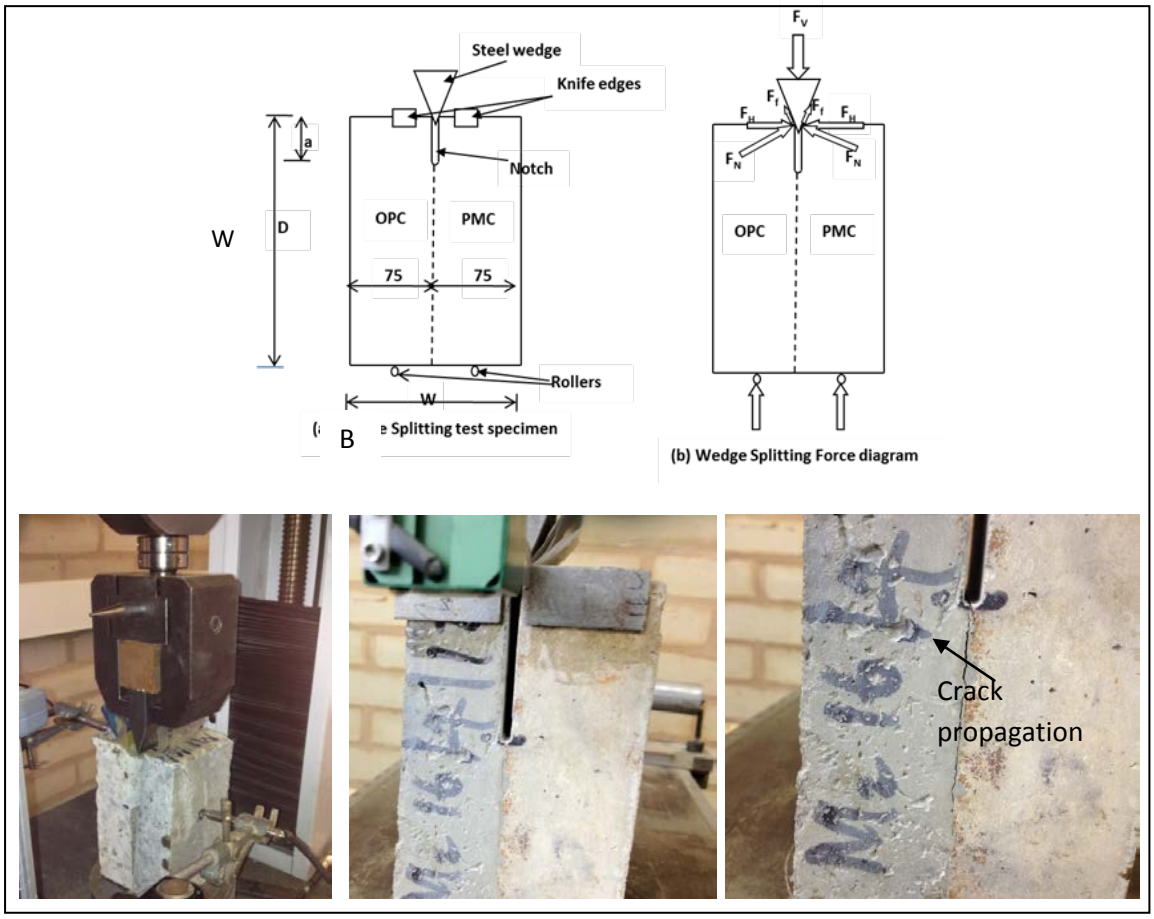

Figure 7.3: Wedge splitting set-up

In the set-up shown in Figure 7.3, a steel wedge was held rigidly between the machine adjustable claws which was positioned mid-way of the specimen's notched mouth via which compressive load was applied to induce a splitting force as the wedge pushed the notched walls sideways. The loading method followed the conventional wedge splitting testing in which the specimen's loading is controlled by the displacement clip gage placed in between the knife edges at the load application line (wedge/notched walls).

The wedge angle was approximately 19.3^0, while the specimen's depth (D), width (W) and thickness (B) were 150, 150, and 75 mm respectively. The initial notch length of 45mm was maintained for all specimens, resulting from the initial finite element notch sensitivity analysis, thus giving a total 105mm depth bonded ligament. Details of the finite element analysis (FEA) are given in section 7.3. Note also that, the presence of two roller supports shown in Figure 7.3 helps eliminate the effect of self-weight on the result during overturning at failure.

Considering the effect of texture, only one degree of surface texture (2.316mm) was implemented following previous findings that bond response at this texture level provides reliable and satisfactory values as those required in the codes. In terms of age however, both early and matured-age, that is 3 and 28-day fracture were tested respectively. In addition, for each combination of age and texture, three replicates were implemented.

By using equation 7.1, the magnitude of the horizontal splitting force relative to CMOD was estimated. Figure 7.4 presents the representative curves from this test. Note, in most structural codes and guidelines such as PCI design Handbook and Australian Bridge design code, the coefficient of friction between steel and hardened concrete generally ranges between 0.4 and 0.5. Thus, in this work, 0.45 was arbitrarily adopted.

In order to estimate the interface fracture energy, the analysis followed the procedures given below:

- The P_H was determined from equation 7.1, using $\mu = 0.45$,
- The P_H vs. CMOD was plotted, and the area under the graph was calculated, which represents the work of fracture,
- The fracture energy was determined by dividing the work of fracture by the area of the bonded ligament.

Following the above procedures, the graphs presented in Figures 7.4 and 7.5 correspond to 3 and 28-day fracture tests respectively.

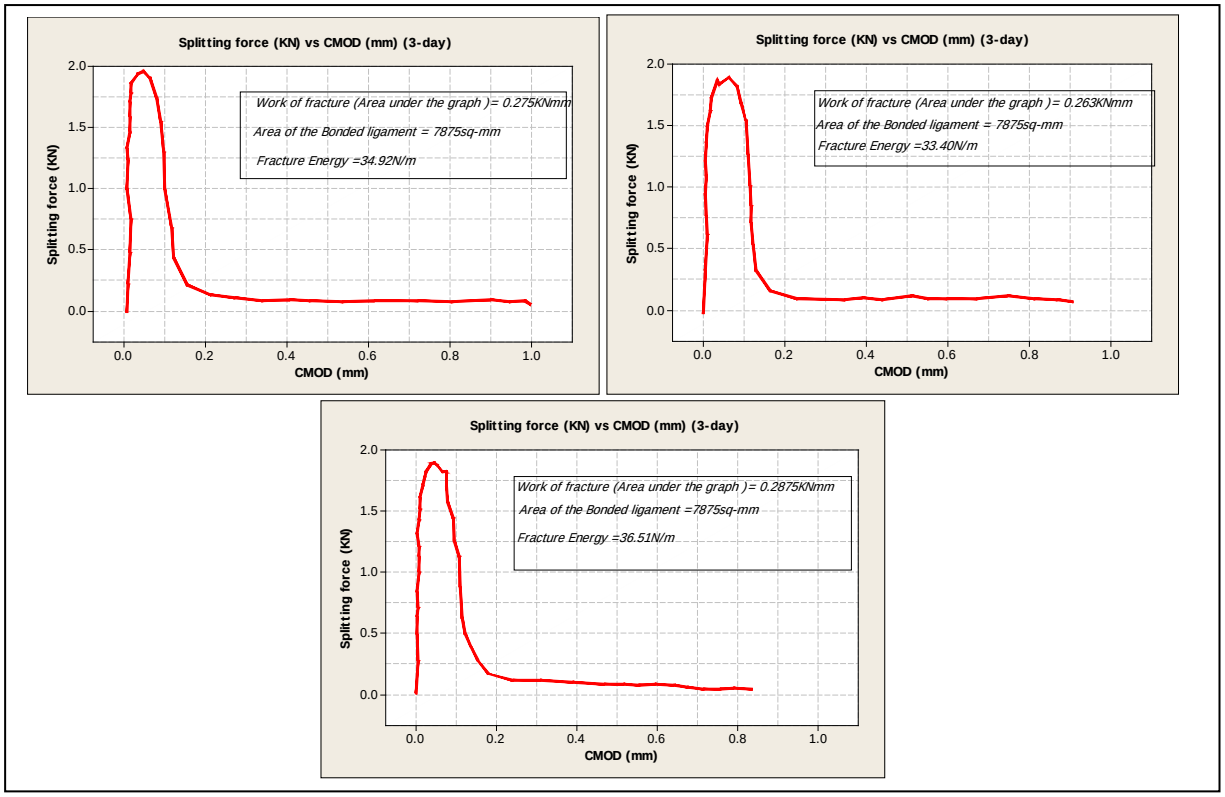

Figure 7.4: Splitting Force – Crack mouth opening displacement curve (3-day)

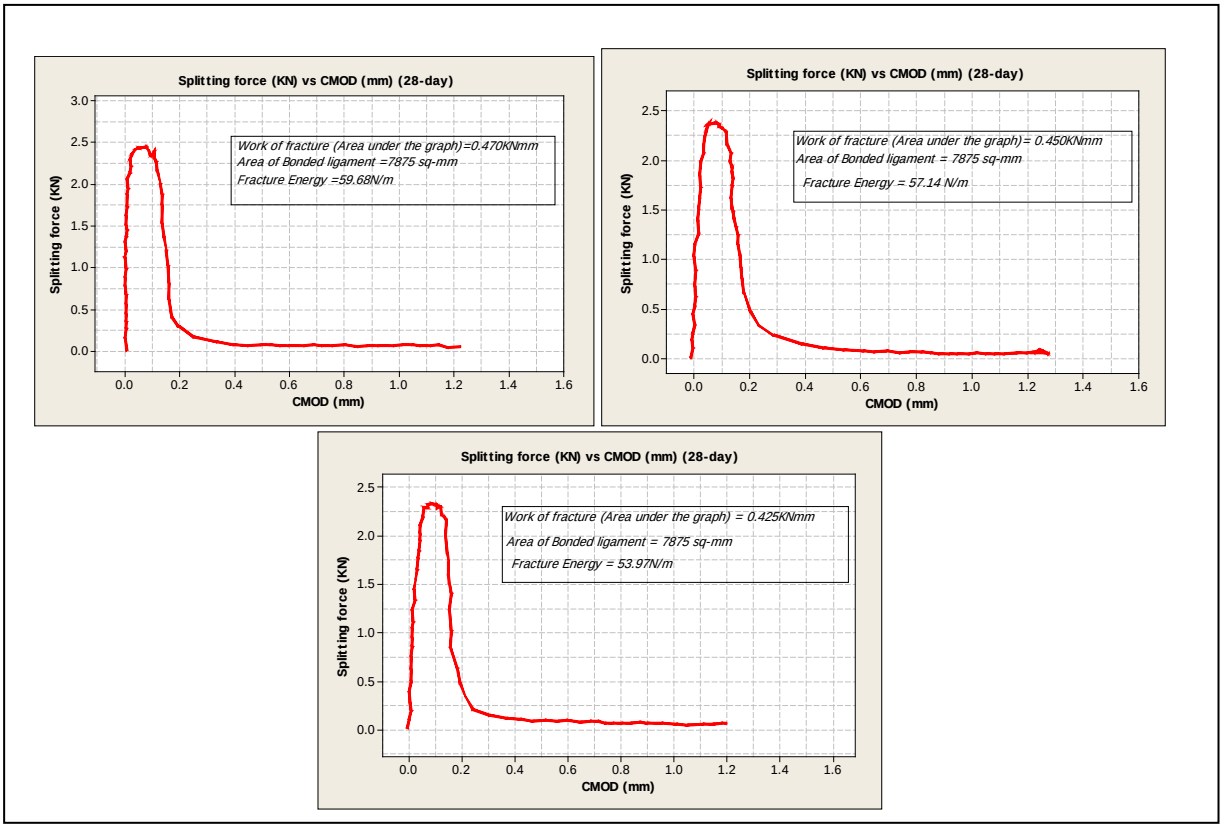

Figure 7.5: Splitting Force – Crack mouth opening displacement curve (28-day)

In Figure 7.4, the splitting force at 3-day ranges between 1.87 and 1.91KN, while the resulting fracture energy (G_F) is estimated within the range $34.96 \pm 1.56 N/m$. On the other hand, the 28-day interface response shown in Figure 75 yields average splitting force of 2.35KN with fracture energy in the range of $56.82 \pm 2.85 N/m$.

No doubt, the values shown here for both early and matured-age are small in magnitude compared to those published values for bulk (single) cementitious materials, which can be in upward of $100 N/m$ (Kishen and Saouma, 2004). However, when compared with bonded specimen results recorded by Kishen and Saouma (2004), for limestone-Concrete interface, a positive correlation exists.

In the single bulk specimens, a perfect bond condition is often assumed; while bonding at the interface is more or less characterized with defects. In this respect, in bonded materials, bond imperfection at the interface remains a major challenge confronting design engineers; hence, techniques for enhancing bonding and fracture energy are in high demand globally.

Moreover, while definite structural failure criteria in terms of material strength for the interface are well established in various codes and design guidelines, requirements for structural fracture are vague and vary circumstantially. Hence, the applications of fracture mechanics approach are mostly employed to describe the progressive propagation process of failure rather than defining failure initiation criteria. On this basis, there are no established design values to compare the above experimental values with; therefore, the fidelity of their strength lies in published literature.

As illustrated in Figures 7.4 and 7.5, it is observed that the fracture energy increases with age which agrees with general observations in the literature. In Bordelon (2007) for instance, it is clear that bulk plain concrete materials are likely to develop sufficient fracture properties, up to 85% in 28 days which in a way correlates with the development of their compressive strengths. However, only about 40% - 50% of their 28-day's fracture energy is likely to develop within 7 days. In this study, considering the values given in Figures 7.4 and 7.5, the fracture energy recorded for 3-day represents about 61.53% of the 28-day's value, which also agrees well with those found in other publications - Zhang et al (2008) and Lim et al (2001).

7.2 Determination of Shear Fracture Parameters

In this section, L-prism specimens were employed as a basis for fracture parameter measurement in terms of shear stress and shear slip. Precisely, the L-prism provides reasonable slip measurement when compared to cylinder specimens. The initial attempt of using cylinder specimens was borne out of the intention of ensuring similar specimen shape for fracture test as those used for stress criterion tests in section 6.0.

Though, the initial finite element analysis illustrated in Figure 7.6 shows that cylinder specimens are likely to yield a more uniform interface stress condition compared to L-prism; means of measuring and obtaining reasonable interfacial slip was however elusive.

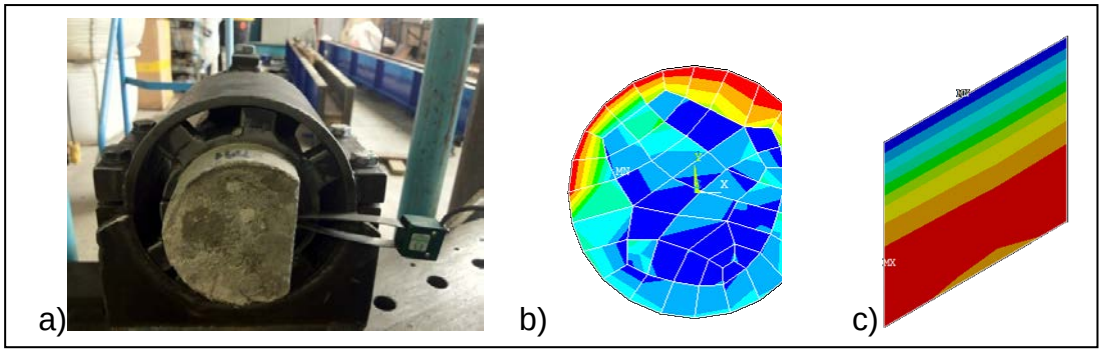

Figure 7.6: a) Direct Cylinder shear test with clip gage and interface stress distribution contours for (b) cylinder specimen and (c) prism specimen

From Figure 7.6b, aside the point of application of load marked in red for the cylinder specimen; relatively, its interface stress distribution contour is more uniform compared to the one resulting from the L-prism. But from experience, for purposes of interface slip measurement, the use of L-prism seems more attractive.

In this respect, the L-prism introduced by Liu *et al*. (1985) was considered; knowing that it has been extensively used for shear transfer across the interface in Mode II fracture testing. Further, in L-prism specimens, research (Watkins and Liu, 1985) has also shown that keeping the lap/depth (a/W) ratio within 0.25 as shown in Figure 7.7 would help achieve a more smooth shear stress distribution. Hence, the specimens used in this work were kept within this limit.

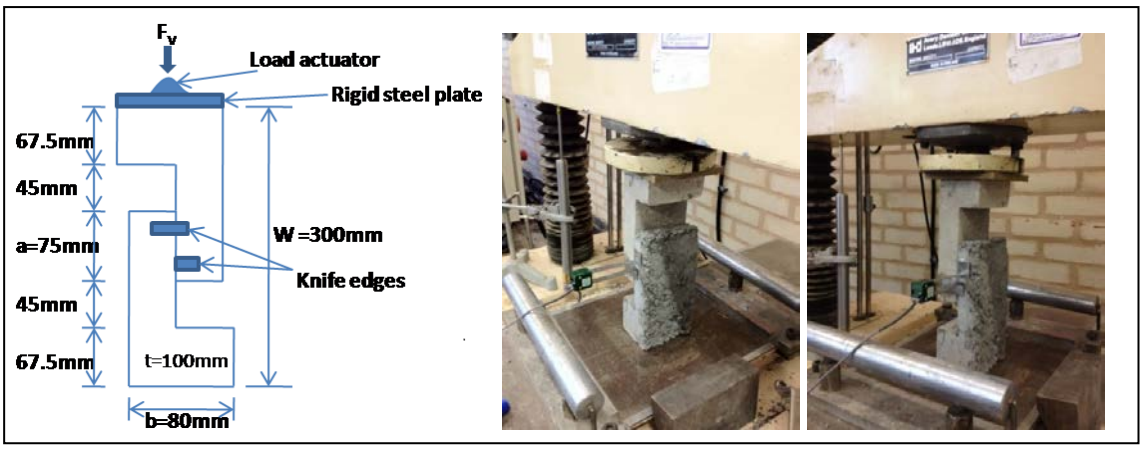

Figure 7.7: Direct L-Prism shear test with clip gage

As shown in Figure 7.7, loading was controlled by clip-displacement at 0.02MPa/s, positioned adjacent to the plane of the interface until failure. The resulting representative load vs. slip responses for ages 3 and 28 are given in Figure 7.8.

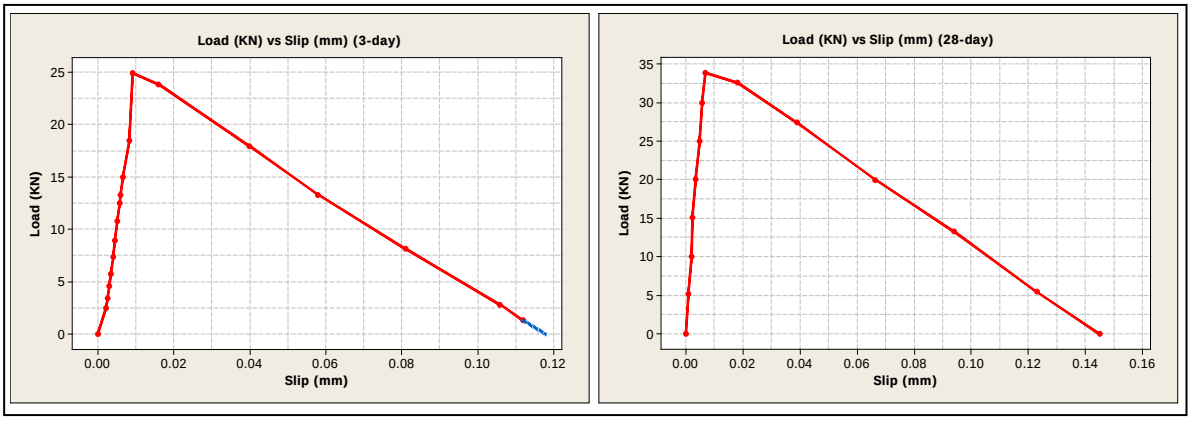

Figure 7.8: L-Prism Interface Load – Slip Response at 3 days and 28 days

From Figure 7.8, the average response in both cases is similar, except that the loss of bond stiffness at the interface did not reduce completely to zero in two out of three specimens tested at 3 days. Also, the observed average peak loads differ by about 9KN, which represents about 35.8% increment in bond strength development between 3 and 28 days.

Reproducing the above responses in form of their corresponding shear stresses, Figure 7.9, was used to estimate the fracture energy in Mode II directly as a fraction of the total area under the curve.

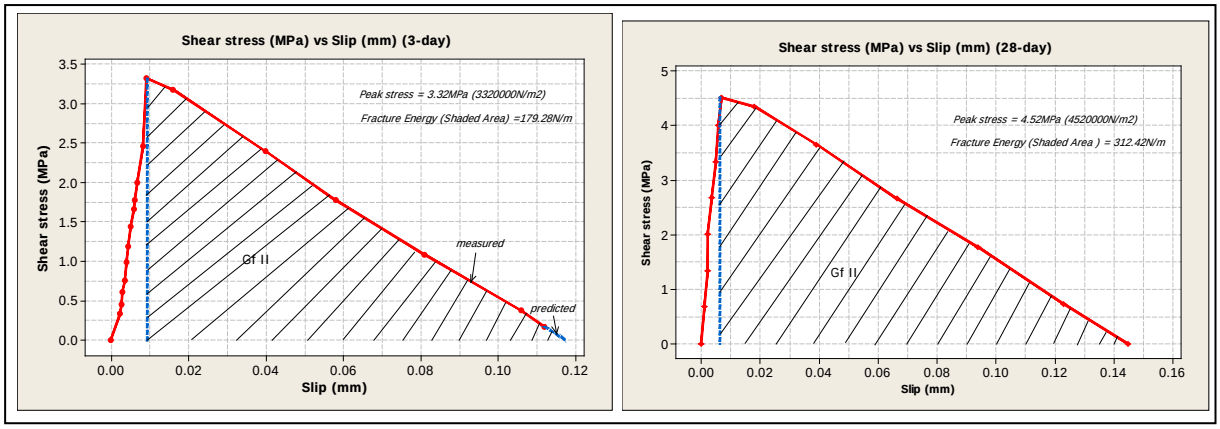

Figure 7.9: L-Prism Interface Shear stress – Slip Response at 3 days and 28 days

In Figure 7.9, the initial ascending part of the curves experiences some measure of machine instability, but gradually eases out towards the peak stress region. In most experimental work of this nature, the interface is expected to respond linearly up to about 40% of its peak stress after which the remaining part of the response assumes nonlinearity up to the peak stress where strain localization occurs. Beyond this point, the interface loses bond gradually, though still able to transfer some degree of stresses as the two materials slip relatively up to a critical point of delamination (crack) where bond is completely broken and the stress comes to zero.

The measured fracture energies in Mode II in these two cases fall within $171.51 \pm 7.77 N/m$ and $307.29 \pm 5.13 N/m$ for three replicates each at 3 and 28 days respectively.

As demonstrated above, it is evident that the fracture energy in Mode II is by far greater than that of Mode I in the order of about 490% and over, hence it can be concluded that the interface is more likely prone to delamination in tension than in shear.

From the tensile and the shear fracture tests described above, sufficient parameters to characterize the interface for numerical delamination modelling and analysis are obtained. In the subsequent sections, numerical methods are employed based on the experimental data to describe delamination failure process in pure Mode I and Mixed-Mode failures.

7.3 Numerical Modelling and Analysis

7.3.1 Optimum Notch Size Selection

As mentioned earlier in section 7.1, prior to choosing an optimum notch length for the laboratory test specimens adopted for Mode I fracture test, an initial or preliminary notch sensitivity test was implemented using a 2D FEA. The analysis follows an interface cohesive zone model, requiring one to specify the interface cohesive strength, the allowable crack opening, and the elastic material properties for the bonded materials.

The use of 2D analysis is generally preferred to that of 3D for ease of investigating and monitoring locally changes occurring at the interface due to both notch and material properties variations. The analysis assumes a plane strain condition.

In details, the following arbitrary values were specified to characterise the cohesive elements which defined the boundary between the two contacting materials:

- The cohesive tensile bond strength = 1MPa
- The critical crack opening = 0.01mm
- The allowable shear bond strength = 2MPa
- The allowable bond slip = 0.02mm

Note here that by specifying shear parameters for the interface as indicated above, a Mixed Mode failure common with bonded dissimilar materials is assumed, though the failure is predominantly a Mode I failure. Apparently, the higher shear failure parameters specified for the model were intently and discretionarily chosen so as to permit the interface to yield in Mode I prior to attaining its critical Mode II failure criteria.

The elastic material properties for the optimum BRCFRPMC and OPC were selected based on the experimentally obtained values given in chapter 6 of this thesis. These values are hereby presented in Table 7.1.

Table 7.1 Material Properties for PMC and OPC

Bulk Material	Elastic Modulus - 28-day (N/ mm^2)	Poissson's Ratio	Density (g/mm^3)
RCFRPMC	19950	0.25	0.002412
OPC	22300	0.18	0.002400

NB: The densities were specified to account for the self-weight of the test specimens.

The 2D geometry of the model shown in Figure 7.10 follows the one given in Figure 7.3 (a & b), with variable notch length of 0, 10, 20, 30, 40, 50, 60 and 70mm, tested consecutively after a preliminary mesh size test. Note, a constant 5mm mesh size was afterward chosen and maintained for all the test specimens.

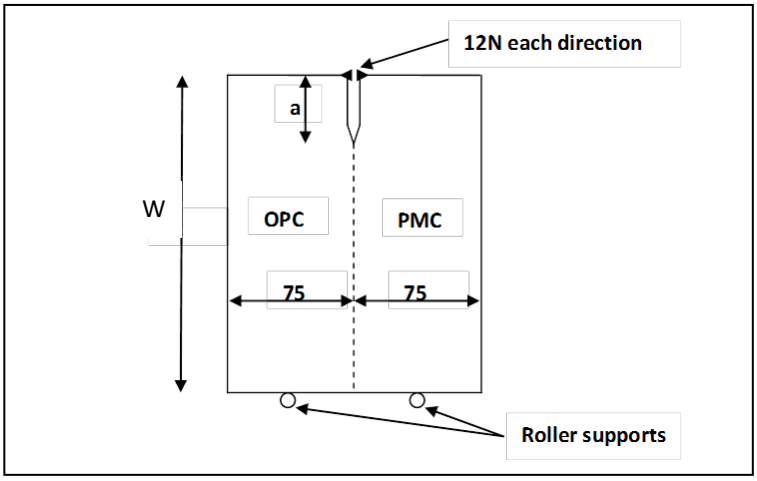

Figure 7.10: 2D Wedge Splitting specimen

From Figure 7.10, the boundary constrains due to roller supports were specified using a zero displacement value (i.e. UY = 0), while the top inner-face sides of the interface were subjected to 12N in each direction. Note, the magnitude of the load was selected through a trial and error method to ensure that a reasonable level of damage would occur at the interface to propagate the initially induced notch or initiate a crack in the model where no crack exists (i.e. a = 0).

Note, the condition of zero-notch was not implemented in the laboratory due to its difficulty, but has been included in this preliminary test to investigate the relative response between a perfectly bonded specimen (condition) and a defective specimen. In this respect, the full

delamination process or history, beginning with interface de-bonding formation to its propagation, can be collectively represented, defined, and described.

Table 7.2 presents the result of the numerical analysis.

Table 7.2 Interface Notch sensitivity Result table

Notch Length (mm)	Relative size (a/W)	Interface Cohesive stress (N/ mm^2)	Relative Interface Stress	Lateral Tensile stress(N/ mm^2)	Lateral Compressive stress (N/ mm^2)
0	0.00	1.13	1.00	1.09	0.32
10	0.07	1.06	0.94	1.07	0.29
20	0.13	1.03	0.91	1.02	0.28
30	0.20	1.04	0.92	1.02	0.31
40	0.27	1.04	0.92	1.02	0.42
50	0.33	1.03	0.91	1.01	0.53
60	0.40	1.13	1.00	1.15	0.65
70	0.47	1.59	1.41	1.54	0.79

From Table 7.2, it is observed that the interface cohesive stress changes with notch size, once interfacial crack has initiated or propagated, depending on the initial specimen condition. The general regression curve and equation defining the relationship between the relative interface stress and that of the notch size is represented in Figure 7.11.

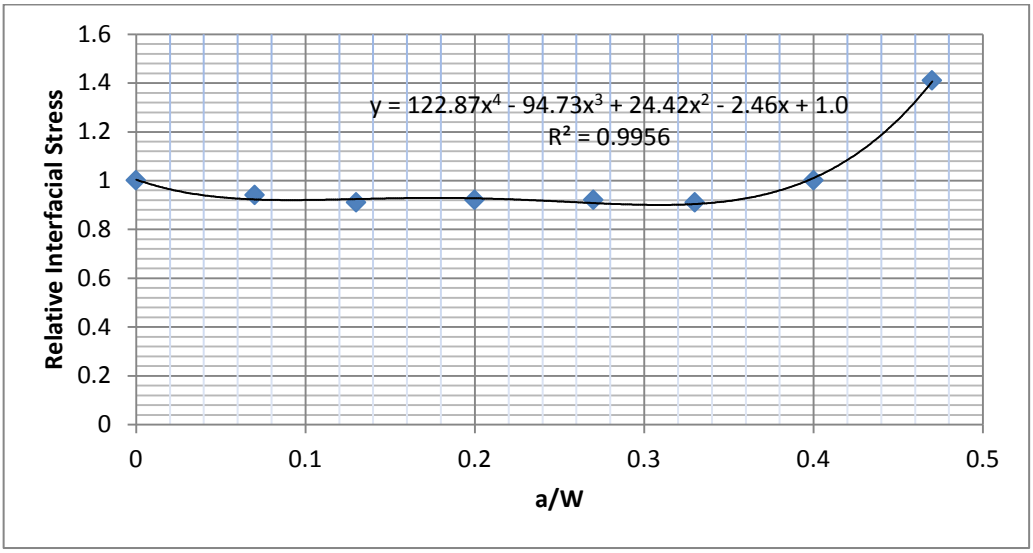

Figure 7.11: Notch-Size Sensitivity Curve

The curve as illustrated was fitted with a fourth-degree polynomial equation which yielded an R-sq. value of about 0.99. In the curve, it is clear that the interface cohesive stress

decreases nonlinearly relative to notch-size between 0 and 0.13. Afterwards, the interface attains an equilibrium stress state for notch lengths ranging between 20 and 50mm. Beyond this range, a noticeable increase in stress was recorded.

For each test undertaken, three stress conditions were investigated relative to one another: the interface cohesive stress (σ_0), the two stresses developing in the bulk materials principal directions, mainly those resulting parallel (σ_x) and perpendicular (σ_y) to the direction of the applied load.

From the eight tests represented in Table 7.2, the effects of lateral bending stresses (i.e. both compression and tensile) on the interface is apparent. The trend of changes of these stresses relative to that of the interface is of particular interest. Thus, the following results are presented to show the relative effects of these stress conditions on the overall response of the interface

Lateral Bending Stress Contour	Interfacial Cohesive Stress Contour
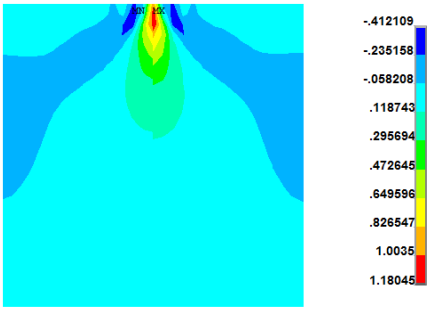 Notch size: 0mm	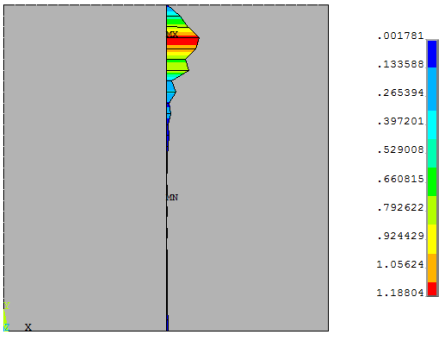 Notch size: 0mm
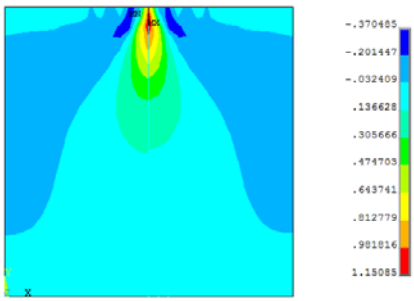 Notch size: 10mm	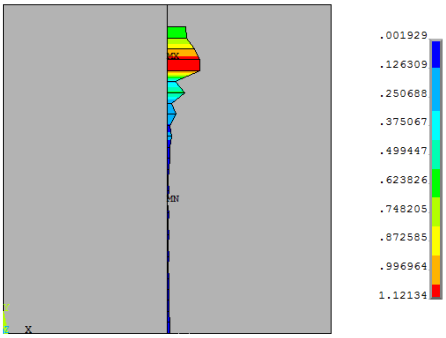 Notch size: 10mm
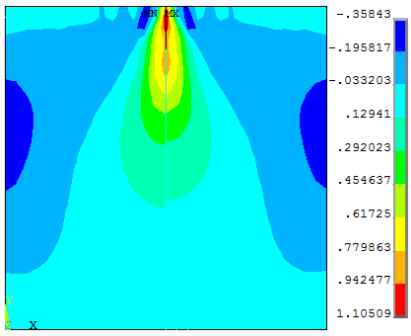 Notch size: 20mm	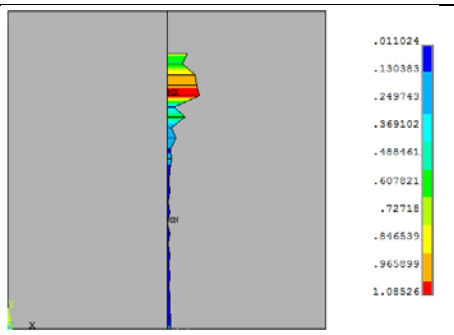 Notch size: 20mm

Figure 7.12: Relative Effects of Notch-size and Lateral Bending on Interface cohesive stress conditions (0 – 20mm).

From the stress contours shown above, it is observed that the compressive lateral bending stress decreases averagely from 0.32 to 0.28MPa with respect to notch-size. Consequently, the resulting cohesive stress at the interface and that of the tensile bending stress occurring adjacent to the region of the interface decrease accordingly. As seen, the overall effects of this compressive bending stress on the interface changes gradually from its locally induced

high tensile effect within the vicinity of the interface to that of a reduced global effect as curvature effect increases due to increased notch-size which causes bending to localize away from the interface. This agrees with elastic bending theory where bending stress is assumed directly related to curvature. Hence, it is assumed that the regime of the stress curve defined by the relative notch-size, 0 to 0.13, is highly dominated by the notch-size effect.

Lateral Bending Stress Contour	Interfacial Cohesive Stress Contour
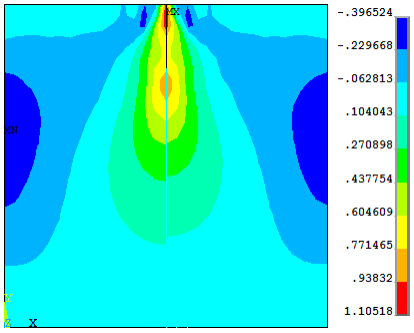 Notch size: 30mm	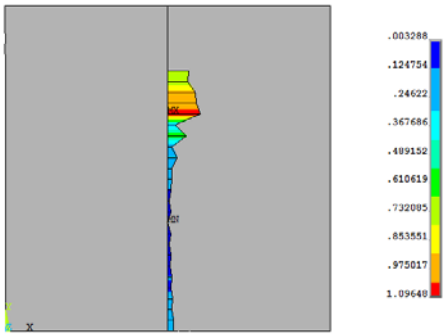 Notch size: 30mm
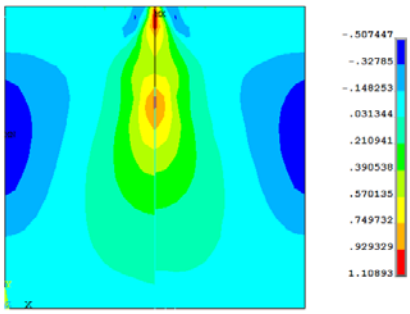 Notch size: 40mm	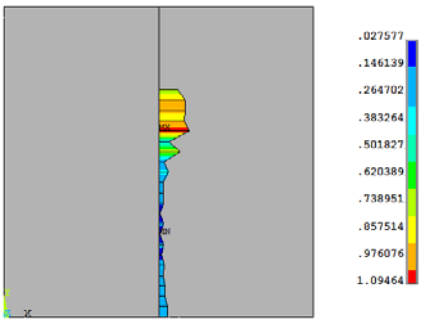 Notch size: 40mm
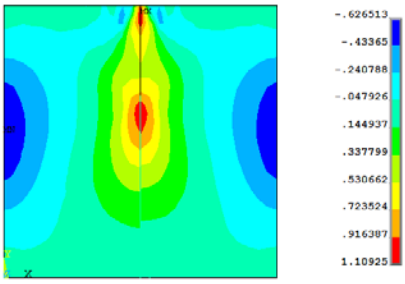 Notch size: 50mm	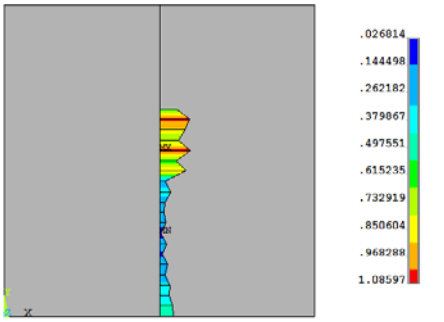 Notch size: 50mm

Figure 7.13: Relative Effects of Notch-size and Lateral Bending on Interface cohesive stress conditions (30 – 50mm).

However, as the global effect of the compressive bending stress increases and and gradually dominates the overall specimen size effects due to increased notch-size, a wider spread of tensile stress was induced and widely distributed at the interface and within its vicinity, thereby keeping the stress condition at the interface in a more stable and uniform state.

The overall interactive response of the stresses at the interface and its vicinity is depicted in Figure 7.14.

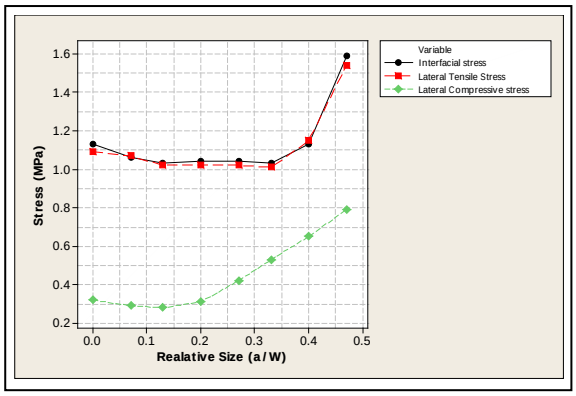

Figure 7.14: Relative Responses of Interface cohesive stress and Lateral Tensile stress to Lateral Compressive stress due to Notch-size

The stable stress state at the interface and its vicinity is expected to vanish as more compressive stress is induced and localizes directly adjacent to the position where cohesive stress occurs under increased notch-size and crack propagation. This condition occurs for notch-size 60 and 70mm, as can be seen in Figures 7.14 and 7.15.

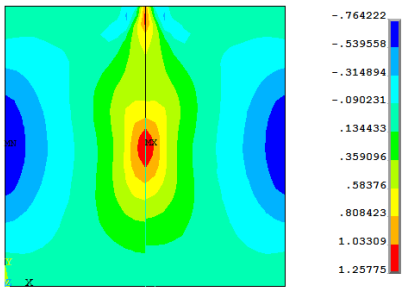

Notch size: 60mm

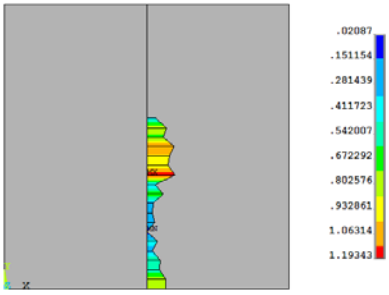

Notch size: 60mm

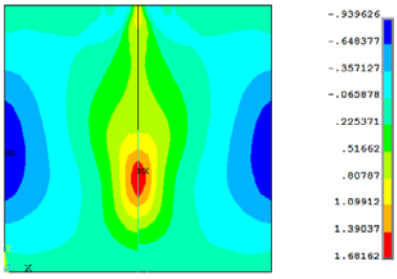

Notch size: 70mm

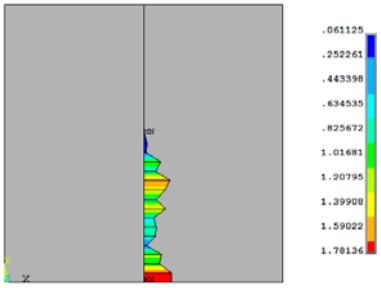

Notch size: 70mm

Figure 7.15: Relative Effects of Notch-size and Lateral Bending on Interface cohesive stress conditions (60 – 70mm).

Clearly, the stable state stress regime defines the range of the optimum notch-size, where notch-size effect is supressed. This bending effect as shown in Figure 7.16 for 50mm notch-size is therefore expected to remain effective or even more dominating for larger notch lengths that are not too far from this range of optimality. In this respect, it makes common sense to assess the responses due to 60 and 70mm notch lengths on this merit. This is so, because with increased notch-size, and in the absence of any lateral bending effect, it is unlikely that a substantial cohesive stress will develop at the interface.

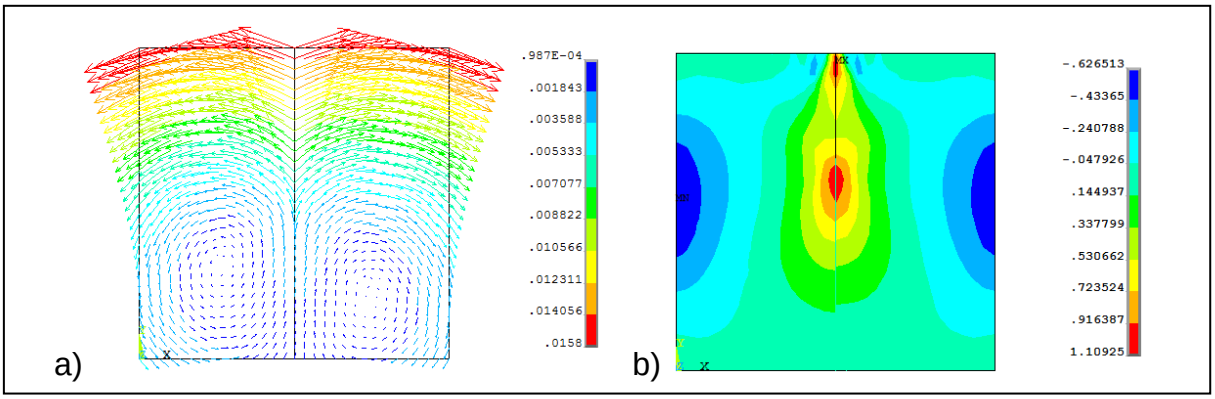

Figure 7.16: Lateral Compressive Effect a) Deformation Vector Plot b) Stress contour Plot

Thus, it is supposed that the continued increase in the stress state at the interface and its vicinity for notch lengths 60 and 70mm illustrated in Figure 8.14 and 8.15 may not be directly connected with the notch-size effect itself, but due to increased compressive bending effect at the far side of the specimen, which consequently is accompanied by increased tensile effect at the interface and its vicinity. Engineering terms, this regime can exclusively be tagged as mainly dominated by compressive bending effects, rather than the combined effects of notch-size and bending. In this respect, three distinct regimes are formed as illustrated in Figure 7.17.

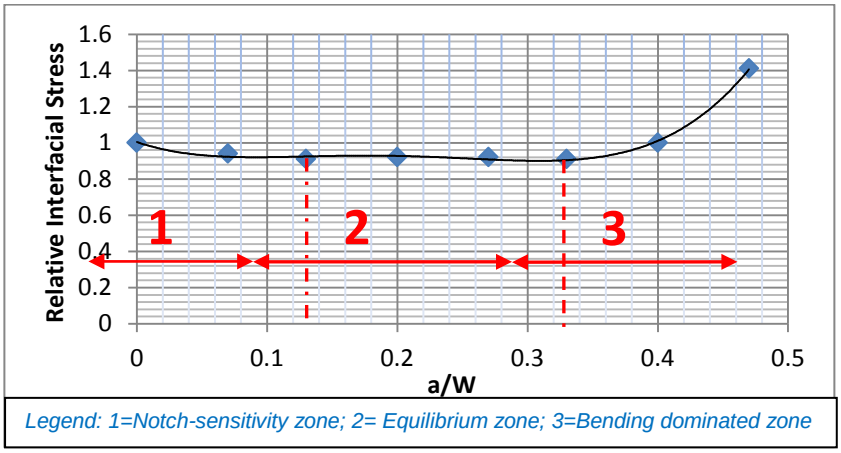

Figure 7.17: Notch-Size Sensitivity Curve

From the curve shown above, the regression equation is given by:

$$y = 122.87x^4 - 94.73x^3 + 24.42x^2 - 2.46x + 1.00 \qquad (7.3a)$$

Where,

$$y = Relative\ interface\ stress = \frac{\sigma_{Ni}}{\sigma_{UN}}(\emptyset)$$

$\sigma_{Ni} = stress\ corresponding\ to\ ith\ noth\ length$

$\sigma_{UN} = stress\ corresponding\ to\ zero\ notch\ specimen$

$\emptyset = f(\alpha, \beta, \frac{a}{W})$

$x = Relative\ specimen\ size = \left(\frac{a}{W}\right)$

$a = notch\ variable\ size\ (mm)$

$W = specimen\ constant\ depth\ (mm) = 150mm$

Therefore, the equation can be re-written as:

$$\frac{\sigma_{Ni}}{\sigma_{UN}}(\emptyset) = 122.87\left(\frac{a}{W}\right)^4 - 94.73\left(\frac{a}{W}\right)^3 + 24.42\left(\frac{a}{W}\right)^2 - 2.46\left(\frac{a}{W}\right) + 1.00 \qquad (7.3b)$$

So that the stresses at the interface for any possible ith notch-size can be expressed as:

$$\sigma_{Ni}(\emptyset) = \sigma_{UN}\left\{122.87\left(\frac{a}{W}\right)^4 - 94.73\left(\frac{a}{W}\right)^3 + 24.42\left(\frac{a}{W}\right)^2 - 2.46\left(\frac{a}{W}\right) + 1.00\right\} \qquad (7.3c)$$

Note here that the expression given in (7.3c) corresponds to the prescribed elastic mismatch between the substrate OPCC and the overlay BRCFRPMC given in Table 7.1. It follows therefore that at different age of the overlay when the elastic properties undergo changes; the expression will change accordingly based on the Dundur's parameters $(\alpha\ and\ \beta)$ given in equation 7.5.

Hence, for every regression equation resulting from a specified elastic mismatch, optimum value for $\left(\frac{a}{W}\right)$ can be estimated by differentiating the regression model and equating the result to zero.

Further, under combined stress conditions due to direct tension and bending discussed earlier, stresses developing at any point along the bonded ligament of the interface can generally be represented by:

$$\sigma_{Ni}(\emptyset) = \sigma_{UN}\left(\frac{P_H}{A} + \frac{My}{I}\right)(\emptyset) \qquad (7.4)$$

Where,

$P_H = horizontal\ force$

$A = area\ of\ the\ bonded\ ligament$

$M = moment\ induced\ by\ P_H$

$I = second\ moment\ of\ area$

$y = distance\ from\ neutral\ axis\ to\ pre-cracked\ tip$, and

$$\emptyset = f(\alpha, \beta, \frac{a}{W}) \qquad (7.5)$$

Thus, as already shown in equations 3.22 and 3.23, using the simplified expressions for Dundur's two parameters for a plane strain problem, the following elastic property table can be drawn for the optimum BRCFRPMC mix at ages 3, 28 and 90 days with respect to the prescribed OPCC elastic properties shown in Table 7.1.

Table 7.3 Measured and Estimated Elastic Mismatch between PMC and OPC

Material	Plane stress E_{pmc} (GPa)	Plane strain E'_{pmc} (GPa) (Estimated)	Poisson's Ratio (Measured)	Poisson's Ratio (Estimated)	$\frac{E'_{pmc}}{E'_{opc}}$	α
PMC 3-day	12.87	14.71	-	0.354	0.638	-0.221
PMC 28-day	19.95	21.28	0.25	-	0.923	-0.040
PMC 90-day	21.22	22.38	-	0.228	0.971	-0.051
OPC	22.30	23.05	0.18	-	-	-

Note here that the estimated Poisson's values shown above were obtained by setting the Dundur's second parameter (β) at constant value of 0.014, which corresponds to the measured elastic properties mismatch between BRCFRPMC and OPCC in Tables 7.1. This approach is commonplace in numerical work of this nature if it is assumed that the effects of β is secondary (Mei *et al*, 2007).

From the above, a direct graphical estimate for Dundur's paramount parameters (α) can be made relative to the ratio of elastic moduli of the bi-material; which may be viewed as age-history curve, as elastic properties of BRCFRPMC change with time.

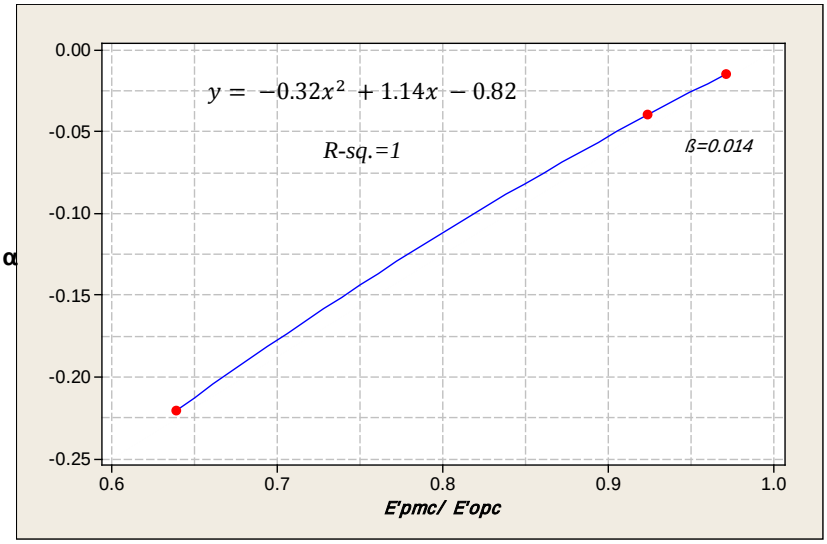

Figure 7.18 Dependence of α on Ratio of Elastic Moduli

As shown in Figure 7.18, it is clear that α increases as the ratio of the elastic modulus of the overlay BRCFRPMC to that of substrate OPC increases. Often, due to the relevance of elastic moduli, α is regarded as paramount in studies involving elastic response of bi-material interface. In the on-going discussion, the effects of the changes in α for ages 3, and 90 days are illustrated in Table 7.4.

Table 7.4: Variation of Relative stress by Dundur's first paramount parameters (α)

Relative size (a/W)	$Relative\ stress$ (α_3)	$Relative\ stress$ (α_{90})
0.00	1.000	1.000
0.07	0.978	0.942
0.13	0.969	0.909
0.20	0.976	0.918
0.27	0.962	0.919
0.33	0.948	0.912
0.4	1.122	0.997
0.47	1.491	1.369

Similarly, if the values in Table 7.4 above is plotted and fitted with a four-degree polynomial model as in Figure 7.11, the corresponding elastic responses of the interface for ages 3 and 90 days can be written as:

For age 3, we have:

$$y = 76.99\left(\frac{a}{W}\right)^4 - 49.97\left(\frac{a}{W}\right)^3 + 9.97\left(\frac{a}{W}\right)^2 - 0.81x + 1.00 \qquad (7.6)$$

While for age 90, we have:

$$y = 108.99\left(\frac{a}{W}\right)^4 - 83.00\left(\frac{a}{W}\right)^3 + 21.58x^2 - 2.26x + 1.00 \qquad (7.7)$$

Now, if each of equations (7.3), (7.7), and (7.8) is differentiated and then equated to zero, the optimum value for $\left(\frac{a}{W}\right)$ is obtained in each case. Consequently, the resulting differential equation in each case, starting with age 3 through 90, is respectively given by:

$$\dot{y} = 307.96\left(\frac{a}{W}\right)^3 - 149.91\left(\frac{a}{W}\right)^2 + 19.94\left(\frac{a}{W}\right) - 0.81 \qquad (7.8)$$

$$\dot{y} = 491.48\left(\frac{a}{W}\right)^3 - 283.19\left(\frac{a}{W}\right)^2 + 48.84\left(\frac{a}{W}\right) - 2.46 \qquad (7.9)$$

$$\dot{y} = 432.40\left(\frac{a}{W}\right)^3 - 249.00\left(\frac{a}{W}\right)^2 + 43.16\left(\frac{a}{W}\right) - 2.26 \qquad (7.10)$$

From equations 7.8, 7.9 and 7.10, the values of $\left(\frac{a}{W}\right)$ for which $\dot{y}$ is zero is mutually approximated to 0.30. In this respect, the corresponding optimum notch length can be estimated using:

$$a = 0.30W = 0.30 * 150 = 45mm$$

As a first approximate solution, this value of a which corresponds to an average material mismatch property between BRCFRPMC and OPCC, was generalized for the laboratory wedge tensile splitting experiments described in section 7.1.

Further, in the analysis, a deduction can be advanced based on equations 7.3a, 7.6, and 7.7, by considering and substituting the optimum value of x or $\left(\frac{a}{W}\right)$ (i.e. 0.30) into the equations consecutively. The resulting values are plotted in the curves shown in Figure 7.20 with respect to Dundur's first parameters (α) and the elastic mismatch ratio (E'_{pmc}/E'_{opc}).

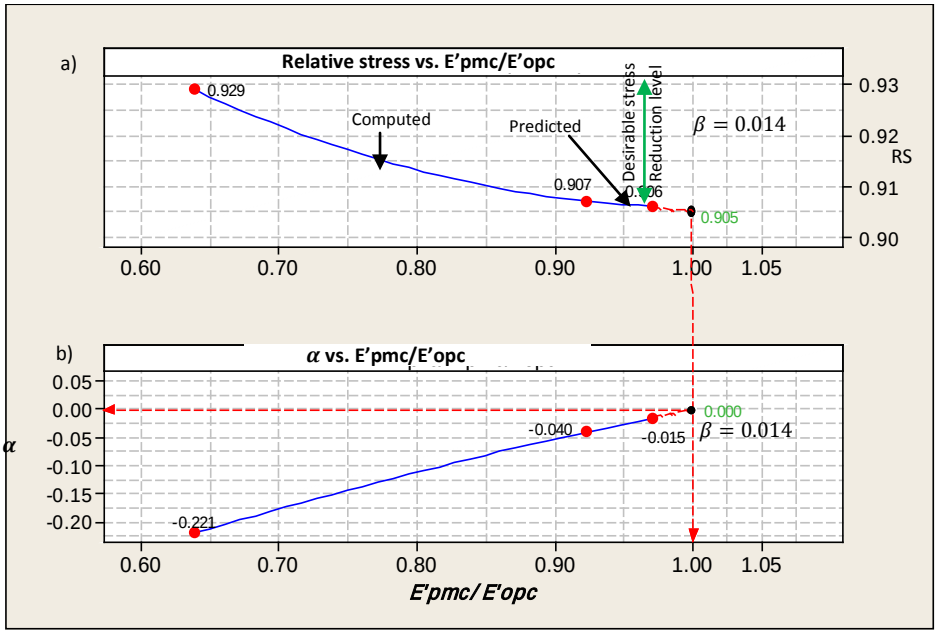

Figure 7.19: Interface stress response to Elastic mismatch between PMC and OPC

As illustrated in Figure 7.19, it is clear that the stress level at the interface during the early-age, which corresponds to the lowest value of (E'_{pmc}/E'_{opc}), is relatively high, but then reduces and approaches a minimum as the ratio of elastic moduli of the bi-material tends to a unit. This change in the elastic moduli is envisaged to occur as the freshly placed overlay BRCFRPMC develops in strength and consequently in elastic properties with time. When this phenomenon of uniformity occurs, the corresponding value of α and its effects in the overall analysis reduces to zero as illustrated in Figure 7.19b, thus implying that only the notch-size effect dictates response at the interface under loading; since the effect of β is treated as secondary.

This state of uniformity between the overlay and the substrate is often referred to as a condition of perfect elastic match. In practice however, especially in cementitious overlay where material properties change relative to age, perfect elastic match is difficult to attain during the early-age of placing the overlay material as clearly shown in Figure 7.19.

As seen, the prescribed optimum BRCFRPMC mix attains the state of uniformity with the substrate OPCC after its 90-day's life history. This represents about 2.6% stress reduction relative to its early-age stress profile. As seen here, in the long term, it is not likely that a substantial level of stress reduction would occur after 90 days of casting. In this respect, it can be concluded that the material design of the interface in this work is reasonable.

7.3.2 Numerical determination of Interfacial Fracture Parameters

In the on-going discussions, it is observed that in order to successfully model and simulate stresses developing at the interface between the overlay and the existing substrate on site, the following parameters are required to characterise the interface for Mixed Mode failure:

- The cohesive interfacial bond tensile strength,
- The cohesive interfacial shear bond strength,
- The interfacial fracture toughness or allowable crack opening width in case of Mode I, or allowable slip for Mode II.

At this stage of the work, all parameters relating to Mode II fracture, that is, the cohesive fracture shear strength, maximum fracture energy, and the allowable slip are already made available. For Mode I fracture however, only the interfacial fracture toughness is given based on the experimental work described in section 7.1. Usually in numerical work of this nature, to complement such a value, it is customary to make use of the cohesive tensile bond strength obtained by direct tensile pull test or indirect tensile (Brazilian splitting) test. It therefore implies that two separate tests are required in determining the fracture parameters in Mode I.

In this study however, an attempt was made to circumvent this approach by proposing that the wedge splitting test described previously is sufficient as a single test geometry for determining the full fracture parameters in Mode I. The attempt here was to ensure that based on the preliminary numerical investigations undertaken in section 7.3.1, it is possible to fit the experimental and numerical results given in section 7.1 and section 7.3.1 respectively in order to compute for the cohesive interfacial bond strength. It is obvious that a direct bond strength value of the interface cannot be determined from the wedge splitting test described in section 7.1, but if coupled with some numerical shrewdness, it is possible to estimate mathematically the required strength at the interface.

For instance, from equation 7.4, it can be shown that:

$$\frac{\sigma_{Ni}}{\sigma_{UN}}(\emptyset) = \left(\frac{P_H}{A} + \frac{My}{I}\right)(\emptyset) \qquad (7.11)$$

Thus, if the left hand side (LHS) of the expression given above is replaced with the numerical values obtained for the optimum notch-size (i.e. 0.30) shown in Figure 7.19a, it follows that for ages 3, 28 and 90, the respective interfacial bond strength can be computed as follow:

For age 3 we write that:

$$0.929 = \left(\frac{P_H}{A} + \frac{My}{I}\right)(\emptyset) \qquad (7.12)$$

For age 28, we write that:

$$0.907 = \left(\frac{P_H}{A} + \frac{My}{I}\right)(\emptyset) \qquad (7.13)$$

While for age 90, we write that:

$$0.906 = \left(\frac{P_H}{A} + \frac{My}{I}\right)(\emptyset) \qquad (7.14)$$

Further, in the above equations, if $\left(\frac{P_H}{A}\right)$ is depicted by DS (direct stress), and $\left(\frac{My}{I}\right)$ is denoted by BS (bending stress); it follows that equation 7.12 for instance yields:

$$0.929 = (DS + BS)(\emptyset)$$

where,

$$BS\ (\emptyset) = 0.929 - DS(\emptyset)$$

Therefore, for a 1-D interfacial delamination model, the above expression becomes:

$$BS\ (\emptyset) = 0.929 - \frac{P_H}{z}(\emptyset)$$

Where, z is the 1-D ligament bond length.

From here, it can be stated mathematically that the $limit$ of $BS(\emptyset)$ as z approaches $\left(\frac{W}{2}\right)$ is $\left(0.929 - \frac{P_H}{z}(\emptyset)\right)$.

Meaning that, $\lim_{z \to \left(\frac{W}{2}\right)} BS(\emptyset) = 0.929 - DS(\emptyset)$

Thus, if z is taken as 74.99mm, which approaches $\frac{W}{2} = 75mm$, then

$$BS\ (\emptyset) = 0.929 - \frac{P_H}{74.99}(\emptyset) \qquad (7.15)$$

If the above expression in (7.15) is replicated for 28 and 90 days, the following equations are obtained respectively:

$$BS\ (\emptyset) = 0.907 - \frac{P_H}{74.99}(\emptyset) \qquad (7.16)$$

$$BS\ (\emptyset) = 0.906 - \frac{P_H}{74.99}(\emptyset) \qquad (7.17)$$

Note here that the value of $P_H = 12N$ in the analysis undertaken in section 7.3.1. Therefore, equations 7.15, 7.16 and 7.17 are respectively re-written as:

$$BS\ (\emptyset) = 0.929 - 0.16 = 0.769 \qquad (7.18)$$

$$BS\ (\emptyset) = 0.907 - 0.16 = 0.747 \qquad (7.19)$$

$$BS\ (\emptyset) = 0.906 - 0.16 = 0.746 \qquad (7.20)$$

Hence, a table showing the percentage of both bending and direct stresses for each age represented in the experiment can be drawn and illustrated by Table 7.5.

Table 7.5: Percentage of Bending and Direct stresses in the total interfacial stress by age

Age (days)	Bending Stress (BS) %	Direct Stress (DS) %
3	82.8	17.2
28	82.4	17.6
90	82.3	17.7
$\%\ Limit$:	82.55 ± 0.25	17.45 ± 0.25

As shown clearly above in Table 7.5, the variation in bending and direct stresses is generally limited to about 0.25% for ages between 3 and 90 days. The bending stress in this case accounts for about 82.5 % while the direct stress is in the vicinity of 17.5%. By implication, if the maximum horizontal (splitting) force can be determined experimentally as illustrated in Figures 7.4 and 7.5, then it is feasible that the corresponding DS for laboratory specimens as those used in section 7.1 can be calculated.

For instance, for ages 3 and 28 test specimens with maximum splitting limit values given in Figures 7.4 and 7.5 as $1.89KN \pm 0.02$ and $2.34KN \pm 0.07$ respectively, it can be shown that:

For age 3 specimens:

$$\frac{1890}{74.99B} = 0.34 = 17.5\% \; of \; TS$$

Where,

$B = 75mm = interface\ width$

$TS = Total\ interface\ stress\ (N/mm^2)$

In this case,

$$TS = \frac{0.34\ X\ 100}{17.5} = 1.94\ N/mm^2$$

For age 28 specimens, the resulting TS is given by:

$$TS = \frac{0.42\ X\ 100}{17.5} = 2.40\ N/mm^2$$

From here, a direct means of validating the above results is to compare the estimated values with those obtained experimentally from the Brazilian splitting test given in Table 6.4. For specimens characterised as R_{z2}, the 3 and 28 days' mean tensile strengths are given as 2.07 and 2.22MPa respectively. By correlation, the estimated values compare well with those of Brazilian test results. Precisely, for age 3, the range of observed values and error falls within $2.01 \pm 0.07MPa$; while that of age 28 falls within $2.31 \pm 0.09MPa$. The limits shown here are acceptable for analytical solutions of this nature. Thus, the proposed method is consistence with established existing methods.

From here, if a bilinear cohesive model is assumed as mentioned in chapter 3, it follows that the only outstanding parameter required for complete fracture process description is the critical crack displacement or opening (u_n^c). Note, u_n^c is computed here based on equation 3.44 shown below:

$$u_n^c = \frac{2G_{Ic}}{\sigma_0}$$

Hence for age 3, the critical crack displacement (u_n^c) is given by:

$$u_{n_3}^c = \frac{2\ X\ 34.96\ X\ 10^{-3}}{2.01} = 0.035mm$$

While for age 28, the critical crack displacement (w_c) yields:

$$u_{n_{28}}^c = \frac{2\ X\ 56.82\ X\ 10^{-3}}{2.31} = 0.050mm$$

By direct comparison, it is evident from the two values shown above that the interface is about 140% more likely to fracture or delaminate at age 3 than at age 28. Thus, age 3 fracture conditions as illustrated in Table 7.6 are generally more critical in fracture analysis, and were used as the FEA failure criteria of the interface.

Table 7.6: Fracture parameters Comparison table

Age (days)	Cohesive tensile strength (σ_0) (N/mm^2)	Allowable shear strength (τ_0) (N/mm^2)	Mode I Fracture toughness (G_{fI}) (N/m)	Mode II Fracture toughness (G_{fII}) (N/m)	Critical crack opening (u_n^c) (mm)	Critical shear slip / displ't (u_t^c) (mm)
3	2.01 ± 0.07	3.56 ± 0.24	34.96 ± 1.56	171.51 ± 7.77	0.035	0.108
28	2.31 ± 0.09	4.69 ± 0.17	56.82 ± 2.85	307.29 ± 5.13	0.050	0.138

At the crack tips along the interface between dissimilar materials, Mixed-Mode oscillatory field is prevalent. Hence, in the subsequent section, analyses based on Mixed-Mode interface fracture are implemented.

7.4 Interfacial Mixed Mode Finite Element Fracture Model for Edge Delamination condition

Consider a bonded concrete overlay system shown in Figure 7.20a resting on elastic foundation, and experiencing a differential length change with the substrate through its thickness, either as a result of thermal gradient or drying shrinkage of the overlay. The curling effects of the uniaxial edge-stress condition can be idealized as shown in Figure 7.20b such that the resulting stresses may be assumed as acting on a beam at the edges rather than on the entire slab surface (Houben, 2006). With increased deformation concentrating at the top edge surface of the overlay during the early curing age, partial or true interface delamination length may be induced along the edges or corners. For

delamination to occur, it is assumed that the interface bonding strength and toughness have been overcome.

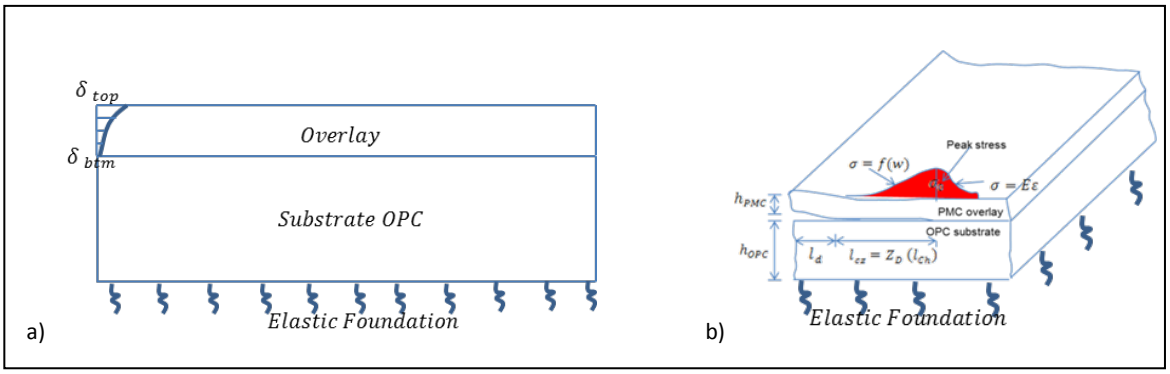

Figure 7.20: Overlay Edge Deformation and Delamination

In order to investigate the mechanism of Mixed-Mode interfacial failure of the above model, a 2D plane strain analysis was implemented with ANSYS FE code based on the idealized model shown in Figure 7.21. Similar buckling-induced delamination model has been implemented elsewhere (Mei *et. al*, 2007) for elastic thin-film structures, but usually without elastic foundation.

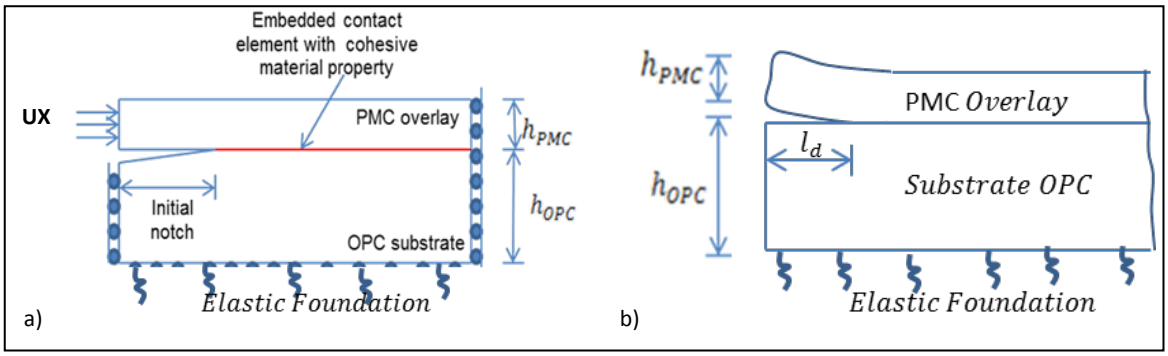

Figure 7.21: Idealized 2D plane strain FEM.

The Finite Element Model shown in Figure 7.21 is basically required to calculate the Mixed-Mode interfacial fracture energy using ANSYS Cohesive Zone Model discussed in chapter 3.0. The model incorporates contact elements with cohesive material properties which define the cohesive law governing the delamination mechanism. In the analysis, the value of Dundur's parameter (β) was held constant, while (α) was varied based on the measured elastic properties of the overlay material during its early and mature curing-age. The idea here was based on the premise that the effect of (β) is secondary (Mei *et al*, 2007) in most practical applications.

In the model, the following geometric and material property inputs were specified:

- A constant Overlay thickness of 100mm: Though in several codes of practice, the minimum constructible overlay thickness of 51mm is permitted; however, for structural strengthening intending to last for 25 year upward, a thickness up to 127mm may be considered, depending on the anticipated traffic loading, condition of underlying pavement, desired service life and the required floor elevation level in situations where head-room imposes a constraint;
- A constant (arbitrary) underlying OPCC pavement thickness of 300mm;
- The Elastic Modulus and Poisson's values correspond to those given in Table 7.3;
- The bond strengths and fracture parameters correspond to those given for early-age 3 in Table 7.6.
- A constant (arbitrary) working pavement length of 1000mm.
- Initial interfacial edge-defect lengths of 0, 50, 100, 200 and 300mm
- The foundation model uses surface effect elements with an arbitrary soil stiffness of $25000N/mm$ and mass density of $1850\ kg/m^3$.
- Mass densities of 2400kg/m^3 and 2467.71kg/m^3 for the underlay and overlay respectively.

From here, in order to simulate the effects of differential length change between the overlay and underlay, two distinct magnitudes of horizontal line displacement loadings (UX) were imposed on the full edge-side (depth) of the overlay as illustrated in Figure 7.21; these enable two separate studies, namely: Partial (incomplete) delamination and true (complete) delamination responses of the interface. The partial delamination study was based on 0.0851mm displacement loading, representing a characteristic observed free deformation due to the drying shrinkage of the overlay, while the true delamination investigation was instigated with an arbitrary value of 0.20mm. Note that all other geometric and material parameters were held constant in both cases.

By classification, a crack is partial or initiates once an initially perfectly bonded interface forms into a fictitious crack, implying that the maximum induced crack displacement still falls below the effective displacement computed from equation 3.35. On the other hand, a crack

is true or propagates as soon as this critical crack condition is reached. In this case, the effective Mixed-Mode displacement was estimated to be $0.114mm$ based on the values given in Table 7.6 for u_n^c and u_t^c .

7.5 Results Analysis and Discussions

7.5.1 Partial (incomplete) interfacial delamination response

In the current loading configuration, the response of the interface to Mixed-Mode delamination under incomplete separation is understudied, given proper reference to the elastic mismatched properties of the bi-material when it changes spontaneously from its early curing-age condition to its matured state.

For all the test specimens, three distinct variables can be associated with the dimensionless delamination function (Z_D) (Mei *et al*, 2007) based on the expression given in equation 7.21.

$$Z_D = f(\frac{l_d}{h_{overlay}}, \alpha, \beta) \qquad (7.21)$$

From equation 7.21, the first parameter in the bracket $\left(\frac{l_d}{h_{overlay}}\right)$ denotes a normalized defect length, and often in practice helps to investigate the edge response of the interface for different initial bond conditions when one of the two Dundur's parameters is fixed. The range of such defect can fall within the limit $0 \leq l_d \leq \infty$. In this case, since the effect of non-zero (β) is treated as secondary, hence it value was held fixed at 0.014 for all possible test specimens. Note here that (l_d) is the initial edge defect length, while ($h_{overlay}$) denotes the overlay thickness.

In order to be able to estimate a reasonable FPZ (l_{cz}) along the interface, for a bi-material interface, the following relationship holds (Gdoutos, 2005):

$$l_{cz} = Z_D\,(l_{Ch}) = Z_D\left(\frac{E^* G_F m}{\lambda_m^2}\right) \qquad (7.22)$$

Where,

Z_D *is as defined in equation* 7.21,

l_{Ch} *is Hillerborg's characteristic length defined by* $\left(\frac{E^* G_F m}{\lambda_m^2}\right)$.

$E^* = average\ elastic\ modulus\ of\ the\ bi-material\ (same\ as\ equation\ 3.27)$,

$\lambda_m = critical\ traction\ for\ mixed\ mode\ damage\ initiation\ (same\ as\ equation\ 3.34)$,

$G_{F^m} = Mixed - Mode\ fracture\ toughness$

In practice, where thickness optimization plays a major role in the design of the overlay, it is more convenient to express the resulting energy release rate in terms of a structural length scale; such that equation 7.22 yields:

$$G_{F^m} = Z_D\left(\frac{l_d}{h_{overlay}}, \alpha, \beta\right) \frac{\lambda_m^2\, h_{overlay}}{E^*} \qquad (7.23)$$

From here, the delamination failure definition can then be given as a function of the normalized interface toughness by re-arranging equation 7.23 in form of equation 3.39; such that:

$$Z_D\left(\frac{l_d}{h_{overlay}}, \alpha, \beta\right) = G_{ic} = \frac{E^* G_{ic}(\Psi)}{\lambda_m^2\, h_{overlay}} \qquad (7.24)$$

In this respect, the delamination failure coefficient (Z_D) can be plotted as a function of the normalized delamination length for different values of (α) shown in Table 7.3. The corresponding response for partial delamination problem is represented in Table 7.7.

Table 7.7: Interface Response to Elastic Mismatch between BRCFRPMC and OPCC

Age (day)	$\frac{E'_{pmc}}{E'_{opc}}$	α	Initial notch length $(L_n)\ mm$	Max. Crack opening $w_c\ (mm)$	Max. Crack slip $\delta_s(mm)$	Effective Interface displ't $(u_m)\ mm$	Cohesive zone length $(l_{cz})\ mm$
3	0.638	-0.221	0	0.011	0.084	0.085	90.00
			50	0.011	0.043	0.044	55.00
			100	0.009	0.025	0.027	35.00
			200	0.006	0.012	0.013	20.00
			300	0.004	0.007	0.008	10.00
28	0.923	-0.040	0	0.013	0.084	0.085	105.00
			50	0.013	0.048	0.050	70.00
			100	0.010	0.030	0.032	45.00
			200	0.007	0.015	0.017	30.00
			300	0.005	0.009	0.010	20.00
90	0.971	-0.015	0	0.013	0.084	0.084	110.00
			50	0.013	0.049	0.051	70.00
			100	0.011	0.030	0.032	45.00
			200	0.007	0.016	0.017	30.00
			300	0.005	0.009	0.010	20.00

From Table 7.7, it is apparent that the observed effective crack displacements due to Mixed-Mode delamination are all below the critical values $(0.114mm)$ specified for failure. Evidently no true crack has developed yet in all the test specimens; however, evidence of crack formation was observed based on the associated cohesive zone lengths shown in Table 7.7 and Appendix A3. The results generally indicate that crack displacements decrease with notch length but tends to shown some degree of growth with α values.

The on-going interface fracture analysis has been implemented based on the parameters associated with equation 7.24. Hence, by re-arranging equation 7.24 in terms of the total interfacial Mixed-Mode energy release rate, it can be shown that:

$$Z_D\left(\frac{L_n}{h_{PMC}}, \alpha, \beta\right) = G_{ic} = \frac{G_{ic}(\Psi)}{\frac{\lambda_m^2 h_{PMC}}{E^*}} \quad (7.25)$$

If the denominator expression in equation 7.25 is denoted by $\emptyset_d$, then the expression becomes:

$$Z_D\left(\frac{L_n}{h_{PMC}}, \alpha, \beta\right) = G_{ic} = \frac{G_{ic}(\Psi)}{\emptyset_d} \quad (7.26)$$

From equation 7.26, the G_{ic} is evaluated numerically as a function of a constant steady-state phase angle Ψ. Thus, Table 7.8 and Figure 7.22 were drawn to represent the relationship between the resulting Mixed-Mode energy release rate $G_{ic}(\Psi)$ and the delamination dimensionless parameter Z_D based on equation 7.26. Note that the $G_{ic}(\Psi)$ values represented here were evaluated from Appendix A4.

Table 7.8: Relationship between Structural dimensionless scale and Delamination dimensionless parameter under crack formation conditions

$\frac{L_n}{h_{PMC}}$	$(\emptyset_d)_3$ N/mm	$(\emptyset_d)_{28}$ N/mm	$(\emptyset_d)_{90}$ N/mm	$(G_{ic}(\Psi))_3$ N/mm	$(G_{ic}(\Psi))_{28}$ N/mm	$(G_{ic}(\Psi))_{90}$ N/mm	Z_{D3}	Z_{D28}	Z_{D90}
0	0.186	0.151	0.147	0.173	0.214	0.227	0.932	1.422	1.539
0.5	0.186	0.151	0.147	0.161	0.172	0.173	0.866	1.141	1.176
1.0	0.186	0.151	0.147	0.096	0.135	0.138	0.515	0.895	0.937
2.0	0.186	0.151	0.147	0.061	0.086	0.086	0.328	0.570	0.586
3.0	0.186	0.151	0.147	0.028	0.057	0.058	0.151	0.379	0.396

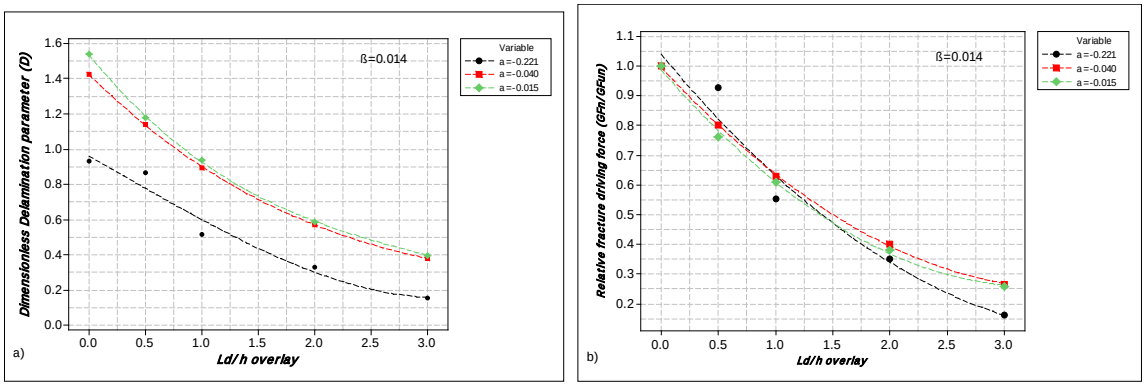

Figure 7.22: Relationships between the Structural Dimensionless length scale and (a) Delamination Dimensionless parameter and b) Relative fracture driving energy under partial delamination condition

From Figure 7.22a, the interface response curves generally indicate that the delamination dimensionless parameter (Z_D) decreases as $\left(\frac{l_d}{h_{overlay}}\right)$ increases in size, but increases with (α) values. Apparently, as the elastic mismatched properties of the bi-material approach unity, the effects of (α) on (Z_D) dwindle and assume asymptotic respond. By implication, it shows that under the current loading, lesser fracture driving energy is generally required to extend an already existing crack along the interface as the BCO structural dimensionless scale increases. Also, it indicates that the interface is generally more prone to cracking extension at its early age than later, because at early age delamination is largely dominated by both material mismatched properties and imperfection in the plane of the interface. The range of fracture risk as seen here falls averagely above 1.8 times that of the matured-age of 28 or 90days.

On the other hand, Figure 7.22b illustrates the relative fracture driving energy response of the interface. Here, it is clear that crack extension from the edge for un-notched specimens is independent of the notch (defect) size, and so a higher driving force is required to open the interface compared to notched specimens. Precisely, the numerical reduction effects on the driving energy are estimated in the proximities of 20%, 40%, 60% and 75% for structural scale of 0.5, 1.0, 2.0 and 3.0 respectively. For exclusive relationship between the elastic mismatch properties and the crack propagation driving energy for a prescribed defect size, the following exponential models are valid:

$$Gic = \begin{cases} e^{\left(\frac{\alpha-1.16}{0.78}\right)} & for\ \left(\frac{l_d}{h_{overlay}}\right)=0 \\ e^{\left(\frac{\alpha-4.92}{2.81}\right)} & for\ \left(\frac{l_d}{h_{overlay}}\right)=0.5 \\ e^{\left(\frac{\alpha-1.07}{0.55}\right)} & for\ \left(\frac{l_d}{h_{overlay}}\right)=1.0 \\ e^{\left(\frac{\alpha-1.35}{0.56}\right)} & for\ \left(\frac{l_d}{h_{overlay}}\right)=2.0 \\ e^{\left(\frac{\alpha-0.74}{0.27}\right)} & for\ \left(\frac{l_d}{h_{overlay}}\right)=3.0 \end{cases} \quad (7.27)$$

From equation 7.27, if no elastic mismatch condition exists, the corresponding values of (G_{ic}) for $\alpha = \beta = 0$ can be evaluated for any initial defect size. In this work, the estimated values based on equation 7.27 and the computed values from ANSYS FEA are shown in Figure 7.23.

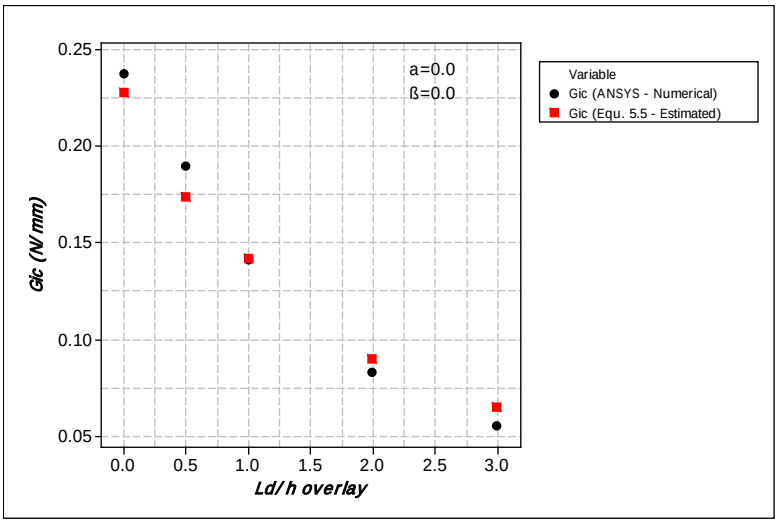

Figure 7.23 Comparison between Numerical and Estimated values of Gic

As seen in 7.23, it is evident that the values estimated from equation 7.27 fit the numerical results well. This implies that for values of (α) ranging between -0.221 and 0.0, equation 7.27 is valid for value of (β) fixed at 0.014 or adjusted accordingly to 0.0.

Note however that the results illustrated here are based on the assumption of a constant phase angle (Ψ) at the oscillatory field during crack extension, but in reality the phase angle may change locally from element to element or relative to a defect size. Hence, in order to determine if the degree of such variations is significant on the observed values, the relationship between the computed interfacial fracture driving energy (G_{ic}) and the phase angle (Ψ) was investigated and subsequently plotted in Figure 7.24.

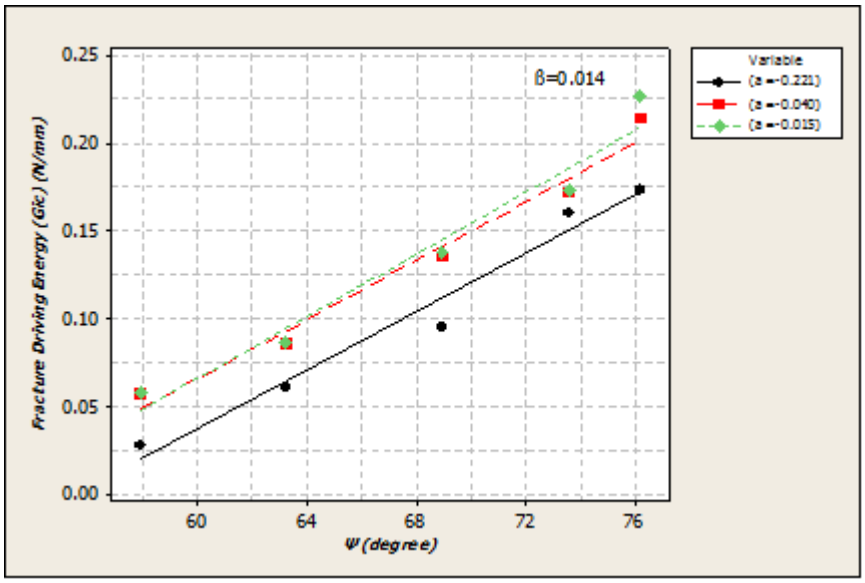

Figure 7.24: Relationship between Interfacial Fracture Driving Energy and Phase-angle

From Figure 7.24, the linear regressions between (G_{ic}) and (Ψ) are given in equations 7.28 to 7.30 from where the degree of variation of interfacial fracture energy due to changes in phase-angle was investigated.

- $For\ \alpha = -0.221$, the regression model yields:

$$G_{ic3} = 0.0083\Psi - 0.459 \qquad (7.28)$$

- $For\ \alpha = -0.040$, the regression model ii given by:

$$G_{ic28} = 0.0084\Psi - 0.439 \qquad (7.29)$$

- $While\ For\ \alpha = -0.015$, the regression model gives:

$$G_{ic90} = 0.0088\Psi - 0.465 \qquad (7.30)$$

Thus, the average differential value $\left(\frac{dG_{ci}}{d\Psi}\right) = 0.0085$, which indicates that the fracture diving energy in this case only changes by 0.85% for every degree change of the phase-angle (Ψ). As demonstrated here, this amount of variation is minimal and insignificant.

Thus, within the limit $(0 \leq \frac{l_d}{h_{overlay}} \leq 3.0)$ of experimentation, the energy release rate only increases by $0.0153N/mm$ for a total of 18° differential (observed) phase angle.

7.5.2 True (complete) interfacial delamination response

It is clear that the observations given in section 7.5.1 relate directly to the magnitude of the applied external displacement. However, for a sufficiently large external displacement loading, the trend of response of the interface may differ from those discussed above. Usually for a complete crack propagation problem, a substantial external load is required. In order to implement a full delamination response of the interface, displacement value in the magnitude of 0.20mm was discretionarily applied. This value after several incremental attempts proved to be adequate in ensuring that all notched and un-notched test specimens undergo complete delamination during testing.

By keeping other geometric and material parameters constant as before, the resulting interfacial response representing the relationship between (Z_D) and $\left(\frac{l_d}{h_{overlay}}\right)$ are represented in Table 7.9 and Figure 7.25.

Table 7.9: Relationship between Structural dimensionless scale and Delamination dimensionless parameter under crack propagation conditions

$\frac{L_n}{h_{PMC}}$	$(\emptyset_d)_3$ N/mm	$(\emptyset_d)_{28}$ N/mm	$(\emptyset_d)_{90}$ N/mm	$(G_{tm}(\Psi))$ N/mm	$(G_{tm}(\Psi))_{28}$ N/mm	$(G_{tm}(\Psi))_{90}$	Z_{D3}	Z_{D28}	Z_{D90}
0	0.186	0.151	0.147	0.148	0.182	0.174	0.797	1.209	1.182
0.5	0.186	0.151	0.147	0.147	0.188	0.191	0.792	1.249	1.297
1.0	0.186	0.151	0.147	0.140	0.175	0.182	0.754	1.162	1.236
2.0	0.186	0.151	0.147	0.158	0.195	0.189	0.851	1.295	1.284
3.0	0.186	0.151	0.147	0.116	0.189	0.194	0.625	1.255	1.318

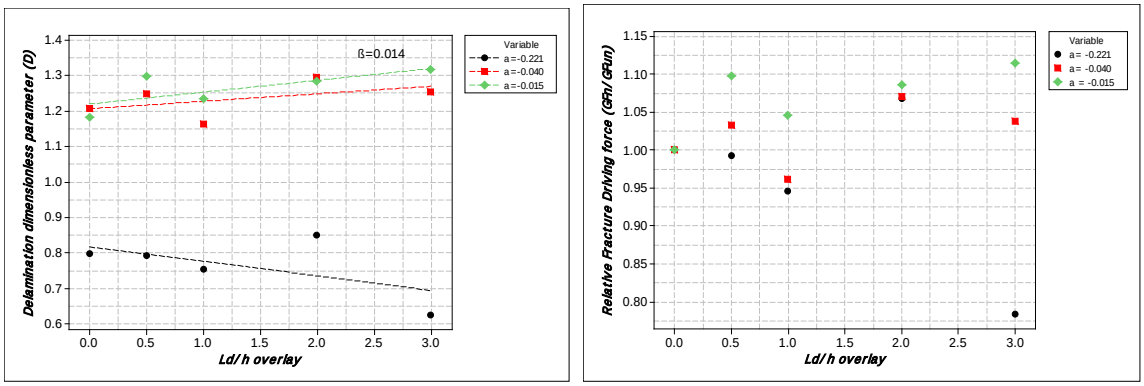

Figure 7.25: Relationships between the Structural Dimensionless length scale and (a) Delamination Dimensionless parameter and b) Relative fracture driving energy under complete delamination propagation condition

It is clear from Figure 7.25 that the interface response curves under complete delamination propagation deviates from those presented in Figure 7.23. In the current load configuration, the interface delamination dimensionless coefficient and the relative fracture driving force show a decline response for extreme low value of (α) as $\left(\frac{l_d}{h_{overlay}}\right) \rightarrow max$, but appear to be steady or increase marginally as the bi-material mismatched properties approach unity. In practical sense, for a more compliant overlay ($\alpha \ll 0$), the delamination driving energy from the edge can be expected to be of a lower magnitude and diminishes concomitantly as the initial notch defect (l_d) increases, when compared to less complaint overlay, where $\alpha \approx 0$.

As in the previous analysis, exclusive relationships between the elastic mismatched properties and the full delamination driving energy for a prescribed defect size, was fitted and given in equation 7.31.

$$Gic = \begin{cases} e^{\left(\frac{\alpha-1.66}{0.98}\right)} & for\ \left(\frac{l_d}{h_{overlay}}\right)=0 \\ e^{\left(\frac{\alpha-1.24}{0.76}\right)} & for\ \left(\frac{l_d}{h_{overlay}}\right)=0.5 \\ e^{\left(\frac{\alpha-1.34}{0.79}\right)} & for\ \left(\frac{l_d}{h_{overlay}}\right)=1.0 \\ e^{\left(\frac{\alpha-1.55}{0.96}\right)} & for\ \left(\frac{l_d}{h_{overlay}}\right)=2.0 \\ e^{\left(\frac{\alpha-0.61}{0.39}\right)} & for\ \left(\frac{l_d}{h_{overlay}}\right)=3.0 \end{cases} \qquad (7.31)$$

Thus, by ignoring the effects of initial defect size (l_d), a comparison between equations 5.5 and 5.6 shows that the interface generally exhibits lesser resistance to delamination driving force in complete separation model than in incomplete separation model. The effects of initial structural defect however appear positive under complete delamination model, but negative in the incomplete delamination model.

For ease of result validation, several values of (Z_D) based on plane stress problems have been observed in the literature (Turon, *et. al.*, 2007), ranging between 0.21 and 1.0. Some of these models are given in Table 5.1; though Hillerborg's and Rice's models, where the values of (D) approach or equal to unity, still remain most common in practice.

Table 7.10: Cohesive zone length and equivalent delamination dimensionless parameter

$Model$	l_{cz}	Z_D
Hui	$2/3\pi\,.E\,Gc/{\lambda_{cm}}^2$	0.21
$Irwin$	$1/\pi\,.E\,Gc/{\lambda_{cm}}^2$	0.31
$Dugdale, Barenblatt$	$\pi/8\,.E\,Gc/{\lambda_{cm}}^2$	0.40
$Rice, Falk$	$9\pi/32\,.E\,Gc/{\lambda_{cm}}^2$	0.88
$Hillerborg$	$E\,Gc/{\lambda_{cm}}^2$	1.00

Evidently, from Table 7.10, no unified value of (Z_D) exist *per se*; a close observation of the response curves shown in Figures 7.23 and 7.25 suggest that the values of (Z_D) depend largely on the initial edge defect size of the interface, the plane of loading, the magnitude of the applied external load, and on the elastic bi-material properties, if any mismatch exists. Thus, in the on-going plane strain problems, it is found that the values of (Z_D) vary numerically between 0.15 and 1.54 for partial delamination problems, and between 0.63 and 1.32 for complete delamination problems.

7.6 Analytical solution for Predicting the Critical Crack displacement and the Failure Mode-Shape of the overlay.

Consider Figure 7.26(a) which depicts the Finite Element Model presented in Figure 7.21 in its un-deformed state. If after deformation, Figure 7.26(b) results, reaction forces and

displacements at designated locations along the interface can be calculated, by assuming an effective interfacial stiffness acting continuously along the plane of the interface.

In the deformed configuration shown in Figure 7.26(c), three designated points $0, 1$ and 2 are identified. Point 0 represents the crack tip with reaction forces (f_0) and (τ_0) acting vertically and horizontally respectively. Due to oscillatory field developing within this vicinity, the resultant force (R_0) forms angle θ with the plane of the interface.

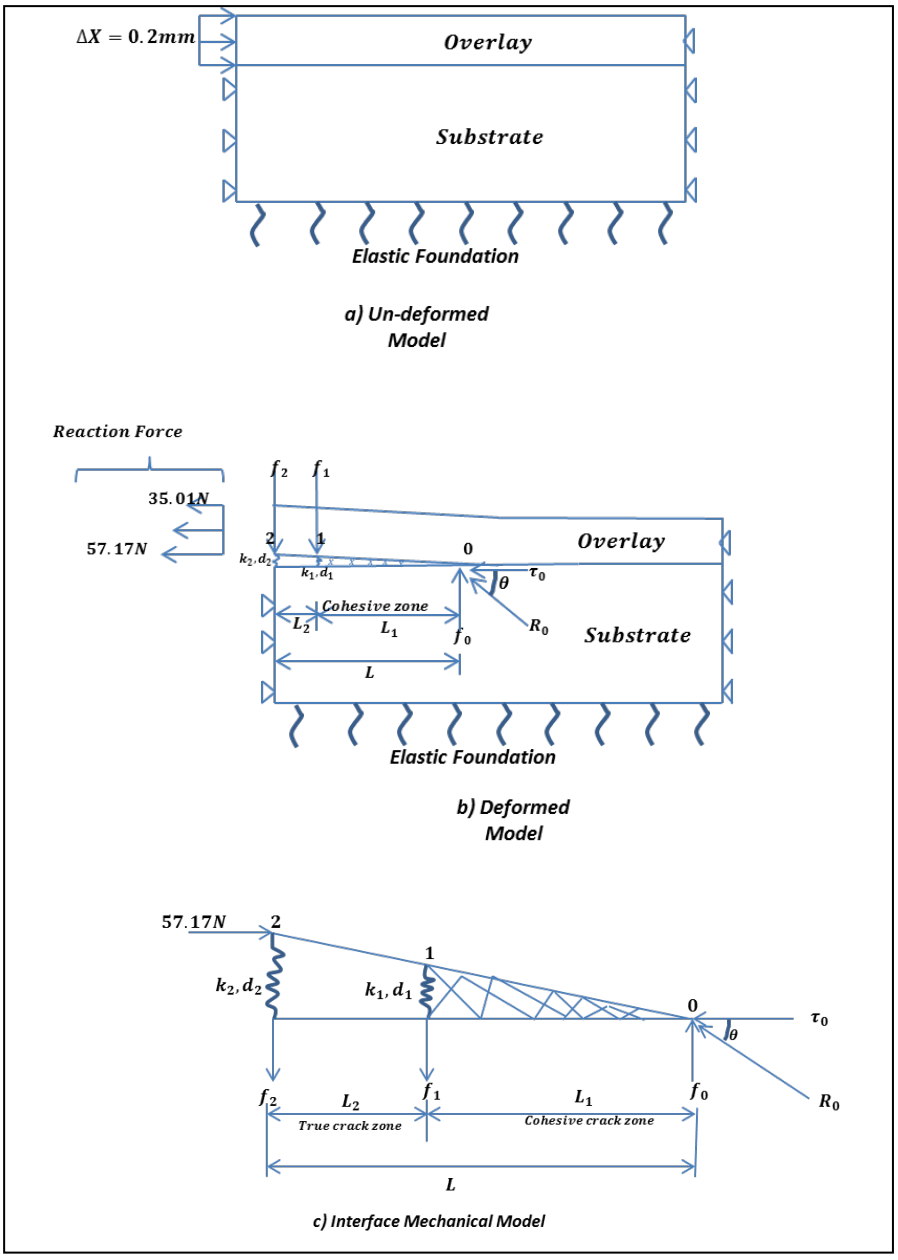

Figure 7.26: Un-deformed, Deformed, and Mechanical Model of a delaminated interface

If the deformation of the interface is initially de-coupled into it normal and tangential form, then a solution can be obtained for Mode I (opening mode) as distinctively depicted at point 1 and 2 of Figure 7.26, and subsequently modified for Mode II and Mixed-Mode. Here, it is assumed that at point 1, crack opening (d_1) approaches the critical value for de-bonding, while the crack front between point 1 and point 2 already exceeded the critical crack opening value. Thus, between points 1 and 2 true crack forms, while fictitious (cohesive) crack lies between points 0 and 1.

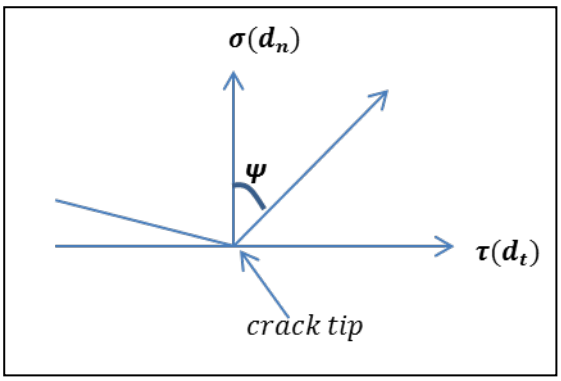

Figure 7.27: Oscillatory field at crack tip

Therefore following Figure 7.27, at crack tip, it can be shown that:

$$\Psi = \arctan\left(\frac{\tau}{\sigma}\right) = \arctan\left(\frac{k_t}{k_n}\right) \qquad (7.32)$$

Where,

σ *and* τ *are the stresses or forces in the normal and tangential directions*

k_n *and* k_t = *corresponding stiffnesses in the normal and tangential directions*

From equation 7.32,

$$k_t = k_n \tan\Psi \qquad (7.33)$$

In this respect, the corresponding effective stiffness can be written as:

$$k_R = \sqrt{k_n^2 + {k_t}^2} = \sqrt{k_n^2 + (k_n tan\Psi)^2} \qquad (7.34)$$

Considering the vertical forces acting on the plane of the interface, it can be shown that:

$$\sum f_y = 0 \qquad (7.35a)$$

Thus,

$$fo - f1 - f2 = 0 \qquad (7.35b)$$

So that at crack tip, we write that:

$$fo = \tau o \tan\theta \qquad (7.36a)$$

Note, for small displacement, $\tan\theta = \left(\frac{d_1}{L_1}\right)$. Therefore equation 7.36a becomes:

$$fo = \tau o \left(\frac{d_1}{L_1}\right) \qquad (7.36b)$$

By substituting for fo in equation 7.35b, it becomes:

$$f1 + f2 = \tau o \left(\frac{d_1}{L_1}\right) \qquad (7.37)$$

Also, it can be evidenced that at crack tip, just prior to sliding or de-bonding, τo =in plane reaction force F. For a prescribed values of F, say $57.17N$, which corresponds to an un-notched specimen with elastic mismatch property, $\alpha = -0.015$, thus $\tau o = 57.17N$.

By taking moments about point 0, equation 7.38:

$$\sum M_0 = 0 \qquad (7.38a)$$

It then follows that:

$$F(d_2) - f_2 L - f_1 L_1 = 0 \qquad (7.38b)$$

For the prescribed test specimen shown in Figure 7.26b, the numerical value of $L = 295$, while that of $L_1 = 60$.

$$\therefore L = 4.92 L_1 \qquad (7.39)$$

Hence, equation 7.38b yields:

$$4.92 f_2 + f_1 = F\left(\frac{d_2}{L_1}\right) = \tau o \left(\frac{d_2}{L_1}\right) \qquad (7.40)$$

By inspection, equations 7.40 and 7.37 compare well. Therefore, re-writing each in form of the constitutive equation, $f = kd$, the following expressions result:

$$k_1 d_1 + k_2 d_2 = \left(\frac{\tau o}{L_1}\right) d_1 \quad (7.41)$$

$$k_1 d_1 + 4.92 k_2 d_2 = \left(\frac{\tau o}{L_1}\right) d_2 \quad (7.42)$$

If $\omega = \left(\frac{k_1}{k_2}\right)$, the system of the equation can be re-written by dividing all through by k_2, so that:

$$\omega d_1 + d_2 = \left(\frac{\tau o}{L_1 k_2}\right) d_1 \quad (7.43)$$

$$\omega d_1 + 4.92 d_2 = \left(\frac{\tau o}{L_1 k_2}\right) d_2 \quad (7.44)$$

This clearly is an Eigenvalue problem, such that the term in the bracket at the RHS is given by:

$$\lambda = \frac{\tau o}{L_1 k_2} \quad (7.45)$$

Thus, in matrix form:

$$\begin{pmatrix} \omega & 1 \\ \omega & 4.92 \end{pmatrix} \begin{pmatrix} d_1 \\ d_2 \end{pmatrix} = \lambda \begin{pmatrix} d_1 \\ d_2 \end{pmatrix} \quad (7.46)$$

Equation 7.46 is of the form: $AX = \lambda X$, and has the following characteristic equation:

$$|A - \lambda I| = 0 \quad (7.47)$$

Assuming a constant normal stiffness (k_n) along the interface, then $k_2 = k_1$, implying that $\omega = 1$. Hence, it can be shown that:

$$\begin{vmatrix} 1-\lambda & 1 \\ 1 & 4.92-\lambda \end{vmatrix} = 0 \quad (7.48)$$

This results in the following quadratic equation,

$$\lambda^2 - 5.92\lambda + 3.92 = 0 \quad (7.49)$$

The solutions to the equation are: $\lambda_1 = 5.16 \; and \; \lambda_2 = 0.76$.

When $\lambda_1 = 5.16$, $d = \begin{pmatrix} d_1 \\ d_2 \end{pmatrix} = \begin{pmatrix} 0.23 \\ 0.97 \end{pmatrix}$; $\lambda_2 = 0.76, d = \begin{pmatrix} -0.97 \\ 0.23 \end{pmatrix}$

In this respect, the values of λ and d are referred to as Eigenvalues and Eigenvectors respectively, and they can geometrically be represented as shown in Figure 7.28.

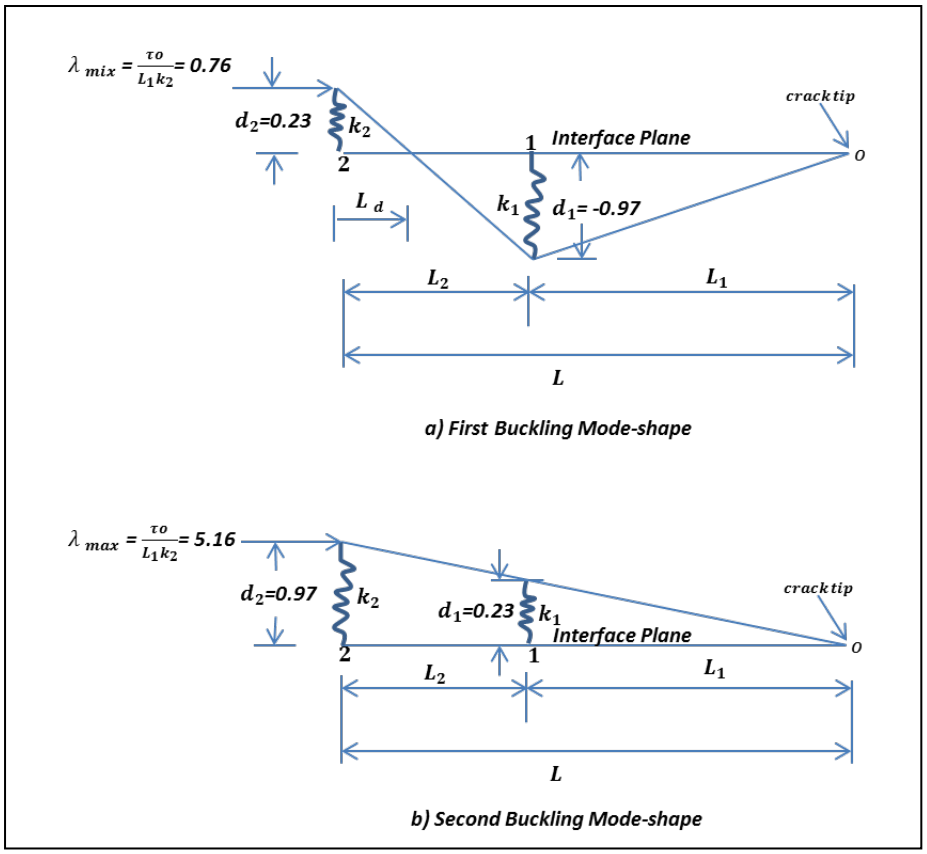

Figure 7.28: Mode I Buckling Mode-shapes

In the on-going Mode I analysis, while the second buckling mode-shape indicates a normal opening mode up to the crack-tip, it is however observed that the first buckling mode-shape indicates a sort of negative deformation value ($d_1 = -0.97$), which suggests a form of inter-penetration between the two solid layers. This phenomenon makes no physical sense, hence a mathematical limiter can be invoked, such that: $d_i \geq 0$ in order to prevent such occurrence. But by interpretation, it can hypothetically be deduced that λ_{min} represents the critical load required to induce an edge opening (d_2) with a delamination crack length of L_d. Beyond the limit of L_d, the overlay experiences a considerable compressive bending over the underlay at the plane of the interface; this prevents the plane from delaminating as more energy or force will be required to drive delamination propagation along the interface as curvature increases.

Hence, from the two mode-shapes, the value of the normal stiffness (k_n) can be evaluated within the limits provided between λ_1 and λ_2 by tentatively setting $\tau o = 57.17$ in equation 7.45 where:

$$k_n = k_2 = \frac{\tau o}{L_1 \lambda_i} \qquad (7.50)$$

From here, k_n is the lesser of k_2 value for each value of λ_i.

Thus, for $\lambda_1 = 5.16$, $k_2 = 0.185N/mm$ and for $\lambda_2 = 0.76$, $k_2 = 1.254N/mm$. In this case, k_n is taken as $0.185N/mm$. Note, for extremely large value of k_n, delamination initiation will not be possible and may result in an unwarranted computational difficulties.

By modifying the above Mode I analysis for Mode II fracture, an effective stiffness which accounts for Mixed-Mode effect can be determined from equations 7.32 to 7.34 where:

$$\tan \Psi = \frac{\tau}{\sigma} = \frac{k_t}{k_n}$$

$$\text{Thus, } k_R = \sqrt{k_n^2 + {k_t}^2} \quad = \quad \sqrt{k_n^2 + \left[k_n \left(\frac{\tau}{\sigma}\right)\right]^2}$$

Note, values for $\tau = 3.56$ and $\sigma = 2.01$ are taken from Table 7.6, and they represent the allowable shear and tensile bond strengths of the interface. Therefore, solving for k_R, $0.376N/mm$ results.

From equation 7.34, $k_t = \sqrt{k_R^2 - {k_n}^2} = 0.327N/mm$

In this respect, at points 1 and 2 shown in Figure 7.28, reduced in-plane shear force is experienced between delamination initiation and propagation process where stiffness reduces significantly. This force usually tends to zero at full de-bonding stage.

Using the value of $k_t = 0.327N/mm$ as given above, the reduced shear force prior to complete debonding or loss of stiffness can be estimated by setting the slip (u_t^c) to the allowable value of $0.108mm$ (see Table 7.6).

Thus,

$$\tau_1 = k_t \, u_t^c = 0.327 \, X \, 0.108 = 0.035N$$

Similarly, solving for f_1 and $f_2$prior to critical de-bonding process, equation 7.37 was used:

$$f1 + f2 = \tau o \left(\frac{d_1}{L_1}\right)$$

By setting d_1 to its limits (allowable crack opening in Mode I), $d_1 = u_t^c = d_n = 0.035mm$. In the current analysis, remember that $L_1 = 60mm$ and $\tau o = 57.17N$.

Therefore, $f1 + f2 = 0.033$, from where it can be written that:

$$f2 = 0.033 - f1 \qquad (7.51)$$

By substituting for $f2$ in equation 7.40, and setting d_2 at a value above the critical d_n. In this case, the measured $d_2 = 0.099mm$ from the current FEA (see Figure 7.30).

Hence, $f1 = 0.017N$ and $f2 = 0.016N$.

Therefore, at point 1 where the interface is approaching the critical crack opening, the effective crack displacement under Mixed-Mode fracture can be estimated using Figure 7.29.

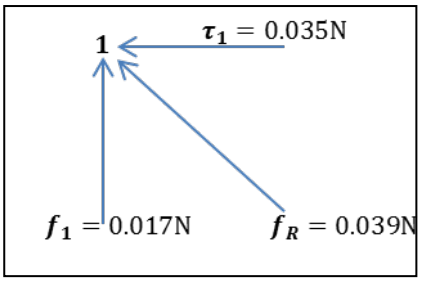

Figure 7.29: Reaction forces at Point 1

The constitutive Mixed-Mode equation is given by:

$$f_R = k_R\, d_R \qquad (7.52)$$

Solving for d_R:

$$d_R = \frac{f_R}{k_R} = \frac{0.039}{0.376} = 0.104mm$$

This value represents the predicted effective crack displacement under the current setting and compares well with $0.114mm$ required for debonding propagation in the FEM described in Figure 7.20.

Further, at critical Mixed-Mode crack propagation, the critical buckling load (τ_{cr}) can be estimated by setting d_1 to $d_R = 0.104mm$ in equation 7.36.

This gives:

$$\tau_{cr} = \tau o = \frac{f o\, L_1}{d_1} = 19.08N$$

In this respect, the corresponding value of λ is then given by equation 7.45.

Therefore, $\lambda = \frac{\tau o}{L_1 k_2} = \frac{\tau_{cr}}{L_1 k_R} = \frac{19.08}{60\ X\ 0.376} = 0.846$

Note, the estimated Mixed-Mode values of τ_{cr} and its corresponding λ are found to be slightly higher than those of Mode I fracture estimated from both equations 7.36 and 7.45 respectively. In Mode I, the resulting value of $\tau_{cr} = 17.33N$, while its $\lambda_{min} = 0.760$.

Lastly, by using equation 7.40, the corresponding value of d_2 can be determined and then used in relation to d_1 to establish the theoretical ratio between the Mixed-Mode critical crack displacement and the edge Crack Month Opening Displacement $(CMOD)$.

Thus, from equation 7.40, it can be shown that:

$$d_2 = \frac{L_1\,(4.92f2 + f1)}{\tau o} = \frac{L_1\,(4.92f2 + f1)}{\tau_{cr}} = 0.301mm$$

Therefore, the theoretical ratio between d_1 and d_2 is given by:

$$\xi_{analytical} = \frac{d_1}{d_2} = \frac{d_R}{d_2} = \frac{0.104}{0.301} = 0.346 \qquad (7.53)$$

In order to validate the above value of ξ, values of d_1 and d_2 corresponding to the current model of ANSYS FEA were obtained and compared with the analytical result given above.

In the ANSYS FEA graph shown in Figure 7.30, the corresponding values of the displacement in Mode I and Mode II along the interface were read-off by the horizontal red lines. Here at point 2, the slip and opening gap give $0.199mm$ and $0.099mm$ respectively

with an effective displacement value (d_2) of $0.222mm$ (see equation 3.35). On the other hand, at point 1, the resulting values of slip and opening gap are given by $0.066mm$ and $0.039mm$ with an approximate effective displacement value (d_1) of $0.077mm$.

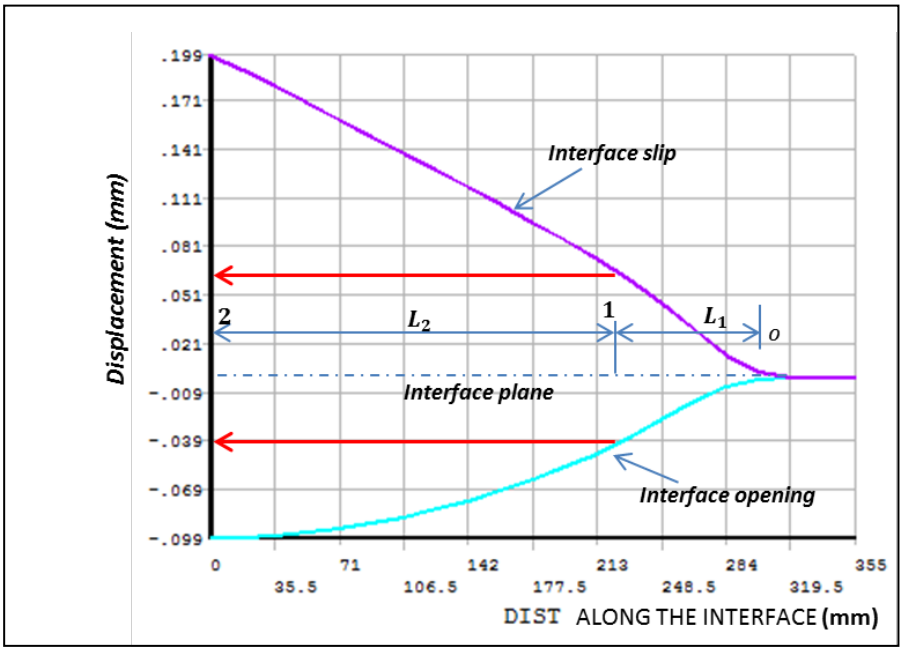

Figure 7.30: Variation of interface slip and opening during Mixed-Mode delamination process

From above, the numerical FEA value of ξ is given by:

$$\xi_{numerical} = \frac{d_1}{d_2} = \frac{0.077}{0.222} = 0.347 \qquad (7.54)$$

Comparing equations 7.53 and 7.54, it can be concluded that the analytical model simulates and compares well with the FEA result.

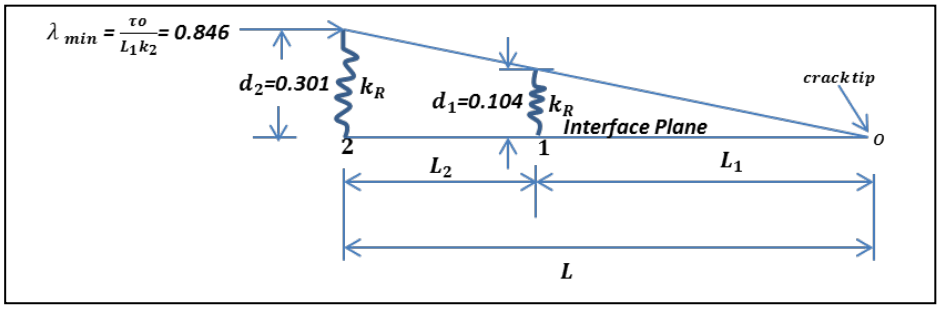

Figure 7.31: Mixed-Mode Buckling Mode-shape

Thus, the final Mode-shape due to Mixed-Mode delamination failure was drawn and illustrated in Figure 7.31.

This chapter presents the interfacial fracture process of the interface in Mode I, Mode II and Mixed-Mode of fracture. Experimental parameters were obtained for tensile and shear fracture modes of failure, and subsequently coupled in Mixed-Mode by FEA. Common differential edge deformation model between the overlay and the underlay was implemented for partial and full delamination studies. The result indicated that both studies exhibited different interfacial response, influenced distinctly and largely by the magnitude of the applied load. Other factors accounted in the analyses included the elastic mismatched properties, initial edge defect size, and the plane of loading. Lastly, analytical solution to the FEA problem was implemented using the proposed *Modified* Eigenvalue Buckling Analysis (MEBA). The result indicated that the proposed analytical method simulates and compares well with the FEA result. The proposed method also provided a good technique for predicting the Mixed-Mode Buckling failure Mode-Shape of the overlay.

8.0 Conclusions and Recommendations

The conclusions and the recommendations given in this section were based on the findings in the cause of undertaking this research project. Each part of the thesis found something different; hence, the findings were classified under the experimental and numerical / analytical works.

8.1 Conclusions

1. The research showed that for a composite material like BRCFRPMC required to satisfy several criteria simultaneously, the use of computational statistical tools is important, considering the level of flexibility and precision required in selecting an optimum mix. Mixture experiments within the context of material modelling were performed in executing such tasks.
2. Typically, quadratic models were fitted for the required properties of the overlay material, though linear models were also found adequate in some cases.
3. The overall material responses and performance were treated for typical early and matured-age of 3 and 28 days from where feasible regions of optimality were established and examined. Through optimization techniques, the optimum mixture

proportion which satisfies multiple responses at the same time was selected within an acceptable level of compromise.

4. The optimum mixture was found to contain about 61% of solid inclusions while the paste phase occupies the remaining 39% by volume of the total mixture. While keeping the solid inclusions constant, the optimum mixture proportion of cement, polymer, and water was found to be 0.7540, 0.0938, and 0.1523 respectively. Quantitatively, these values indicated that about $612.84kg/m^3$ of cement would be required, while both SBR polymer and water were considered at $76.24kg$ and $123.79kg$ respectively per cubic meter of the mixture.
5. The optimum consistency-time for full consolidation of the designed overlay material (BRCFRPMC) and its overall composite behaviour with the substrate ordinary Portland cement concrete (OPCC) was established between 34.05 and 34.87 seconds, while the resulting apparent maximum density achieves between 97.11% - 98.03 %TAFD.
6. The optimum mixture achieved about 35.21MPa and 54.94MPa compressive strength at 3 and 28 days, with tensile strength ranging between 12.14% and 16.16% of its compressive strength.
7. Because the optimum mixture exhibited a high early tensile strength, it indicated that the material should be able to withstand significant tensile stresses before cracking during restrained drying shrinkage, so long the induced strain is gradually applied.
8. The measured coefficient of thermal expansion between the overlay and the underlay OPCC were relatively close, thus showing that the overlay was thermally compatible with the OPCC.
9. The thermal analysis showed that thermal cracking under partial restraint of the interface was unlikely. For thermal cracking to occur, full axial restraint of the overlay would be required at a predicted differential temperature $> 23.87℃$ and a tensile stress well above 6.58MPa. Similarly, the predicted thermal stresses at the interface were generally less that those measured experimentally for the bond shear and tensile strength.
10. The investigations in this work demonstrated also that the material design of cementitious overlay material typically introduces some degree of intrinsic elastic mismatched problem at early age. In this work, the observed elastic modulus due to the overlay was 12.87GPa while that of the OPCC was 22.30GPa. In terms of

thermal cracking tendency of the overlay, overlay materials with lower elastic properties are preferred, but it also induces stress gradient problems in the BCO systems which are generally undesirable in the vicinity of the interface.

11. The interfacial bond strength tests revealed that the optimum mixture exhibited good bonding capability with the substrate OPCC both in tension and shear. The bond tests achieved 2.01MPa to 2.31MPa tensile and 3.56MPa to 4.69MPa shear strength.
12. In the bond strength tests, the results indicated that both surface texture and age had positive effects on tensile and shear strength. However, the overall contribution of surface texture appears more beneficial in shear than in tensile. This is explicable because the mechanics of interfacial de-bonding and interlocking differ in both cases. Specifically, the estimated benefits of surface texture on shear over tensile strength range averagely between 14% and 31% for equal differential texture levels.
13. The delamination parameter Z_D and the Mixed-Mode energy release rate (G_{ic}) vary numerically, and depend largely on: the initial edge defect size, the magnitude of the applied external load, elastic mismatched properties of the bonded dissimilar materials, and the loading plane configuration of the model (plane stress or plane strain).
14. The numerical values of Z_D in this research work varied between 0.15 and 1.54 for partial delamination problems, and between 0.63 and 1.32 for complete delamination problems.
15. Generally, a clear distinction exists between more compliant overlay materials (where $\alpha \ll 0$) and less compliant materials where $\alpha \approx 0$. The FEA results showed that lesser driving force is generally required to delaminate the former.
16. The results obtained from the proposed *Modified* Eigenvalue Buckling Analysis (MEBA) indicated that the analytical method simulates and compares well with the FEA result. The proposed method also provided a good technique for predicting the Mixed-Mode Buckling failure Mode-Shape of the overlay.

8.2 Recommendations

The followings are recommended for future works:

1. Mixed-Mode laboratory testing on bonded samples is recommended for subsequent investigations due to its practical importance,
2. Full scale thermal experimental investigations on bonded samples are recommended in order to establish the threshold of the interface response to temperature changes,
3. Full scale shrinkage testing between the overlay and the underlay in their bonded state is recommended in order to validate the analytical approached adopted in this study,
4. Full-scale roller-compaction of the optimum mixture is recommended to validate its response under the vibrating roller, and the resulting consolidation level achieved,
5. Extending the Finite Element Analysis to account for other forms of delamination other than the edge model investigated here is recommended.
6. Exclusive study of the effects of Dundur's parameter (α) on the failure mode shape of the overlay using MEBA is recommended.

References

AASHTO (1993) “Guide for Design of Pavement Structures,” Washington, DC: American Association of State Highway and Transportation Officials.

AASHTO (1998) “Supplement to the AASHTO Guide for Design of Pavement Structures,” Washington, DC: American Association of State Highway and Transportation Officials.

ACI 207.5R-99 (1999), “Roller-Compacted Mass Concrete*,” ACI Committee Report*, Farmington Hills, Ml, USA.

ACI 211.1 (1991) Standard practice for selecting proportions for normal, heavyweight, and mass concrete. ACI Committee Report, Farmington Hills, Ml, USA.

ACI 211.3R (2002) Guide for selecting proportions for no-slump concrete. ACI Committee Report, Farmington Hills, Ml, USA.

ACI 224R-01 (2001) “Control of Cracking in Concrete Structures,” *American Concrete Institute,* Farmington Hills, Ml, USA.

ACI 318 – 05 (2005) “Building Code Requirements for Structural Concrete and Commentary,” *American Concrete Institute,* Farmington Hills, Ml, USA.

ACI 325.10R-10 (2010) “Report on Roller-Compacted Concrete Pavements,” *ACI Committee Report*, Farmington Hills, Ml, USA.

ACI 548.1R-92 (1992) “Guide for the Use of Polymers in Concrete,” *ACI Committee Report,* Farmington Hills, Ml, USA.

ACI 548.4-93 (1993) “Standard Specification for Latex-Modified Concrete Overlays,” *ACI Committee Report,* Farmington Hills, Ml, USA.

ACI 548.3R-03 (2003), “State-of-the-Art Report on Polymer-Modified Concrete,” *ACI Committee Report*, Farmington Hills, Ml, USA.

American Concrete Pavement Association (ACPA), *Concrete in Highway Transportation - Concrete Paving - 100 Years of Progress through Innovation.* http://www.pavement.com/Concrete_Pavement/ November 1991 [3 December 2009].

American Concrete Pavement Association (ACPA) (2001).

Alfano, G. and Crisfield, M.A. (2001) “Finite Element Interface Models for the Delamination Anaylsis of Laminated Composites: Mechanical and Computational Issues,” *International Journal for Numerical Methods in Engineering*, 501701-1736.

Annual Local Authority Road Maintenance (ALARM) Survey 2009 http://www.asphaltindustryalliance.com/ April 2009 [15 November 2009].

Armaghani, J.M., T.J. Larsen, and L.L. Smith. (1987) “Temperature Response of Concrete Pavement,” *Transportation Research Record 1121*. Washington, DC: Transportation Research Board (TRB), National Research Council, pp. 23–33.

AS 5100.1 (2004) “Bridge Design – Scope and general Principles,” *Australian Standard*

Asad, M., Baluch, M.H., and Al-Gadhid, A.H. (1997) “Drying shrinkage stresses in concrete patch repair systems,” *Magazine of Concrete Res.,* London, 49, 283 – 293.

Asbahan, R. E. (2009) “Effects of the Built-in Construction Gradient and Environmental Conditions on Jointed Plain Concrete Pavements,” PhD Dissertation, University of Pittsburgh.

ASTM C150 – 02 (2002), “Standard Specification for Portland Cement,” *ASTM International*, West Conshohocken, USA.

ASTM C496-90 (1991) **“**Standard Test Method for Splitting Tensile Strength of Cylindrical Concrete Specimens,**”** *ASTM International*, West Consshohocken.

ASTM C469 / C469M – 94, (1994) “Standard Test Method for Static Modulus of Elasticity and Poisson's Ratio of Concrete in Compression,” *ASTM International*, West Consshohocken.

ASTM C496 / C496M - 11 (2011) “Standard Test Method for Splitting Tensile Strength of Cylindrical Concrete Specimens,” *ASTM International*, West Conshohocken, USA.

ASTM C1170 / C1170M - 08 (2008), “Standard Test Method for Determining Consistency and Density of Roller-Compacted Concrete Using a Vibrating Table,” *ASTM International*, West Conshohocken, USA.

ASTM C1439-99 (1999) Standard test methods for polymer-modified mortar and concrete. ASTM International, West Conshohocken, USA.

ASTM C1439 - 08 (2008), “Standard Test Methods for Evaluating Polymer Modifiers in Mortar and Concrete,” *ASTM International*, West Conshohocken, USA.

ASTM C138 (2001) Standard test method for density (unit weight), yield, and air content (Gravimetric). ASTM International, West Conshohocken, USA.

ASTM (D792-00) (2000) “Standard Test Methods for Density and Specific Gravity (Relative Density) of Plastics by Displacement,” *ASTM International*, West Conshohocken, USA.

ASTM D792 (2008) Standard Test Methods for Density and Specific Gravity (Relative Density) of Plastics by Displacement. ASTM International, West Conshohocken, USA.

Atkinson, C., Avila, J., Betz, E. and Smelser, R.E. (1982) “The rod pull out problem, theory and experiment,” *Journal of Mechanics and Physics of Solids*, 30, 97 – 120.

Barenblatt, G. I. (1962), “The Mathematical theory of equilibrium cracks in brittle fracture,” *Advanced Applied Mechanics*, 7, 55–129.

Barthelemy and Haftka, Review of approximation techniques http://www.brad.ac.uk [1 April 2009].

Bazant, Z.P. (1984) “Size effect in blunt fracture: Concrete, rock, metal, *Journal of Engineerinf Mechanics,” ASCE* **110**(4) 518 – 535.

Bazant Z.P. and Pijaudier-Cabot, G. (1989) “Measurement of Characteristic Length of Nonlocal Continuum,” *Journal of Engineering Mechanics*, **115**(4) 755 – 767.

Bazant, Z. P., Yu, Q., and Zi, G. (2002) “Choice of standard fracture test for concrete and its statistical evaluation,” *International Journal of Fracture*, 118, 303 – 337.

Bazant, Z. P. and Zi, G. (2003) “Size effect law and fracture mechanics of the triggering of dry snow slab avalanches,” *Journal of Geophysical research*, **108**(B2), 2119.

BCA. ‘Whitetop’ - Concrete overlays and inlays. Publication 46.032, British Cement Association, Crowthorne. 1993.

Beushausen, H.D. (2005) Long-Term Performance of Bonded Overlays Subjected to Differential Shrinkage. PhD Thesis, University of Cape Town, South Africa.

Bissonnette, B., Alexander M. V., and Kurt F. von Fay (2012) Best Practices for Preparing Concrete Surfaces Prior to Repairs and Overlays - Report Number MERL 12-17. U.S. Department of the Interior Bureau of Reclamation Technical Service Center Denver, Colorado

Blaga, A. and Beaudoin, J.J. (1985) “Polymer Modified Concrete,” *Canadian Building Digest. CBD*, 242, Ottawa, USA.

Bordelon, A. C. (2007) “Fracture behavior of concrete materials for rigid pavement systems,” *MSC THESIS, UNIVERSITY OF Illinois*.

Bower, A.F. (2010) *Applied Mechanics of Solid*, Taylor and Francis Group, LLC.

Box, G.E.P. and Draper, N.R. (1987) *Empirical Model-Building and Response Surfaces*, 1st edn. John Wiley & Sons Inc.

Bradury, R. D., (1938) “Reinforced concrete pavements,” *Wire Reinforcement Institute*, Washington DC.

BS 1881 -117 (1983) “Testing concrete: Method for determination of tensile splitting strength,” *British Standard Institute.*

BS 598-3 (1985) “Sampling and examination of bituminous mixtures for roads and other paved areas, Methods for design and physical testing,” *British Standard Institute*

BS 8110 -2 (1985) “Structural use of Concrete - Part2: Code of practice for special circumstances,” *British Standard Institute.*

BS EN 12390-6 (2000) “Testing hardened Concrete. Testing Splitting Strength of test specimens,” *British Standard Institute.*

BS EN 1504-3 (2005) “Products and systems for the protection and repair of concrete structures. Definitions, requirements, quality control and evaluation of conformity. Structural and non-structural repair,” *British Standard Institute.*

Brühwiler, E. and Wittmann, F.H. (1990) “The wedge splitting test, a new method of performing stable fracture mechanics test,” *Engineering Fracture Mechanics*, 35, 117-125.

Buyukozturk O. and Hearing, B. (1998) “Crack propagation in concrete composites influenced by interface fracture parameters,” *International Journal of Solids and Structures*, **35**(31-32) 4055 – 4066.

Caballero, A., Willam, K.J., and Carol, I. (2008) “Consistent tangent formulation for 3D interface modeling of cracking/fracture in quasi-brittle materials,” *Computer Methods in Applied Mechanics and Engineering,* Volume 197, Issues 33-40*,* pp*.* 2804 - 2822.

Carlsson, L.A. and Prasad, S., (1993) “Interfacial fracture of sandwich beams,” Engineering Fracture Mechanics, 44(4) 581 – 590.

Carter, P., Gurjah, S. and Wong, J (2002) “Debonding of Highway Bridge Deck Overlays – Observations from Alberta,” Canada. *Concrete International*, 51 - 58.

Casias, T. J., Goldsmith, V. D., and Benavidez, A. A. (1988) “Soil Laboratory Compaction Methods Applied to RCC. In: *Proceedings, Roller Compacted Concrete II,”* ASCE, February, San Diego, Calif., p: 107-122.

Cauwelaert, F. Van (2004) *Pavement Design and Evaluation: The required mathematics and its applications*. Edited by M.J.A. Stet. Federation of the Belgian Cement Industry, Brussels.

CEB-FIP-90 (1993) *Model code for Concrete Structures*, 1st edn. Thomas Telford.

Chandra, N. (2002) “Evaluation of interfacial fracture toughness using cohesive zone model,” Composite: Applied science and manufacturing, Part A 33, 1433 – 1447.

Charalambides, P. G., Cao, H.C. Lund, J. Evans, A.G. (1990) “Development of a test method for measuring the mixed mode fracture resistance of bimaterial interfaces,” *Mechanics of Materials*, 8, 269 – 283.

Cornec, A., Scheider, I. and Schwalbe, K. (2003) “On the practical application of the cohesive model,” *Engineering Fracture Mechanics,* **70**(14), 1963-1987.

Cornell, (2002) *Experiments with Mixtures – Designs, Models, and the Analysis of Mixture Data*, 3rd edn. John Wiley & Sons Inc

Czarnecki, L. and Lukowski, P. (1998) “Optimization of Polymer-Cement Concrete, In: Brandt A.M. ed. *Optimization methods for material design of cement-based composites*,” E & FN Spon, London and New York, pp. 231- 250.

Czarnecki, L., Garbacz, A., Lukowski, P., and Clifton, J.R. (1999), **“**Optimization of Polymer Concrete Composites: Final Report,” NISTIR 6361.

Das, B. M. (1999) *Principles of Foundation Engineering*, 4th edn. PWS Publishing.

Dantu, P. (1958) “Study of the distribution of stresses in a two-component heterogeneous medium. *Symposium Non-Homogeneity in Elasticity and Plasticity*,” *Warsaw*. Pergamon Press, London, pp. 443 – 451.

Delatte, N.J., Fowler, D.W., McCullough, B.F., and Grater, S.F. (1998) “Investigating Performance of Bonded Concrete Overlays,” *Journal of Performance of construction facilities*, 12, No. 2, 62-70.

Delatte, N.J. (2008) *Concrete Pavement Design, Construction and Performance*, 1st edn. Taylor & Francis.

Dias da Silva, V. (2006) *Mechanics and Strength of Material.* Springer.

Dugdale, D.S. (1960) “Yielding of steel sheets containing slits,” *Journal of the Mechanics and Physics of Solids*, 8, 100- 104.

Dundurs, J. (1969) “Edge-Bonded Dissimilar Orthogonal Elastic Wedges Under Normal and Shear Loading,” ASME Journal of Applied Mechanics, 36, 650 – 652.

Eisenmann, J. (1979) *Concrete Pavements – Design and Construction* (in German) Wilhelm Ernst & Sohn, Berlin/Munich/Düsseldorf.

Elice, M. and Planas, J. (1989) “Material Models. In: Elfgren L. *Fracture Mechanics of Concrete Structures, From theory to applications*, *RILEM REPORT*,” Chapman and Hall, 16 – 66.

Emberson, N.K. and Mays, G.C. (1990) “Significance of Property Mismatch in the Patch Repair of Structural Concrete – Part 1: Properties of Repair Systems. *Magazine of Concrete Research,”* 42, No. 152, 147-160.

Emmons, P.H. and Vaysburd, A.M. (1996) “System concept in design and construction of durable concrete repairs,” *Construction and Building Materials*, **10** (1), 69 – 75.

Engineering statistical eHandbook, (2003) *NIST/SEMATECH e-Handbook of Statistical Methods*, http://www.itl.nist.gov/div898/handbook/, date.

Eurocode 2 (BS EN, 1992) “Design of Concrete Structures.”

Falk, M.L., Needleman, A., Rice J.R. (2001) “A critical evaluation of cohesive zone models of dynamic fracture,” *Journal de Physique IV, Proceedings*, 543-550.

Garg, S.K. (2005) *Soil Mechanics and Foundation Engineering*, 6th edn. Khanna Publishers.

Gdoutos, E.E. (2005) *Fracture Mechanics: An Introduction*, 2nd edn. Springer.

Gohnert, M. (2003) “Horizontal shear transfer across a roughened surface,” *Cement and Concrete Composites*, 25, 379- 385.

Gözlüklü, B. (2009) “Delamination analysis by using cohesive interface elements in laminated composites,” *MSc. Thesis in Mechanical Engineering, Middle East Technical University*.

Granju, J.L. (2001) “Debonding of Thin Cement – Based Overlays,” *Journal of materials in civil engineering*, 13, No. 2, 114-120.

Granju, J.L. (1996) “Thin Bonded Overlays – About the Role of Fibre Reinforcement on the Limitation of Their Debonding,” *Advanced Cement Based Material*, 4, 21 – 27.

Griffiths, G. and Thom, N. (2007) *Concrete Pavement Design Guidance Notes*, 1st edn. Taylor & Francis.

Guinea, G. V., Planas, J. and Elices, M. (1994) “A general bilinear fitting for the softening curve of concrete,” *Materials and Structures*, 27, 99 – 105.

Guinea, G. V., Planas, J. and Elices, M. (2000) “Assessment of the tensile strength through size effect curves,” *Engineering Fracture Mechanics*, 65, 189 – 207

Gupta, A. and Gupta, B.L. (2003) “Roads, Railways, Bridges, Tunnels and Harbour Dock Engineering,” 5th edn. Standard Publishers.

Hall, K., Dawood, D., Vanikar, S. Tally Jr., R., Cackler, T., Correa, A., Deem, P., Duit, J. Geary, G., Gisi, A., Hanna, A., Kosmatka, S., Rasmussen, R., Tayabji, S., and Voigt, G. (2007) *Long-Life Concrete Pavements in Europe and Canada,* Federal Highway

Administration U.S., Department of Transportation American Association of State Highway and Transportation Officials.

He, M. Y. and Hutchinson, J.W. (1989) “Crack deflection at an interface between dissimilar elastic materials,” *International Journal of Solids and Structures*, 25, 1053 – 1067.

Harper, P.W. and Hallet, S.R. (2008) “Cohesive Zone Length in Numerical Simulations in Composite Delamination,” *Engineering Fracture Mechanics,* 75, 4774–4792.

Harrington, D., DeGraaf, D., Riley, R., Rasmussen, R.O., Grove, J. and Mack, J. (2007) *Guide to Concrete Overlay Solutions.* National Center for Concrete Pavement Technology (CP Tech Center), Iowa State University.

Hogg, A. H. A. (1938) “Equilibrium of a thin plate, symmetrically loaded, resting on an elastic foundation of infinite depth. *Philosophical Magazine*,” Series 7, Vol. 25, March, pp.576 – 582.

Holl, D. L. (1938) “Equilibrium of a thin plate, symmetrically loaded, on a flexible subgrade,” *Iowa State Coll. J. Sci.*, 12(4), July, Ames, IA, 455 – 459.

Houben, L. J. M. (2003) “Structural design of Pavement – Part IV: Design of Concrete Pavements, Lecture Notes CT4860,” Faculty of Civil Engineering and Geosciences, TU Delft; Delft.

Hillerborg, A., Modeer, M. and Petersson, P.E. (1976) “Analysis of crack formation and crack growth in concrete by means of fracture mechanics and finite elements,” *Cement and Concrete Research*, 6, 773 – 782.

Huang, Y.H. (2004) *Pavement Analysis and Design, 2nd Edition*, Upper Saddle River, NJ: Prentice-Hall.

Hughes, B.P. and Lubis, B. (1996) “Roller compacted sheets of polymer modified mortar,” *Cement and Concrete Composites*, 18, No.1, 41- 46.

Hughes, B. P. (2006) “Optimum design for sustainable concrete pavements. Proceedings of the Institute of Civil Engineers,” *Engineering Sustainability 159*, 127 - 132.

Hui, C.Y., Jagota, A., Bennison, S.J., Londono, J.D. (2003) “Crack blunting and the strength of soft elastic solids,” *Proceedings of the Royal Society of London A*, 459, 1489-1516.

IDOT (2000). Test Method No. Iowa 406-C: Method of Test for Determining the Shearing Strength of Bonded Concrete. Iowa Department of Transportation, Ames, IA, May

Illinois Department of Transportation (IDOT, “2005) Bureau of Material and Physical Research, *Maintenance, Repair and Rehabilitation (PTA-M3 (Eff. 10/1996, Rev. 02/2005) – Pavement Technology Advisory, Bonded Concrete Overlay.*

Ioannides, A. M., Thompson, M. R., and Barenberg, E. J. (1985) “Westergaard solutions reconsidered,” Transportation Research Record 1043.

Ioannides, A. M. (2006) “Concrete Pavement Analysis: the first eighty years,” *International Journal of Pavement Engineering*, 7, No. 4, 233 – 249.

Irwin, G.R. (1960) “Plastic zone near a crack and fracture toughness. In *Proceedings of the Seventh Sagamore Ordnance Materials Conference,”* vol. IV, 63-78, New York: Syracuse University.

Janssen, D. J. and Snyder, M. B. (2000) “Temperature-Moment Concept for Evaluating Pavement Temperature Data,” Technical Note No. 19948. *Journal of Infrastructure Systems.* American Society of Civil Engineers. Reston, VA, 6: (2), 81-83.

Jeong, J.H. and Zollinger, D.G. (2004) “Early-age curling and warping behavior: insights from a fully instrumented test-slab system,” *Journal of the Transportation Research* Board 1896, Transportation Research Record, Washington, DC, 66–74.

Jepsen, M.T. (1999) “Green Concrete. *Concrete Centre Danish Technological Institute, Denmark*.

Johnson, A. *Pavement Design Principles* http://www.clemson.edu *[7 November 2009].*

Johnson, K.L. (1985) *Contact Mechanics*. Cambridge University Press.

Karadelis, J.K. and Koutselas, K. (2003) "Sustainable 'Green' Overlays for Strengthening and Rehabilitation of Concrete Pavements. In: *Proceedings, 10th International Conference, Structural Faults + Repair*," London, UK, ISBN 0-947644-52-0, 94 (also on CD-ROM).

Kelley, E. F. (1939) "Application of the results of research to the structural design of concrete pavements, Proceedings of the American Concrete Institute," *Journal of the American Concrete Institute*, 437 – 464.

Kerali, H. *Introduction to Highway Development & Management (HDM-4)* http://hdm4.piarc.org 2000 [7 November 2009].

Kikuchi, N. and Oden, J.T. (1988) "Contact Problems in Elasticity: A study of Variational Inequalities and Finite Element Methods," SIAM, Philadelphia.

Kirsch, (1898) *Die Theorie der Elastizität und die Bedürfnisse der Festigkeitslehre.* Zeitschrift des Vereines deutscher Ingenieure, 42, 797–807.

Kishen, J.M., and Saouma, V.E. (2004) "Fracture of Rock-Concrete Interface: Laboratory Test and Application," *ACI Structural Journal May/June Technical Paper Title 101-S33.*

Lahitou, L., Choi, S., and Won, M. (2008) *Debonding in Bonded Concrete Overlays over Continuously Reinforced Concrete Pavements*. Center for Transportation Research, The University of Texas at Austin, FHWA/TX-09/0-4893-4.

Lepech, M.D., Keoleian, G.A., Qian, S. and Li, V.C. (2008) "Design of green engineered cementitious composites for pavement overlay application. In: *Proceedings of the International Symposium on Life-Cycle Civil Engineering,"* Taylor & Francis Group, London, ISBN 978-0-415-46857-2, 837-842.

Lim, Y.M., Kim, M.K., and Shin, S.K. (2001) "Numerical Simulation for Quasi-Brittle Interface Fracture in Cementitious Bi-material System," *Fracture Mechanics of Concrete Structures 73-80*

Liu, K., Barr, B.I.G., and Watkins (1985) “Mode II fracture of fibre reinforced concrete materials,” *Int. J. Cement Composite and Lightweight Concrete*, **7**(2), 93-101.

Liu, Y. (2003) Lecture notes: “Introduction to the Finite Element Method.” University of Cincinnati, USA.

Loseberg, A. (1960) *Structural Reinforced Concrete Pavements*, Doktorsavhandlingar Vid Chalmars Tekniska Hogskola, Gotesborg, Sweeden.

Majidzadeh, K. (1988) “A Mechanistic Approach to Rigid Pavement Design. In: Stock A.F. ed. *Concrete Pavement*,” Elsevier Applied Science Publishers LTD, UK.

Mayhew, H. C. and Harding, H. M. (1987) *Thickness Design of Concrete Roads*, Research Report 87, Transport and Road Research Laboratory, ISSN 0266 5247.

Mays, G. and Wilkinson, W. (1987) “Polymer Repairs to Concrete; Their Influence on Structural Performance,” *ACI Special Publication* SP-100-22.1, 351-375.

McLean, R. A. and Anderson, V. L. (1966), “Extreme Vertices Design of Mixture Experiments,” *Technometrics*, 8(3) 447-454

Megson, T. H. G. (2000) *Structural and Stress Analysis*, 2nd edn. BUTTERWORTH HEINEMANN.

Mehta, K.P. and Monteiro, J.M. (2006) CONCRETE: *Microstructure, Properties, and Materials*, 3rd edn. The McGraw - Hill Companies, Inc.

Mei, H., Pang, Y. and Huang, R. (2007) “Influence of Interfacial delamination on Channel cracking of elastic thin-films,” *Int. Journal of Fracture,* 148, 331 – 342.

Mei, H., Gowrishankar, S., Liechti, K.M. and Huang, R. *Initial and Propagation of interfacial delamination integrated thin-film structures* http://www.utexas.academia.edu/ShravanGowrishankar [12 *November 2010].*

Meyerhof, G. G. (1962) “Load carrying capacity of concrete pavements, Proceedings of the American Society of Civil Engineers,” *Journal of the Soil Mechanics and Foundations Division*.

Mindess, S. (1996) Test to determine the mechanical properties of the interfacial zone. In: Maso J.C. ed. *Interfacial Transition Zone in Concrete, RILEM REPORT 11.* E & FN SPON, 47 – 66.

Minitab 16 statistical software for Quality Improvement.

Mohamed, A. R. and Hansen, W. (1997) "Effect of Nonlinear Temperature Gradient on Curling Stress in Concrete Pavements," *Transportation Research Record 1568*. TRB, National Research Council. Washington, D.C. pp. 65-71.

Morgan, D.R. (1996) "Compatibility of concrete repair materials and systems," *Construction and Building Material*, 10, No.1, 57-67.

Mormonier, M.F., Desarmot, G., Barbier, B. and Letalenet, J.M. (1988) "A study of the pull-out test by a finite element method (in French)," *Journal of Theoretical and Applied Mechanics*, 7, 741 – 765.

Morrison, J.K., Shah, S.P. and Jena, Y.S. (1988) "Analysis of fibre debonding and pullout in composites," *ASCE Journal of Engineering Mechanics*, **114**(2), 277 – 294.

Mowris S. (1996) "Whitetopping Restores Air Traffic at Spirit of St. Louis" Concrete Construction.

Myers, R. H., and Montgomery, D. C., (1995), "Response Surface Methodology: Process and Product Optimization Using Designed Experiments*,"* John Wiley & Sons, New York, NY

Nawy, E.G. and Ukadike, M.M. (1983) "Shear Transfer in Concrete and Polymer Modified Concrete Members Subjected to Shearing Loads," *Journal of Testing and Evaluation, JTEVA,* **11**(2), 89 – 98.

Ohama, Y., and Kan, S. (1982) "Effects of Specimen Size on Strength and Drying Shrinkage of Polymer-Modified Concrete," *International Journal of Cement Composites and Lightweight Concrete*, **4**(4).

Ohama, Y., (1984) Polymer-Modified Mortars and Concrete. In: *Concrete Admixtures Handbook*. 337-429.

Ohama, Y. (1995) *Handbook of Polymer-Modified Concrete and Mortars*, 1st edn. Noyes Publications.

Ojdrovic, R. P., Stojimirovic, A.L., and Petroski, H.J. (1987) “Effect of age on splitting tensile strength and fracture resistance of concrete,” *Cement and Concrete Research*, 17, 70 – 76.

Karadelis, N.K., Koutselas, K., Lin, Y., Olubanwo, A., and Xu, Y. (2012) Sustainable, Bonded Overlays for the Repair and Strengthening of Concrete Pavements, *Global Magazine of Concrete Society*, **46**(07) 34-36.

Ouyang, C., Shah, S. P., and Swartz, S. E. (1995) *Fracture Mechanics of Concrete: Applications of Fracture Mechanics to Concrete Rock and other Quasi-Brittle Materials,* John Wiley.

Pasternak, P. L. (1954) Fundamentals of a new method of analysis of structures on elastic foundation by means of two subgrade coefficients, Gosudarstvennoe Izdatel’stvo Literatury po Stroitel’stvu I Arkhitekture, Moscow (in Russian).

Pavement Management Systems, Organization for Economic Co-operation and Development – OECD. Road Transport Research, Paris, 1987.

PCI (2011) *Design Handbook: Precast and Prestressed Concrete*, 7th Edn. Errata.

Petersson, P.E. (1981) “Crack Growth and Development of Fracture Zones in Plain Concrete and Similar Materials,” *Report* TVBM – 1006, Division of Building Materials, Lund Inst. of Technology, Lund, Sweden.

Pickett, G. (1951) “A study in the corner region of concrete slabs under large corner loads,” *Concrete Pavement Design for Roads and Streets*, Portland Cement Association Chicago, pp 77 – 87.

Pickett, G. and Ray, G.K. (1951) “Influence charts for concrete pavements,” Trans., ASCE, **116**, 49 – 73.

Portland Cement Association (PCA) (1966) *Thickness Design for Concrete Pavements*, Skokie, IL: Portland Cement Association.

Portland Cement Association (PCA) (1984) *Thickness Design for Concrete Highway and Street Pavements, Engineering Bulletin EB109P*, Skokie, IL: Portland Cement Association.

Rehabilitation. http:// www.pavementinteractive.org [2 October 2009].

Rice, J. R. and Sih, G. C. (1965) “Plane problems of cracks in dissimilar media.” *Journal of Applied Mechanics*, 418-423.

Rice, J.R. (1980) “The mechanics of earthquake rupture,” *Physics of the Earth's Interior, Proc. International School of Physics "Enrico Fermi"*, Course 78, 1979; ed. A.M. Dziewonski and E. Boschhi), Italian Physical Society and North-Holland Publ. Co., 555-649.

Rice, J. R. (1988) “Elastic fracture concepts for interfacial cracks,” *Journal of Applied Mechanics*, 55, 98 – 103.

RILEM Committee 50-FMC (1985) “Determination of the fracture energy of mortar and concrete by means of three-point-bend tests on notched beams,” RILEM Draft Recommendation, *Material and Structures*, **18**(106) 285 – 290.

Rocco, C., Guinea, G.V., Planas, J. and Elice, M. (1999) “Size effect and boundary condition in the brazilian test: theoretical analysis,” *Material and Structures*, 32, 436 – 444.

Rocco, C., Guinea, G.V., Planas, J. and Elice, M. (2001) “Review of the splitting-test standards from a fracture mechanics point of view,” *Cement and Concrete Research*, 31, 73 – 82.

Ruiz, J. M., Rasmussen, R. O., Chang, G. K., Dick, J. C., Nelson, P. K., Ferragut, T. R. (2005) *Computer-Based Guidelines for Concrete Pavements Volume I—Project Summary*, FHWA-HRT-04-121, Federal Highway Administration, McLean, VA 22101.

Saucier, F., and Pigeon, M. (1991) Durability of new-to-old concrete bondings. In: *Proceedings, ACI int. Conf. On Evaluation and Rehabilitation of Concrete Structures and Innovation in Design*, ACI, Detroit, 689 – 706.

Shah, H. and Stang, S.P. (1986) “Failure of fibre-reinforced composites by pullout fracture,” *Journal of Materials Science*, **21**(3), 953 -957.

Shah, H. and Stang, S.P. (1996) Micromechanics of interface in fibe-reinforced cement materials. In: Maso J.C. ed. *Interfacial Transition Zone in Concrete, RILEM REPORT 11.* E & FN SPON, 75 – 100.

Scheffe, H. (1958) “Experiments with Mixtures,” Journal of Royal Statistical Society, Ser. B, 21, 344-360.

Schmauder, S. (1987) "Theory of the Elastic Interface Crack", *Fortschrittsberichte der Deutschen Keramischen Gesellschaft: Werkstoffe, Verfahren, Anwendung 1986/1987, Beiheft zu CFI (Ceramic Forum International)* **2**, pp. 101-108.

Silfwerbrand, J. Beushausen, H. and Courard, L. (2012) Bond. In: Bissonnette, B., Courard, L., Fowler, D.W., and Granju, J. ed. State-of-the-Art Report of the RILEM Technical Committee 193-RLS, Springer, 51-79.

Simon, M.J., Lagergren, E.S., and Snyder, K.A. (1987), “Concrete Mixture Optimization using Statistical Mixture Design Methods.” In: Proceedings of PCI/FHWA, International Symposium on High Performance Concrete, New Orleans, Louisiana, 230 – 244.

Simon, M.J (2003), “*Concrete Mixture Optimization Using Statistical Methods*,” FHWA-RD-03-060, Federal Highway Administration, Washington, DC.

Suo, Z. and Hutchinson**,** J. W. (1989) “Sandwich specimens for measuring interface crack toughness,” *Materials Science and Engineering***,** A107**,** 135-143.

Suprenant, B. (1988) “Bonding new concrete to old,” *Concrete Construction*, 33, No. 7, 676-680.

Šušteršič, J. (2007) “Overlays on Bridge Decks made from High-Performance Fibre-Reinforced Concrete,” *Quark Magazine,* 146 – 151*.*

Swamy and Mangat (1975) “The onset of cracking and ductility of steel fiber concrete,” *Cement and Concrete Reseach*, **5**, 37 – 53.

Swedish National Road Administration (SNRA) (2004) “General Technical Regulations for Bridges,” Publication No. 2004:56, Borlange, Sweden.

Tang, T. (1994) “Effect of load-distributed width in split tension of un-notched and notched cylindrical specimens,” *Journal of Testing and Evaluation*, **22**(5) 401 – 409.

The Highways Agency, *Design Manual for Road and Bridges*, Vol. 7, Pavement Design, HD 26/06.

Thompson, M. R. (1996) “Mechanistic-empirical flexible pavement design: An overview,” Transportation Research Record 1539, Transportation Research Board, National Research Council, Washington, DC, pp. 1 – 5.

Timoshenko, S. P. and Goodier, J. N. (1970) *Theory of Elasticity*, 3rd edn. McGraw-Hill, New York.

Titus-Glover, L., Mallela, J., Darter, M.I., Voigt, G., and Waalkes, S. (2005) *Enhanced Portland Cement Concrete Fatigue Model for StreetPave*, *Transportation Research Record No. 1919*, Washington, DC: Transportation Research Board, 29–37.

TRRL (1969) “Instructions for Using the Portable Skid Resistance Tester,” Road Note 27, *Transport and Road Research Laboratory HMSO.*

Turon, A., Davila C.G., Camanho P.P., Costa, J. (2007) “An Engineering Solution for Mesh Size Effects in the Simulation of Delamination Using Cohesive Zone Models,” *Engineering Fracture Mechanics,* 74, 1665–1682.

Van Cauwelaert, F. (2004) *Pavement Design and Evaluation: The required mathematics and its applications*. Edited by M.J.A. Stet. Federation of the Belgian Cement Industry, Brussels.

Van Gemert, D., Czarnecki, L., Maultzsch, M., Schorn, H., Beeldens, A., Lukowski, P., & Knapen, E. (2005), “Cement concrete and concrete–polymer composites: Two merging worlds: A report from 11th ICPIC Congress in Berlin, 2004”. *Cement and Concrete Composites*, Vol. 27, No. 9-10, 926-935.

Walraven, J.C. (2007) “Strengthening and bond between new and old concrete – Overlay Design Concept,” *Group Concrete Structures*, Delft University of Technology.

Watkins, J. and Liu, K.L.W. (1985) “A finite element study of the short beam test specimen mode II loading,” *Int. J. Cement Composite and Lightweight Concrete,* **7**(1), 39-47.

Westergaard, H. M. (1926) “Stresses in Concrete Pavements computed by Theoretical Analysis,” Public Roads, Vol. 7, No 12, pp.23 – 35.

Westergaard, H. M. (1939) “Stresses in Concrete Runways of Airport,” *Proceedings*, Highway Research Board, Vol. 19, pp. 197 – 205.

Westergaard, H. M. (1947) “New Formulas for Stresses in Concrete Pavement of Airfields,” *Proceedings*, American Society of Civil Engineers, Vol. 73, pp 687 – 701.

Whitney, D.P., Isis, P., McCullough, B.F., and Fowler, D.W. (1992) “An Investigation of various factors affecting bond in bonded concrete overlays,” *Res. Rep.* 920-5, Centre for Transportation Research, University of Texas at Austin, Austin, Tex.

Williams, M. L. (1959) “The stresses around a fault or crack in dissimilar media.” *Bulletin of the Seismological Society of America*, 49(2), 199-204.

Winkler, E. (1867) Die Lehre von der Elastizitt und Festigkeit, (Theory of Elasticity and Strength), H. Dominicus, Prague (in Germany).

Wittmann, F.H., Rokugo, K., Bruhwiller, E., Mihashi, H. and Simopnin, P. (1988) Fracture energy and strain softening of concrete as determined by compact tension specimens. *Material and structure (RILEM, Paris)*, 21, 21 – 32.

Wriggers, P. (2002) *Computational Contact Mechanics*, 2nd edn. John Wiley & Sons, Ltd.

Yoder, E.J. (1964) *Principles of pavement Design,* 3rd edn. John Wiley & Sons Inc.

Ye, T. Suo, Z. and Evans A.G. (1992) “Thin film cracking and the roles of substrate and interface,” *International Journal of Solids and Structures*, 29, 2639 – 2648.

Zhang, D., Furuuchi, H., Hori, A., and Ueda, T. (2008) “Influence of Interface roughness on PCM-Concrete Interfacial Fracture Parameters,” *The 3rd ACF International Conference-ACF/VCA.*

APPENDIX A1: Compressive Strength Table

PMC compressive strength test					
Mix ID	**Sample ID**	***Compressive strength (MPa)***			
		3 days	***14 days***	***28 days***	***90 days***
M1	CS1 - M1	35.06	52.18	63.58	67.23
	CS2 - M1	41.87	45.25	59.78	72.11
	CS3- M1	39.04	50.75	61.47	75.14
	CS4 - M1	38.59	51.15	60.21	67.95
	CS5 - M1	37.76	49.01	61.49	65.91
Mean Compressive strength (σc)		***38.47***	***49.67***	***61.31***	***69.67***
Standard Deviation (σ^{-})		***2.45***	***2.72***	***1.48***	***3.84***
Coefficient of variation (Cv) %		***6.37***	***5.48***	***2.41***	***5.51***
Characteristic strength		***34.45***	***45.20***	***58.88***	***63.38***
M2	CS1 - M2	44.50	54.27	66.24	73.99
	CS2 - M2	40.68	49.31	60.38	67.87
	CS3- M2	41.02	46.63	61.81	74.06
	CS4 - M2	39.22	51.61	62.72	72.86
	CS5 - M2	39.04	50.87	62.87	69.07
Mean Compressive strength (σc)		***40.89***	***50.54***	***62.80***	***71.57***
Standard Deviation (σ^{-})		***2.20***	***2.83***	***2.16***	***2.90***
Coefficient of variation (Cv) %		***5.37***	***5.59***	***3.44***	***4.06***
Characteristic strength		***37.29***	***45.90***	***59.26***	***66.81***
M3	CS1 - M3	34.21	44.94	54.76	68.85
	CS2 - M3	33.83	42.22	52.62	64.94
	CS3- M3	32.78	42.71	53.01	65.42
	CS4 - M3	35.82	43.06	53.00	66.82
	CS5 - M3	34.19	42.53	53.34	66.63
Mean Compressive strength (σc)		***34.16***	***43.09***	***53.35***	***66.53***
Standard Deviation (σ^{-})		***1.09***	***1.08***	***0.83***	***1.52***
Coefficient of variation (Cv) %		***3.20***	***2.50***	***1.56***	***2.28***
Characteristic strength		***32.37***	***41.33***	***51.98***	***64.04***
M4	CS1 - M4	34.69	45.72	59.89	60.18
	CS2 - M4	36.80	42.57	56.78	58.85
	CS3- M4	35.88	42.51	54.95	59.29
	CS4 - M4	34.71	46.94	55.89	59.51
	CS5 - M4	32.88	44.47	56.88	61.70
Mean Compressive strength (σc)		***34.99***	***44.44***	***56.88***	***59.91***
Standard Deviation (σ^{-})		***1.47***	***1.95***	***1.86***	***1.11***
Coefficient of variation (Cv) %		***4.21***	***4.38***	***3.26***	***1.86***
Characteristic strength		***32.57***	***41.25***	***53.83***	***58.08***

APPENDIX A1: Compressive Strength Table

M5	CS1 - M5	41.06	52.55	61.84	69.42
	CS2 - M5	41.78	53.48	59.54	68.27
	CS3- M5	36.68	46.96	59.66	66.18
	CS4 - M5	37.67	48.22	58.91	66.18
	CS5 - M5	35.75	45.76	60.91	65.89
Mean Compressive strength (σc)		***38.59***	***49.39***	***60.17***	***67.19***
Standard Deviation (σ^{-})		***2.68***	***3.43***	***1.18***	***1.57***
Coefficient of variation (Cv) %		***6.95***	***6.95***	***1.96***	***2.34***
Characteristic strength		***34.19***	***43.76***	***58.23***	***64.61***
M6	CS1 - M6	36.95	37.12	47.10	60.03
	CS2 - M6	30.75	43.26	55.48	57.28
	CS3- M6	32.42	40.00	50.55	61.09
	CS4 - M6	32.40	40.92	49.41	59.00
	CS5 - M6	32.44	38.71	52.47	58.35
Mean Compressive strength (σc)		***32.99***	***40.00***	***51.00***	***59.15***
Standard Deviation (σ^{-})		***2.33***	***2.32***	***3.17***	***1.47***
Coefficient of variation (Cv) %		***7.06***	***5.79***	***6.21***	***2.49***
Characteristic strength		***29.17***	***36.20***	***45.81***	***56.73***
M7	CS1 - M7	36.16	40.49	54.74	58.48
	CS2 - M7	35.46	43.99	51.44	53.93
	CS3- M7	34.91	42.06	51.88	55.77
	CS4 - M7	32.89	40.36	49.86	56.76
	CS5 - M7	35.16	41.55	52.70	55.91
Mean Compressive strength (σc)		***34.92***	***41.69***	***52.12***	***56.17***
Standard Deviation (σ^{-})		***1.23***	***1.47***	***1.79***	***1.65***
Coefficient of variation (Cv) %		***3.51***	***3.53***	***3.44***	***2.94***
Characteristic strength		***32.90***	***39.28***	***49.19***	***53.46***
M8	CS1 - M8	32.48	45.94	55.71	62.41
	CS2 - M8	35.74	41.49	52.45	56.89
	CS3- M8	35.24	42.71	53.78	59.03
	CS4 - M8	31.42	42.84	52.85	59.46
	CS5 - M8	35.92	42.51	51.97	57.34
Mean Compressive strength (σc)		***34.16***	***43.10***	***53.35***	***59.03***
Standard Deviation (σ^{-})		***2.07***	***1.68***	***1.48***	***2.18***
Coefficient of variation (Cv) %		***6.05***	***3.89***	***2.77***	***3.70***
Characteristic strength		***30.77***	***40.35***	***50.93***	***55.45***

APPENDIX A1: Compressive Strength Table

M9	CS1 - M9	33.34	40.04	50.93	59.81
	CS2 - M9	30.71	39.85	47.44	55.79
	CS3- M9	30.41	38.60	49.42	57.85
	CS4 - M9	27.50	37.51	49.67	57.98
	CS5 - M9	30.28	37.60	48.23	58.50
Mean Compressive strength (σc)		***30.45***	***38.72***	***49.14***	***57.99***
Standard Deviation (σ^{-})		***2.07***	***1.20***	***1.35***	***1.45***
Coefficient of variation (Cv) %		***6.79***	***3.10***	***2.75***	***2.50***
Characteristic strength		***27.06***	***36.75***	***46.93***	***55.60***
M10	CS1 - M10	34.95	44.79	56.89	66.55
	CS2 - M10	36.81	45.48	58.31	62.35
	CS3- M10	34.70	46.44	55.94	65.92
	CS4 - M10	36.59	45.37	55.88	66.07
	CS5 - M10	35.76	47.02	56.53	66.27
Mean Compressive strength (σc)		***35.76***	***45.82***	***56.71***	***65.43***
Standard Deviation (σ^{-})		***0.95***	***0.89***	***0.99***	***1.74***
Coefficient of variation (Cv) %		***2.65***	***1.95***	***1.74***	***2.65***
Characteristic strength		***34.21***	***44.36***	***55.09***	***62.58***
M11	CS1 - M11	35.39	45.86	56.30	62.11
	CS2 - M11	36.58	44.40	54.58	60.56
	CS3- M11	36.83	45.42	56.43	61.63
	CS4 - M11	36.81	47.84	58.65	59.85
	CS5 - M11	38.46	45.28	54.44	62.09
Mean Compressive strength (σc)		***36.81***	***45.76***	***56.08***	***61.25***
Standard Deviation (σ^{-})		***1.09***	***1.28***	***1.71***	***1.00***
Coefficient of variation (Cv) %		***2.97***	***2.79***	***3.05***	***1.64***
Characteristic strength		***35.02***	***43.66***	***53.27***	***59.60***
M12	CS1 - M12	37.01	49.18	60.20	67.72
	CS2 - M12	37.90	50.84	58.20	68.55
	CS3- M12	38.64	47.25	58.81	65.66
	CS4 - M12	38.38	48.47	62.02	67.17
	CS5 - M12	37.99	50.23	58.18	66.21
Mean Compressive strength (σc)		***37.98***	***49.19***	***59.48***	***67.06***
Standard Deviation (σ^{-})		***0.62***	***1.42***	***1.64***	***1.16***
Coefficient of variation (Cv) %		***1.63***	***2.88***	***2.76***	***1.73***
Characteristic strength		***36.97***	***46.87***	***56.79***	***65.16***

APPENDIX A1: Compressive Strength Table

M13	CS1 - M15	33.22	44.28	55.44	62.05
	CS2 - M15	33.06	44.33	53.02	62.63
	CS3- M15	35.92	44.30	56.82	65.15
	CS4 - M15	33.57	43.44	54.29	62.37
	CS5 - M15	36.13	44.51	54.43	62.07
Mean Compressive strength (σc)		***34.38***	***44.17***	***54.80***	***62.85***
Standard Deviation ($\bar{\sigma}$)		***1.52***	***0.42***	***1.42***	***1.31***
Coefficient of variation (Cv) %		***4.41***	***0.95***	***2.59***	***2.08***
Characteristic strength		***31.89***	***43.48***	***52.48***	***60.71***

APPENDIX A2: PMC Tensile Strength Result Table

PMC CYLINDER INDIRECT TENSILE STRENGTH					
Mix ID	Sample ID	Tensile strength (MPa)			
		3 days	14 days	28 days	90 days
M1	PTS1 - M1	6.08	6.21	6.49	6.32
	PTS2 - M1	5.89	6.09	6.29	6.45
	PTS3 - M1	6.06	6.15	6.35	6.37
	PTS4 - M1	5.98	6.10	6.44	6.67
	PTS5 - M1	5.94	6.17	6.31	6.41
Mean Tensile strength (σt)		***5.99***	***6.14***	***6.38***	***6.44***
Standard Deviation (σ^{-})		***0.08***	***0.05***	***0.09***	***0.14***
Coefficient of variation (Cv) %		***1.34***	***0.81***	***1.35***	***2.10***
M2	PTS1 - M2	6.08	6.49	6.81	6.78
	PTS2 - M2	4.98	6.29	6.53	6.87
	PTS3 - M2	5.51	6.37	6.60	6.75
	PTS4 - M2	5.67	6.46	6.72	6.70
	PTS5 - M2	5.41	6.40	6.71	6.68
Mean Tensile strength (σt)		***5.53***	***6.40***	***6.67***	***6.76***
Standard Deviation (σ^{-})		***0.40***	***0.08***	***0.11***	***0.08***
Coefficient of variation (Cv) %		***7.23***	***1.23***	***1.64***	***1.11***
M3	PTS1 - M3	5.34	6.98	7.46	8.09
	PTS2 - M3	5.65	6.82	7.27	7.88
	PTS3 - M3	5.53	6.87	7.09	7.91
	PTS4 - M3	5.40	6.96	7.34	7.84
	PTS5 - M3	5.60	6.89	6.99	7.76
Mean Tensile strength (σt)		***5.50***	***6.90***	***7.23***	***7.90***
Standard Deviation (σ^{-})		***0.13***	***0.07***	***0.19***	***0.12***
Coefficient of variation (Cv) %		***2.38***	***0.95***	***2.62***	***1.55***
M4	PTS1 - M4	5.56	6.11	5.91	6.33
	PTS2 - M4	6.09	5.73	6.21	6.23
	PTS3 - M4	5.88	5.85	6.13	6.17
	PTS4 - M4	5.63	6.01	6.02	6.32
	PTS5 - M4	5.97	5.89	6.10	6.40
Mean Tensile strength (σt)		***5.83***	***5.92***	***6.07***	***6.29***
Standard Deviation (σ^{-})		***0.23***	***0.15***	***0.11***	***0.09***
Coefficient of variation (Cv) %		***3.86***	***2.48***	***1.88***	***1.44***

APPENDIX A2: PMC Tensile Strength Result Table

M5	PTS1 - M5	5.73	7.07	7.43	7.69
	PTS2 - M5	5.69	6.89	7.11	7.79
	PTS3 - M5	5.70	6.95	7.19	7.61
	PTS4 - M5	5.67	6.90	7.29	7.50
	PTS5 - M5	5.74	6.81	7.25	7.53
Mean Tensile strength (σt)		***5.71***	***6.92***	***7.25***	***7.62***
Standard Deviation ($\bar{\sigma}$)		***0.03***	***0.10***	***0.12***	***0.12***
Coefficient of variation (Cv) %		***0.53***	***1.38***	***1.65***	***1.56***
M6	PTS1 - M6	5.82	7.24	7.68	7.82
	PTS2 - M6	5.72	7.09	7.55	7.94
	PTS3 - M6	5.67	6.98	7.59	7.89
	PTS4 - M6	5.85	7.19	7.37	8.11
	PTS5 - M6	5.79	7.29	7.46	7.79
Mean Tensile strength (σt)		***5.77***	***7.16***	***7.53***	***7.91***
Standard Deviation ($\bar{\sigma}$)		***0.08***	***0.12***	***0.12***	***0.13***
Coefficient of variation (Cv) %		***1.30***	***1.73***	***1.59***	***1.60***
M7	PTS1 - M7	5.48	6.41	6.69	6.77
	PTS2 - M7	5.78	6.59	6.83	6.79
	PTS3 - M7	5.60	6.42	6.57	6.91
	PTS4 - M7	5.59	6.37	6.71	6.88
	PTS5 - M7	5.70	6.48	6.61	6.83
Mean Tensile strength (σt)		***5.63***	***6.45***	***6.68***	***6.84***
Standard Deviation ($\bar{\sigma}$)		***0.11***	***0.09***	***0.10***	***0.06***
Coefficient of variation (Cv) %		***2.04***	***1.33***	***1.51***	***0.86***
M8	PTS1 - M8	4.79	6.33	6.71	6.73
	PTS2 - M8	4.89	6.41	6.57	6.81
	PTS3 - M8	4.84	6.17	6.65	6.78
	PTS4 - M8	4.79	6.21	6.51	6.71
	PTS5 - M8	4.87	6.30	6.63	6.65
Mean Tensilestrength (σt)		***4.84***	***6.28***	***6.61***	***6.74***
Standard Deviation ($\bar{\sigma}$)					
Coefficient of variation (Cv) %					

APPENDIX A2: PMC Tensile Strength Result Table

M9	PTS1 - M9	4.99	6.21	6.18	6.46
	PTS2 - M9	4.53	6.17	6.11	6.58
	PTS3 - M9	4.70	6.15	6.36	6.46
	PTS4 - M9	4.68	5.89	6.27	6.41
	PTS5 - M9	4.88	6.00	6.21	6.82
Mean Tensile strength (σt)		***4.76***	***6.08***	***6.23***	***6.55***
Standard Deviation ($\bar{\sigma}$)		***0.18***	***0.13***	***0.09***	***0.17***
Coefficient of variation (Cv) %		***3.78***	***2.21***	***1.52***	***2.53***
M10	PTS1 - M10	5.61	6.92	6.97	7.08
	PTS2 - M10	5.50	6.80	7.13	7.46
	PTS3 - M10	5.56	6.83	7.05	7.23
	PTS4 - M10	5.51	6.64	6.97	7.22
	PTS5 - M10	5.57	6.72	7.09	7.36
Mean Tensile strength (σt)		***5.55***	***6.78***	***7.04***	***7.27***
Standard Deviation ($\bar{\sigma}$)		***0.04***	***0.11***	***0.07***	***0.15***
Coefficient of variation (Cv) %		***0.81***	***1.59***	***0.99***	***2.04***
M11	PTS1 - M9	5.55	6.74	6.50	7.13
	PTS2 - M9	5.49	6.13	7.12	7.22
	PTS3 - M9	5.71	6.35	6.87	6.95
	PTS4 - M9	5.63	6.33	6.58	7.00
	PTS5 - M9	5.58	6.60	6.98	7.10
Mean Tensile strength (σt)		***5.59***	***6.43***	***6.81***	***7.08***
Standard Deviation ($\bar{\sigma}$)		***0.08***	***0.24***	***0.26***	***0.11***
Coefficient of variation (Cv) %		***1.52***	***3.78***	***3.86***	***1.52***
M12	PTS1 - M9	6.49	6.67	7.00	7.18
	PTS2 - M9	5.31	6.53	6.87	7.38
	PTS3 - M9	5.88	6.61	6.94	7.19
	PTS4 - M9	6.05	6.47	6.88	7.14
	PTS5 - M9	5.77	6.59	6.96	7.26
Mean Tensile strength (σt)		***5.90***	***6.57***	***6.93***	***7.23***
Standard Deviation ($\bar{\sigma}$)		***0.43***	***0.08***	***0.06***	***0.10***
Coefficient of variation (Cv) %		***7.23***	***1.16***	***0.81***	***1.33***

APPENDIX A2: PMC Tensile Strength Result Table

M13	PTS1 - M9	5.65	6.58	6.47	7.14
	PTS2 - M9	5.50	6.64	7.09	6.70
	PTS3 - M9	5.52	6.58	6.84	6.84
	PTS4 - M9	5.47	6.41	6.55	7.03
	PTS5 - M9	5.42	6.76	6.95	6.89
Mean Tensile strength (σt)		***5.51***	***6.59***	***6.78***	***6.92***
Standard Deviation ($\bar{\sigma}$)		***0.09***	***0.13***	***0.26***	***0.17***
Coefficient of variation (Cv) %		***1.55***	***1.92***	***3.86***	***2.48***

APPENDIX A3: FINITE ELEMENT ANALYSIS CONTOURS (DELAMINATION FORMATION PROCESS)

Cohesive stress (Mode I)	Cohesive stress (Mode II)	Cohesive stress (Mixed Mode)
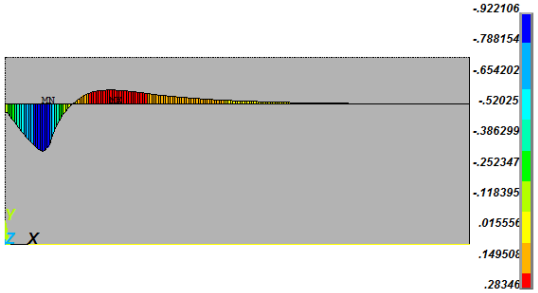		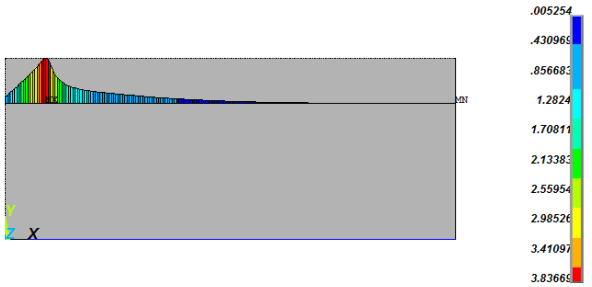
Notch size: 0.00mm ; Elastic prop. (α)=-0.221	***Notch size: 0.00mm ; Elastic prop. (α)=-0.221***	***Notch size: 0.00mm ; Elastic prop. (α)=-0.221***
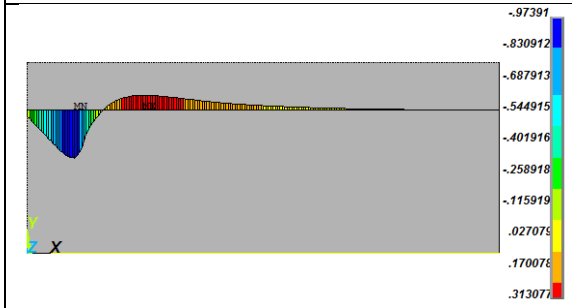	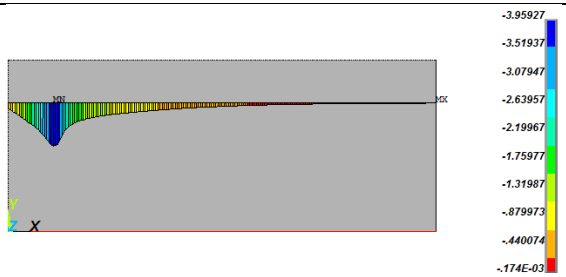	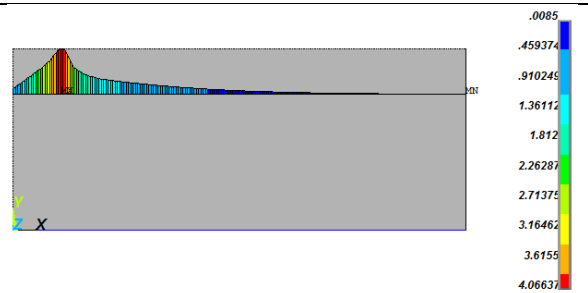
Notch size: 0.00mm ; Elastic prop. (α)=-0.040	***Notch size: 0.00mm ; Elastic prop. (α)=-0.040***	***Notch size: 0.00mm ; Elastic prop. (α)=-0.040***
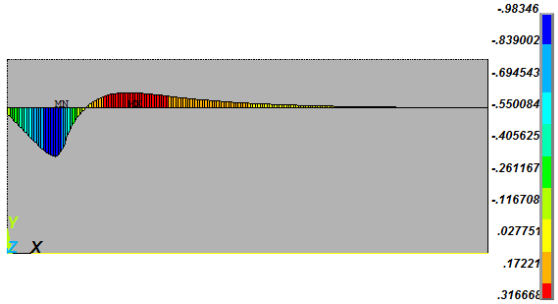	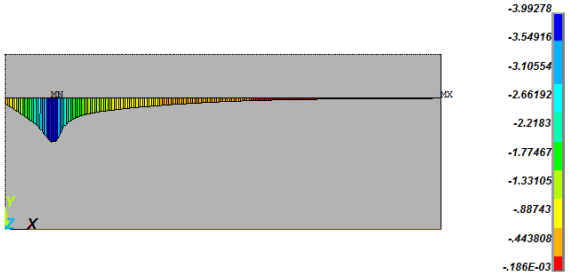	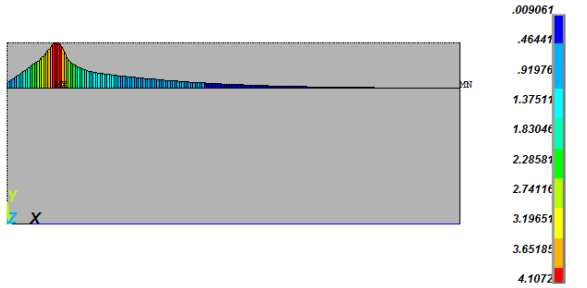
Notch size: 0.00mm ; Elastic prop. (α)=-0.015	***Notch size: 0.00mm ; Elastic prop. (α)=-0.015***	***Notch size: 0.00mm ; Elastic prop. (α)=-0.015***

APPENDIX A3: FINITE ELEMENT ANALYSIS CONTOURS (DELAMINATION FORMATION PROCESS)

Cohesive stress (Mode I)	Cohesive stress (Mode II)	Cohesive stress (Mixed Mode)
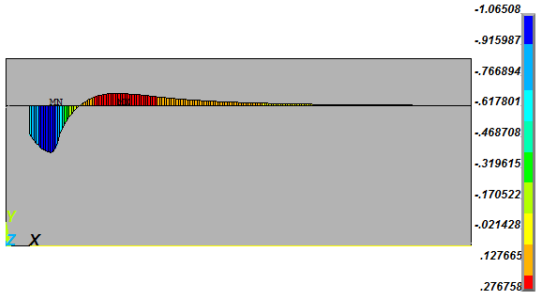 ***Notch size: 50.00mm ; Elastic prop. (α)=-0.221***	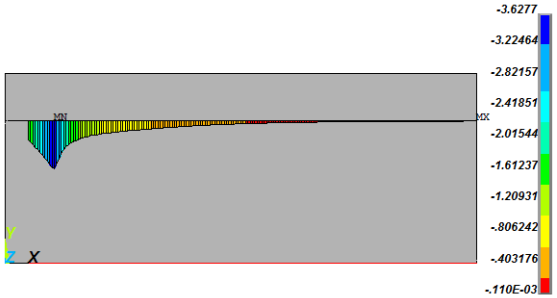 ***Notch size: 50.00mm ; Elastic prop. (α)=-0.221***	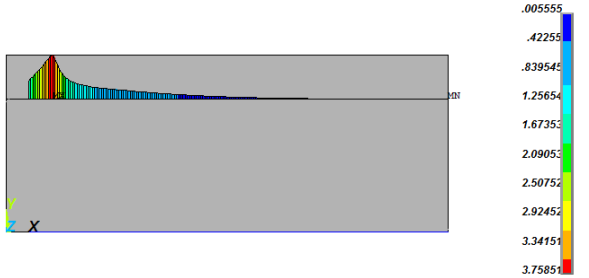 ***Notch size: 50.00mm ; Elastic prop. (α)=-0.221***
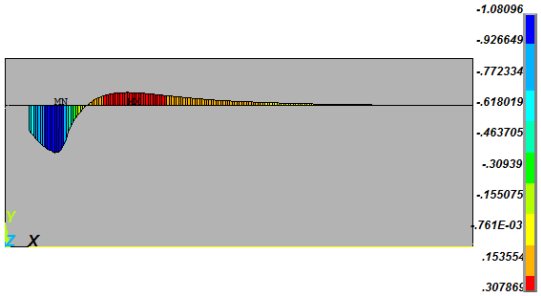 ***Notch size: 50.00mm ; Elastic prop. (α)=-0.040***	 ***Notch size: 50.00mm ; Elastic prop. (α)=-0.040***	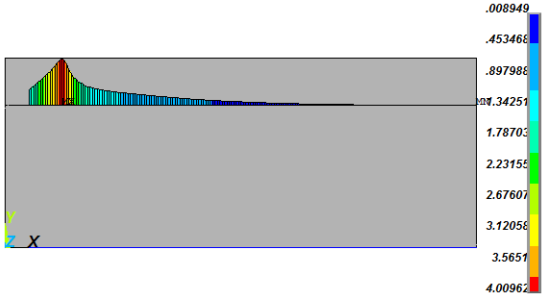 ***Notch size: 50.00mm ; Elastic prop. (α)=-0.040***
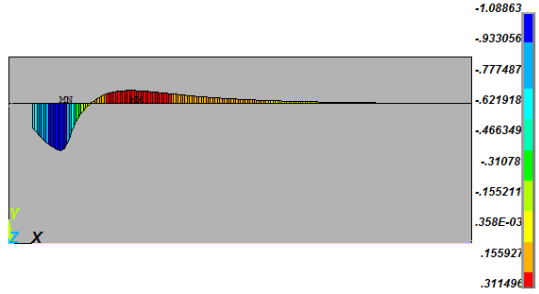 ***Notch size: 50.00mm ; Elastic prop. (α)=-0.015***	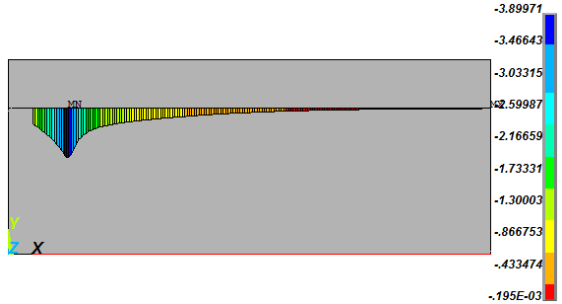 ***Notch size: 50.00mm ; Elastic prop. (α)=-0.015***	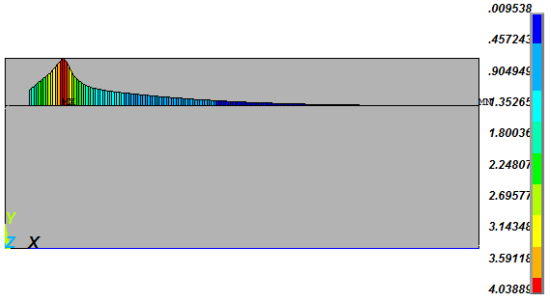 ***Notch size: 50.00mm ; Elastic prop. (α)=-0.015***

APPENDIX A3: FINITE ELEMENT ANALYSIS CONTOURS (DELAMINATION FORMATION PROCESS)

Cohesive stress (Mode I)	Cohesive stress (Mode II)	Cohesive stress (Mixed Mode)
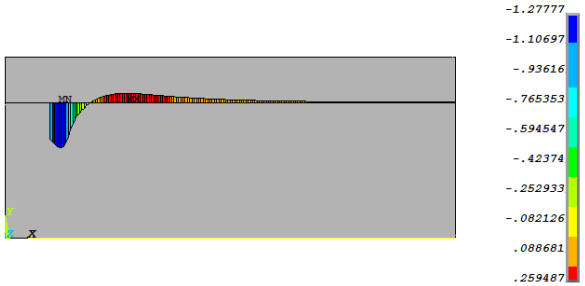 ***Notch size: 100.00mm ; Elastic prop. (α)=-0.221***	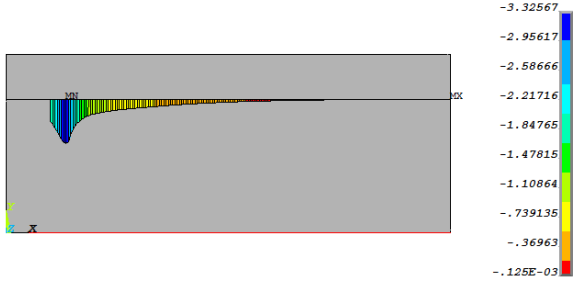 ***Notch size: 100.00mm ; Elastic prop. (α)=-0.221***	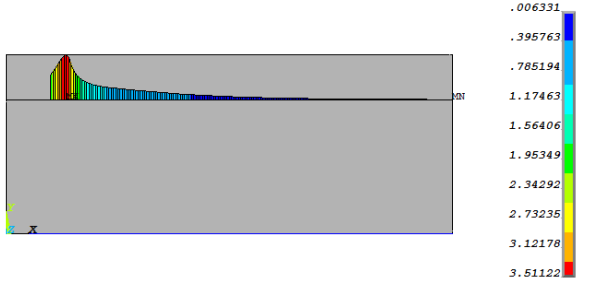 ***Notch size: 100.00mm ; Elastic prop. (α)=-0.221***
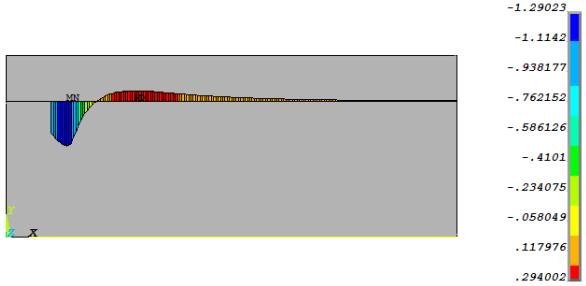 ***Notch size: 100.00mm ; Elastic prop. (α)=-0.040***	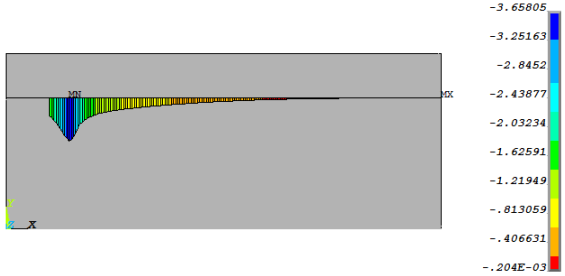 ***Notch size: 100.00mm ; Elastic prop. (α)=-0.040***	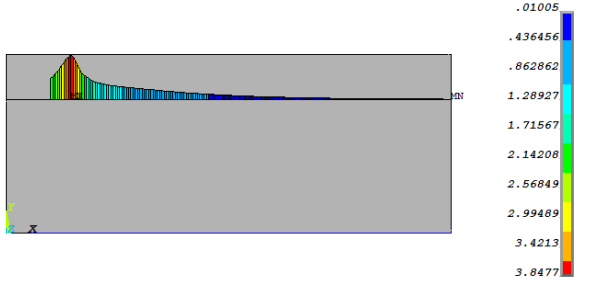 ***Notch size: 100.00mm ; Elastic prop. (α)=-0.040***
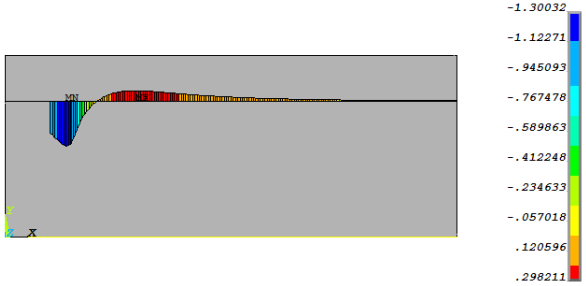 ***Notch size: 100.00mm ; Elastic prop. (α)=-0.015***	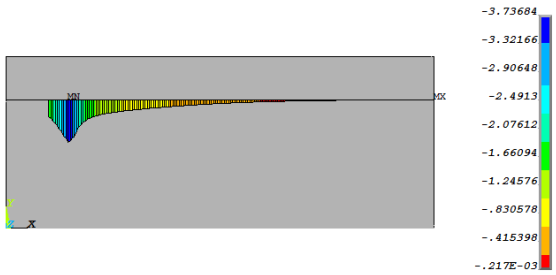 ***Notch size: 100.00mm ; Elastic prop. (α)=-0.015***	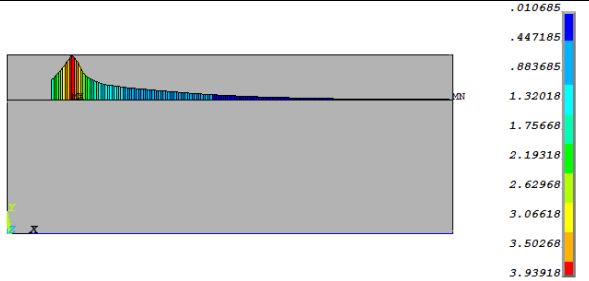 ***Notch size: 100.00mm ; Elastic prop. (α)=-0.015***

APPENDIX A3: FINITE ELEMENT ANALYSIS CONTOURS (DELAMINATION FORMATION PROCESS)

Cohesive stress (Mode I)	Cohesive stress (Mode II)	Cohesive stress (Mixed Mode)
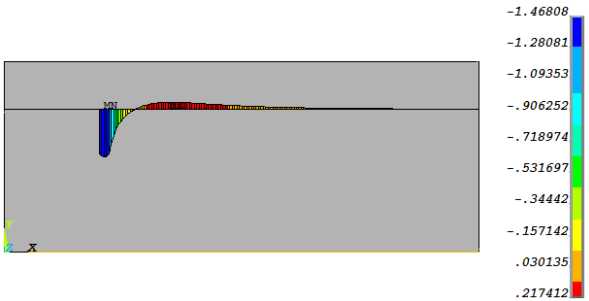 ***Notch size: 200.00mm ; Elastic prop. (α)=-0.221***	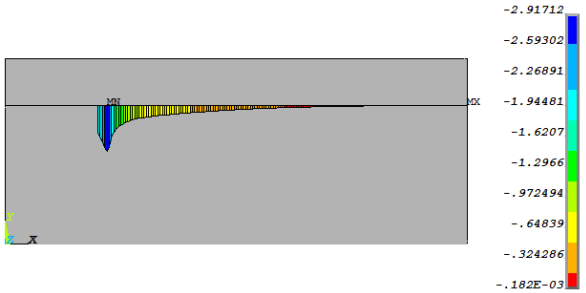 ***Notch size: 200.00mm ; Elastic prop. (α)=-0.221***	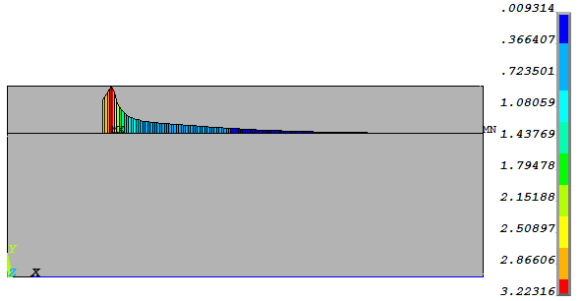 ***Notch size: 200.00mm ; Elastic prop. (α)=-0.221***
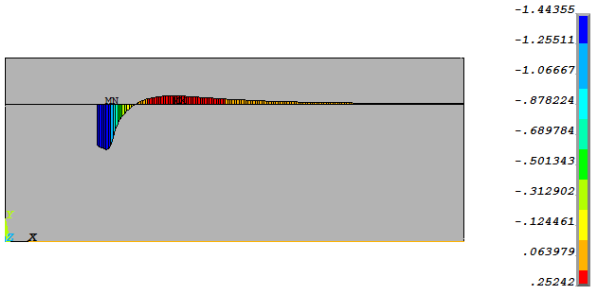 ***Notch size: 200.00mm ; Elastic prop. (α)=-0.040***	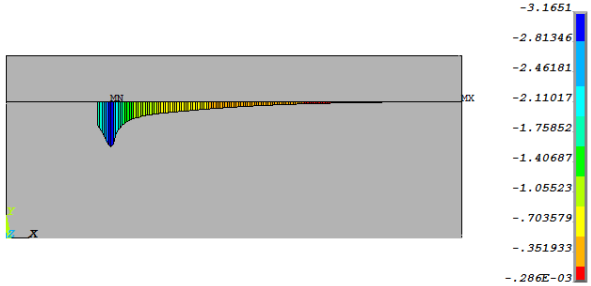 ***Notch size: 200.00mm ; Elastic prop. (α)=-0.040***	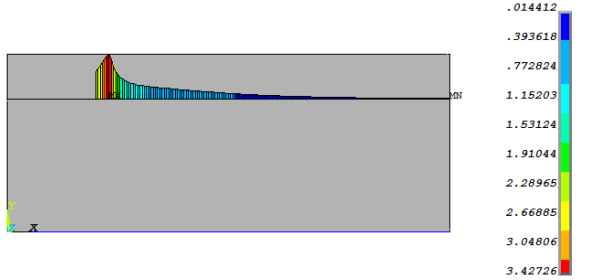 ***Notch size: 200.00mm ; Elastic prop. (α)=-0.040***
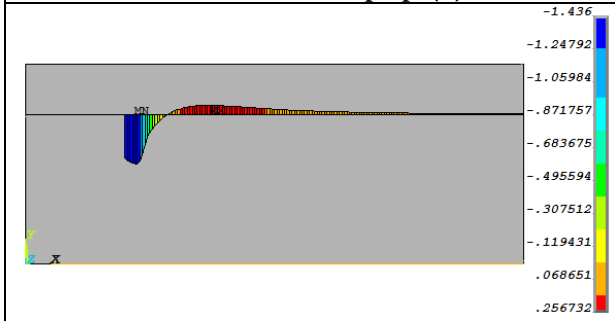 ***Notch size: 200.00mm ; Elastic prop. (α)=-0.015***	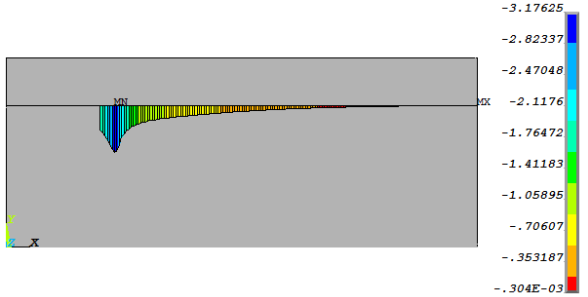 ***Notch size: 200.00mm ; Elastic prop. (α)=-0.015***	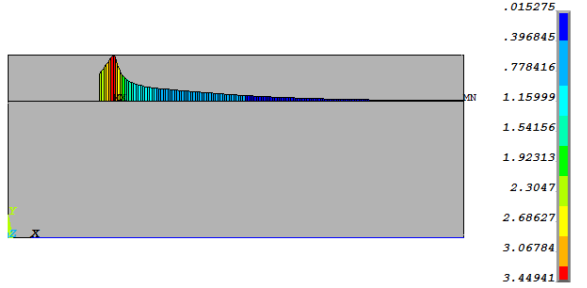 ***Notch size: 200.00mm ; Elastic prop. (α)=-0.015***

APPENDIX A3: FINITE ELEMENT ANALYSIS CONTOURS (DELAMINATION FORMATION PROCESS)

Cohesive stress (Mode I)	Cohesive stress (Mode II)	Cohesive stress (Mixed Mode)
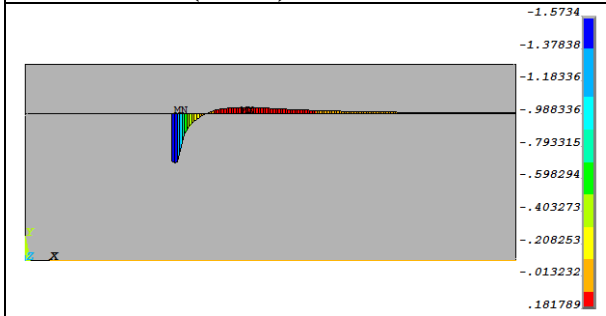	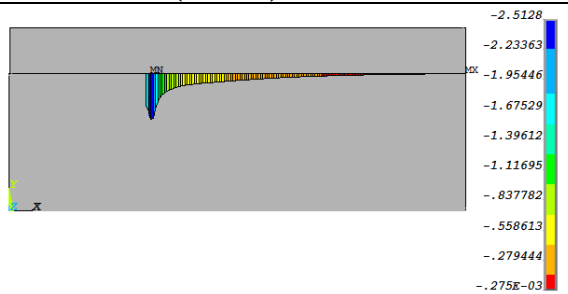	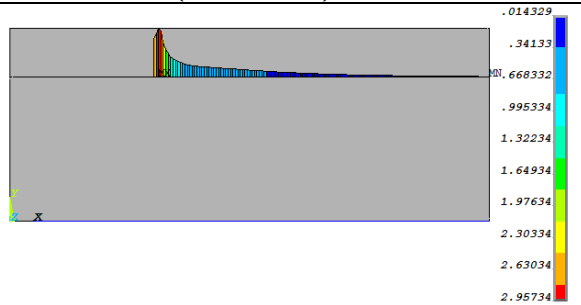
Notch size: 300.00mm ; Elastic prop. (α)=-0.221	***Notch size: 300.00mm ; Elastic prop. (α)=-0.221***	***Notch size: 300.00mm ; Elastic prop. (α)=-0.221***
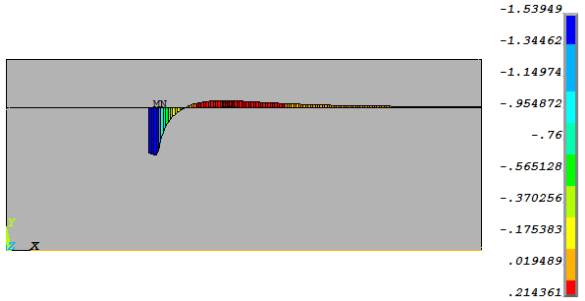	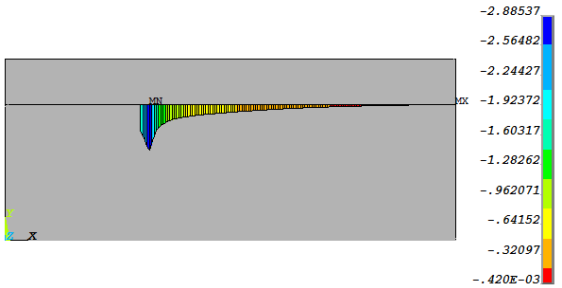	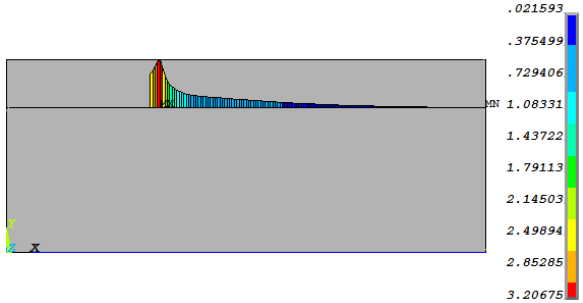
Notch size: 300.00mm ; Elastic prop. (α)=-0.040	***Notch size: 300.00mm ; Elastic prop. (α)=-0.040***	***Notch size: 300.00mm ; Elastic prop. (α)=-0.040***
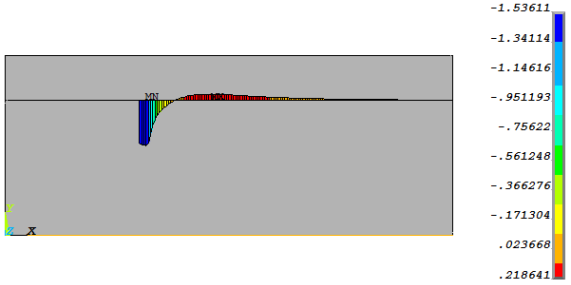	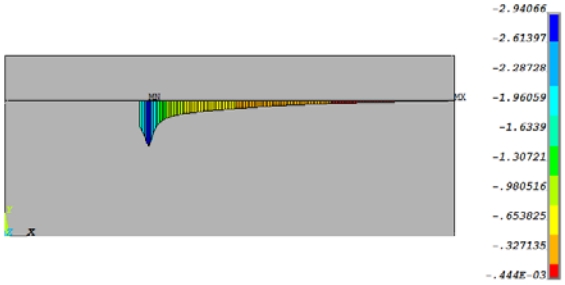	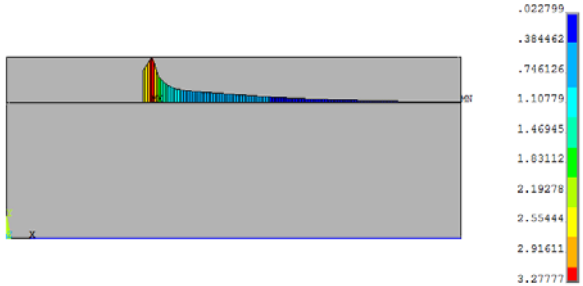
Notch size: 300.00mm ; Elastic prop. (α)=-0.015	***Notch size: 300.00mm ; Elastic prop. (α)=-0.015***	***Notch size: 300.00mm ; Elastic prop. (α)=-0.015***

APPENDIX A4: FINITE ELEMENT ANALYSIS CONTOURS (DELAMINATION PROPAGATION PROCESS)

Cohesive stress (Mode I)	Cohesive stress (Mode II)	Cohesive stress (Mixed Mode)
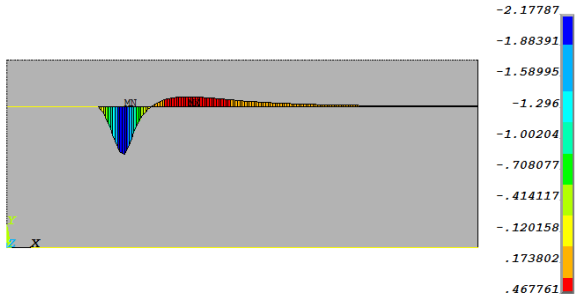 ***Notch size: 0.00mm ; Elastic prop. (α)=-0.221***	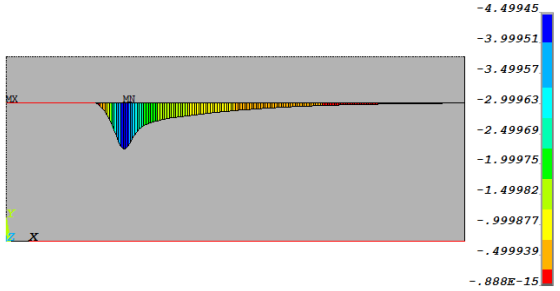 ***Notch size: 0.00mm ; Elastic prop. (α)=-0.221***	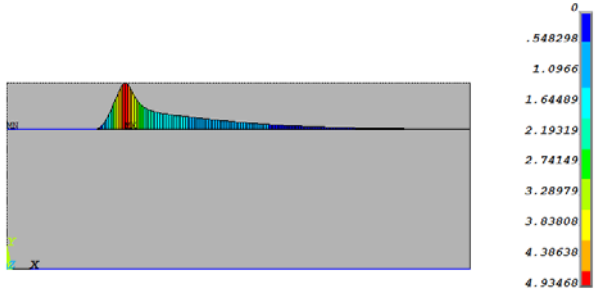 ***Notch size: 0.00mm ; Elastic prop. (α)=-0.221***
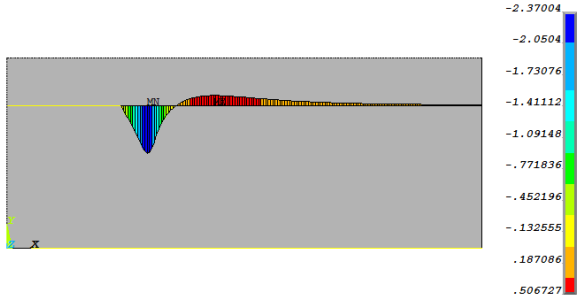 ***Notch size: 0.00mm ; Elastic prop. (α)=-0.040***	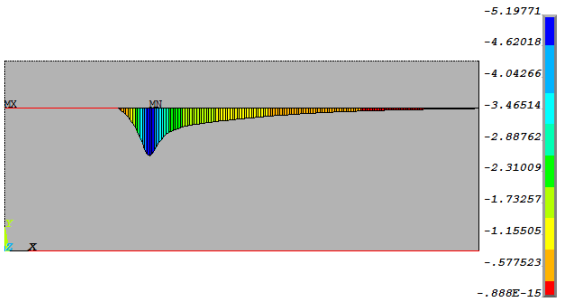 ***Notch size: 0.00mm ; Elastic prop. (α)=-0.040***	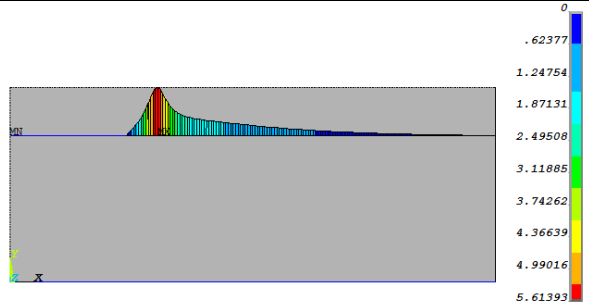 ***Notch size: 0.00mm ; Elastic prop. (α)=-0.040***
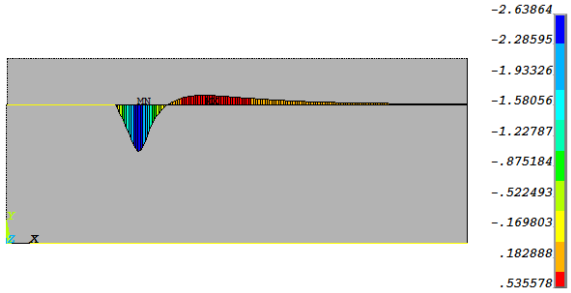 ***Notch size: 0.00mm ; Elastic prop. (α)=-0.015***	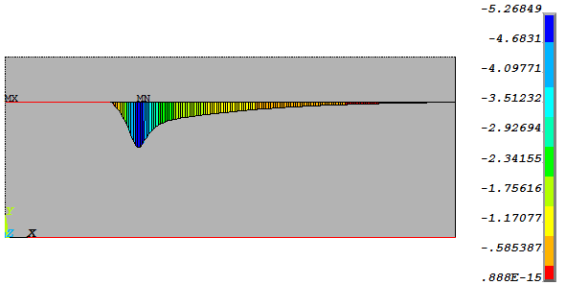 ***Notch size: 0.00mm ; Elastic prop. (α)=-0.015***	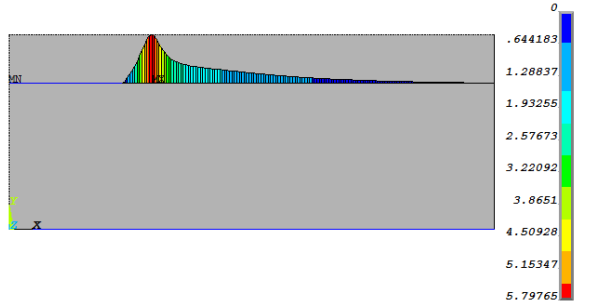 ***Notch size: 0.00mm ; Elastic prop. (α)=-0.015***

APPENDIX A4: FINITE ELEMENT ANALYSIS CONTOURS (DELAMINATION PROPAGATION PROCESS)

Cohesive stress (Mode I)	Cohesive stress (Mode II)	Cohesive stress (Mixed Mode)
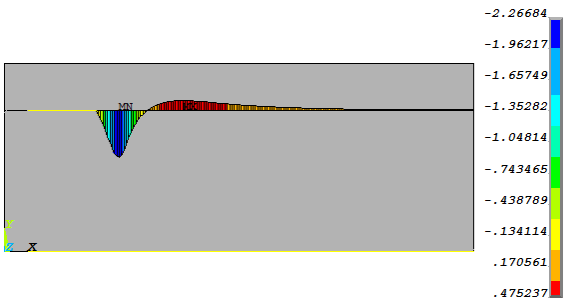 ***Notch size: 50.00mm ; Elastic prop. (α)=-0.221***	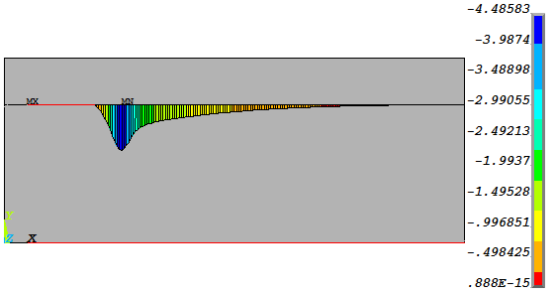 ***Notch size: 50.00mm ; Elastic prop. (α)=-0.221***	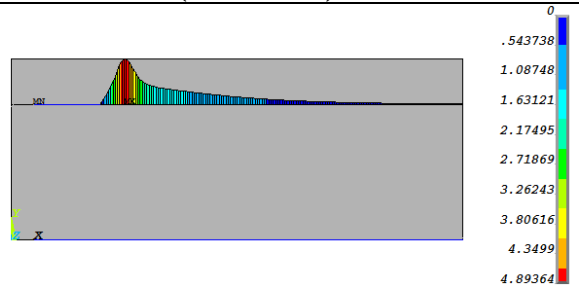 ***Notch size: 50.00mm ; Elastic prop. (α)=-0.221***
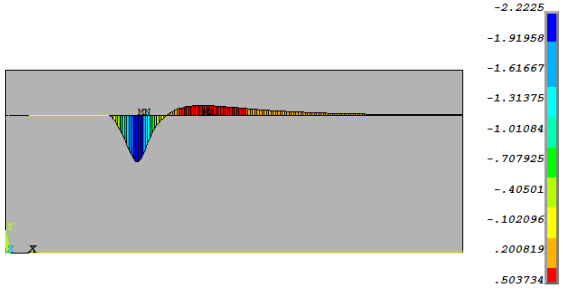 ***Notch size: 50.00mm ; Elastic prop. (α)=-0.040***	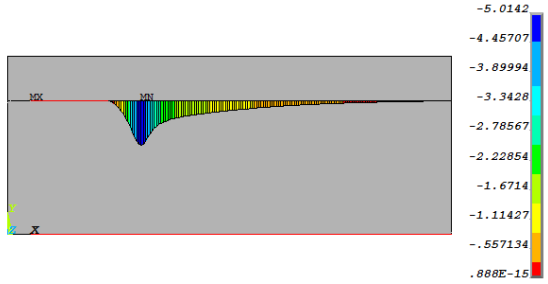 ***Notch size: 50.00mm ; Elastic prop. (α)=-0.040***	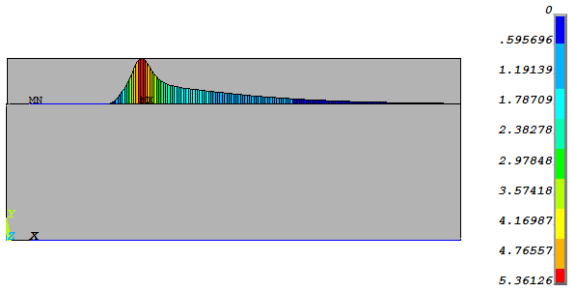 ***Notch size: 50.00mm ; Elastic prop. (α)=-0.040***
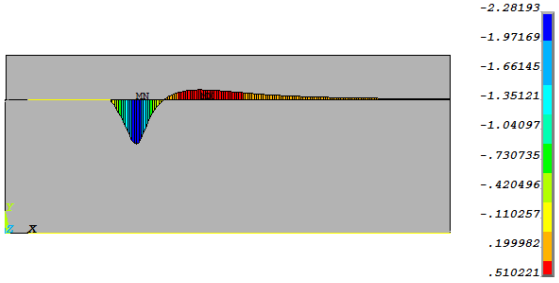 ***Notch size: 50.00mm ; Elastic prop. (α)=-0.015***	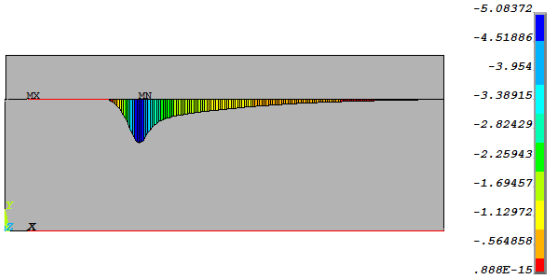 ***Notch size: 0.00mm ; Elastic prop. (α)=-0.015***	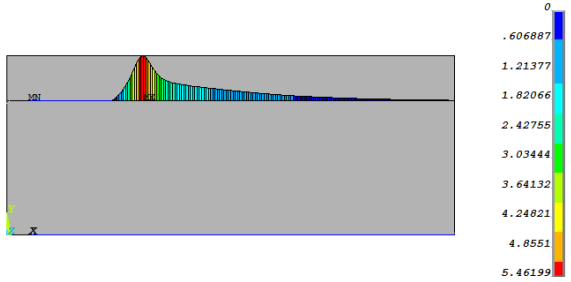 ***Notch size: 0.00mm ; Elastic prop. (α)=-0.015***

APPENDIX A4: FINITE ELEMENT ANALYSIS CONTOURS (DELAMINATION PROPAGATION PROCESS)

Cohesive stress (Mode I)	Cohesive stress (Mode II)	Cohesive stress (Mixed Mode)
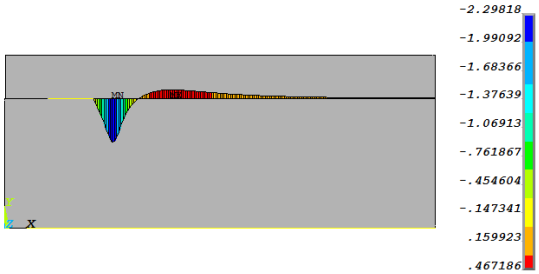	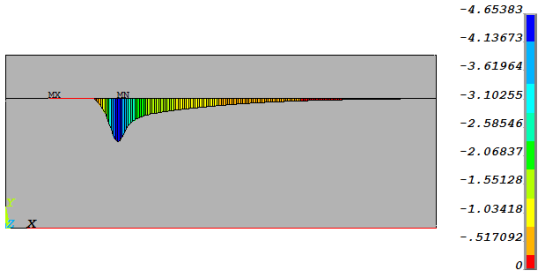	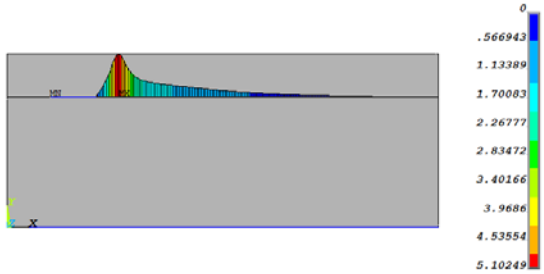
Notch size: 100.00mm ; Elastic prop. (α)=-0.221	***Notch size: 100.00mm ; Elastic prop. (α)=-0.221***	***Notch size: 100.00mm ; Elastic prop. (α)=-0.221***
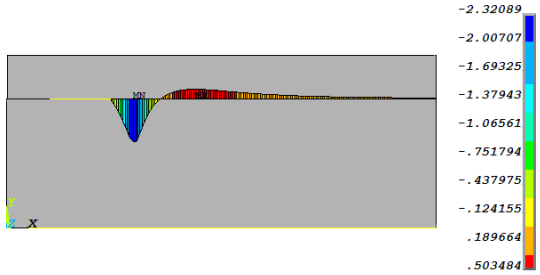	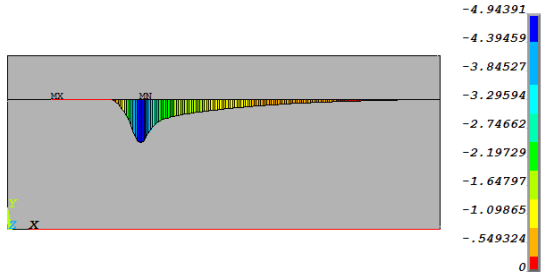	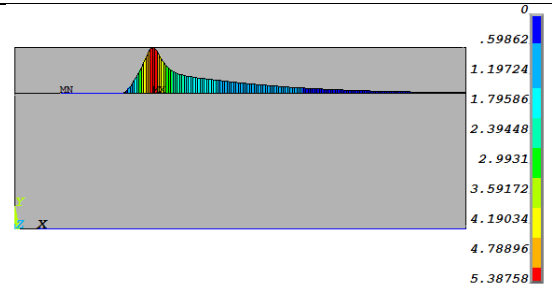
Notch size: 100.00mm ; Elastic prop. (α)=-0.040	***Notch size: 100.00mm ; Elastic prop. (α)=-0.040***	***Notch size: 100.00mm ; Elastic prop. (α)=-0.040***
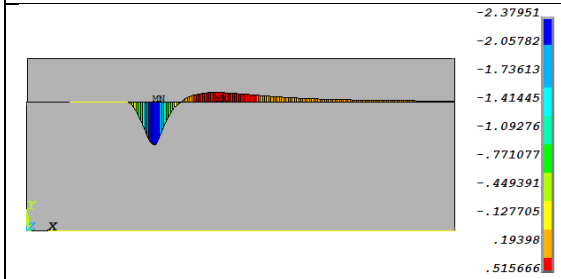	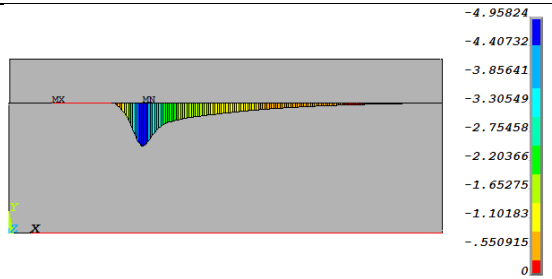	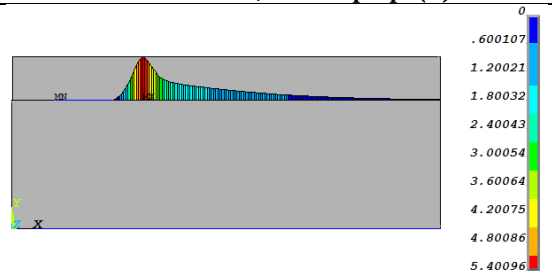
Notch size: 100.00mm ; Elastic prop. (α)=-0.015	***Notch size: 100.00mm ; Elastic prop. (α)=-0.015***	***Notch size: 100.00mm ; Elastic prop. (α)=-0.015***

APPENDIX A4: FINITE ELEMENT ANALYSIS CONTOURS (DELAMINATION PROPAGATION PROCESS)

Cohesive stress (Mode I)	Cohesive stress (Mode II)	Cohesive stress (Mixed Mode)
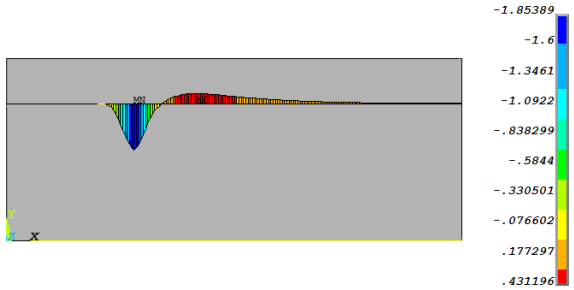 ***Notch size: 200.00mm ; Elastic prop. (α)=-0.221***	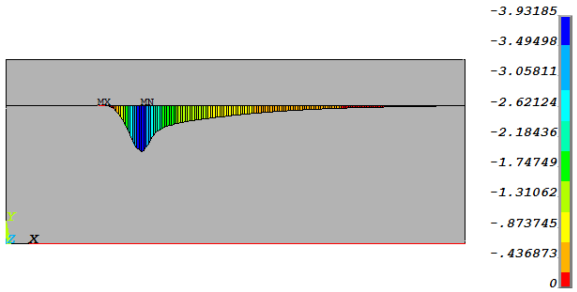 ***Notch size: 200.00mm ; Elastic prop. (α)=-0.221***	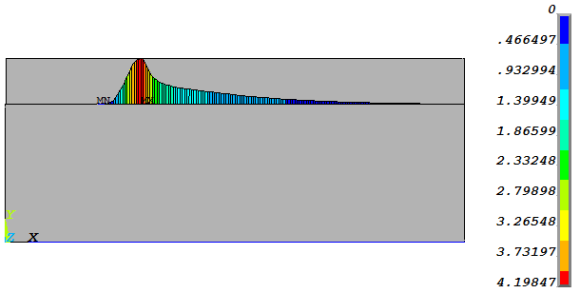 ***Notch size: 200.00mm ; Elastic prop. (α)=-0.221***
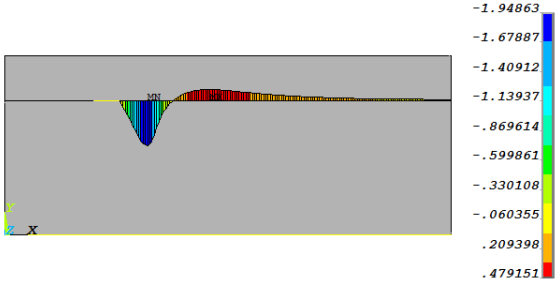 ***Notch size: 200.00mm ; Elastic prop. (α)=-0.040***	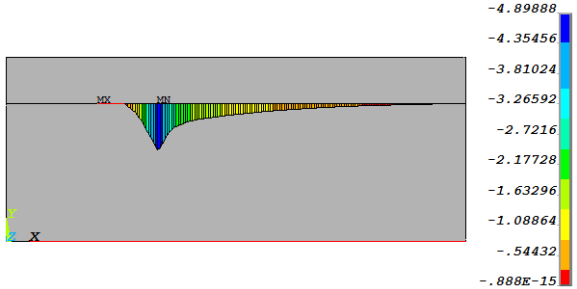 ***Notch size: 200.00mm ; Elastic prop. (α)=-0.040***	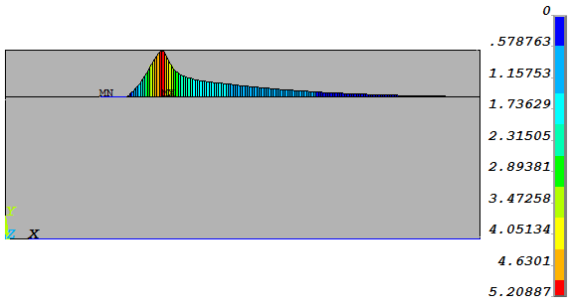 ***Notch size: 200.00mm ; Elastic prop. (α)=-0.040***
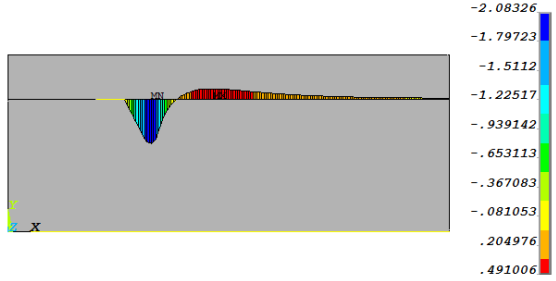 ***Notch size: 200.00mm ; Elastic prop. (α)=-0.015***	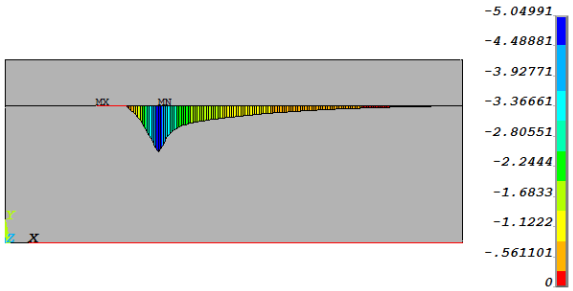 ***Notch size: 200.00mm ; Elastic prop. (α)=-0.015***	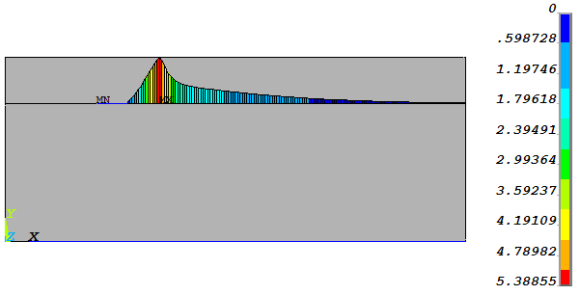 ***Notch size: 200.00mm ; Elastic prop. (α)=-0.015***

APPENDIX A4: FINITE ELEMENT ANALYSIS CONTOURS (DELAMINATION PROPAGATION PROCESS)

Cohesive stress (Mode I)	Cohesive stress (Mode II)	Cohesive stress (Mixed Mode)
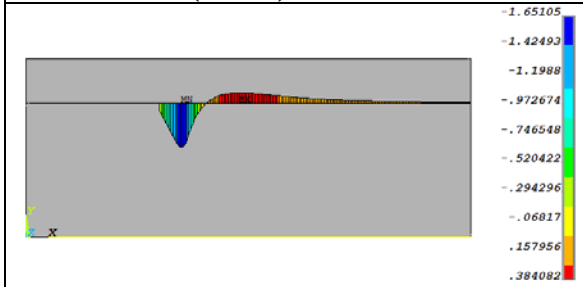 ***Notch size: 300.00mm ; Elastic prop. (α)=-0.221***	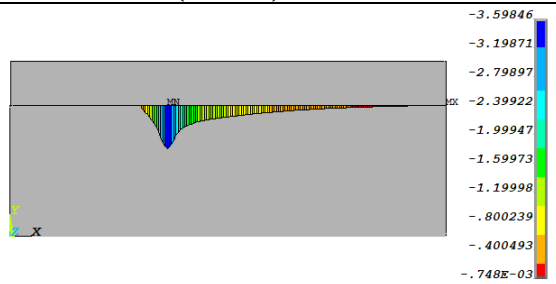 ***Notch size: 300.00mm ; Elastic prop. (α)=-0.221***	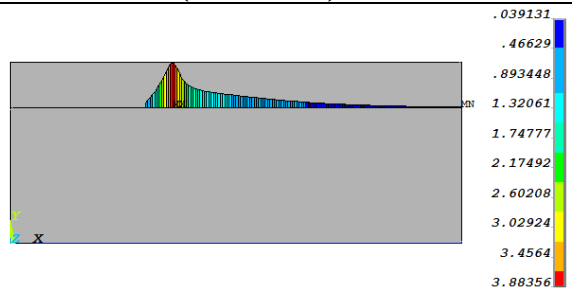 ***Notch size: 300.00mm ; Elastic prop. (α)=-0.221***
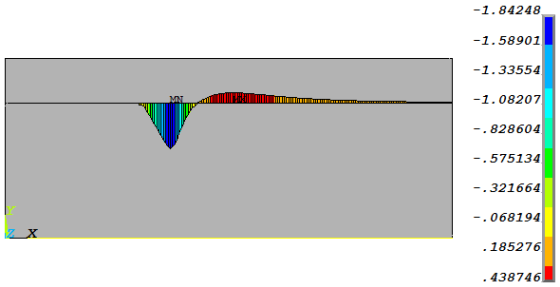 ***Notch size: 300.00mm ; Elastic prop. (α)=-0.040***	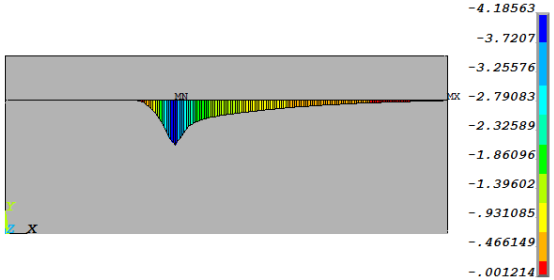 ***Notch size: 300.00mm ; Elastic prop. (α)=-0.040***	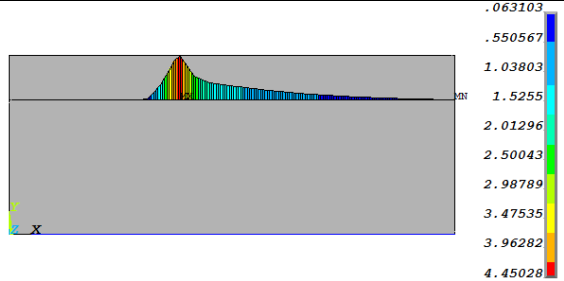 ***Notch size: 300.00mm ; Elastic prop. (α)=-0.040***
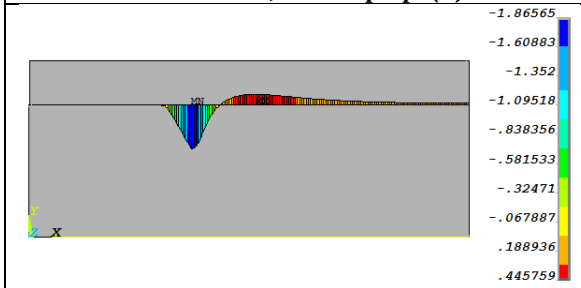 ***Notch size: 300.00mm ; Elastic prop. (α)=-0.015***	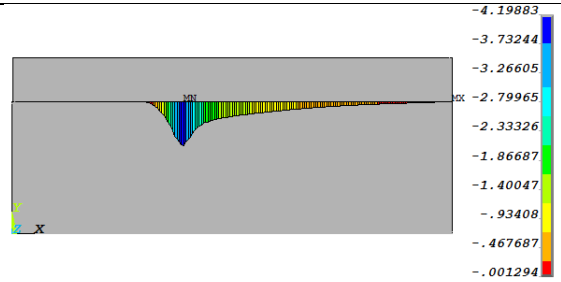 ***Notch size: 300.00mm ; Elastic prop. (α)=-0.015***	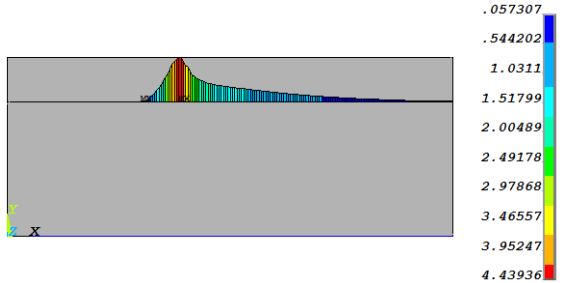 ***Notch size: 300.00mm ; Elastic prop. (α)=-0.015***